Limit on Majorana Neutrino Mass with Neutrinoless Double Beta Decay from KamLAND-Zen

著者	Yoshida Hisataka
学位授与機関	Tohoku University
学位授与番号	11301甲第15564号
URL	http://hdl.handle.net/10097/58802

博士論文

Limit on Majorana Neutrino Mass with Neutrinoless Double Beta Decay from KamLAND-Zen

(KamLAND-Zen でのニュートリノを伴わない二重ベータ崩壊測定による
ニュートリノのマヨラナ質量への制限)

吉田　学立

平成 25 年

Abstract

Neutrinoless double beta decay is allowed in the Majorana neutrino scenario, however, the scenario is a beyond the standard model, and it has not been observed so far. The half-life of neutrinoless double beta decay depends on the nuclear matrix element (NME), the phase space factor, and the Majorana neutrino mass. We can calculate the Majorana neutrino mass by measuring the half-life of neutrinoless double beta decay, and thus constrain the absolute neutrino mass, which no one knows.

KamLAND-Zen is an experiment of search for neutrinoless double beta decay with KamLAND Detector. The construction of KamLAND-Zen started in the summer of 2011, and data acquisition started in October 2011. The data taking of KamLAND-Zen 1st phase was suspended for the purification campaign to reduce the backgrounds, which started in June 2012. This thesis mainly describes in the detail the analysis and results from KamLAND-Zen 1st phase, which were summarized in an article published in Physical Review Letters [1].

The exposure of KamLAND-Zen 1st phase is 89.5 kg-year of ^{136}Xe, which is the highest exposure of a double beta decay experiment in the world up to now. We did not observe the signal of neutrinoless double beta decay, and deduced a lower limit on the half-life of $0\nu\beta\beta$ decay as $T^{0\nu}_{1/2} > 1.9 \times 10^{25}$ year at 90 % confidence level (C.L.) as the most stringent limit so far for this isotope.

The EXO-200 is an experiment for neutrinoless double beta decay search with ^{136}Xe, and they reported the lower limit on the half-life of $0\nu\beta\beta$ decay as $T^{0\nu}_{1/2} > 1.6 \times 10^{25}$ year at 90 % C.L.. By reproducing the EXO-200 experiment with Toy Monte Carlo and $\Delta\chi^2$ method, the combined result from KamLAND-Zen and EXO-200 gave the lower limit as $T^{0\nu}_{1/2} > 3.4 \times 10^{25}$ year at 90 % C.L.. This corresponds to a Majorana neutrino mass limit $\langle m_{\beta\beta} \rangle < (120 - 250)$ meV, where the range is based on a representative range of available NME calculations. Using these calculations, the result excludes at 97.5% C.L. the range expected from the report of the neutrinoless double beta decay detection in ^{76}Ge claimed by a part of the HEIDELBERG-MOSCOW Collaboration[2].

In conclusion, we achieved the most stringent limit on neutrinoless double beta decay from KamLAND-Zen 1st phase, and excluded at 97.5% C.L. the claim of the its detection in ^{76}Ge with EXO-200 experiment and the available NME calculations.

Acknowledgments

It is my exquisite pleasure to finish doctor course and take a degree of Doctor of Philosophy in RNCS, Tohoku University. This accomplishment was supported by many people and institutes for over 5 years, and I would like to express my gratitude here.

First, I would like to show my greatest appreciation to Prof. Kunio Inoue, who is my superviser and a spokesperson of KamLAND/KamLAND-Zen experiments. He invited me to join KamLAND and KamLAND-Zen Collaboration as a student, and I could obtain valuable advises and persistent help from him to improve my study. My deepest appreciation goes to Associate Prof. Junpei Shirai. He let me know how interesting particle physics is in his lecture, and also gave me incisive comments for my study. Associate Prof. Masayuki Koga and Dr. Kengo Nakamura supported me in Kamioka. Their technical advise, educational comment and appropriate feedback have been a great help to understand and operate the detectors and apparatus onsite.

I would like to thank the collaborators in RCNS, Associate Prof. Tadao Mitsui, Dr. Kyoko Tamae, Dr. Itaru Shimizu, Dr. Yoshihito Gando, Dr. Haruo Ikeda, Dr. Koji Ishidoshiro, Dr. Kota Ueshima, Dr. Hiroko Watanabe, Dr. Azusa Gando, Dr. Yasuhiro Takemoto and Dr. Daisuke Motoki. I learned many things under the mentorship of them, not only things related to physics. Especially, my intellectual debt is to Dr. Itaru Shimizu, who helped and supported me in the analytical processes. In addition, my life in Sendai and Kamioka have been enjoyable together with them including all students in RCNS. These five years in RCNS has been worthwhile, and will be priceless and precious memory in my life.

Special thanks also to foreign collaborators, especially Patrick Decowski, Jason Detwiler in the writing committee for the third result of KamLAND-Zen. We had meaningful discussions to defense against referees, and finally our manuscript was accepted in Physical Review Letters owing to their enormous contribution. For this thesis, Tommy O'Donnell gave me dedicated comments and advises about English as well as physics. Thanks to his contributions, the thesis could be completed. I feel cordial gratitude for Tommy.

Also, I gratefully appreciate the financial support of JSPS Fellowship that made it possible to complete my challenge.

On a final note, I would like to express my gratitude to my family for their moral support and encouragements.

Contents

List of Figures

List of Tables

Chapter 1

Introduction

Neutrinos have played a key role in particle physics for many years after W. Pauli postulated their existence in 1930. The neutrino is an interesting character in the standard model (SM) of particle physics, which has neutral charge and only weak interaction with the other particles. We assumed the absolute neutrino mass is zero in the SM for a long time. However, today we know they have small non-zero masses because of the discovery of neutrino oscillation.

At Research Center for Neutrino Science (RCNS) in Tohoku university, the study of neutrino oscillation has been performed with KamLAND detector for more than a decade. In addition to the result from the other experiments for neutrino oscillation, the evidence of neutrino oscillation is derived from KamLAND experiment, resulting that neutrino has non-zero absolute mass because neutrino oscillation is caused by neutrino mass mixing. It means that neutrino is a particle beyond the SM.

The non-zero neutrino absolute mass implies that neutrino may be a Majorana fermion which is a fermion such that the particle and anti-particle are identical. This hypothesis is also beyond the SM, and there are many interesting scenarios predicted to explain our matter dominant universe if the hypothesis were true. Now, we are on the next stage of neutrino study to answer to the question whether neutrino is Dirac or Majorana particle. The search for neutrinoless double beta decay is an available probe to answer the question. Furthermore, the measurement of neutrinoless double beta decay half-life can contribute to our knowledge of the effective Majorana neutrino mass. We can know how much neutrino is lightweight by the measurement of the decay.

Double beta decay is a rare nuclear process occurring in even-even nuclei, such as ^{76}Ge and ^{136}Xe, for which ordinary beta decay is energetically forbidden or highly suppressed by large spin differences. There were some experiments for double beta decay observation so far, and there are many experiments on going or planned to start. A part of the Heidelberg-Moscow Collaboration claimed the detection of neutrinoless double beta decay in ^{76}Ge. The first claim has been reported in 2001, and the latest result was published in 2006 by H. V. Klapdor-Kleingrothaus and I. V. Krivosheina, which is called KK-Claim. They got the half-life of neutrinoless double beta decay in ^{76}Ge as $T^{0\nu}_{1/2} = 2.23^{+0.44}_{-0.32} \times 10^{25}$ year, and the peak had 6 σ C.L., corresponding to the Majorana neutrino mass $\langle m_{\beta\beta} \rangle = 320 \pm 30$ meV. However, there are several suspicious points in their result, and this result has not been accepted in the double beta decay community. The KK-Claim should be tested by the other double beta decay experiments as soon as possible, because there also has not been any confirmation or refutation for KK-Claim so far.

There is a great worth measuring the half-life of neutrinoless double beta decay to mention the Majorana neutrino mass. By the measurement of neutrino oscillation, we know precise parameters of Δm^2, which is the mass-squared difference of neutrinos. On the other hand, we can not determine the neutrino mass hierarchy with only Δm^2, which can be restricted as Normal Hierarchy (NH), Inverted Hierarchy (IH) and Quasi-Degenerated Hierarchy (QD). The effective Majorana neutrino mass can constrain the hierarchy if the mass is reasonable value with Δm^2. Neutrinoless double beta decay is also a probe for the neutrino mass hierarchy.

We started KamLAND-Zen as international collaboration experiment in Kamioka mine for neutrinoless double beta decay of ^{136}Xe with KamLAND detector. We are well-acquainted with KamLAND detector, and it has already been constructed and established as a detector with the cleanest (without radioactive impurities) environment. The low background rate is very important for double beta decay because the half life of the decay is much long (typically longer than 10^{22} years). Therefore, KamLAND detector is suitable for the measurement of double beta decay, and has an advantage in the reliability of the detector with the experience for the past decade. The target mass is 300 kg of ^{136}Xe, which is the largest in the past and current double beta decay experiments. KamLAND-Zen is new generation experiment which has a strong competitive power and expected to lead in the international double beta decay community.

The construction of KamLAND-Zen was completed in the summer 2011, and the data taking started in October 2011. KamLAND-Zen 1st phase is suspended on June in 2012 for the purification campaign to reduce the backgrounds. The 1st phase includes the period of filtration campaign in February 2012 and the period after that, and we could get data of 213 days as livetime from KamLAND-Zen 1st phase. The finalized analysis result of KamLAND-Zen 1st phase is a main topic, and related issues are described in the thesis.

Chapter 2

Neutrino Physics and Double Beta Decay

The physical matter is thought to consist of the particles which are the ultimate small, and they have no structure. The properties of the particles have been investigated by various experiments for quarks which are constitutive of nucleons and mesons, charged leptons such as orbital electron in the atoms, and bosons to mediate the forces. The neutrino is one of the particles to be investigated. However, neutrinos are neutral charged particles and affected by only weak interaction with much small cross section. It is difficult to detect and study neutrinos due to this, therefore there are still unknown properties of neutrinos remaining in theoretical and experimental side.

Some predicted and observed properties of neutrino can be beyond the Standard Model of particle physics (SM), and that is why neutrino is interesting particle and useful probe to validate the models beyond the SM. Neutrino physics and double beta decay as being important probe in particle physics are mentioned in this chapter.

2.1 Neutrino Physics

The matter constitutive particles can be categorized into 2 types of fermions, so called quarks and leptons. Each type has 2 different electric charged particles, and there are similar particles which is different of the mass, we defined the difference as a generation. Table 2.1 shows the summary of particles of 2 fermion types categorized with the charge and the generation. Neutrino is charge neutral particle, and neutrino is not constitutive particle of the matter, in fact. In addition, the mass of neutrino is enormously small compared with the other particles, and the reason is still unknown.

Table 2.1: The constitutive particles of matter.

	charge	1st generation	2nd generation	3rd generation
quark	$+2/3$	u	c	t
	$-1/3$	d	s	b
lepton	-1	e	μ	τ
	0	ν_e	ν_μ	ν_τ

In this section, the potential mysterious properties of neutrino appear with historical beginning of neutrino physics, neutrino oscillation and small neutrino mass.

2.1.1 Beginning of Neutrino Physics

Postulation of the Neutrino

The neutrino was introduced by W. Pauli in 1930 for the compensation of non-conservation of beta-decay electron energy and momentum [3]. The observed energy of beta-decay electron is a continuous spectrum, which is not consistent with theoretical calculation without neutrino. W. Pauli came up with an introduction of the fermion (spin = 1/2) with neutral charge, a much smaller mass compared with proton, finite small magnetic moment and the penetration power at least 10 times greater than that of the gamma ray. This idea worked well, and E. Fermi constructed the equation of the interaction between neutrino and the other particle in 1933 [4] 3 years after Pauli's conjecture. The interaction is represented by a product with four spinor fields, and called as the four Fermi interaction. E. Fermi established the theoretical equations of beta decay, and it is shown in equation 2.1.

$$n \rightarrow p + e^{-} + \overline{\nu}_e \tag{2.1}$$

At that time, Fermi assumed that neutrino mass is zero with considering the empirical energy spectrum of decay electron. The zero mass neutrino is introduced into the standard model (SM) today.

Discovery of Neutrinos

The discovery of neutrino was accomplished by F. Reines and C. L. Cowan, Jr. in 1956 [5]. They detected inverse beta decay process (equation 2.2) followed by $e^{+}e^{-} \rightarrow 2\gamma$ and a gamma ray from neutron capture on Cd in a large scintillator using an anti-neutrino beam from a nuclear pile.

$$\overline{\nu}_e + p \rightarrow n + e^{+} \tag{2.2}$$

The positron which is emitted in the process immediately annihilate with electron, and the neutron is captured on proton and emits gamma ray. They observed these coincidence events, and experimentally demonstrated the existence of neutrino with inverse double beta decay process. The observed neutrino was electron anti-neutrino ($\overline{\nu}_e$), we know today.

Subsequently, L. M. Lederman, M. Schwartz and J. Steinberger showed that more than one type of neutrino exists by first detecting interactions of the muon neutrino in 1962 [6]. They found that the neutrino which is generated by decay of charged pion interacts not with electrons but muons, and it is called muon neutrino.

The tau neutrino was associated when the third type of lepton, tau, have been discovered in 1975 at the Stanford Linear Accelerator Center. However, it took many years to detect the tau neutrino because of difficulty of their generation. In 2000, the interaction of tau neutrino was finally discovered by DONUT collaboration at Fermilab using nuclear emulsion [7].

The number of light neutrino types is deduced from collider experiments. The most precise measurements of the number of light neutrino types, N_ν, come from studies of Z boson production in $e^{+}e^{-}$ collisions. The invisible partial width, Γ_{inv}, is determined by subtracting the measured visible partial widths, corresponding to Z decays into quarks and charged leptons, from the total Z width. The invisible width is assumed to be due to N_ν light neutrino species each contributing the neutrino partial width Γ_ν as given by the Standard Model (SM). In order to reduce the model dependence, the SM value for the ratio of the neutrino to charged leptonic partial widths, $(\Gamma_\nu/\Gamma_l)_{\rm SM} = 1.991 \pm 0.001$, is used instead of $(\Gamma_\nu)_{\rm SM}$ to determine the number of light neutrino types in the following.

$$N_\nu = \frac{\Gamma_{\rm inv}}{\Gamma_l}\left(\frac{\Gamma_\nu}{\Gamma_l}\right)_{\rm SM}$$

The combined result from four LEP experiments give $N_\nu = 2.984 \pm 0.008$ [8].

Solar Neutrino Problem

After discovery of neutrinos, neutrino is used as powerful prove to investigate cosmological issues such as unknown structure of the Sun due to the strong penetrating power of neutrinos. The observation of solar neutrinos directly addresses the theory of stellar structure and evolution, which is the basis of the standard solar model (SSM).

The first report of solar neutrino observation is given by J. N. Bahcall and R. Davis in 1976 [9]. They counted the anti-neutrino with ^{37}Cl via inverse beta decay process ($\nu_e + {}^{37}\mathrm{Cl} \rightarrow {}^{37}\mathrm{Ar} + e^-$) in Homestake mine. However, the counting rate was only one third of the expected rate from SSM, resulting solar neutrino problem.

The solar neutrino problem was a major discrepancy between measurements of the numbers of neutrinos flowing through the Earth and theoretical models of the solar interior, lasting from the mid-1960s to about 2002. The discrepancy has since been resolved by new understanding of neutrino physics, requiring a modification of the SM. The solution is neutrino oscillation which implies that the neutrinos have non-zero mass and is not predicted in the original SM, and described in next section 2.1.2.

2.1.2 Neutrino Oscillation

The idea of neutrino oscillation first came up with analogy of neutral kaon mixing by B. Pontecorvo in 1952. Although such matter-antimatter oscillation has not been observed, this idea formed the conceptual foundation for the quantitative theory of neutrino flavor (type) oscillation. The theory of neutrino flavor oscillation was elaborated by Pontecorvo in 1967 after Maki, Nakagawa, and Sakata developed the idea with neutrino mixing matrix in 1962. The unitary matrix is called Pontecorvo—Maki—Nakagawa—Sakata (PMNS) or Maki—Nakagawa—Sakata (MNS) matrix which contains information on the mismatch of quantum states of leptons when they propagate freely and when they take part in the weak interactions.

In the theory of neutrino oscillation, the neutrino flavor eigenstates $|\nu_\alpha\rangle$ $(\alpha = e, \mu, \tau)$ can be expressed as a linear combination of the mass eigenstates $|\nu_i\rangle$ $(i = 1, 2, 3)$ with U^* which is a complex conjugate of a 3×3 PMNS unitary matrix U.

$$|\nu_\alpha\rangle = \sum_{i=1}^{3} U^*_{\alpha i}|\nu_i\rangle \tag{2.3}$$

One can write the mass eigenstates with respect to the flavor eigenstates as follows.

$$|\nu_i\rangle = \sum_{\alpha=e,\mu,\tau} U_{\alpha i}|\nu_\alpha\rangle \tag{2.4}$$

The PMNS matrix can be written with introduced a Dirac CP-violating phase δ and two Majorana phases α_1 and α_2 as following.

$$U = \begin{pmatrix} c_{12}c_{13} & s_{12}c_{13} & s_{13}e^{-i\delta} \\ -s_{12}c_{23} - c_{12}s_{23}s_{13}e^{i\delta} & c_{12}c_{23} - s_{12}s_{23}s_{13}e^{i\delta} & s_{23}c_{13} \\ s_{12}s_{23} - c_{12}c_{23}s_{13}e^{i\delta} & -c_{12}s_{23} - s_{12}c_{23}s_{13}e^{i\delta} & c_{23}c_{13} \end{pmatrix} \begin{pmatrix} e^{i\frac{\alpha_1}{2}} & & \\ & e^{i\frac{\alpha_2}{2}} & \\ & & 1 \end{pmatrix}, \tag{2.5}$$

where $s_{ij} = \sin\theta_{ij}, c_{ij} = \cos\theta_{ij} (i, j = 1, 2, 3)$. Each mass eigenstation has a definite mass and energy, hence its propagation can be described by the time-dependent Schrödinger equation. In vacuum, with $\hbar = 1$,

$$i\frac{d}{dt}|\nu_i(t)\rangle = \hat{H}|\nu_i(t)\rangle = E_i|\nu_i(t)\rangle, \tag{2.6}$$

where $\hat{H}$ is the Hamiltonian operator in vacuum and E_i is the energy of ν_i. The wave function can be written as follows.

$$|\nu_i(t)\rangle = e^{-iE_it}|\nu_i(0)\rangle. \tag{2.7}$$

The flavor eigenstate propagate is described using equation 2.3, 2.4 and 2.7 in the following.

$$\begin{aligned} |\nu_\alpha(t)\rangle &= \sum_{i=1}^{3} U_{\alpha i}^{*}\, e^{-iE_it}|\nu_i(0)\rangle & (2.8)\\ &= \sum_{\beta=e,\mu,\tau}\sum_{i=1}^{3} U_{\alpha i}^{*}U_{\beta i}\, e^{-iE_it}|\nu_i(0)\rangle. & (2.9)\end{aligned}$$

The amplitude of the transition from $|\nu_\alpha(t)\rangle$ to $|\nu_\beta\rangle$ is given by

$$\langle\nu_\beta|\nu_\alpha(t)\rangle = \sum_{i=1}^{3} U_{\alpha i}^{*}\, U_{\beta i}\, e^{-iE_it}\ . \tag{2.10}$$

The transition probability $P(\nu_\alpha \to \nu_\beta)$ is described with the amplitude (equation 2.10 as follows.

$$\begin{aligned} P(\nu_\alpha \to \nu_\beta) &= |\langle\nu_\beta|\nu_\alpha(t)\rangle|^2 \\ &= \sum_{i=1}^{3}\sum_{j=1}^{3} U_{\alpha i}^{*}U_{\beta i}\, U_{\alpha j}^{*}U_{\beta j}\, e^{-i(E_i-E_j)t}\ . & (2.11)\end{aligned}$$

Therefore, the transition probability for a neutrino with the energy E_ν and propagating distance L, is calculated with PMNS matrix U (equation 2.5) and neutrino mass-squared differences $\Delta m_{ij}^2 = |m_i^2 - m_j^2|$.

$$\begin{aligned} P(\nu_\alpha \to \nu_\beta)(E_\nu, L) = \delta_{\alpha\beta} &- 4\sum_{i>j}\mathrm{Re}(U_{\alpha i}^{*}U_{\beta i}\, U_{\alpha j}^{*}U_{\beta j})\sin^2\frac{\Phi_{ij}}{2} \\ &+2\sum_{i>j}\mathrm{Im}(U_{\alpha i}^{*}U_{\beta i}\, U_{\alpha j}^{*}U_{\beta j})\sin^2\Phi_{ij} & (2.12)\end{aligned}$$

Here, $\delta_{\alpha\beta}$ is Kronecker's delta which corresponds 1 when $\alpha = \beta$ and 0 when $\alpha \neq \beta$. Φ_{ij} is described with Δm_{ij}^2, E_ν and L in the following.

$$\Phi_{ij} = \frac{\Delta m_{ij}^2}{2E_\nu}L = \frac{1.267\Delta m_{ij}^2[\mathrm{eV}^2]}{E_\nu[\mathrm{MeV}]}L[\mathrm{m}]. \tag{2.13}$$

As shown in equation 2.12, the neutrino flavor changes into another flavor in flight, and the flavor can change into original one again. That is why the phenomena is named as neutrino oscillation, and the neutrino mixing angle (θ_{ij}) and the mass-squared differences (Δm_{ij}^2) are determined from a measurement of the survival probability.

Neutrino Oscillation Measurement

The solar neutrino observation by Homestake experiment, GALLEX/GNO and SAGE experiments with ^{71}Ga, Kamiokande/Super-Kamiokande experiment and SNO experiment showed the discrepancies between measurement and prediction of solar neutrino from the standard solar model (SSM) without neutrino oscillation. However, their measurements did not turn out the evidence of neutrino oscillation due to the theoretical uncertainties of the SSM, which means that the prediction of solar neutrino flux depends on the SSM.

The reactor neutrino experiments such as KamLAND experiment could have demonstrated the neutrino oscillation without SSM uncertainties of neutrino source in 2000s. The KamLAND experiment provided the oscillation spectrum of electron anti-neutrino from nuclear reactor in 2002 [28], 2004 [29] and 2008 [30] as shown in Fig 2.1. Finally, the solar neutrino problem is solved with neutrino oscillation which is the phenomena beyond the SM.

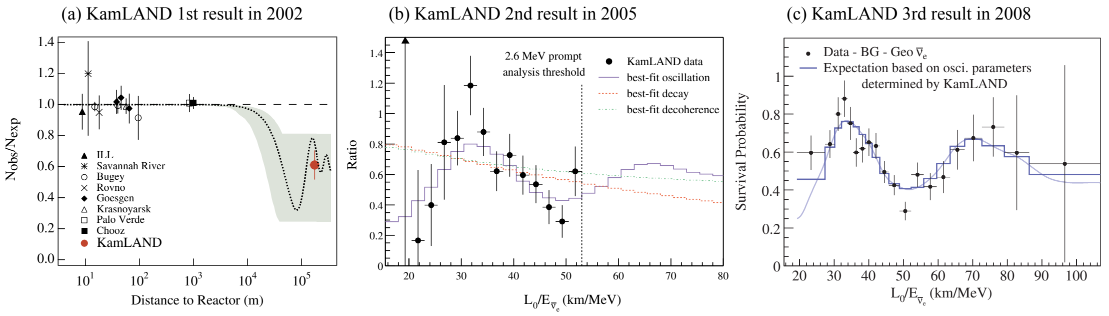
(a) KamLAND 1st result in 2002

(b) KamLAND 2nd result in 2005

(c) KamLAND 3rd result in 2008

Fig 2.1: The results of reactor $\overline{\nu}_e$ flux measurement from KamLAND experiment. The neutrino oscillation due to mass mixing is the best description in each spectrum. (a) shows the ratio of measured to expected $\overline{\nu}_e$ flux from reactor experiments from the first result in 2002 [28]. The solid circle is the KamLAND result plotted at a flux-weighted average distance of $\sim$ 180 km. (b) shows the ratio of the observed $\overline{\nu}_e$ spectrum to the expectation for no-oscillation versus L_0/E ($L_0 = 180$ km) from the second result in 2004 [29]. (c) shows the ratio of the background and geo-neutrino subtracted $\overline{\nu}_e$ spectrum to the expectation for no-oscillation from the third result in 2008 [30].

In addition to solar and atmospheric neutrino observations and reactor neutrino measurements, long baseline experiments such as MINOS, K2K and T2K reported compelling evidence for ν_μ disappearance, while evidence for ν_τ appearance due to $\nu_\mu \rightarrow \nu_\tau$ oscillation was demonstrated by the Super-Kamiokande and OPERA collaborations. As a consequence of the results of the experiments quoted above the existence of oscillations or transitions of the solar ν_e, atmospheric ν_μ and $\overline{\nu}_\mu$, accelerator ν_μ (at L $\sim$ 250 km, L $\sim$ 295 km and L $\sim$ 730 km) and reactor $\overline{\nu}_e$ (at L $\sim$ 180 km), driven by non-zero neutrino masses and neutrino mixing, was firmly established.

Further important developments took place more recently in the period starting from June 2011. First, the T2K Collaboration reported indications for $\nu_\mu \rightarrow \nu_e$ oscillations, that is, of appearance of ν_e in a beam of ν_μ. The MINOS Collaboration also obtained data consistent with $\nu_\mu \rightarrow \nu_e$ oscillations. Subsequently, the Double Chooz Collaboration reported indications for disappearance of reactor $\overline{\nu}_e$ at L $\sim$ 1.1 km. Also, strong evidence for reactor $\overline{\nu}_e$ disappearance at L $\sim$ 1.65 km and L $\sim$ 1.38 km was obtained respectively in the Daya Bay and RENO experiments (with statistical significance of 5.2 σ and 4.9 σ). Further evidences for reactor $\overline{\nu}_e$ disappearance (at 2.9 σ) and for $\nu_\mu \rightarrow \nu_e$ oscillations (at 3.1σ) were reported by the Double Chooz and T2K experiments, while the Daya Bay Collaboration presented updated, more precise results on reactor $\overline{\nu}_e$ disappearance in 2013.

Neutrino Oscillation Parameters

The latest neutrino oscillation parameters derived from a global fit of the current neutrino oscillation data [15] are summarized in Table 2.2.

Table 2.2: The best-fit values of 3 flavor neutrino oscillation parameters. The parameters are derived from a global fit of the current neutrino oscillation data [15]. The results shown are obtained with the old reactor $\overline{\nu}_e$ fluxes. Δm^2 is defined as : $\Delta m^2 = m_3^2 - (m_2^2 + m_1^2)/2$. Thus, $\Delta m^2 = \Delta m_{31}^2 - \Delta m_{21}^2/2$ for Normal Hierarchy (NH); $m_1 < m_2 < m_3$, and $\Delta m^2 = \Delta m_{31}^2 + \Delta m_{21}^2/2$ for Inverted Hierarchy (IH); $m_3 < m_1 < m_2$. The values (values in brackets) correspond to those for NH (for IH).

Parameters	Best-fit values with $\pm 1\sigma$
$\Delta m_{21}^2 [10^{-5}\mathrm{eV}^2]$	$7.54_{-0.22}^{+0.26}$
$\Delta m^2 [10^{-3}\mathrm{eV}^2]$	$2.43_{-0.10}^{+0.06}, (2.42_{-0.11}^{+0.07})$
$\sin\theta_{12}$	$0.307_{-0.016}^{+0.018}$
$\sin\theta_{23}$	$0.386_{-0.021}^{+0.024}, (0.392_{-0.022}^{+0.039})$
$\sin\theta_{13}$	$0.0241 \pm 0.0025, (0.0244_{-0.0025}^{+0.0023})$
δ/π	$1.08_{-0.31}^{+0.28}, (1.09_{0.26}^{0.38})$

2.1.3 Neutrino Mass

The Standard Model of particle physics (SM) assumes that neutrinos are massless. The neutrino oscillation which requires neutrinos to have non-zero masses, however, was experimentally established as described in section 2.1.2. The absolute masses of neutrinos are one of the most curious topics in the particle physics today, while the mass-squared differences are given by the oscillation experiments.

The neutrino masses have been predicted with various approaches, and we know that they are quite small compared with the other particles (e.g. electron mass, $m_e = 0.511$ MeV) as shown in Fig 2.2, although the absolute mass scale of neutrinos is still undefined. The approaches are introduced in the following.

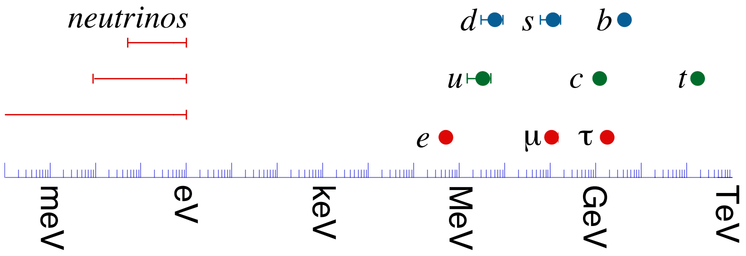

Fig 2.2: Mass scale of particles. The quarks are drawn in green and blue points, and charged leptons are drawn in red. The neutrino mass is indicated with the ranges from various predictions. The figure was contributed by H. Murayama [14].

from Neutrino Oscillation

The mass-squared differences are provided by the neutrino oscillation experiments, and they are summarized in Table 2.2. The hierarchy of neutrinos, however, is also unknown due to the definition of the parameters. The Normal Hierarchy (NH) indicates the order of neutrino mass eigenstate $m_1 < m_2 < m_3$, and Inverted Hierarchy (IH) indicates $m_3 < m_1 < m_2$. If the absolute mass scale of neutrino is enough large $m_1 \cong m_2 \cong m_3$, the hierarchy is degenerate (Quasi-Degenerate, QD). The possible neutrino mass hierarchies allowed by neutrino oscillation experiments are drawn in Fig 2.3.

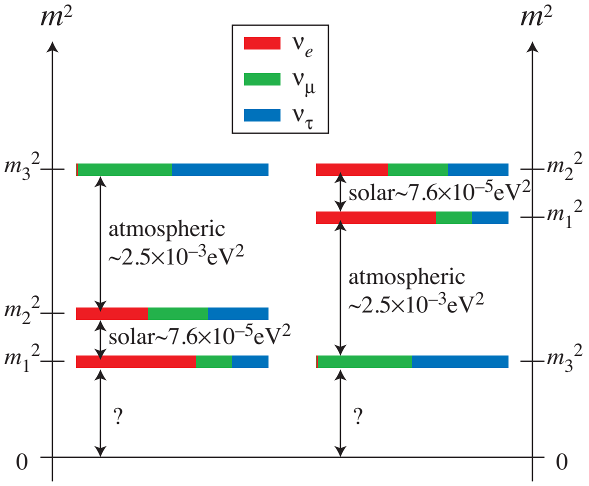

Fig 2.3: Possible neutrino mass hierarchies allowed by oscillation experiments. The left figure indicates NH ($m_1 < m_2 < m_3$), and right one indicates IH ($m_3 < m_1 < m_2$). The figure was contributed by H. Murayama [14].

All three types of hierarchies (NH, IH and QD) are compatible with the existing constraints on the absolute scale of neutrino mass.

from Cosmology

The Cosmic Microwave Background (CMB) data of the WMAP experiment, combined with supernovae data and data on galaxy clustering can be used to obtain an upper limit on the sum of neutrino masses. Depending on the model complexity and the input data used one obtains [17]; $\sum_j m_j \leq (0.3 - 1.3)$ eV at 95% C.L.

In March 2013, the Planck Collaboration reported their first constraints on total mass of neutrinos [18]. Assuming the existence of three massive neutrinos and the validity of the ΛCDM (Cold Dark Matter) model, and combining their data on the CMB temperature power spectrum with the WMAP polarisation low-multipole ($l \leq 23$) data and ACT high-multipole ($l \geq 2500$) CMB data [19], [20], the Planck Collaboration reported the following upper limit on the sum of the neutrino masses [18].

$$\sum_j m_j < 0.66 \text{ eV}, \qquad \text{at 95\% C.L.}$$

from Direct Measurement

The direct measurement of neutrino mass can be performed on kinematics calculation with beta decay process. Typically, the end point of ^{3}H (Tritium) beta decay is measured to estimate $\overline{\nu}_e$ mass. The discrepancy between the end point from theoretical calculation and measurement should correspond to $\overline{\nu}_e$ mass in the beta decay process as shown in Fig 2.4.

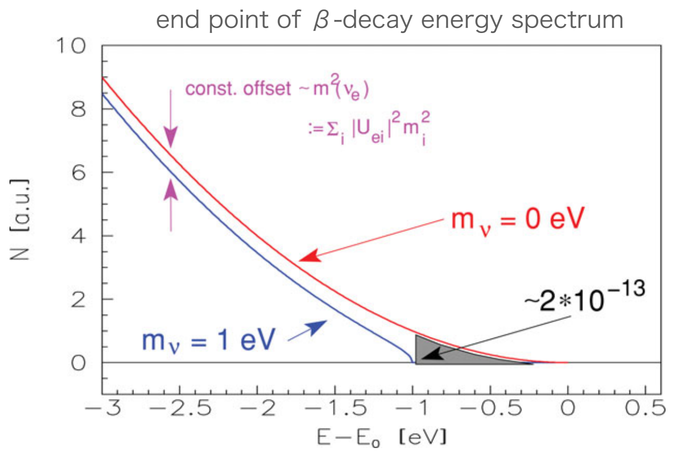

Fig 2.4: End point of electron energy spectrum of ^{3}H beta decay. Expanded beta spectrum of an allowed or super-allowed beta decay around its endpoint for $m_{\nu_e} = 0$ is drawn in red line, and for an arbitrarily chosen neutrino mass of 1 eV drawn in blue line. In the case of tritium beta decay, the gray-shaded area corresponds to a fraction of 2×10^{-13} of all tritium beta decays. The figure is provided from [21].

The most stringent upper bounds on the $\overline{\nu}_e$ mass were obtained by the Troitzk experiment [22] in 2011.

$$m_{\overline{\nu}_e} < 2.05 \text{ eV}, \qquad \text{at } 95\% \text{ C.L.}.$$

The Mainz experiment [23] also provided the similar limit in the past, $m_{\overline{\nu}_e} < 2.3$ eV at 95% C.L..

This kind of direct measurement requires higher energy resolution of the detector and large statistics. The sensitivity of the direct measurement will be improved by the KATRIN experiment which is planed to start from 2015 in Germany. The target of the sensitivity is 0.2 eV.

from Neutrinoless Double Beta Decay

The measurement of neutrinoless double beta decay is also probe to predict absolute neutrino mass, and it is a main topic in this thesis. Although the measurement of neutrinoless double beta decay can not directly contribute to the absolute neutrino mass, the effective Majorana neutrino mass can be obtained with some theoretical calculations from nuclear physics. The effective Majorana neutrino mass is sensitive for neutrino mass hierarchy, while the neutrino oscillation is not. The detail of neutrinoless double beta decay is discussed in next section 2.2.

Neutrino Mass Hierarchy

The measurement of neutrino oscillation provides the mass-squared differences, and the allowed region and excluded region for neutrino masses can be drawn as a function of the lightest neutrino mass m_{light} which corresponds to m_1 in NH, or m_3 in IH. Fig 2.5(a) shows the constraints on the lightest neutrino mass m_{light} coming from cosmological experiments, and Fig 2.5(b) shows that from direct measurement with beta decay. The red (green) bands indicate the expected region in the NH (IH) from oscillation experiments, respectively.

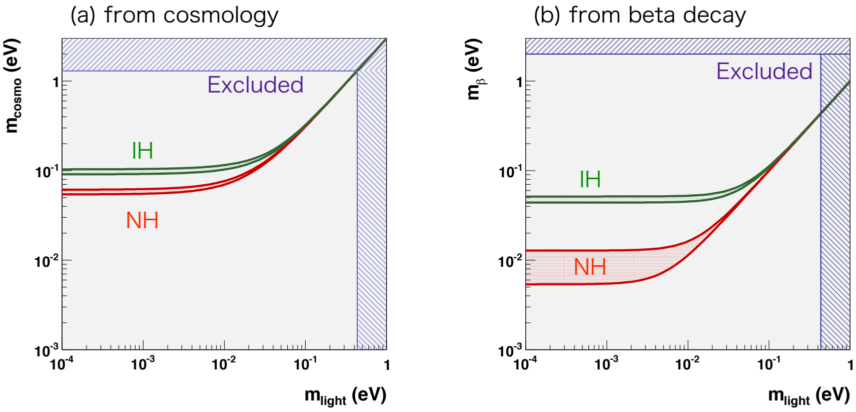

Fig 2.5: Constraints on the lightest neutrino mass coming from cosmological (a) and beta decay (b) experiments. The red and green bands correspond to the normal and inverted hierarchy, respectively. The cosmological constraint on m_{light} is also shown in (b), together with the upper limit on m_β from tritium beta decay experiments.

For now,the constraints do not distinguish between NH and IH as shown in Fig 2.5.

2.2 Double Beta Decay

Double beta decay is a rare nuclear process observable in even-even nuclei for which ordinary beta decay is energetically forbidden or highly suppressed by large spin differences. Standard double beta decay proceeds by a second-order weak interaction emitting two electron anti-neutrinos and two electrons, called two neutrino double beta ($2\nu\beta\beta$) decay. Fig 2.6 shows a general level diagram of double beta decay in even-even nuclei X(Z, A) with proton number Z and total nucleon number A.

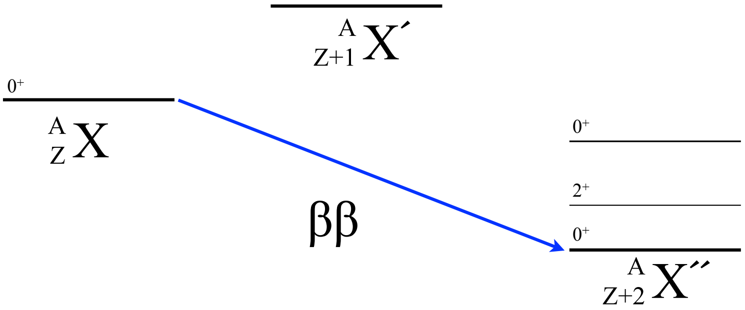

Fig 2.6: A general level diagram for double beta decay process. An initial nucleus X(Z, A) with proton number Z and total nucleon number A decays to X"(Z+2, A), emitting two electrons in the process. The level of nucleus X'(Z+1, A) is higher than that of the initial nucleus, and it is forbidden to decay.

The process of double beta decay is experimentally demonstrated for around 10 nuclei over a period of more than 20 years. The half-lives of $2\nu\beta\beta$ decay ($T^{2\nu}_{1/2}$) measured are summarized in Table 2.3. The half-life of ^{136}Xe $2\nu\beta\beta$ decay have never measured before the EXO-200 and KamLAND-Zen experiments, and there was only the lower limit on the half-life given by DAMA experiment.

Table 2.3: Current best direct measurements of $2\nu\beta\beta$ half-lives. The values reported are taken from the averaging procedure described in [24].

Isotopes	$T^{2\nu}_{1/2}$ [year]	Experiments
^{48}Ca	$(4.4 \pm 0.6) \times 10^{19}$	Irvine TPC, TGV, NEMO3
^{76}Ge	$(1.5 \pm 0.1) \times 10^{21}$	PNL-USC-ITEP-YPI, IGEX, H-M
^{82}Se	$(0.92 \pm 0.07) \times 10^{20}$	NEMO3, Irvine TPC, NEMO2
^{96}Zr	$(2.3 \pm 0.2) \times 10^{19}$	NEMO2, NEMO3
^{100}Mo	$(7.1 \pm 0.4) \times 10^{18}$	NEMO3, NEMO2, Irvine TPC
^{116}Cd	$(2.8 \pm 0.2) \times 10^{19}$	NEMO3, ELEGANT, Solotvina, NEMO2
^{130}Te	$(6.8^{+1.2}_{-1.1}) \times 10^{20}$	CUORICINO, NEMO3
^{150}Nd	$(8.2 \pm 0.9) \times 10^{18}$	Irvine TPC, NEMO3

If the neutrino is a massive Majorana particle, double beta decay might occur without the emission of neutrinos, and this process is called neutrinoless double beta ($0\nu\beta\beta$) decay. Majorana neutrinos are a natural feature of many high-energy physics theoretical models to be investigated. The hypothesis of Majorana neutrino requires non-zero neutrino masses, and that have already demonstrated by the neutrino oscillation phenomena. The Feynman diagrams of double beta decay processes are seen in Fig 2.7. In $2\nu\beta\beta$ decay process (Fig 2.7(a)), the diagram is just double of single beta processes. In $0\nu\beta\beta$ decay process (Fig 2.7(b)), the electron anti-neutrino going out at one vertex is absorbed at the other vertex as a neutrino (exchange of light Majorana neutrino), and the process is neutrinoless. This would violate lepton number conservation by two units ($|\Delta L| = 2$). Therefore, neutrinoless double beta decay is forbidden in the SM.

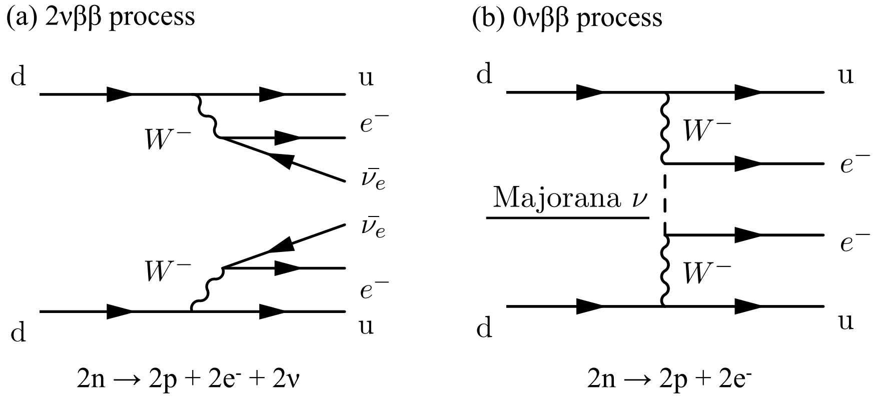

Fig 2.7: Feynman diagrams for double beta decay processes. (a) shows $2\nu\beta\beta$ process with two electron and neutrinos, and (b) shows $0\nu\beta\beta$ process without the emission of neutrinos.

Fig 2.8 shows the energy spectra of two electrons ($T_1 + T_2$) normalized with Q-Value of double beta decay for $2\nu\beta\beta$ and $0\nu\beta\beta$. The spectra of $2\nu\beta\beta$ is continuous shape similar to beta decay, while that of $0\nu\beta\beta$ is a peak at Q-Value. Theoretically, the peak of $0\nu\beta\beta$ decay is mono-energetic delta function because no light particle (neutrino) other than the electrons is emitted. In fact, the peak is smeared by the detector resolution to be observed. The $2\nu\beta\beta$ and $0\nu\beta\beta$ decays are, in principle, distinguished with spectroscopic approach if the resolution of the detector is enough good.

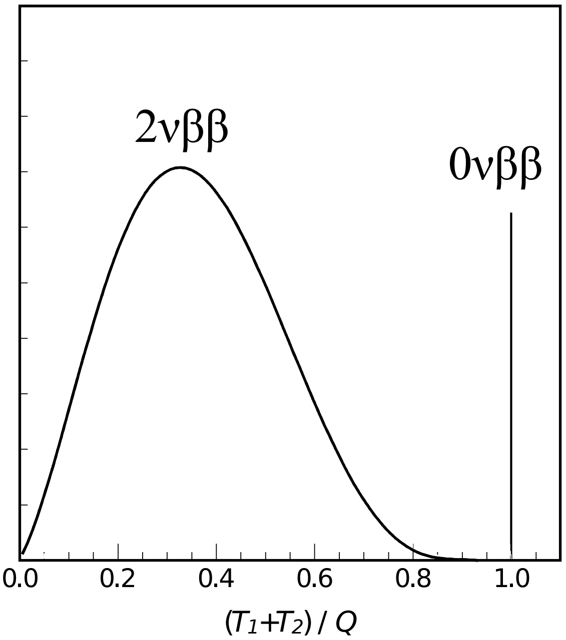

Fig 2.8: Energy spectra of two electrons for double beta decays. The kinetic energy of two electrons ($T_1 + T_2$) is normalized with Q-Value. The spectra for $2\nu\beta\beta$ decay and $0\nu\beta\beta$ decay are drawn, respectively.

2.2.1 Majorana Neutrino Mass

Neutrinoless double beta decay can arise from a diagram (Fig 2.7(b)) in which the parent nucleus emits a pair of virtual W bosons, and then these W exchange a Majorana neutrino to produce the outgoing electrons. The rate is non-zero only for massive, Majorana neutrinos. The reason is that the exchanged neutrino in Fig 2.7(b) can be seen as emitted (in association with an electron) with almost total positive helicity. Only its small, negative helicity component is absorbed at the other vertex by the Standard Model electroweak current. Considering that the amplitude is in this case a sum over the contributions of the three light neutrino mass states ν_i, and that is also proportional to U_{ei}^2, we conclude that the modulus of the amplitude for the $0\nu\beta\beta$ process must be proportional in this case to the effective Majorana neutrino mass $\langle m_{\beta\beta} \rangle$.

$$\langle m_{\beta\beta} \rangle \equiv \left| \sum_{i=1}^{3} U_{ei}^2 \, m_i \right| \tag{2.14}$$

In the case where light Majorana neutrino exchange is the dominant contribution to $0\nu\beta\beta$, the inverse of the half-life for the process can be written as follows.

$$(T_{1/2}^{0\nu})^{-1} = G_{0\nu} |M^{0\nu}|^2 \langle m_{\beta\beta} \rangle^2 \ , \tag{2.15}$$

where $G_{0\nu}$ is phase space factor of $0\nu\beta\beta$ decay, $M^{0\nu}$ is nuclear matrix element (NME) of $0\nu\beta\beta$ decay. The phase space factor $G_{0\nu}$ can be calculated analytically, in principle with reasonable accuracy. The NME is evaluated using nuclear models, although with considerable uncertainty, as discussed in the next section 2.2.2. In other words, the value of the Majorana neutrino mass $\langle m_{\beta\beta} \rangle$ in equation 2.15 can be inferred from a non-zero $0\nu\beta\beta$ rate measurement, albeit with some nuclear physics uncertainties. Conversely, if a given experiment does not observe the $0\nu\beta\beta$ process, the result can be interpreted in terms of an upper bound on $\langle m_{\beta\beta} \rangle$.

If light Majorana neutrino exchange is the dominant mechanism for $0\nu\beta\beta$, it is clear from equation 2.15 that $0\nu\beta\beta$ is in this case directly connected to neutrino oscillations phenomenology, and that it also provides direct information on the absolute neutrino mass scale, as cosmology and beta decay experiments do (see section 2.1.3). The relationship between $\langle m_{\beta\beta} \rangle$ and the actual neutrino masses m_i is affected by the items below.

1. the uncertainties in the measured oscillation parameters
2. the unknown neutrino mass hierarchy (normal or inverted)
3. the unknown phases in the neutrino mixing matrix (both Dirac and Majorana)

The relationship between $\langle m_{\beta\beta} \rangle$ and the lightest neutrino mass m_{light} which is equal to m_1 or m_3 in the NH and IH respectively, is illustrated in Fig 2.9, similar to Fig 2.5. The red band indicates the expected region in NH, and green band indicates that in IH. The excluded region in m_{light} comes from cosmological constraint. The measurement of neutrinoless double beta decay can constrain in vertical direction with Majorana neutrino mass.

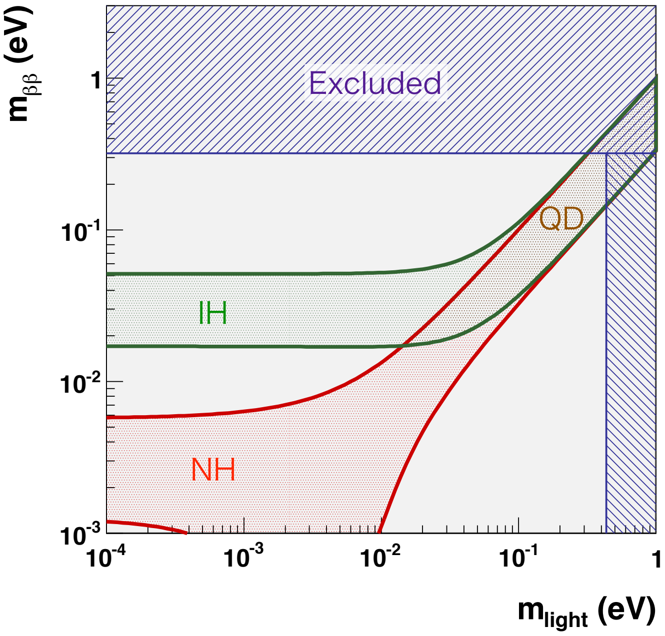

Fig 2.9: The Majorana neutrino mass as a function of the lightest neutrino mass. The red (green) band corresponds to the normal (inverted) hierarchy, respectively, in which case m_{light} is equal to m_1 (m_3). The vertically-excluded region comes from cosmological bounds ($m_{\text{light}} < 0.43$ at 95% C.L.), and the horizontally-excluded one from $0\nu\beta\beta$ constraints ($m_{\beta\beta} < 0.32$ at 90% C.L. with ^{76}Ge measurement).

There are only lower limits on Majorana neutrino mass $\langle m_{\beta\beta} \rangle$, and no evidence for the observation of $0\nu\beta\beta$ decay except the KK-Claim described in the latter section. The measurement of neutrinoless double beta decay could contribute to the absolute mass scale of neutrinos, and it is the only probe to investigate whether if neutrino is Dirac or Majorana particle.

2.2.2 Nuclear Matrix Element

The dominant uncertainties in the conversion from half-life of $0\nu\beta\beta$ decay to Majorana neutrino mass $\langle m_{\beta\beta}\rangle$ come from the nuclear matrix element (NME) $M^{0\nu}$ because NME calculation depends on the nuclear models and parameters.

NME for $2\nu\beta\beta$ decay $M^{2\nu}$ can be obtained from the measurements of $2\nu\beta\beta$ half-life, and can be compared with the theoretical calculations. On the other hand, NME for $0\nu\beta\beta$ decay $M^{0\nu}$ can not be determined due to the unknown Majorana neutrino mass term as seen in equation 2.15, and it is important to choose reasonable calculation to obtain $\langle m_{\beta\beta}\rangle$.

The reliability of the NME calculations has improved owing to the efforts in nuclear physics, but the ranges of $M^{0\nu}$ values are wide and NME calculations still have high dependency of nuclear models and the nuclei. Fig 2.10 shows the variety of NME calculations for each calculation model and nucleus, and Fig 2.11 shows the phase space factors $G_{0\nu}$ for each isotope. The NME values varies with calculation techniques, and the difference between minimum and maximum values make large uncertainty for Majorana neutrino mass. By contrast, the phase space factors are determined to be certain values as shown in Fig 2.11.

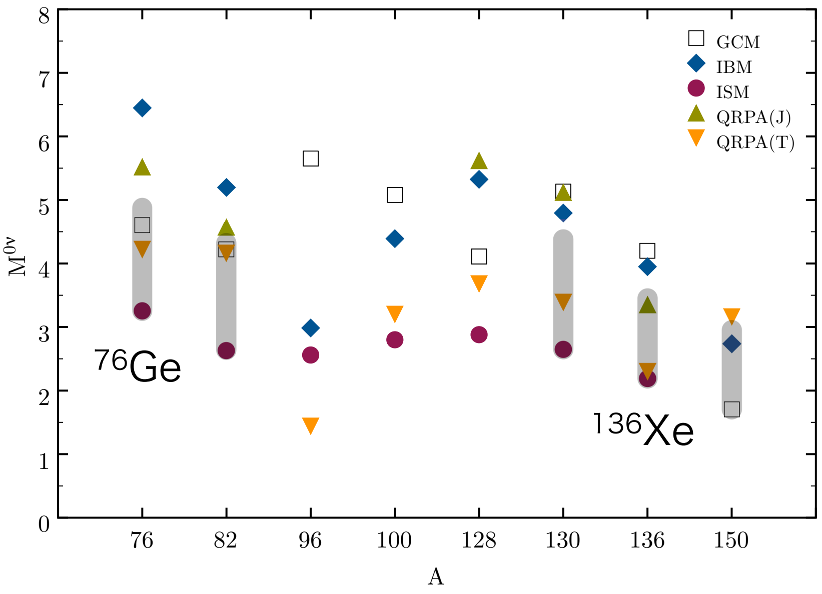

Fig 2.10: Recent NME calculations from different techniques for different nuclei. The NME values of calculation techniques GCM, IBM, ISM, QRPA(J) and QRPA(T) with UCOM short range correlation are drawn, and all the calculations use $g_A = 1.25$. The shaded intervals correspond to the proposed physics-motivated ranges (see text for discussion) The figure is contributed from [25].

How to determine the uncertainties of NME calculations is a controversial problem, because the uncertainty taken as the range from the minimum value to the maximum is large for the current physically motivated models. The proposal of the treatment is made by [25], and the shaded bands in Fig 2.10 correspond to their physics-motivated ranges.

In this work, we also applied reasonable NME calculations to obtain Majorana neutrino

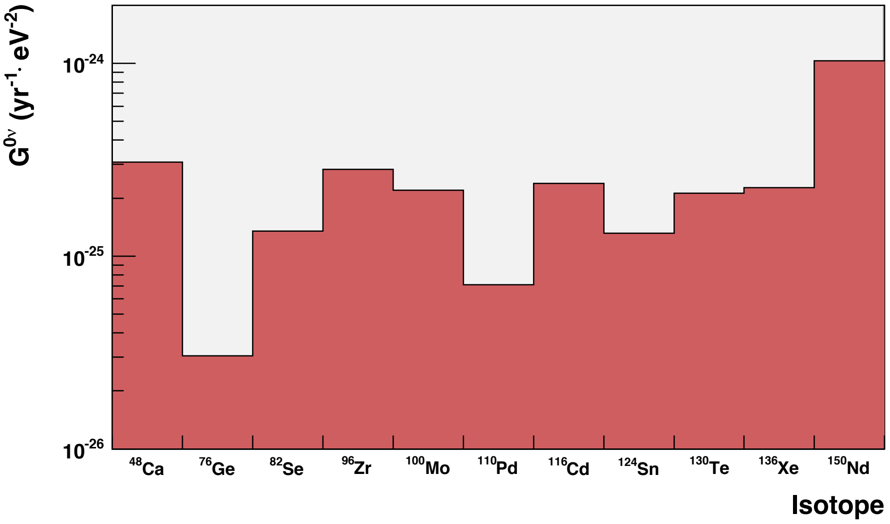

Fig 2.11: The values of phase space factors for $0\nu\beta\beta$ decay isotopes with $Q > 2$MeV. Values are taken from [26, 27]. The figure is contributed from [25].

mass from the half-life of ^{136}Xe $0\nu\beta\beta$ decay. However, to be conservative we applied all available calculations for the comparison between the claim in ^{76}Ge and our results. The NME calculations we applied in this work are described in chapter 9.

2.2.3 Indirect Measurements for Double Beta Decay

There are indirect approaches to measure the half-life of double beta decay which are categorized into geochemical and radiochemical methods.

Geochemical measurement is suitable for double beta decay isotopes whose daughters are noble gases such as ^{130}Te (decays to ^{130}Xe). While, radiochemical measurement is suitable for isotopes with daughters that have short half-lives and thus rarely exist in nature, such as ^{238}U. The strategy of both measurement is counting the number of daughter nuclei, therefore they can not separate the decay mode of double beta decay ($2\nu\beta\beta$ or $0\nu\beta\beta$). In addition since suitable isotopes are limited due to the methods used, only a few isotopes are measured with indirect way.

The $2\nu\beta\beta$ half-lives with indirect measurement are summarized in Table 2.4.

Table 2.4: Current indirect measurements of $2\nu\beta\beta$ half-lives. ECEC stands for the double electron capture process.

Isotopes	$T^{2\nu}_{1/2}$ [year]	Measurement
^{128}Te	$(2.2 - 7.7) \times 10^{24}$	Geochemical
^{130}Te	$(8 - 27) \times 10^{20}$	Geochemical
^{130}Ba (ECEC)	2.2×10^{21}	Geochemical
^{238}U	2.0×10^{21}	Radiochemical

2.2.4 Experimental Approaches to $0\nu\beta\beta$ with ^{76}Ge

Germanium is used as semiconductor detector to detect traversing charged particles or the absorption of photons, and ^{76}Ge is a even-even nucleus which is one of the sources for double beta decay. The Ge detector has high energy resolution ($\sim$ few keV), and the enrichment of ^{76}Ge is well established. Some of the past, ongoing, and planned experiments to study ^{76}Ge double beta decay with Ge detector are introduced in the following.

HEIDELBERG-MOSCOW

HEIDELBERG-MOSCOW experiment operated five enriched (86% enrichment) ^{76}Ge detectors in an extreme low-level environment in the Gran Sasso underground laboratory. The detectors had high energy resolution ($\sim$ 4 keV FWHM at Q-Value; 2.039 MeV), and the total mass of ^{76}Ge was 10.96 kg. The data taking was performed in 1990-2003, and the energy spectra of double beta decay are shown in Fig 2.12 [47].

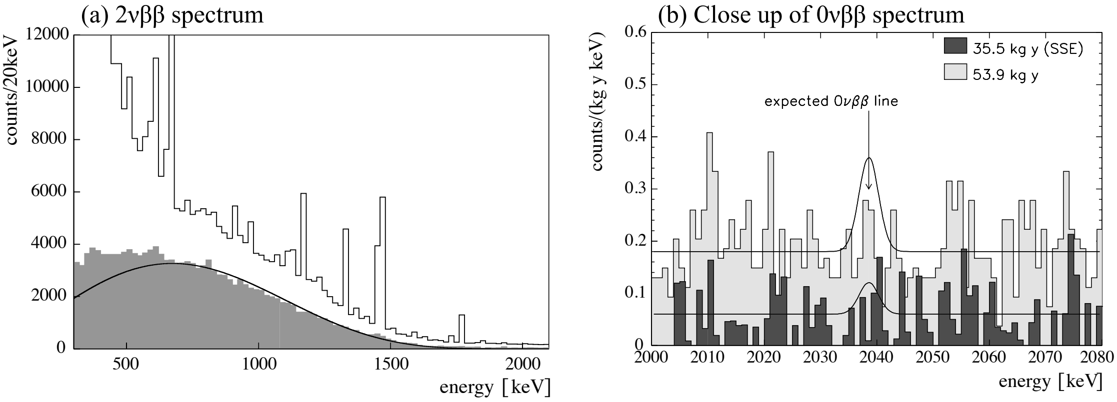
(a) 2vββ spectrum

(b) Close up of 0vββ spectrum

Fig 2.12: Energy spectra of double beta decay from HEIDELBERG-MOSCOW experiment [47]. (a) shows summed spectra of all five detectors in 47.7 kg-year of measurement together with the residual spectrum after subtracting all identified background components. The solid line indicates the best fit of $2\nu\beta\beta$ signal. (b) shows shows the combined spectrum of the five detectors after 53.93 kg-year, and the spectrum of point-like interactions, corrected for the detection efficiency, after 35.5 kg-year in the region of interest for the $0\nu\beta\beta$ decay.

The half-life of ^{76}Ge $2\nu\beta\beta$ decay was measured to be

$$T^{2\nu}_{1/2}(^{76}\mathrm{Ge}) = (1.55 \pm 0.01(stat)^{+0.19}_{-0.15}(syst)) \times 10^{21} \text{ [year]},$$

with exposure of 47.7 kg-year of ^{76}Ge. A lower limit of ^{76}Ge $0\nu\beta\beta$ decay half-life was obtained with exposure of 35.5 kg-year as follows.

$$T^{0\nu}_{1/2}(^{76}\mathrm{Ge}) > 1.9 \times 10^{25} \text{ [year] (90\% C.L.)}.$$

The result of $0\nu\beta\beta$ decay from HEIDELBERG-MOSCOW experiment was the most stringent limit at that time.

KK(KKDC)-Claim

The neutrinoless double-beta decay detection claim in ^{76}Ge was reported by a part of the Heidelberg-Moscow Collaboration in 2001[39], 2004 [40] and 2006[2]. The latest claim is called the KK-Claim, which is reported by H. V. Klapdor-Kleingrothaus and I. Krivosh in 2006. (The former claim by 4 people in 2004 was known as KKDC-Claim.)

They argue, with improvement of analytical techniques such as pulse shape discrimination, the signal of $0\nu\beta\beta$ decay in ^{76}Ge is observed in HEIDELBERG-MOSCOW experiment, and the half-life is;

$$T^{0\nu}_{1/2}(^{76}\text{Ge}) = (2.23^{+0.44}_{-0.31}) \times 10^{25} \text{ [year]}.$$

The significance of the detection is more than 6 σ. The energy spectrum which they claimed as signal of ^{76}Ge $0\nu\beta\beta$ decay is shown in Fig 2.13.

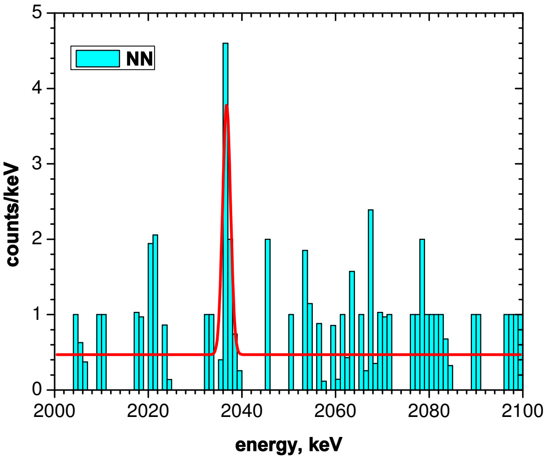

Fig 2.13: Energy spectrum of the claimed ^{76}Ge $0\nu\beta\beta$ decay signal from KK-Claim [2].

The half-life of ^{76}Ge $0\nu\beta\beta$ decay corresponds to the Majorana neutrino mass: $\langle m_{\beta\beta}\rangle = 0.32 \pm 0.03$ eV. However, the claim of the detection has been a controversial issue in the community of double beta decay due to the analytical treatment of data, and to be tested by the other experiments.

IGEX

The International Germanium Experiment (IGEX) is an experiment which searches neutrinoless double beta decay search in ^{76}Ge with enriched Ge detector. The experiment was performed in 1990s, at three different locations; in Homestake mine in US, at Canfranc in Spain and Baskan Neutrino Observatory in Russia. The final result was reported in 2002 [48] with 117 mol-year (8.88 kg-year) of ^{76}Ge data after applying pulse shape discrimination techniques. They obtained the lower limit of ^{76}Ge $0\nu\beta\beta$ decay half-live,

$$T^{0\nu}_{1/2}(^{76}\text{Ge}) > 1.57 \times 10^{25} \text{ [year] (90\% C.L.)}.$$

This limit corresponds to the upper limit of the Majorana neutrino mass range of $0.33 - 1.35$ eV.

GERDA

The Germanium Detector Array (GERDA) experiment at the Gran Sasso Laboratory in Italy also searches the neutrinoless double beta decay in ^{76}Ge. They reported the result from the first phase of GERDA [41], data taken in 2011 - 2013, with 21.6 kg-year of ^{76}Ge exposure. After pulse shape discrimination, they accomplished low background level and the obtained energy spectrum shown in Fig 2.14. In the upper panel, the red dashed line corresponds to $T^{0\nu}_{1/2}(^{76}\mathrm{Ge}) = 1.19 \times 10^{25}$ year from the KKDC-Claim in 2004 [40] and blue line indicates their limit;

$$T^{0\nu}_{1/2}(^{76}\mathrm{Ge}) > 2.1 \times 10^{25}\ [\mathrm{year}]\ (90\%\ \mathrm{C.L.}).$$

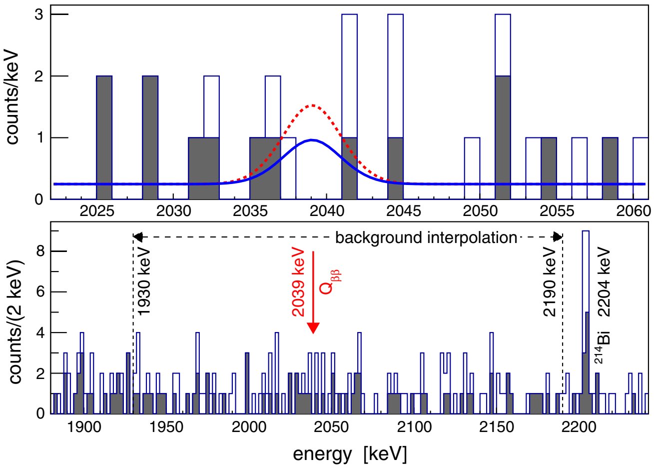

Fig 2.14: Energy spectrum of $0\nu\beta\beta$ decay from GERDA experiment [41]. The combined energy spectrum from all Ge detectors without (with) PSD is shown by the open (filled) histogram. In the upper panel, the spectrum zoomed to Q-Value is superimposed with the expectations (with PSD selection). The red dashed line indicates the $0\nu\beta\beta$ signal expected from KKDC-Claim, and blue line indicates the 90 % C.L. upper limit derived from GERDA 1st phase. The lower panel shows the region used for the background interpolation.

The result from GERDA phase I is consistent with the limits by the HEIDELBERG-MOSCOW and IGEX experiments. The GERDA Collaboration tried to combine these results in ^{76}Ge with some assumptions and extrapolated parameters, and obtained the combined limit of ^{76}Ge $0\nu\beta\beta$ decay;

$$T^{0\nu}_{1/2}(^{76}\mathrm{Ge}) > 3.0 \times 10^{25}\ [\mathrm{year}]\ (90\%\ \mathrm{C.L.}).$$

The limit is the most stringent limit on the half-life of ^{76}Ge $0\nu\beta\beta$ decay, and they said that KKDC-Claim in 2004 [40] is disfavored with Bayesian test. However, the KK-Claim in 2006 [2] is still controversial and not rejected with ^{76}Ge experiments yet.

Future Prospects

HEIDELBERG-MOSCOW and IGEX finished their operation, and GERDA is on going and plans to move on the next stage called as the second phase by increasing the mass of ^{76}Ge. The target of the half-life in the second phase of GERDA is over 10^{26} year, and the experiment will start in 2014.

MAJORANA is also an experiment planed to search for ^{76}Ge $0\nu\beta\beta$ decay with high purity Ge detector.

2.2.5 Experimental Approaches to $0\nu\beta\beta$ with ^{136}Xe

The double beta decay in ^{136}Xe has received a lot of attention in recent years due to the KamLAND-Zen and EXO-200 experiments. Xenon is stable noble gas, can be used as scintillator, can be efficiently enriched and easy to purchase compared with the other isotopes which are candidates of double beta decay. The double beta decay experiments using ^{136}Xe have some advantages, and achieved the best result among all double beta decay experiments, in fact.

In this section, the review of double beta decay experiments with ^{136}Xe is introduced.

DAMA

DAMA is an experiment with liquid xenon scintillation detector performed at the Gran Sasso National Laboratory to measure double beta decay in ^{134}Xe and ^{136}Xe. The result from DAMA experiment was reported with the exposure of 1.1 kg-year for ^{134}Xe and 4.5 kg-year for ^{136}Xe in 2002 [38]. They got the limits on the half-life of $2\nu\beta\beta$ and $0\nu\beta\beta$ decay as follows.

$$\begin{aligned}
&T^{0\nu}_{1/2}(^{134}\mathrm{Xe}) > 5.8 \times 10^{22}\ \text{[year] (90\% C.L.)}\\
&T^{2\nu}_{1/2}(^{136}\mathrm{Xe}) > 1.0 \times 10^{22}\ \text{[year] (90\% C.L.)}\\
&T^{0\nu}_{1/2}(^{136}\mathrm{Xe}) > 1.2 \times 10^{24}\ \text{[year] (90\% C.L.)}
\end{aligned}$$

They could not reliably obtain the half-life of ^{134}Xe $2\nu\beta\beta$ decay due to the small statistics. These limits are first measurements of ^{136}Xe double beta decay.

KamLAND-Zen

KamLAND-Zen is an experiment for ^{136}Xe double beta decay. It is a modification of KamLAND detector with organic liquid scintillator loaded with xenon gas. The construction of KamLAND-Zen started in 2011, and the first result was reported early in 2012. The quick and reliable performance of KamLAND-Zen is contributed from the existing KamLAND detector, and that is why KamLAND-Zen has high competitive power with high scalability.

The first result gave the most precise half-life of ^{136}Xe $2\nu\beta\beta$ decay and the limit on the half-life of $0\nu\beta\beta$ decay [33], and the second result, with increased exposure, reported new limits on Majoron emitting processes [34]. The third result is reported in late 2012 [1], and this thesis includes the result. The results are described throughout this thesis.

EXO-200

The Enriched Xenon Observatory (EXO-200) is an experiment for ^{136}Xe neutrinoless double beta decay where 200 kg of target nuclei ^{136}Xe (enriched 80%) is used as scintillator. The detector is a time projection chamber (TPC) which detects both scintillation light and ionization by charged particles. The experiment started in early 2011, and the first report was for ^{136}Xe $2\nu\beta\beta$ decay published in 2011 [35] before KamLAND-Zen 1st result. The half-life of ^{136}Xe $2\nu\beta\beta$ decay is : $T^{2\nu}_{1/2}(^{136}\mathrm{Xe}) = (2.11 \pm 0.04(stat) \pm 0.21(syst)) \times 10^{21}$ year. This half-life is inconsistent with the limit from DAMA experiment [38]. However, KamLAND-Zen supported the result from EXO-200 with KamLAND-Zen 1st result [33].

In 2012, the updated result is reported together with a limit on the half-life of $0\nu\beta\beta$ decay [36]. They obtained the following half-lives results:

$$\begin{aligned}
T^{2\nu}_{1/2}(^{136}\mathrm{Xe}) &= (2.23 \pm 0.017(stat) \pm 0.22(syst)) \times 10^{21},\\
T^{0\nu}_{1/2}(^{136}\mathrm{Xe}) &> 1.6 \times 10^{25}\ \text{[year] (90\% C.L.)}.
\end{aligned}$$

The lower limit on the half-life of ^{136}Xe $0\nu\beta\beta$ decay was the most sensitive result before update of KamLAND-Zen [1]. The energy spectrum of double beta decay and the discussion can be seen in chapter 7 and chapter 9.

The EXO Collaboration plans to scale up the mass of ^{136}Xe to more than ton to increase their sensitivity with a larger detector.

2.2.6 The Other Experimental Approaches to $0\nu\beta\beta$

Double beta decay experiments with ^{76}Ge and ^{136}Xe are the main focus of study and discussion in this thesis because of historical claim. However, there are several experiments using the other isotopes as introduced in the review of double beta decay [25].

The various measurements with different isotopes are key to reduce the uncertainties in NME calculations and models, leading to small uncertainties on the Majorana neutrino mass prediction. Table 2.5 shows the summary of current best limits on $0\nu\beta\beta$ decay half-lives for several isotopes of interest.

Table 2.5: Current best limits on $0\nu\beta\beta$ half-lives in the most interesting nuclei before this work (KamLAND-Zen 3rd result). All values are lower limits of $0\nu\beta\beta$ half-life at 90% C.L.. The values of exposure [kg-year] in brackets are calculated from provided information.

Isotopes	$T^{0\nu}_{1/2}$ [year]	Exposure [kg-year]	Experiments
^{48}Ca	$> 5.8 \times 10^{22}$	(4.25)	ELEGANT VI (2008) [42]
^{82}Se	$> 3.6 \times 10^{23}$	(3.60)	NEMO-3 (2011) [43]
^{96}Zr	$> 9.2 \times 10^{21}$	(0.031)	NEMO-3 (2011) [43]
^{100}Mo	$> 1.1 \times 10^{24}$	(26.7)	NEMO-3 (2011) [43]
^{150}Nd	$> 1.8 \times 10^{22}$	(0.093)	NEMO-3 (2010) [44]
^{116}Cd	$> 1.7 \times 10^{23}$	(0.126)	Solotvina (2003) [45]
^{130}Te	$> 2.8 \times 10^{24}$	19.75	CUORICINO (2011) [46]
^{76}Ge	$> 1.9 \times 10^{25}$	35.5	Heidelberg-Moscow (2001) [47]
	$> 1.57 \times 10^{25}$	(8.88)	IGLEX (2002) [48]
	$> 2.1 \times 10^{25}$	21.6	GERDA (2013) [41]
^{136}Xe	$> 6.2 \times 10^{24}$	38.6	KamLAND-Zen (2012) [34]
	$> 1.6 \times 10^{25}$	32.5	EXO-200 (2012) [36]

Chapter 3

KamLAND-Zen 1^{st} Phase

The **KamLAND-Zen** experiment is constructed for neutrinoless double beta decay search using the **KamLAND** detector, and named after **Ze**ro-**n**eutrino (neutrinoless) double beta decay. In the 1^{st} phase of KamLAND-Zen, 300 kg of enriched ^{136}Xe gas was dissolved in a newly developed liquid scintillator and filled in a nylon balloon of 3.08 m in diameter installed in the center of the KamLAND detector. And we observe double beta decay signals from ^{136}Xe with KamLAND detector.

This chapter contains the overview of the KamLAND-Zen experiment and the KamLAND detector, the preparation, construction and some operations in the KamLAND-Zen 1^{st} phase.

3.1 Overview of KamLAND-Zen Experiment

KamLAND-Zen is a next experiment using KamLAND detector after solar phase of KamLAND. Fig 3.1 shows the overview of the KamLAND-Zen detector. The idea is very simple, ^{136}Xe loaded liquid scintillator (Xe-LS) is filled into the highly transparent smaller balloon at the center of the detector to observe the double beta decay signal from ^{136}Xe.

3.1.1 Experimental Design

KamLAND-Zen experiment is a next generation double beta decay experiment to test KK-Claim, and also inverted hierarchy of neutrino mass in the future. KamLAND-Zen has a high scalability by changing the size of the inner balloon depending on the available mass of target isotope, ^{136}Xe. The construction and the start of the experiment can be made rapid by using an existing detector, KamLAND, which have been running for 10 years. Because of these 2 reasons, KamLAND-Zen has strong competitive power in the international double beta decay experiment community, over the years by enlarging the target mass.

We adopted ^{136}Xe as the target isotope of double beta decay in the 1^{st} phase. However, we can change the target isotope to observe double beta decay signal in different isotope. It is important to measure the half-life of double beta decay which can contribute to the theoretical calculation of nuclear matrix elements. KamLAND detector itself has a high potential for the measurement of double beta decay due to the low background activities. The detailed explanation of KamLAND detector is found in the next section (section 3.2).

The low background rate in KamLAND detector is very important to measure $0\nu\beta\beta$ decay because the expected $0\nu\beta\beta$ decay event rate should be extremely low. KamLAND detector has the ultra purified liquid scintillator by the distillation, and there are active shields, the outer detector (OD), the buffer oil (BO) layers and LS surrounding the inner balloon. In addition, the detector is located in Kamioka mine where the intensity of

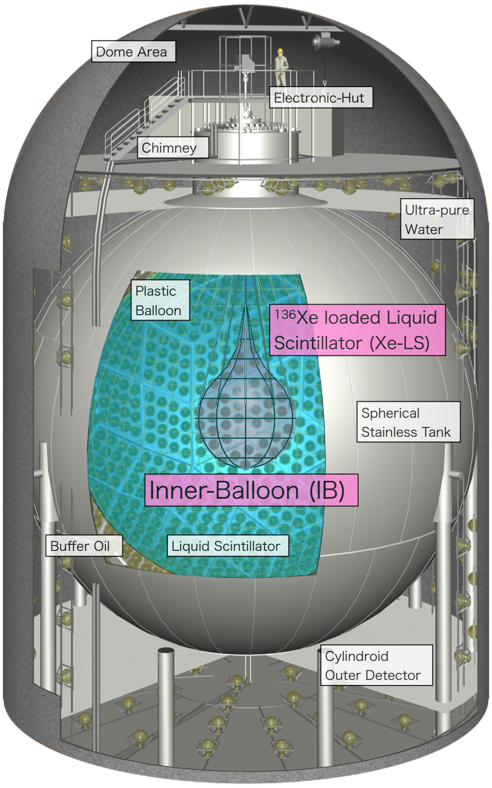

Fig 3.1: A drawing of KamLAND-Zen experiment. The inner balloon with 300 kg of ^{136}Xe loaded LS is installed to the center of KamLAND detector. The double beta decay signals are observed using PMTs of the KamLAND detector.

cosmic ray is relatively small (10^{-5} compared to that on the ground). The established low background environment in KamLAND is desirable and much suited for double beta decay experiment.

In the KamLAND-Zen 1$^{\text{st}}$ phase, the target nuclei of the double beta decay is 300 kg of ^{136}Xe, and this is the largest mass for double beta decay experiment in the world so far. There was no measurement of double beta decay in ^{136}Xe but only the lower limit of the half-life by DAMA experiment [38] before KamLAND-Zen and EXO-200. The Q-value of double beta decay in ^{136}Xe is 2.458 MeV [62], and the $2\nu\beta\beta$ half-life is estimated $\sim 10^{21}$ years. This longer half-life of $2\nu\beta\beta$ is advantageous for the measurement of $0\nu\beta\beta$ decay, because $2\nu\beta\beta$ is intrinsic and unavoidable background for $0\nu\beta\beta$ decay. ^{136}Xe occupies 8.7% of natural xenon gas, and the method of enrichment (centrifugal separation technique) is available. In fact, we could purchase high purified (∼91%) ^{136}Xe gasses. Xenon gas dissolves into liquid scintillator with relatively high solubility (∼ 3 wt%), and it is a chemically stable noble gas which can be handled easily to dissolve/extract into/from organic liquid.

There are many advantage points using KamLAND detector and ^{136}Xe as the target isotope, like summarized as follows.

The advantages of using KamLAND detector and Xe are :

- There is no need to construct the detector.
- The detector has been operated successfully and well-understood.
- The background rates are the least in the experimental energy range in the world.
- The intensity of cosmic ray is relatively small in Kamioka mine, contributes to the low background environment.

- The experiment is scalable to increase the sensitivity.
- The observation of reactor- and geo-neutrinos can continue during KamLAND-Zen using the outside region of the inner balloon.

The advantages of ^{136}Xe as the isotope for double beta decay are :

- The solubility of Xe gas in LS is high ($\sim$ 3 wt%).
- An natural abundance of ^{136}Xe is appreciable (8.9%).
- The enrichment technique for ^{136}Xe is established by the centrifugal separation.
- The "Ton" scale amount of ^{136}Xe in the future seems feasible because of above 3 reasons.
- The error of the nuclear matrix element in ^{136}Xe is relatively small.
- Xenon gas is a chemically stable noble gas which can be handled easily.
- It is not difficult to extract Xe gas from LS after the experiment.
- The Q-value of the double beta decay in ^{136}Xe is relatively high (2.467 MeV).
- The half-life of two neutrino double beta decay is very long.

3.1.2 Signal and Background Estimation

The estimation of signal and background for KamLAND-Zen experiment is performed with GEANT4 simulation. GEANT4 simulation in KamLAND detector is well studied and optimized with actual experimental data in the past years. It is important to compute the energy spectrum to measure the signal from double beta decay in the spectroscopic way. The energy resolution of KamLAND detector is not so much good ($6.8\%/\sqrt{E}$) compared with semiconductor detector such as Ge detector, therefore the study of detector response is needed to estimate the real energy with visible energy.

The simulation conditions are summarized below.

1. KamLAND detector (Fig 3.2)
    - Outer Detector (water, Cherenkov detector)
    - Inner Detector (buffer oil outer, BOO)
    - Inner Detector (buffer oil inner, BOI)
    - Inner Detector (KamLAND LS, PC(20%) + NP(80%) + PPO(1.36g/l))
2. Inner Balloon and Strings (Fig 3.2)
    a) Inner Balloon
        - Radius : 1.58 m
        - Material : Nylon-6
        - Thickness : 25 μm
        - Density : 1.14 g/cm^3
        - Weight : 700 g

    b) Strings
        - Vectran, 0.24mmϕ
        - Density : 1.14 g/cm^3
        - Longitudinal 10, Horizontal 7 (total $\sim$ 180 m)
        - Weight : 15g ($\sim$1.5% of inner balloon weight)
3. Xe loaded Liquid Scintillator
    - 90% enriched ^{136}Xe 400kg (3.0wt%)
    - Xe-LS (PC(19.8%) + Decane(80.2%) + PPO(2.7g/l))
    - Density : 0.777 g/cm^3 (same as KamLAND LS, assumption)
    - Light Yield : same as KamLAND LS, assumption

4. Resolution

   - Energy : 6.8%/$\sqrt{E}$
   - Vertex : 12.5cm/$\sqrt{E}$

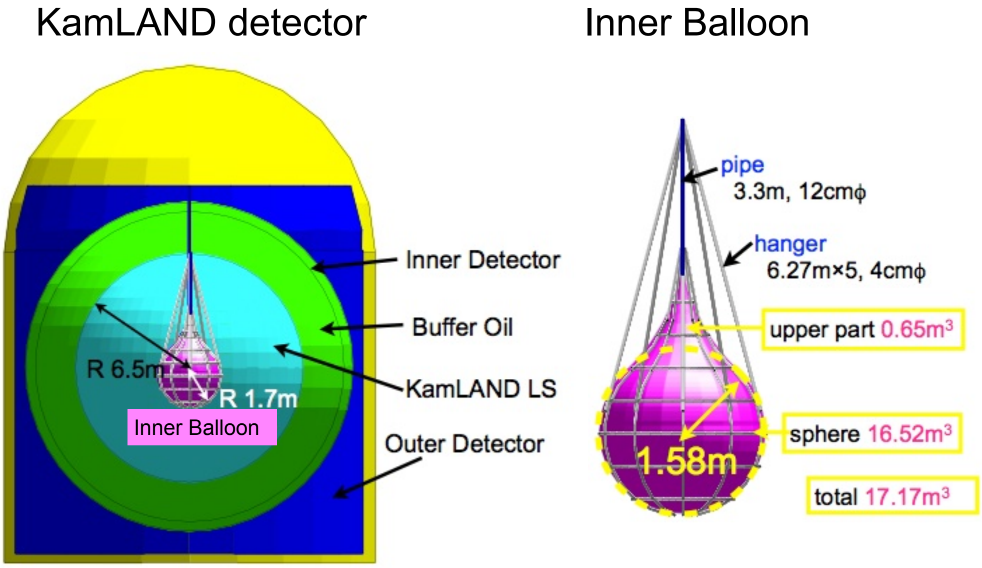

Fig 3.2: The simulation conditions for KamLAND-Zen.

The simulation result is shown in Fig 3.3 as visible energy spectrum in KamLAND detector. The half-life of $0\nu\beta\beta$ decay is assumed that corresponding to $\langle m_{\beta\beta}\rangle = 150$ meV as effective Majorana mass, and the half-life of $2\nu\beta\beta$ is fixed to 2.11×10^{21} years, corresponding to the measurement by EXO-200 in 2011 [35].

$2\nu\beta\beta$ Background

$2\nu\beta\beta$ spectrum can be clearly seen in Fig 3.3, while $2\nu\beta\beta$ is an intrinsic background for $0\nu\beta\beta$ decay, and it can not be removed or separated as far as current energy resolution is concerned. The longer half-life of $2\nu\beta\beta$, the higher sensitivity of $0\nu\beta\beta$ half-life because of lower event rate in $0\nu\beta\beta$ energy region. Fig 3.4 shows the schematic spectrum of $2\nu\beta\beta$ v.s. $0\nu\beta\beta$ with difference factor of half-life. If half-life of $2\nu\beta\beta$ is shorter by the factor of 10^{-6}, it's difficult to separate $0\nu\beta\beta$ spectrum from $2\nu\beta\beta$ spectrum.

The half-life of ^{136}Xe is measured by EXO-200 in 2011, corresponding to 2.11×10^{21} years, and it enough long to separate $0\nu\beta\beta$ decay events in KamLAND.

^{8}B Solar Neutrino Background

The ^{8}B solar neutrino events are also unavoidable background events, and the event rate is in proportion to the fiducial volume. However, the shape of spectrum is flat as shown in Fig 3.3, and the flux has already measured in KamLAND. ^{8}B solar neutrino events can not be tagged, but they are analytically treated with the simultaneous spectrum fitting, although the uncertainty of the flux is remaining.

In the future, the event rate of double beta decay in the fiducial volume becomes higher by the higher the concentration of ^{136}Xe in the fiducial volume under the pressurized Xe condition, so-called "pressurized phase". In the phase, the event rate of ^{8}B solar neutrino in the fiducial volume relatively decrease.

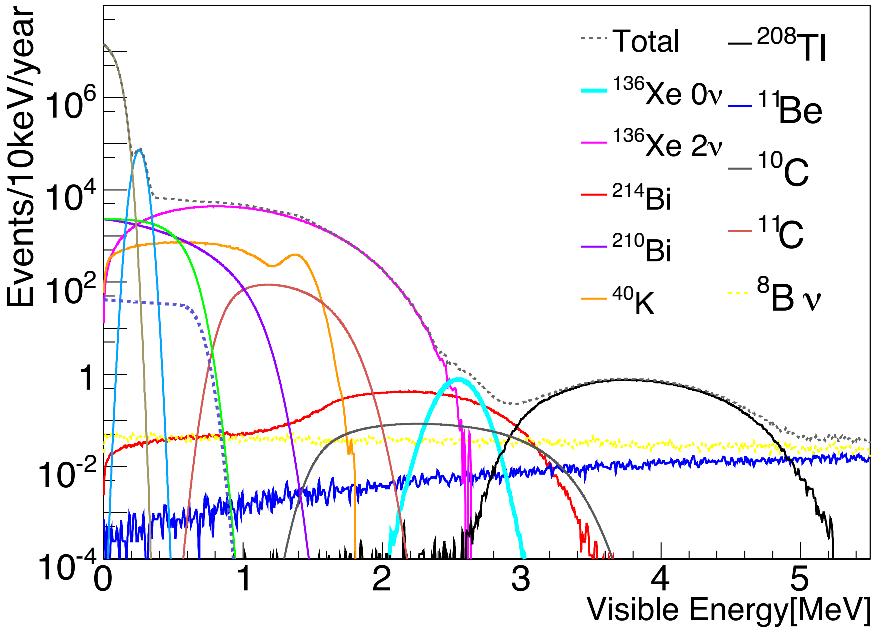

Fig 3.3: The simulation of energy spectrum in KamLAND-Zen. The spectrum of ^{136}Xe $2\nu\beta\beta$ is clearly observed, and the peak spectrum of ^{136}Xe $0\nu\beta\beta$ decay is contaminated by backgrounds. ^{214}Bi is one of the decay in ^{238}U chain, and ^{208}Tl is one of the decay in ^{232}Th chain. ^{40}K is also contained in liquid scintillator. They are included in liquid scintillator or materials of inner balloon. ^{11}Be, ^{11}C and ^{10}C are spallation products which are generated by high energy cosmic ray muon with ^{12}C in LS. ^{8}B neutrino is a solar neutrino flux, which is proportional to the fiducial volume.

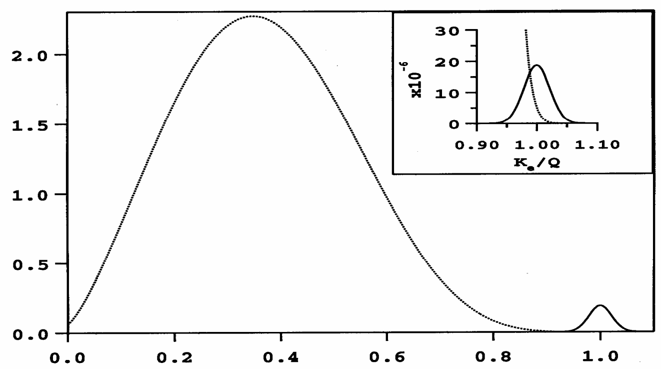

Fig 3.4: The schematic spectrum of $2\nu\beta\beta$ v.s. $0\nu\beta\beta$. If a half-life of $2\nu\beta\beta$ is shorter, the separation of $2\nu\beta\beta$ and $0\nu\beta\beta$ is better than longer case.

^{10}C **Decay Background**

^{10}C is one of the spallation product in liquid scintillator by cosmic muon. The production rate is measured in KamLAND, and it's 21.1 ± 1.8 events/day/kton [31]. ^{10}C is radioactive isotope and undergoes β^++γ decay with life time of 27.8 sec. The Q value of the decay is 3.65 MeV, and observed as continuous spectrum like shown in Fig 3.3. There is difficulty to tag ^{10}C decay due to such long life time. However, ^{10}C is produced with neutron at the probability of 90%, and therefore it can be tagged by the triple delayed coincidence with muon event, neutron capture event and ^{10}C β^+decay. Fig 3.5 shows schematic drawing of the triple delayed coincidence.

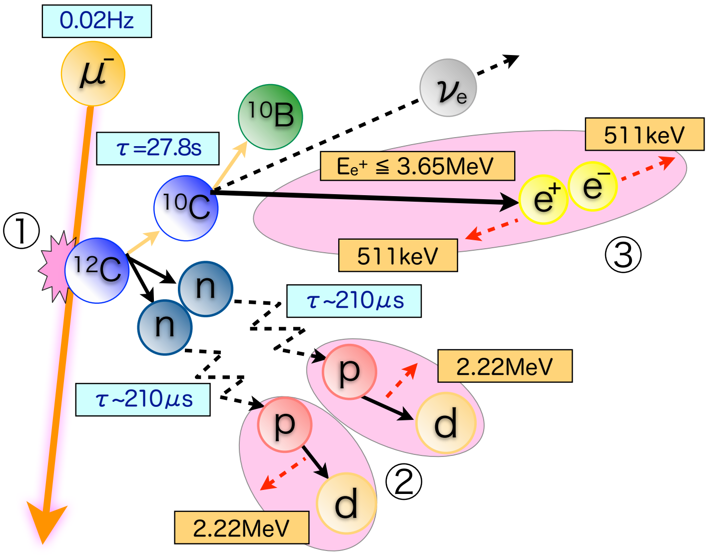

Fig 3.5: The triple delayed coincidence for ^{10}C tagging. A cosmic muon smashes ^{12}C in the liquid scintillator, and produce ^{10}C as one of spallation products. One or two spallation neutrons are produced at the same time, and they are captured by ^{1}H and ^{12}C with life time of 206 μsec. After that, ^{10}C decay in the life time of 27.8 sec. These 3 events are tagged with energy, muon track, vertex distance and temporal difference.

In spite that neutron capture events after cosmic muon should be detected to tag ^{10}C decay events, not all neutron capture events could be acquired by current electronics and daq system because of dead time caused by the duration of analog to digital conversion. For the sake of dead time free data acquisition, new electronics and daq system is developed with Flash-ADC and large storage buffer. It was named MoGURA, which stands for "*Module for General-Use Rapid Application*", and already installed to KamLAND. Although, the data acquired by MoGURA is not applied in this thesis because current sensitivity of $0\nu\beta\beta$ decay is still lower than ^{10}C decay backgrounds, and MoGURA daq system has not been optimized for the detection of neutron capture events after muon yet in the begging of the first phase of KamLAND-Zen.

^{214}Bi **Decay Background**

^{214}Bi is one of the daughter nuclei in decay series of ^{238}U, and β^-+γ decay of ^{214}Bi is one of the most serious backgrounds for $0\nu\beta\beta$ decay signal. They can be tagged, however, by the delayed coincidence shown in Fig 3.6. Tag1 in Fig 3.6 is common maneuver to tag ^{214}Bi and ^{214}Po applied in KamLAND. The concentration of ^{238}U which is the supplier of ^{214}Bi in liquid scintillator, can be reduced to negligible level of ^{214}Bi event rate by the purification of distillation and water extraction.

However, the delayed event of ^{214}Po may not be observed in the liquid scintillator due to the energy deposit inside the film of IB because the event is alpha decay which has

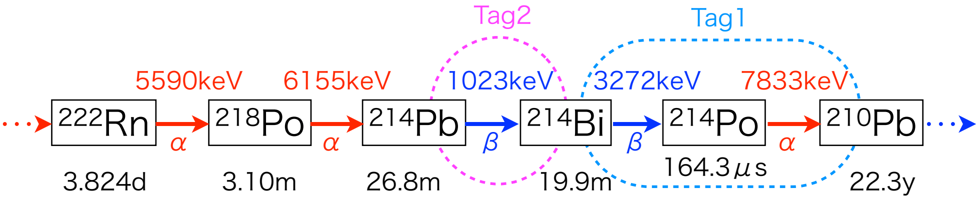

Fig 3.6: The Tag1 and Tag2 in decay chain of ^{238}U. Tag1 is generally applied as ^{214}Bi-Po tagging, and efficiency is high due to the short decay time of ^{214}Po, 164 μsec. While Tag2 is complementally applied to improve the efficiency of ^{214}Bi tagging in the case that alpha decay of ^{214}Po can not be detected by the large energy loss in the film.

shorter attenuation length. The tagging efficiency depends on the thickness of the film and energy threshold to observe in KamLAND DAQ. Assuming that the thickness of the film is 25 μm, the efficiency of the alpha of ^{214}Po penetrate through the film is 0.801, the detection efficiency including energy loss in the film and quenching factor of the alpha by 0.3 MeV of energy threshold is 0.655. As a result, the total efficiency of Tag1 is 0.525. Here, Tag2 in Fig 3.6 is available to improve the tagging efficiency of ^{214}Bi in spite of the longer life time, 19.9 minutes. The $\beta + \gamma$ decay of ^{214}Pb which is parent of ^{214}Bi has higher detection efficiency than alpha decay of ^{214}Po. Even if we missed an alpha decay of ^{214}Po, it is possible to tag ^{214}Bi using 1 hour time window and vertex cut to suppress the accidental background events. Fig 3.7 is schematic view of cut condition for Tag2. These selection criteria require low accidental background rate, mainly from ^{40}K. Assuming that the dead time caused by Tag2 veto is less than 10%, the concentration of ^{40}K must be less than 10^{-11} g/g. The efficiency of 1 hour time window is 0.876, and the detection efficiency of ^{214}Pb is 0.774. Total efficiency of Tag2 is 0.678, thus total tagging efficiency of ^{214}Bi is 0.847 using Tag1 and Tag2.

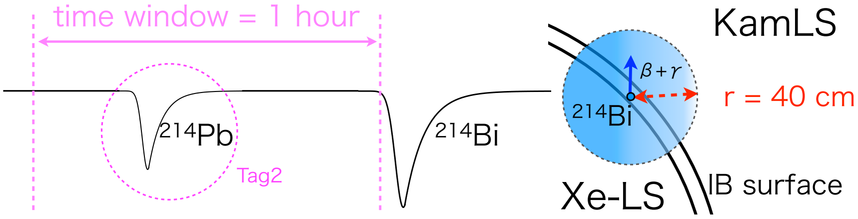

Fig 3.7: The condition of event selection for Tag2. The time window from ^{214}Bi event is 1 hour, and the distance from ^{214}Bi event is within 40 cm radius.

The Other Backgrounds

The other backgrounds for $0\nu\beta\beta$ are ^{208}Tl and ^{11}Be. They have less contribution for $0\nu\beta\beta$ energy region. ^{208}Tl is daughter nuclei in ^{232}Th decay chain, and potentially contained in the liquid scintillator and the film materials. However, the shape of energy spectrum shown in Fig 3.3 implies that contribution to the $0\nu\beta\beta$ energy region is very small as far as the concentration is reasonably low. This condition require the limit of concentration in the material to fabricate inner balloon. ^{11}Be is also spallation product same as ^{10}C, and the production rate is 1.4 ± 0.3 events/day/kton [32]. The Q value of ^{11}Be is 11.5 MeV, thus the contribution to $0\nu\beta\beta$ energy region is smaller and expected event rate can be negligible compared with ^{10}C.

Summary of Background Estimation

The major backgrounds for $0\nu\beta\beta$ spectrum are $2\nu\beta\beta$, ^{8}B solar neutrino, β^{+}decay of ^{10}C which is produced in LS by cosmic muon and β^{-}decay of ^{214}Bi in ^{238}U decay chain. The former 2 backgrounds are essentially unavoidable because they are single events in fiducial volume. On the other hand, the latter 2 backgrounds can be tagged or removed by the delayed coincidence or veto as discussed above. To maximize the sensitivity for $0\nu\beta\beta$, the tagging efficiency of these background events also should be maximized. Table 3.1 shows the summary of expected event rate of the backgrounds for $0\nu\beta\beta$ decay.

Table 3.1: The summary of expected background event rate for $0\nu\beta\beta$. The unit of event rate is events / year, and the total background (Total BG) event rate include the other minor background not listed here.

^{136}Xe $2\nu\beta\beta$	^{8}B solar	^{10}C	^{214}Bi	Total BG	^{136}Xe $0\nu\beta\beta$
1.93 ± 0.15	0.20 ± 0.01	2.44 ± 0.01	3.15 ± 0.01	8.93 ± 0.21	17.79 ± 0.02

All background events we expected in $0\nu\beta\beta$ energy region before actual measurement is listed in Table 3.1. However, we had found unexpected background there after start of KamLAND-Zen experiment. The unexpected background is discussed in section 6.5.

3.2 KamLAND detector

KamLAND stands for **Kam**ioka **L**iquid-scintillator **A**nti-**N**eutrino **D**etector , and is a detector for anti-neutrino observation with liquid scintillator just as the name.

This section introduces a brief review of the KamLAND detector such as detector view, photodetector, electronics and liquid scintillator, including their performance.

3.2.1 KamLAND Site

KamLAND detector is located in 1,000 m depth under the top of Mt. Ikenoyama, in Kamioka mine, in Gifu prefecture, in Japan (Fig 3.8). The 1,000 depth of rock corresponds to 2,700 m depth water equivalent, and it reduces the cosmic ray backgrounds in factor 10^{-5} compared with ground level (Fig 3.9). KamLAND detector is constructed in the place after Kamiokande detector, and size of the hole is completely same as it. However an idea of the detector is much different due to the purpose to detect low energy neutrino from reactor.

3.2.2 Schematic View of the Detector

The shape of KamLAND detector is a cylindrical hole, which is used as Kamiokande detector. The cross section view of KamLAND detector is shown in Fig 3.10. There are 2 detectors, Outer-Detector (OD) for cosmic muon and fast neutron veto counter and Inner-Detector (ID) for neutrino detection. The details of these detectors are described in latter subsection.

The hemispherical cave above detectors is called dome area where chimney, electronics hut (E-hut) and the other equipments such as calibration system are located. We have made an effort to keep dome area clean, because there is a direct connection part (chimney) to ID, to reject any possibility of the interfusion of radioactive impurities. The E-hut is a container box for the electronics to digitize the analog signal from PMTs, and devices related to data taking. The signal cables from PMTs are collected into E-hut, and

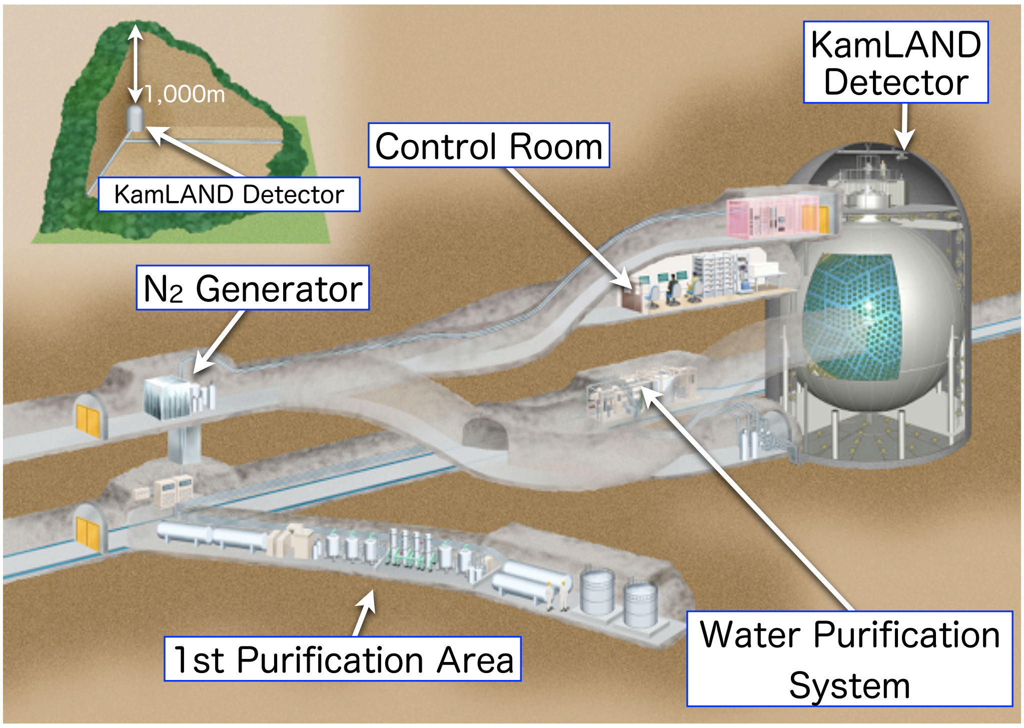

Fig 3.8: The site map of KamLAND area. There are 4 access tunnel to KamLAND detector, and some systems installed in KamLAND area. There are a 2nd purification area and newly constructed 25 m^3 tank area, not drawn in this figure. The depth of Kamioka mine is 1,000 m as rock overburden under Mt. Ikenoyama, and the minimum length is around 900 m even if in the horizontal directions.

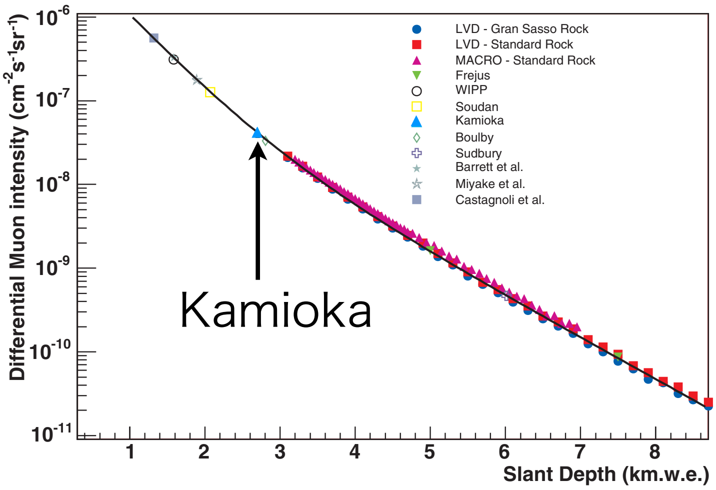

Fig 3.9: Measurements of the differential muon flux as a function of slant depth from Castagnoli, Barrett, Miyake, WIPP, Soudan, Kamioka, Boulby, Gran Sasso, Frejus and Sudbury. Note that the measurements for Sudbury is reported as the number of muons per day. The effective detector acceptance for this measurements is calculated in order to obtain the muon flux.

connected to the electronics. The HV room is located between mine load and dome area, and there are HV units and some computers there. DAQ computers are located in the room next to control room, which is named PC-farm. They have sometimes been replaced to new ones to upgrade operating system and hardware to improve the quality of daq operations.

There are many systems and devices related to KamLAND detector, such as water purification system, nitrogen gasses generator, daq computers and so on. I pick up important parts of the detector, especially related to KamLAND-Zen experiment, to explain in latter subsections.

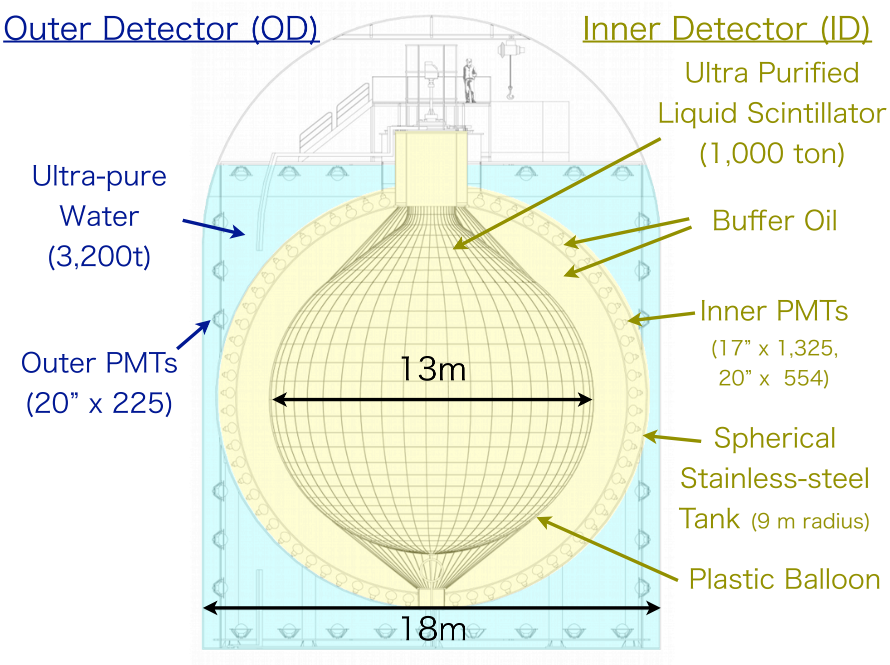

Fig 3.10: The cross section of KamLAND detector. Outer-Detector (OD) is a cylindrical hole surrounded by the rock and filled with ultra-pure water. The vesel of Inner-Detector is a spherical stainless tank inside OD. The plastic balloon inside the tank is filled with ultra purified liquid scintillator, and outer of the balloon is filled with mineral oil as buffer. The buffer oil is separated by acryl panel shield on the PMTs to 2 layers, named buffer oil inner (BOI) and outer (BOO). The purpose of the layers is to keep BOI clean and reject the impurities from PMTs to BOI. Both detectors have photomultiplier tubes to detect the light in the detector.

3.2.3 Outer Detector (OD)

The vesel of OD is 19 m in diameter and 20 m in height cylindrical rock cavity used for former Kamiolande detector. OD is filled with ultra-pure water purified by water purification system in KamLAND area, and always added ultra-pure water because of water leak on the sidewall of the rock cavity. The ultra-pure water is supplied for keeping water level and cooling against the heat from PMTs of ID, and the amount of water supply is around 17.5 $m^3/hour$.

OD has 225 20-inch PMTs, while the number of available ones is only around 100 at present in a decade passed after construction. Even if the number of available PMTs is smaller, OD can detect the cosmic ray in high efficiency of more than 99.7% (Fig 3.11). The wall of the rock cavity is covered with black Tyveck sheet to increase the light correction efficiency by the reflection.

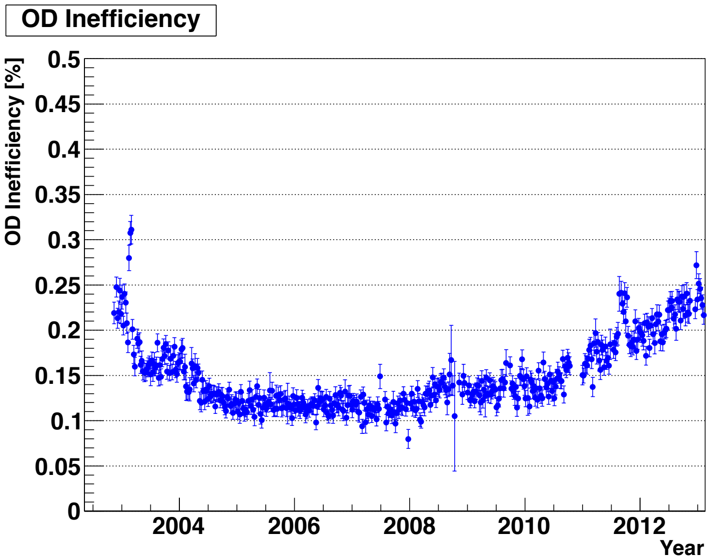

Fig 3.11: The transition of OD inefficiency in this 10 years. The inefficiency is calculated in formula of "N($Q_{17} > 10^4$ p.e.) && $N^{OD}_{200} < 5$ hits divided by N($Q_{17} > 10^4$ p.e.)". N($Q_{17} > 10^4$ p.e.) is number of events which total charge of ID's 17-inch PMTs is over 10^4 p.e., and N^{OD}_{200} is number of hits in OD PMTs during 200 nsec. We usually treat the event as a cosmic ray muon detected when N^{OD}_{200} is over 5 hits or N($Q_{17} > 10^4$ p.e.), thus the formula means that ratio of the events couldn't be detected in OD among the events could be detected in ID.

3.2.4 Inner Detector (ID)

ID is a main detector of KamLAND and surrounded by the stainless steel spherical tank as vesse and supported by the structure. There are 3 layers inside ID, Buffer Oil Outer (BOO), Buffer Oil Inner (BOI) and Liquid Scintillator (LS) in plastic balloon in order from the outside. In BOO layer, there are 17-inch and 20-inch PMTs placed with the structure of diamond shape to hold PMTs (Fig 3.12). The Buffer Oil layers are separated by the transparent acrylic wall put on the each structure, to keep BOI from being dirty by the impurities in BOO comes from PMTs and the holders.

The numbers of 17-inch PMTs and 20-inch PMT are 1,325 and 554, totally 1,849 PMTs are used for ID. The photo coverages by 17-inch PMTs and 20-inch PMTs are 22% and 12%, thus totally 34% of inner spherical surface of ID is covered with photodetectors. The scintillation light is detected by these photomultipliers, and the signals from PMTs are recorded by the electronics in E-hut. These photomultipliers and electronics are described in the latter subsections.

The plastic balloon is made of 5 layers of plastic films with high transparency of more than 90% for 370 $\sim$ 500 nm wavelength, and especially 96% for 400 nm wavelength. The thickness of the film is 135 μm, and the film is constructed with 5 layers of EVOH-Nylon-Nylon-Nylon-EVOH. Nylon has 25 μm thickness and high light transparency and strength, while EVOH has 15 μm thickness and low gas permeability. The balloon is kept its spherical shape of 13 m in diameter by 44 of longitudinal and 30 of lateral ropes. There is a possibility that the tention to the ropes become higher depending on the difference of the density between LS and BO can be changed by the temperature of them, therefore the ropes to hang the balloon is mechanically strong and made of super fiber (Kevlar). The physical tensions of every 44 ropes are always monitored by load cell to know the condition of the balloon. There seems no rope has been cut or disconnected after the construction according to the load cell values.

Fig 3.12: The picture of PMT geometry inside ID before LS filling. The spherical shape is formed with combination of the diamond shape structures holding 16 PMTs. The transparent acrylic walls cover each diamond shape structure to separate BOO and BOI.

Liquid Scintillator (LS) and Buffer Oil (BO)

The plastic spherical balloon is filled with 1,000 tons ($1171 \pm 25m^3$) of LS which is the largest mass as target of liquid scintillator detector in the world, still today. KamLAND LS was developed to have excellent high output of scintillation light and high optical transparency to detect antineutrinos with energy as low as 1 MeV. In addition, impurities in LS should be as possible as less because the impurities which usually include radioactive isotopes potentially become backgrounds of the signals.

KamLAND LS is a mixture of 80% of dodecane ($\mathrm{C_{12}H_{26}}$), 20% of pseudocumene (PC, 1,2,4-Trimethylbenzene) as 2 organic solvents, and 1.36 g/l of PPO (2,5-Diphenyloxazole) as fluorescent solute. The properties of each component of KamLAND LS are summarized in Table 3.2.

BO is surrounding the plastic balloon to shield gamma rays and neutrons from surrounding materials such as PMTs, stainless steel tank and rocks containing ^{208}Tl and ^{40}K. To reduce the load of the balloon, the specific gravity of the BO is adjusted to be 0.04% less than that of the LS. For this purpose, the BO is a mixture of mineral oils, dodecane ($\mathrm{C_{12}H_{26}}$) and isoparaffin ($\mathrm{C_nH_{2n+2}}, \mathrm{n} \sim 14$). The composition ratio of dodecane to isoparaffin is 53 : 47. LS and BO are flammable liquids should be treated under the control of Fire Defense Low in such a huge amount.

KamLAND LS was filled to ID after water extraction and nitrogen purge operations at first. The water extraction and nitrogen purge were operated in 1$^{\mathrm{st}}$ purification area near the entrance gate of KamLAND area. The radioactive impurities in LS was enough few due to these operations to observe reactor neutrino, while they are quite high concentrations to observe solar neutrinos. The energy spectrum of solar neutrinos is broaden to lower ($\sim$ few 100 keV) energy region, we decided to remove the radioactive impurities such as ^{40}K, ^{210}Pb and the other isotopes which are sources of low energy backgrounds in LS to lower the threshold.

The LS distillation system and high-purity nitrogen gas generator were constructed in KamLAND area in 2006 and the first distillation campaign has started in 2007. The LS distillation system has distillation towers for each component of LS and nitrogen purge

Table 3.2: The properties of KamLAND LS components.

Parameters	Dodecane (N12)	Pseudocumene (PC)	PPO
chemical formula	$C_{12}H_{26}$	C_9H_{12}	$C_{15}H_{11}NO$
chemical structure	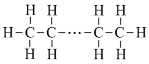 $H{-}\overset{H}{\underset{H}{C}}{-}\overset{H}{\underset{H}{C}}{\cdots}{-}\overset{H}{\underset{H}{C}}{-}\overset{H}{\underset{H}{C}}{-}H$	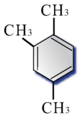	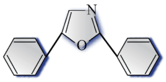
density at 15 °C [g/cm^3]	0.7526	0.8796	-
flashing point at 1 atm. [°C]	54	83	72
boiling point at 1 atm. [°C]	216	169	360
melting point at 1 atm. [°C]	-10	-44	72

tower. First of all, the distillation was operated to separate LS to the components by the difference of the boiling point of them. And then, each component is mixed each other with adjusting the density and PPO concentration to make a layer in the balloon to replace LS in high efficiency. This distillation flow is repeatably operated in cascade with data taking to monitor LS quality. Finally, the distillation campaign has completed in 2009, the total volume of processed LS is over 5,000 m^3 corresponding to four full volume exchange of LS in the balloon.

3.2.5 KamLAND Photodetector

KamLAND detector has 2 types of Hamamatsu photomultiplier tubes (PMTs) as photodetector to detect the scintillation light in ID. One of them is 1,325 specially developed 17-inch fast PMT custom-designed for KamLAND, and the other is 554 20-inch PMT inherited from Kamiokande detector. The schematic view of 17-inch and 20-inch PMTs are shown in Fig 3.13.

The 17-inch PMTs were developed based on 20-inch PMTs with the aim of considerable improvements in energy and time response. The big difference between 17-inch and 20-inch PMTs is dynode shape. The 17-inch PMTs have the line focus type dynode, and the effective region on the photocathode plane is limited by masking the outer fringe, unmasked area is 17-inch size, to obtain better timing and energy resolutions than that of 20-inch PMTs. That's why 17-inch PMT is called "17-inch" while it is same size as 20-inch PMTs. Thanks to these modifications, 17-inch PMTs is significantly improved in transit-time-spread (TTS) and peak-to-valley ratio (P/V). TTS is improved from $\sim$ 5.5 to $\sim$ 3.0 nsec in FWHM, and P/V is increased from $\sim$ 1.5 to $\sim$ 3.0 measured using 1 p.e. pulse height distribution.

The signals from 17-inch PMTs are used for vertex calculation because they have good timing resolutions. On the other hand, energy is estimated with both 17-inch and 20-inch PMTs to get better energy resolution by adding 20-inch to enlarge the photo coverage of the ID spherical surface.

The correlation of quantum efficiency with the wavelength of light is shown in Fig 3.14. It depends mainly on the material of the photo-cathode, bialkali, although individual differences exist because of variation in the thickness of the material.

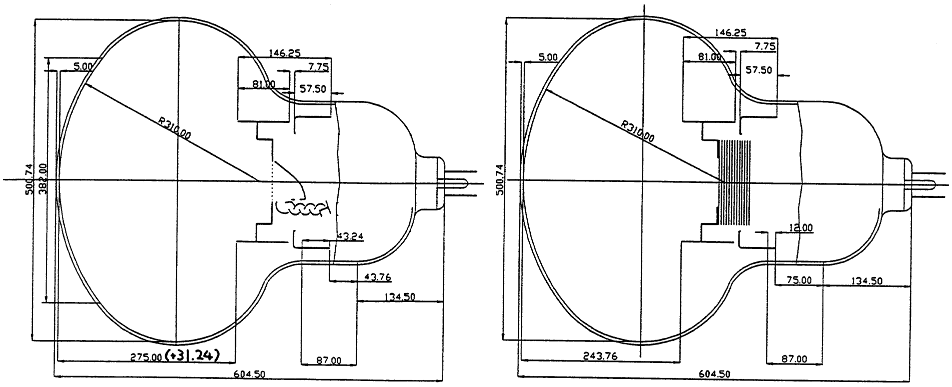

Fig 3.13: The diagrams of 17-inch PMT and 20-inch PMT for KamLAND. 20-inch PMT is given from former Kamiokande detector, and set in ID and OD both. The size of 17-inch PMT is same as that of 20-inch, and the surface of 17-inch PMT is covered with black sheet to maximize the correction efficiency. 17-inch PMT is developed to get better timing resolution by the line focus dynode based on 20-inch PMT, and set only in ID. The photo-cathode is made of bialkali, same ones for 17-inch and 20-inch.

3.2.6 KamLAND Data Acquisition System

KamLAND data acquisition (DAQ) system can be categorized to the three devices like in Fig 3.15. KamFEE is an electronics board to digitize the analog signals from PMT. KamLAND Trigger electronics module (KamTrigger) receives hit information which is discriminated with KamFEE, and issues the waveform acquisition commands to KamFEE by some trigger decision. DAQ computer operates DAQ via network by the control KamFEEs and Trigger module. These electronics is synchronized with 40MHz frequency clock, and time information is recorded for each event (trigger) in timestamp, the unit of which is clock (CLK), corresponding to 25 nsec.

KamLAND Front-End Electronics (KamFEE)

The electronics board for waveform digitization is called KamLAND Front-End Electronics (KamFEE or FEE) developed in Berkeley. The schematic diagram of KamFEE is shown in Fig 3.16. The size of the board is VME 9U, 1 slot and there are 12 channel signal input ports on the front panel. KamFEE board is based on the technology of Analog Transient Waveform Digitizer (ATWD), which has an array of condensers and maintains waveform information in analog charge. The ATWD allows the fast sampling of the PMT pulses as a function of time with 128 10-bit samples in 1.5 nsec steps. When the discriminator is triggered, the overwrite on the array is stopped and the waveform is saved (”hold”) for 175 nsec by ”capture” command from the FPGA. After that, if a trigger command is issued from KamTrigger, this waveform is digitized within $\sim 25\ \mu$sec. If no trigger command is issued, the ”hold” is canceled after the 175 nsec and ATWD restarts the sampling.

An input analog signal is divided to three line to amplify with different factor ($\times 20$, $\times 5$ and $\times 0.5$) to precisely record the waveform in different voltage range. The amplitudes are named High, Middle and Low gain channels (P-gain, H-gain and L-gain). The each waveform in each gain channel is survived or removed depending on the maximum or the minimum signal peak height when it is recorded to sdram to reduce the data size. In addition, there are 2 ATWD for each input not to miss the waveform during the digitization which takes $\sim 25\ \mu$sec. The digitized waveform is stored in the memory (RAM) for the 12

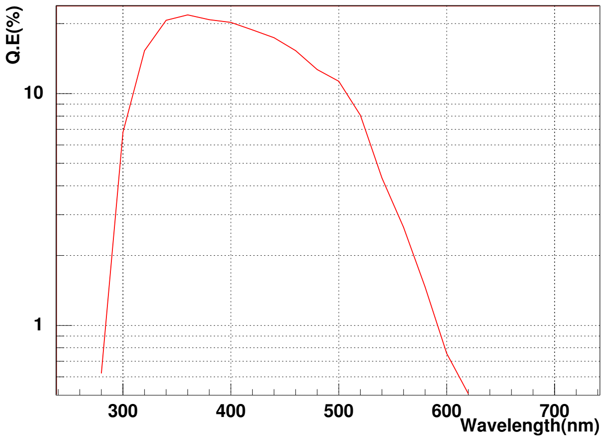

Fig 3.14: The quantum efficiency of KamLAND PMT. This efficiency is measured by Hamamatsu Photonics company. The average of quantum efficiency at KamLAND LS wavelength (380 $\sim$ 400 nm) is $\sim$ 20 %.

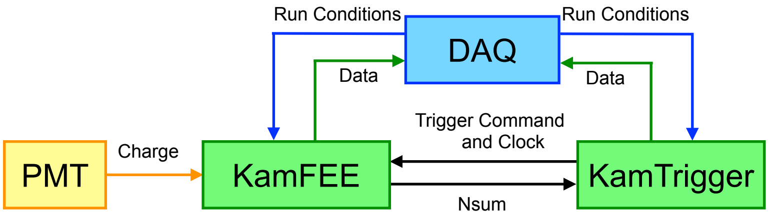

Fig 3.15: The schematic diagram of the communication among PMT, DAQ computers and electronics. PMT gives charge information with analog signal to KamFEE, and KamFEE discriminates the analog signal and gives Nsum (Hit information) to KamTrigger. KamTrigger provides clock information by synchronization and digitization command to KamFEE. DAQ computers controls the these electronics and record waveform and trigger data.

channels on the board, and transfered to front-end PC via VME interface and fiber cable.

As just described, KamFEE can record the waveform from PMT in high efficiency except the short period such as the moment with high event rate after high energy cosmic ray goes through the detector. We can minimize the effect of these dead time by veto after high energy cosmic ray events, and total dead time can be acceptable and not much long because KamLAND detector is located in the underground.

KamLAND Trigger (KamTrigger)

KamLAND Trigger electronics is a big module, VME 20U and occupy the full slots. The GPS (Global Positioning System) receivers are located at the entrance of Kamioka mine and Mozumi office, and one of them provides the accurate time information to KamLAND DAQ system. The GPS receiver at mine entrance has been used to provide it, and it was switched to the receiver at Mozumi office after the failures of GPS lock because of broken antenna cable at mine entrance. Note that there is a delay of the GPS time due to long cable from entrance to KamLAND. KamTrigger generates timestamp with own 40MHz clock and 1PPS signal provided by the GPS receiver for each event (trigger). The timestamp is, also being provided to each KamFEE board to synchronize time information,

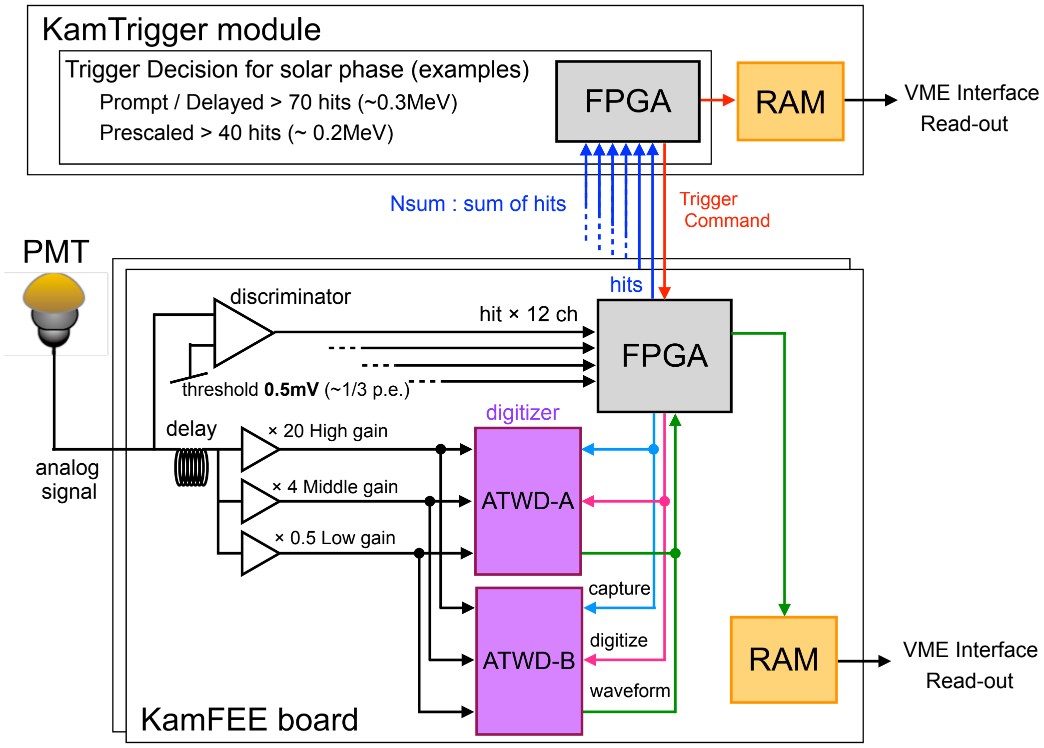

Fig 3.16: The schematic diagram of KamLAND Front-End Electronics.

and calibrate the waveform sampling interval in ATWD chip of KamFEE board.

KamTrigger is connected to every 200 KamFEE boards with the parallel cables. It receives hit informations (0 $\sim$ 12 hits / clock) from every KamFEE boards on every clocks, and computes the **Nsum**, which is digital sum of hits in the 125 nsec (5 clock) window. If Nsum excesses a preset threshold, the acquire trigger command is sent to the KamFEE boards. There are several preset thresholds to issue several trigger commands, such as ID Prompt Trigger, ID Prescale Trigger, OD Top Single Trigger and so on. They are called ID / OD Nsum triggers, which is issued by Nsum value for ID or OD. On the other hand, there are two triggers which is issued not by Nsum but time information. GPS Trigger is issued at the start of the run and every 32 seconds thereafter, and it sends an acquisition trigger command to the KamFEE board for OD. The other is 1 PPS Trigger, which is issued every second in synchronization with the GPS time, and it sends an acquisition trigger command to the all KamFEE board to study the background events. The remaining triggers are categorized to History Triggers, Calibration Triggers and the Other Triggers.

The list below is summary of primary triggers for physics analysis of KamLAND-Zen.

- **ID Nsum Triggers**
  - **ID Prompt (Delayed) Trigger** : **ID Prompt Trigger** is issued as an acquisition trigger command to all the KamFEE boards when ID Nsum excesses ID-Prompt-Trigger threshold, equal to 70 hits for solar phase and KamLAND-Zen 1$^{\text{st}}$ phase. The threshold corresponds to $\sim$ 0.3 MeV, and it's enough low to measure the energy spectrum of ^{136}Xe double beta decay. This trigger is/was used for prompt events of inverse beta decay, which is anti-neutrino detection event, and the threshold was 120 hits before LS purification. **ID Delayed Trigger** is issued as an acquisition trigger command to all the KamFEE boards when ID Nsum excesses ID-Delayed-Trigger threshold within 1msec window following a

prompt trigger. This trigger was used for delayed events with lower threshold than that of prompt trigger. The threshold is, however, same as prompt trigger (70 hits) for now, and there is no advantage of delayed trigger.
  - **ID Prescale Trigger** : To study and measure the lower energy spectrum, **ID Prescale Trigger** is issued in the time window preliminarily scaled to shorter with lower ID-Prescale-Trigger threshold. It sends an acquisition trigger command to the all KamFEE boards. By amplification with prescale factor, we can reconstruct the lower energy spectrum than usual prompt trigger threshold. In addition, this trigger is available for the source calibration DAQ by decreasing the trigger rate with shorter time window.

- **GPS Triggers**
  - **GPS Trigger** : This trigger is issued at the start of the run and every 32 seconds thereafter. It sends a global acquisition command to the OD FEE cards, and issues an interrupt to the GPS interface module on the VME to record the GPS time.
  - **1PPS Trigger** : This trigger is issued every second in synchronization with the GPS time. It sends the acquisition trigger command to the all KamFEE cards.

- **Other Triggers**
  - **Disable / Enable Trigger** : **Disable Trigger** is issued on the condition that the trigger is disabled owing to almost fullness of the data buffer. While **Enable Trigger** is issued on the condition that the trigger is enabled after recovery from buffer fullness. They both do not issue any acquisition trigger command. However they are important to calculate the dead time due to the electronics.

KamLAND Data Acquisition System

The KamLAND Data Acquisition (KamDAQ) system is required to read data from electronics devices and store the data onto the strage devices. Each 20 KamFEE board is inside 1 VME create which supplies the power and holds the boards as the container. At E-hut, 10 VME crates are for KamFEE boards, and 1 for the trigger electronics, and 4 are for the backup. We totally have 15 VME crates used as the interface for data transferring, and they are each connected to one Front-End PC at PC-Farm exclusively through pair of VME-PCI bus bridge cards and an 200m of optical fiber cable. The front-end PCs are connected to back-end PCs with 100Base-T and 1000Base-T ethernet and network switching hubs.

Data buffering, data stream conjunction, and data flow control are naturally involved in the data transportation process. In addition to data readout, transportation and recording, data monitoring is also an important task of a DAQ system. Since a DAQ system is the only software that works with data in realtime and also the only software that has direct connections to electronics devices. There are responsibilities to monitor the data, display conditions to operators, and control the devices appropriately. The DAQ system is also an interface of the devices to operators. Electronics devices are configured by the DAQ software based on operators ’control and/or automated control, and the DAQ system itself is controlled by operators ’ command. DAQ system is required to detect and notify any system failures, and to reject improper operator commands. The system needs to provide a framework on which processes distributed over a network work efficiently in cooperation. The framework includes remote process control, command/message exchanging, and parameter sharing.

The KamDAQ system software, namely KiNOKO which stands for "Kinoko Is Network distributed Object-oriented KamLAND Online-system", was designed to comprehensively handle these requirements by making practical use of recently developed computer technologies such as distributed object systems and component architectures. The distributed object system has realized a seamlessly integrated parallel processing environment over networked computers, which leads to true scalability covering from a single process system to a multiple computer system. Reuse of well-tested system components has naturally increased the system stability and reliability.

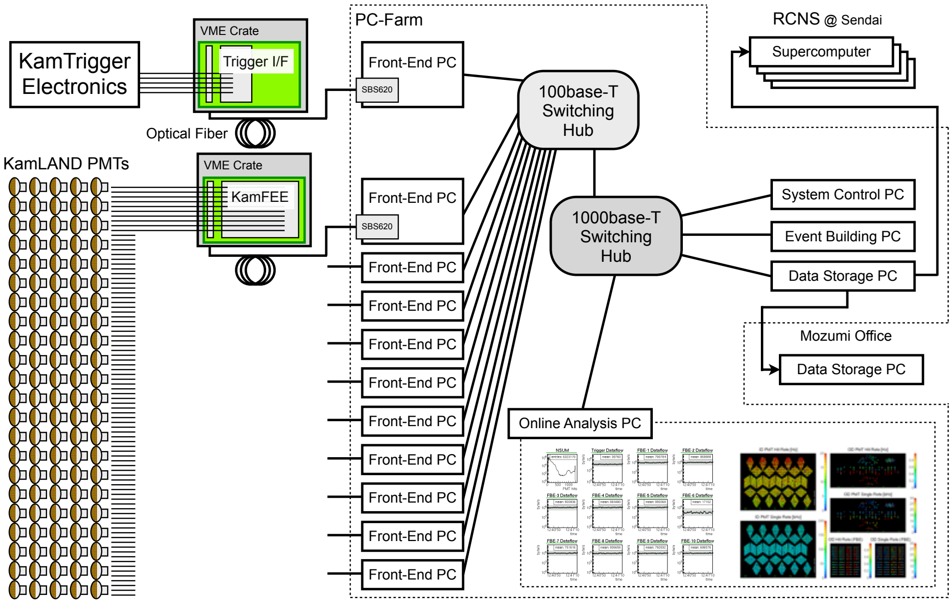

Fig 3.17: The schematic diagram of DAQ computers and network. An analog signal from KamLAND PMT is connected to KamFEE board and digitized. The digitized signals are collected via VME I/F to Front-End PCs, and controlled, event built and real-time analyzed by Back-End PCs. The real-time analyzed result can been checked in online viewers on DAQ computer. The data is stored in the mine (PC-Farm) and computers in Mozumi office, and finally transferred to Sendai.

The DAQ system software, KiNOKO, has been opened to the public and has widely been applied to a number of other experiments, from a single channel CAMAC system to a high-rate signal sampling application with multiple computers. Feedbacks from these applications have been contributing toward further improvements of the system usability and stability, and by the time of KamLAND operation, the system had become stable enough.

Furthermore, KiNOKO and KamDAQ system has been running in this 10 years stable without serious problem, even front-end and back-end PCs have been updated and replaced twice so far. And also, we could derive some interesting results in neutrino physics from KamLAND data with KamDAQ system. The KamDAQ system are reliable an stable system we proudly have.

Fig 3.17 shows the schematic diagram of KamFEE, VME crate, front-end and back-end PCs and the network of them. The digitized waveform data is collected via 100base-T and 1000base-T network, and there are some back-end PCs to analyze data, to record data, to sort data with event ID and to control the DAQ system. The realtime data analysis is for monitoring the current data flow, hit rate, trigger rate and so on, to notify the status of KamDAQ to the operators (shifters). The event building is processed for sorting the waveform data by the timestamp and constructing the event packets to make the analysis easier. The data storage PC stores the data in the local storage for few days, and transfers to Mozumi office and RCNS in Sendai. The raw waveform data is stored in the tape devices at computer room in RCNS permanently after the waveform analysis has done, and removed from the disk.

3.3 KamLAND-Zen Preparation

The construction of KamLAND-Zen has started in May 2011. There were many preparation and R&D for the construction. Such as liquid scintillator which is loaded Xe gasses, the measurement of Xe gasses quality, the clean room for installation, and the other items were developed and studied.

This section includes the preparation and R&D for the related issues before the start of the construction.

3.3.1 Inner Balloon

The Inner Balloon (IB) is one of the most important items which holds Xe-loaded liquid scintillator (Xe-LS) inside for years. It should have good light transparency to observe signals from the balloon without attenuation, and high tightness of the gas and liquid to keep Xe-LS from leaking to outside. The radioactivity of the materials for the balloon should be as low as possible to minimize the background contribution from the balloon. In addition, it should be physically strong to keep the shape of the balloon and hang the weight of the Xe-LS and itself because it is impossible to construct the supporting structure under the balloon in KamLAND ID. The size of the balloon is determined by the volume of Xe-LS depends on how much amount of Xe gas we can use. However, we have to consider how to fold and shrink the balloon to smaller because the diameter of the gate to install the balloon at chimney is fixed.

There are many requirements for IB considering experimental plan and background estimation, like described in the following.

Balloon Design

The size of IB is determined by the density of Xe-LS and available Xe amount, to minimize the differential pressure between inside and outside IB. Purchased and available amount of xenon gasses is approximately 400 kg, the solubility of xenon into LS is 3 wt% at atmospheric pressure, and the density of Xe-LS should be 777.7 kg/m^3 (+0.05% heavier than KamLAND LS). Therefore the diameter of IB sphere is defined as 3.16 m and the volume is 16.5 m^3 with teardrop shape as shown in Fig 3.18. The IB consists of 3 parts ; sphere, cone and pipe made of film, and they are combined to make tear drop shape. The film pipe is connected to corrugated tube (Fig 3.18(b)(d)) extended from chimney in KamLAND detector. The IB supporting structure consists 12 belts and 12 strings connected each other (Fig 3.18(c)). The belts are made of 3 cm width films and welded by the heat in the same manner as IB, and strings are vectran.The strings are connected to load-cell to measure the tention of each string at M5 flange in chimney.

The total mass of IB is $\sim$ 800 g, and the IB is hanged with 12 nylon belts and 12 vectran strings from chimney part of KamLAND.

Film Selection for Inner Balloon

The material for IB is plastic film which is time-proven as material of the outer balloon in KamLAND. They have high transparency, enough strength and easiness to handle.

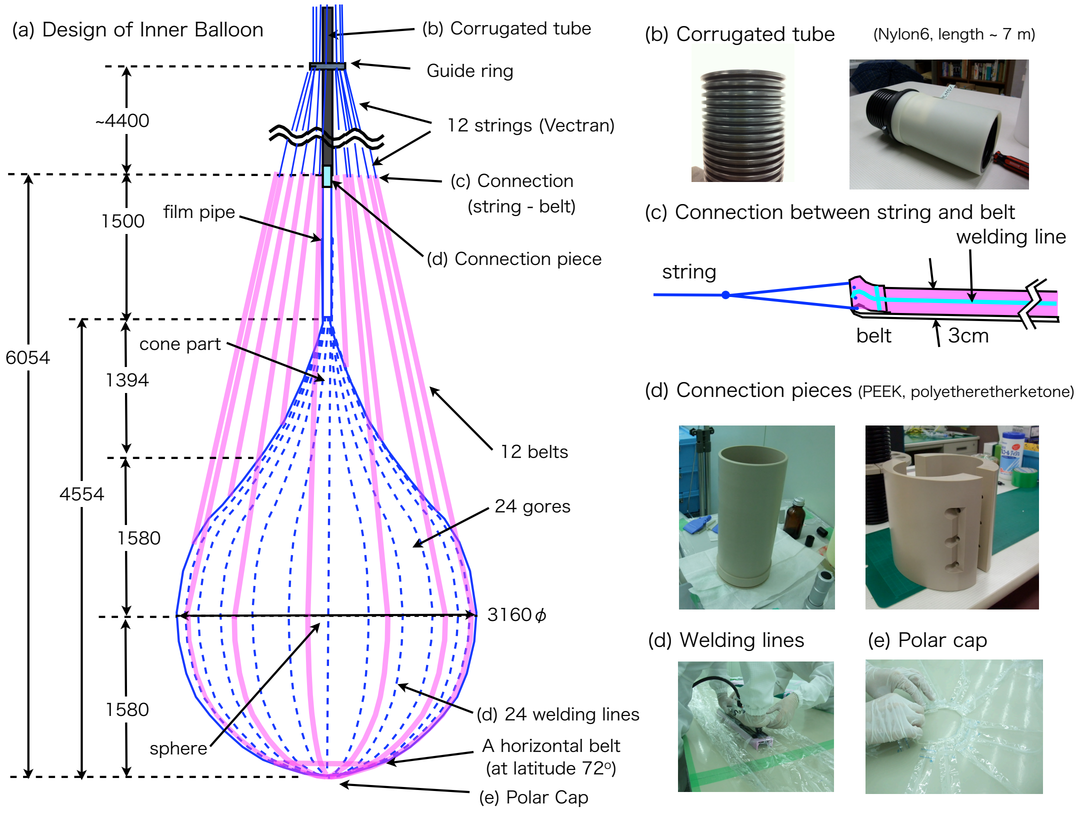

Fig 3.18: Design drawing of Inner Balloon. The lengths are written in unit of mm in (a). 7 meter length corrugated pipe made of nylon (b) is connected to the balloon with pieces made of PEEK(d). IB is hanged with 12 nylon belts and 12 strings made of vectran connected each other (c). 24 gores are welded by the heat, results 12 welding lines (d) in spherical part. Bottom of IB is held by the polar cap (e).

However, the requirement of the material for IB is more stringent than that for the outer balloon as noted in detail below because the film for IB should be much thinner due to some experimental requests.

(a) Light Transparency

The light transparency of the film should be high (more than 95%) not to attenuate the scintillation light through the film. The wavelength of scintillation light is 370 $\sim$ 450 nm in KamLAND, and the film must have high transparency in the range.

(b) Physical Strength

IB is pressurized by the density difference between Xe-LS and KamLAND LS, and also subjected by the force during the installation. There are no supporting structure under the balloon, and IB is hanged and support the weight itself. Therefore, the film should have more than 10 N/cm in the rupture strength calculated with the density difference assumed as $\Delta\rho = 1.0\%$ including safety factor.

(c) Gas Tightness

We empirically know the plastic films have high tightness for liquid. And gas tightness also should be good, and we have to validate and estimate the leak of xenon gas. The enriched xenon gas is very expensive, and it must be held in the balloon. The target value is less than 1.0% leakage of total xenon gasses, corresponding to 4 kg/year of the leakage.

(d) Thickness

The thickness of the film is important parameter for the light transparency. The transparency of the thinner film is higher than that of thicker one. In addition, the thickness determines the detection efficiency of alpha particles in the film. An alpha particle can not penetrate much in thick nylon film. As discussed in section 3.1.2, 25 μm thickness is a candidate considering the detection efficiency and easiness of the handling.

(e) Radioactive Impurities

The radioactivities of the film is serious condition for fiducial volume decision. The Higher event rates from impurities in the film, the worse FOM we got if 100% of fiducial volume is available, where FOM stands for "Figure of Merit" calculated with the equation, $FOM = \frac{S}{\sqrt{S+B}}$, S is a number of signal events and B is a number of background events. To use 100% of fiducial volume of IB, the radioactivities of ^{238}U, ^{232}Th and ^{40}K are severely circumscribed by the calculation of FOM, and the efficiency of tagging discussed in section 3.1.2. The targets value of the concentration were $(10^{-12}, 10^{-12}, 10^{-11})$, ideally $(10^{-13}, 10^{-13}, 10^{-12})$ for (^{238}U, ^{232}Th, ^{40}K).

(f) Welding Method

How to weld the films and make balloon is also considerable from a standpoint of mechanical strength, Xe gas tightness, the easiness to handle and potential sources of the background event same as film materials.

The selected film for IB material which satisfies the requirements is one made by Toyobo company. **(a) light transparency** is measured and it is 99.4 ± 0.3 % at 400 nm wavelength. **(b) physical strength** was confirmed by the measurement of rupture strength, which is 4.9 kgf/cm, corresponding to the tolerance of up to 6 % density difference between inside and outside liquid scintillator. The target of density difference is less than 0.1 %, namely, safety factor is enough large, 60. **(c) gas tightness** is also measured with xenon gas, and the leakage amount of xenon gas is less than sensitivity of the detector. The estimated amount of Xe gas leakage is less than 1.3 kg per 5 years. **(d) thickness** of the film is 25 μm, and **(f) welding method** is thermal welding. The welding condition such as temperature, duration of heating and cooling is tested and established. The concentrations of **(e) radioactive impurities** were measured by company, and they are $(9 \times 10^{-12}, 11 \times 10^{-12}, < 1.2 \times 10^{-11})$, and $(2 \times 10^{-12}, 3 \times 10^{-12}, 2.3 \times 10^{-12})$ after ultra pure water washing for (^{238}U, ^{232}Th, ^{40}K). The concentration of ^{40}K is estimated value from measurement of just K with natural abundance of 0.0117 %. By ultra pure washing, radioactivities of ^{238}U, ^{232}Th and ^{40}K are compatible with requirement. This film made by Toyobo company is used for IB fabrication after ultrasonic cleaning with ultra pure water.

Fabrication of Inner Balloon

The Inner Balloon (IB) is fabricated at super clean room to avoid contamination from radioactive impurities contained in dust in the air. The super clean room is classified into class 1, which generally means the number of counted dust larger than 0.5 μm in 1 feet^3 is less than 1, and located in a facility of Tohoku University in Sendai. All equipments and devices to fabricate IB are cleaned up by wiping with pure water and/or alcohol before bringing to the clean room. IB is fabricated with 25 μm nylon film, very thin to be carefully handled. The procedure of the fabrication is following, and each step is shown in Fig 3.19.

1. Film cutting, washing and checking
   The film is cut in 5.5 m length for gore parts and 7.5 m length for the belts from film roll. After ultrasonic washing with pure water, the film is dried and checked scratch and pin hole by human eyes. If there is a scratch whose location is unable to avoid to use, the film is discarded.
2. Film clipping and welding
   The film is clipped for each part such as 24 gores which are main films to form spherical shape. Each gore is welded by heat with 30cm length heating machine after welding method (heat temperature, duration and so on) is established. When 24 gores are merged, the spherical shape is formed. In addition to gore part, cone, pipe part and belts are clipped and welded. Sphere, cone part and pipe part are finally welded by the heat to assemble IB.
3. Leak hunting and patching the leak
   Leak is checked with helium detector which has the sensitivity $\sim 9 \times 10^{-7}\mathrm{Pam}^3/\mathrm{s}$ depending on ambient air in the clean room. The IB is inflated with helium, and moving sniffer to detect the leak point. Several leak points are found mainly at boundaries of welding line, and patched with nylon piece and *"Aron Alpha 202"* which is a kind of krazy glue. The glue have been tested for compatibility with LS and Xe tightness after confirmation of the excellent cleanliness of radioactivities.
4. Assembling IB with supporting belts
   The supporting structure is carefully constructed with 12 nylon belts not to tangle each other. The structure is assembled after IB is folded to small diameter to go through the hole at chimney.
5. Wrapping IB into the box
   After assembling, IB and supporting structure are covered with an inner envelope made of same films. The inner envelope is finally removed after deployment into the detector. Outer envelope covers them as protection films in the box. The box is put into air-tight bag and filled with nitrogen gas. The bag is also wrapped by the packing material for transportation.
6. Transportation of the box to the mine
   The box is sent to Kamioka, and moved to the dome area in the mine. It is unpacked in the clean room above the chimney of KamLAND.

The IB fabrication has started in May 2011, and finally assembled IB in the box arrived to the mine without any damage in August 2011. The clean room for the fabrication is located in Sendai, and the period of fabrication was just after Fukushim-I nuclear reactor accident (11th March 2011). This is controversial in terms of the unexpected backgrounds originated by the fall-out from the accident. Chapter 6 discusses the backgrounds.

3.3.2 Xe-loaded Liquid Scintillator (Xe-LS)

The target of KamLAND-Zen is $^{136}\mathrm{Xe}$, and it is dissolved to liquid scintillator to observe scintillation light from double beta decay signal, named Xe-LS. The density of Xe-LS should be slightly heavier to reduce the load for the IB and to avoid to float IB. Optical performances of Xe-LS are also required as same level of KamLAND LS. We found dissolving Xe gas make LS density heavier and light yield worse, and the recipe of Xe-LS is decided to solve the problems. Xe-LS consists 82% of decane, 18% of pseudocumene (1,2,4-trimethylbenzene) by volume, 2.7 g/liter of the fluor PPO (2,5-diphenyloxazole) and 3 wt% of enriched xenon gas. Dodecane (N-12) used for KamLAND LS is replaced to decane (N-10) which has $\sim 2\%$ lighter density to adjust the density of Xe-LS. The PPO concentration of Xe-LS is twice higher than KamLAND-LS to compensate the decrease of light yield by xenon loading. Although the measured light yield of Xe-LS is 3% lower than

1. Film cutting and washing with ultrasonic and pure water

2. Film clipping and welding machine

3. Leak hunting and patching the leak point

4. Assembling with supporting belts

5. Wrapping IB into the box

6. Transportation the box to mine

Fig 3.19: The pictorial procedure of inner balloon fabrication. The numbers above each picture correspond the numbers of steps in the procedure of the fabrication.

KamLAND-LS, it is still within expected range to be able to analytically correct. The isotopic abundances in the enriched xenon were measured by residual gas analyzer to be $(90.93 \pm 0.05)\%$ ^{136}Xe and $(8.89 \pm 0.01)\%$ ^{134}Xe, and other xenon isotopes are negligible.

Dummy-LS is used to inflate IB before Xe-LS filling, therefore it does not contain xenon. The density is adjusted without xenon gas by increasing ratio of PC, and PPO concentration is same as Xe-LS for the case of mixing with Xe-LS in IB.

Same as KamLAND-LS, liquid scintillator for Xe-LS (also Dummy-LS) is purified before installation through the purification system. The purification system of KamLAND is described in detail in [65]. The purification is performed in each component, and a flow of Xe-LS is summarized in Fig 3.20. Dummy-LS goes through same processes except Xe dissolving in Xe system.

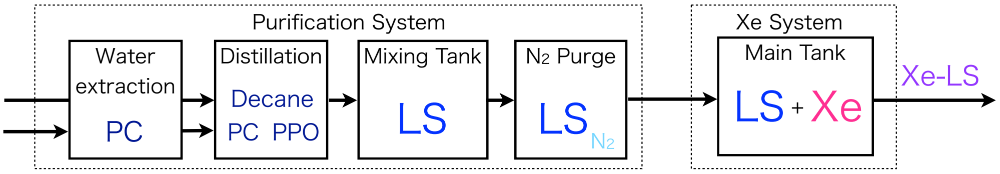

Fig 3.20: The flow of Xe-LS purification and mixing. After purchase of each component, water extraction is operated for PC. Decane, PC and PPO go thorough the distillation sytema and mixed to LS. Xe is dissolved into LS at main tank in Xe system after purged with nitrogen gas.

The concentration of ^{238}U and ^{232}Th in Xe-LS after purification is much less than before. They are discussed in chapter 6 and summarized in Table 6.5.

Xe System

The Xe system is constructed at 3rd access tunnel to KamLAND detector for xenon dissolving into liquid scintillator in 2010-2011. Main operations of the system are receiving liquid scintillator sent from purification system, dissolving xenon gas into the liquid scintillator, adjusting the density of liquid scintillator, and sending liquid scintillator with or without xenon into inner balloon through chimney part of KamLAND. In addition, the ability of xenon salvage from Xe-LS for the emergency situation is required. The system is an interface of input / output of liquid scintillator into / from the inner balloon, thus all activities for KamLAND-Zen are operated through the system.

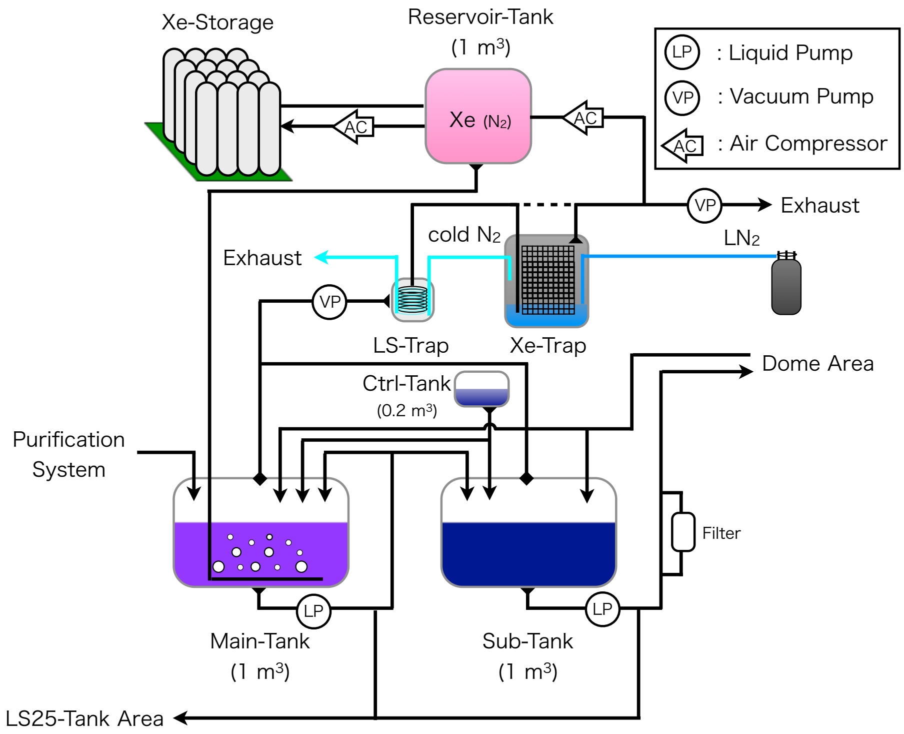

Fig 3.21: Overview of Xe system. Only essential tanks, traps and pipe lines are drawn to simplify the system drawing. There are also many meters, gauges, pipe lines and valves to control liquid and gasses no drawn here in the system. Main-Tank is mainly used for dissolving xenon into LS as its name suggests. Sub-Tank is for sending LS to dome area, where input/output lines to/from IB are located. Xe-Storage bottles are connected to Reservoir-Tank which controls the pressure of Main/Sub-Tanks. Xe-Trap is cubicle to collect frozen Xe after LS removed by LS-Trap using liquid nitrogen (LN_2).

The system has Xe gas storage tank, dissolving tank, sending tank, density control tank and several buffer tanks shown in Fig 3.21. These tanks are connected with the pipe lines, valves, pumps, compressors and various meters such as flow meter, density meter and pressure gauge. The system is too complicate to describe in detail, therefore Fig 3.21 includes only essential components.

3.3.3 Clean Roon at Chimney

For IB installation, the chimney of KamLAND detector needed to be converted to clean room. There were the equipments for source calibration operation before. The clean tent, glove box and devices for source calibration have been removed in July 2011 to construct the clean room. Fig 3.22(a)(b) show the design of clean room constructed on the scaffold around chimney. The clean room has four HEPA fan units on the ceiling and two large HEPA fan units on the floor, and been kept cleanliness level inside clean room. The accomplished cleanliness level is class 10 $\sim$ 100 depending on the location in the clean room, and the level is enough clean to install the IB. Measured radon level in the clean room is 1.5 $\sim$ 2.0 pCi/l, corresponding 56 $\sim$ 74 Bq/m^3.

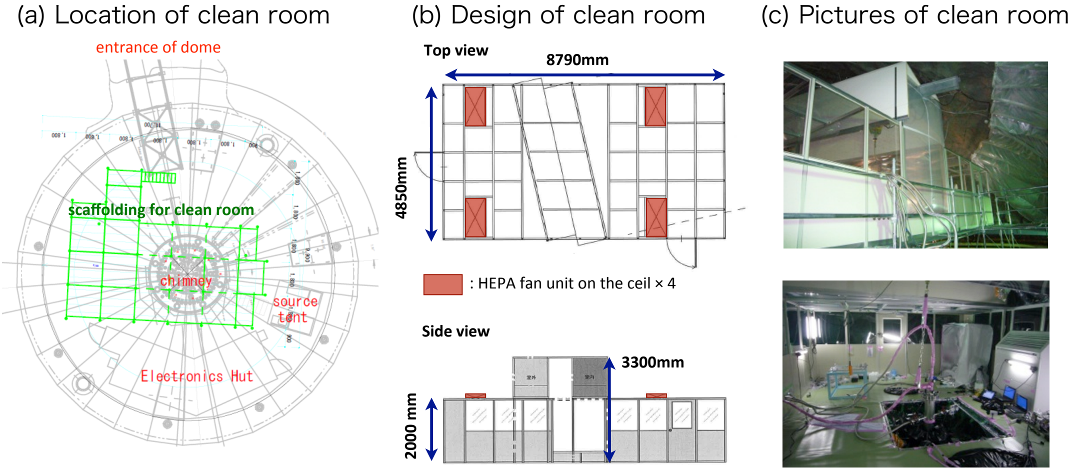
(a) Location of clean room
(b) Design of clean room
(c) Pictures of clean room

Fig 3.22: Design of clean room location and pictures. (a) shows design of scaffold construction for clean room on the chimney in dome area. The outside/inside view of constructed clean room is seen in (b)/(c).

3.4 KamLAND-Zen Construction

The construction phase of KamLAND-Zen has started in August 2011. First of all, we carefully installed IB into KamLAND detector with monitoring cameras. Then, we filled 16.5 m^3 of Dummy-LS to inflate IB, and replaced Dummy-LS with Xe-LS. The strategy of installation is graphically summarized in Fig 3.23.

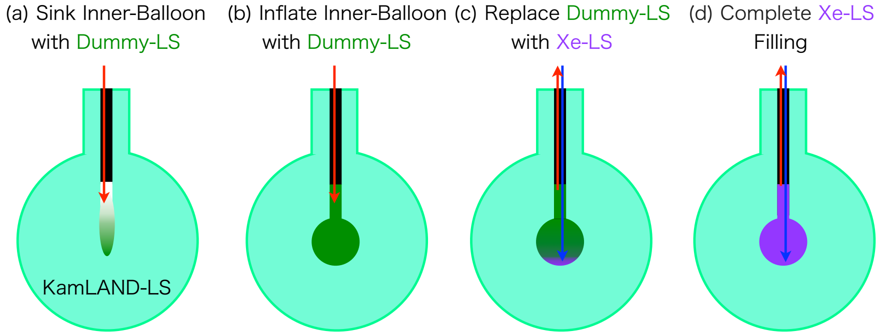
(a) Sink Inner-Balloon with Dummy-LS
(b) Inflate Inner-Balloon with Dummy-LS
(c) Replace Dummy-LS with Xe-LS
(d) Complete Xe-LS Filling

Fig 3.23: Strategy of inner balloon installation. The installation of IB with relatively heavier Dummy-LS at first (a), and then, Dummy-LS is filled until IB is completely inflated (b). The teflon tube is installed into the IB, and Dummy-LS is replaced with Xe-LS (c). Finally, the IB is filled with Xe-LS (d).

3.4.1 Installation of Inner Balloon into KamLAND

Before installation of IB, the monitoring system is installed into the detector. The system consists of 2 camera units and 2 LED light housings, and camera units are seen in Fig 3.24. The camera units have two movable cameras at the side and bottom and LED light (Fig 3.24(a)). The units are tested for LS compatibility and leakage before installation. Their installed positon is drawn in Fig 3.24(c) mainly to monitor the neck part of IB, and the picture taken with bottom camera is shown in Fig 3.24(b). Two camera units are simultaneously installed from the holes around the center hole which is used for IB installation to check the positions each other, and LED units are also installed from near holes to illuminate inside the detector.

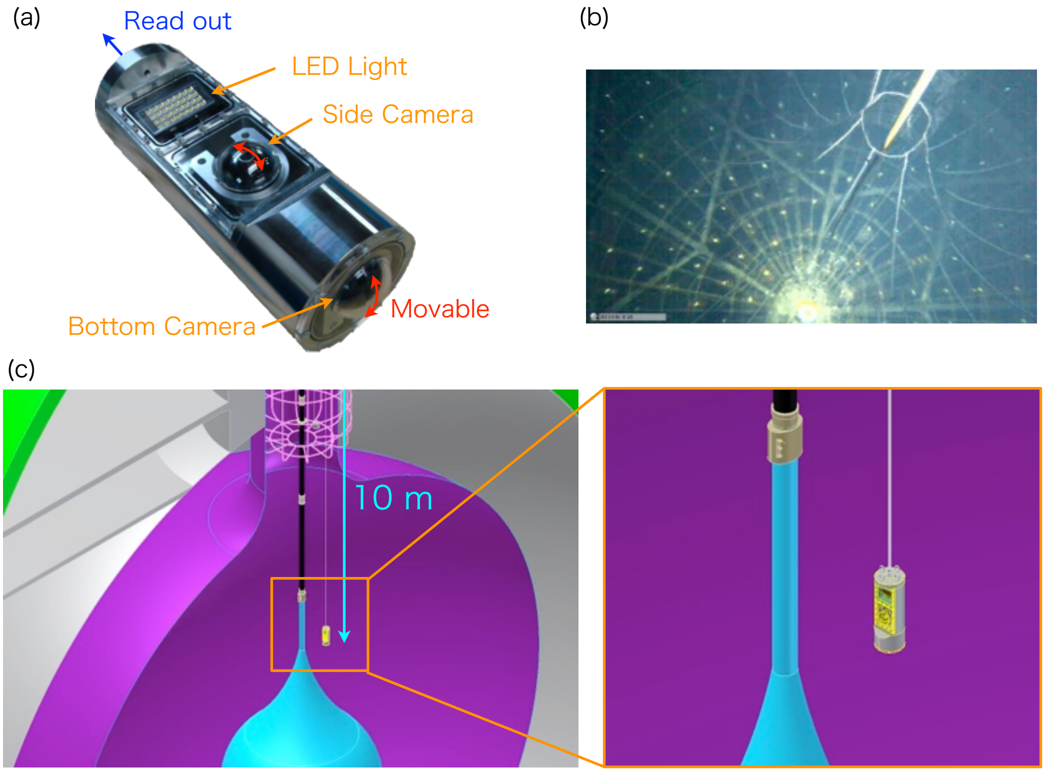

Fig 3.24: Monitoring system for IB installation. (a) shows picture of a camera unit, and it has a side camera, bottom camera and LED light. (b) is a picture taken by the bottom camera of (a). (c) is the view of the installation of the camera units. The main purpose of the camera units is to monitor neck part of IB, and camera units are located there.

The box sent from Sendai is unpacked in the clean room and the outer envelope covering the IB is removed. Three corrugated tubes are connected each, and the leak at the connection parts is checked with a helium detector. The IB, the corrugated tube, 12 strings and belts are assembled, while IB is still folded to be installed from the small hole into the detector. Inner envelope covers the IB to protect it during the installation, and will be removed just after the IB deployment.

After the monitoring system and IB have been ready, the installation of IB was performed on 17th August 2011. Around 20 people worked to manually install in the clean room as shown in Fig 3.25(a)-(c). Since the length of IB and connected corrugated tube is $\sim$ 14 meter, the IB is slowly moved by hands into the center hole as shown in Fig 3.25(b). It took $\sim$ 2 hours to completely install IB to the center of the detector. After manual installation, the inner envelope is removed, and then Dummy-LS filling was started to inflate the IB.

(a) IB installation

(b) IB installation

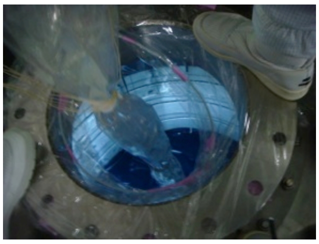

(c) IB installation

(d) M5 flange

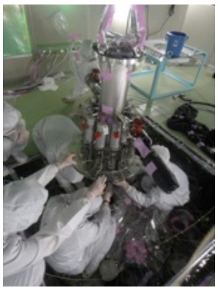

(e) Load cell

Fig 3.25: Pictures of IB installation. (a)-(c) show pictures during IB manual installation work. (d) shows M5 flange, and (e) is load cell unit attached to the flange to measure the load of 12 strings hanging the IB.

Fig 3.25(d) shows M5 flange which connects to corrugated tube and has 12 load cell units (shown in Fig 3.25(e)) to measure tention of 12 strings suspending the IB.

3.4.2 LS Filling

Dummy-LS Filling

Dummy-LS filling is done to inflate the IB after the installation, and the operation flow is drawn in Fig 3.26. The Dummy-LS is purified in the purification system and sent to Main-Tank in Xe system after nitrogen purge. And then, Dummy-LS is moved to Sub-Tank after degassing and compensation to atmospheric pressure with nitrogen gas. The density of Dummy-LS is adjusted by adding PC in Ctrl-Tank in Sub-Tank just before sent to the IB. The flow rate of Dummy-LS into the IB is $\sim$ 250 liter/hour, and a sequential operation proceeds $\sim$ 620 litter / batch. The filling temperature is controlled to be $\sim$ 10 °C and kept stable with cooling chiller because temperature changes the density of LS. We operated Dummy-LS filling while watching the shape of the IB by the monitoring system.

The total filled volume is calculated with integrating the volume of the flowmeter, and Dummy-LS filling is stopped when the total volume is 17 m^3 which corresponds to the design value of the IB. It took 6 days to fill Dummy-LS, and the filling was finished at the end of August. The shape of the IB can be checked by looking the vertex distribution of ^{222}Rn events tagged by ^{214}Bi-Po delayed coincidence technique, and the distribution can be seen in Fig 3.27(a). The outer thick black line indicates the outer balloon of KamLAND detector, and the inner thin black line indicates the boundary of the IB at designed location. Rn events above the IB comes from the monitoring system, and the Rn is uniformly distributed in the IB. There are no evidence of leakage from IB found from Rn distribution. On the other hand, KamLAND LS overflowed to buffer tanks in the first purification area due to the volume expansion of IB.

After the filling, a teflon tube is inserted down to near the bottom of IB for Xe-LS filling. In addition, the tube is used for agitation of Dummy-LS to uniform the density in the IB before Xe-LS filling.

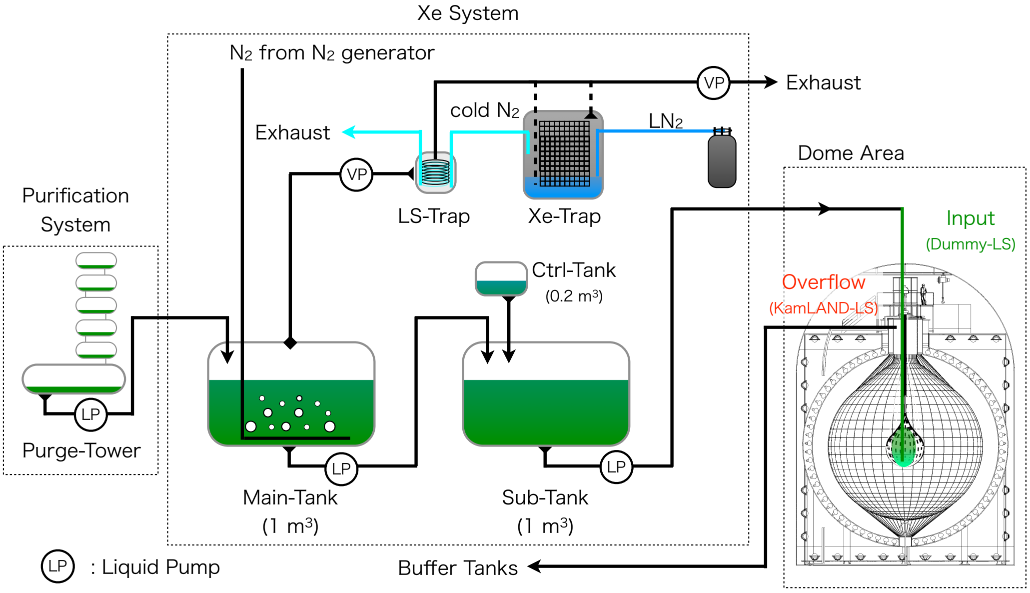

Fig 3.26: Diagram of Dummy-LS filling operation. The Dummy-LS is sent from purification system to Main-Tank. In the Main-Tank, the Dummy-LS is degassed and sent to Sub-Tank with nitrogen supplied from nitrogen generator. The density of Dummy-LS is adjusted by adding PC in Ctrl-Tank, and finally sent to the IB through dome area. KamLAND LS overflows to buffer tanks at the first purification area due to the volume expansion caused by the filling.

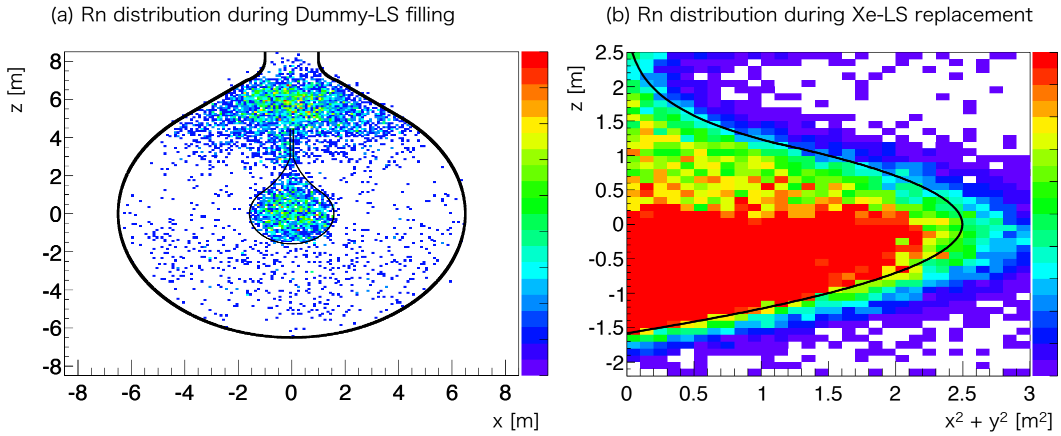
(a) Rn distribution during Dummy-LS filling

(b) Rn distribution during Xe-LS replacement

Fig 3.27: Radon distribution during LS the filling. (a) shows vertex distribution of ^{222}Rn tagged with ^{214}Bi-Po delayed coincidence events in the whole detector. The thick black line indicated boundary of the outer KamLAND balloon, and the thin line indicates boundary of the inner balloon. (b) shows closeup of ^{222}Rn distribution during the Xe-LS filling. There is a boundary of ^{222}Rn events in the Xe-LS made with the difference of the densities between Xe-LS and Dummy-LS.

Xe-LS Filling

Same as Dummy-LS, Xe-LS is purified in the purification system and sent to the Main-Tank after nitrogen purge. In the Main-Tank, Xe is dissolved to the liquid scintillator from Reservoir-Tank after degassing, and Xe-LS is sent to the Sub-Tank. The density of Xe-

LS is adjusted in the Sub-Tank, and the residual xenon in the Main-Tank is collected back to the Reservoir-Tank. The operation flow of Xe-LS filling is drawn in Fig 3.28. The Xe-LS is filled to the bottom of IB through a long teflon tube, and Dummy-LS is simultaneously drained from the tube used for Dummy-LS filling. The integrated volumes of filling and draining are balanced by controlling the flow rate (average ∼ 150 liter/hour). The Dummy-LS is interchanged to Xe-LS by carefully forming a layer with the density difference between Dummy-LS and Xe-LS. The boundary between Dummy-LS and Xe-LS is clearly seen with ^{222}Rn concentration as shown in Fig 3.27(b).

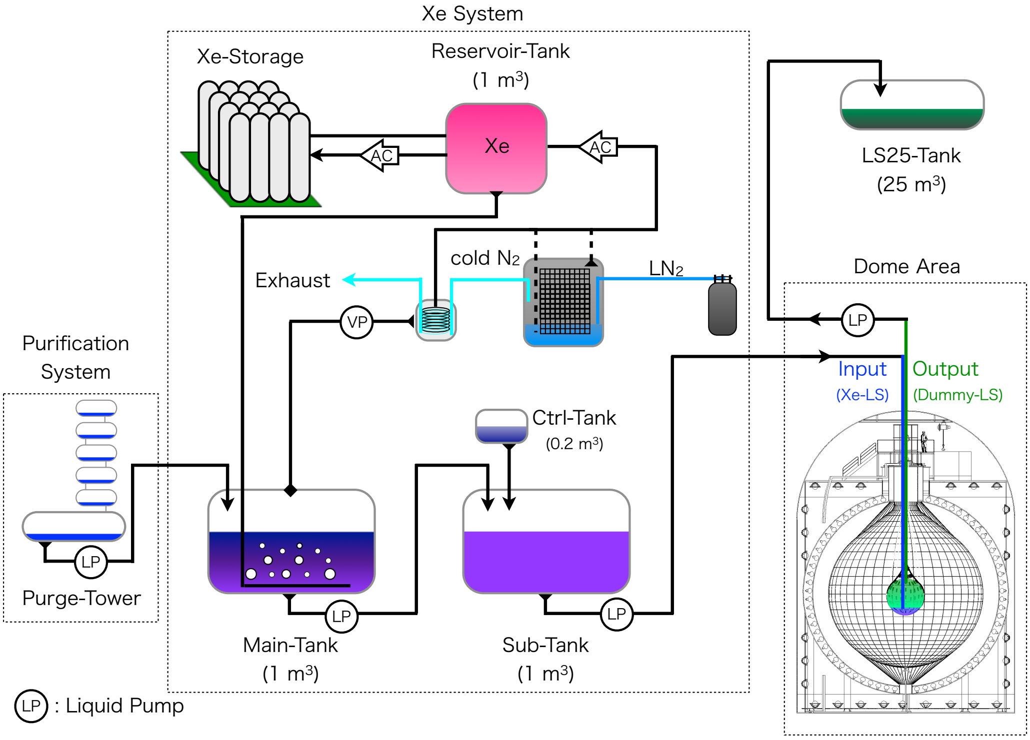

Fig 3.28: Diagram of Xe-LS filling operation. The Xe-LS is sent from the purification system to Main-Tank. In the Main-Tank, Xe is dissolved to Xe-LS through Reservoir-Tank after degassing, and then, Xe-LS is sent to Sub-Tank. The density of Xe-LS is adjusted by adding PC in Ctrl-Tank, and finally sent to the IB through dome area. At the same time, Dummy-LS in the IB is drained and sent to LS25-Tank to balance the IB volume.

However, we found that the drained Dummy-LS contains a small amount of xenon by checking the Xe concentration with gas-chromatography. The drained Dummy-LS is sent to LS25-Tank which was constructed near the entrance of the KamLAND area in the mine, and the LS25-Tank has air tightness to keep the xenon gas in the tank. Therefore, we can collect the returned enriched ^{136}Xe gas from LS25-Tank later, and actually we collected it and the residual ^{136}Xe gas in the Xe system too. The amount of installed ^{136}Xe is calculated with the consumed amount in the storage bottle and collected amount, and also estimated with measurement of sampled Xe-LS using gas-chromatography. The Xe mass estimation is discussed in the latter section 7.1.1, and 315.99 ± 1.08 kg of ^{136}Xe is installed to the IB as a result.

The total volume of the filled Xe-LS is 16.58 m^3 considering the volume expansion due to the temperature deviation. After the Xe-LS filling was finished, the monitoring system and the teflon tube are removed, and finally the construction of KamLAND-Zen detector has been completed on 12th October 2011.

3.5 KamLAND-Zen Operations

The construction of KamLAND-Zen has been completed in October 2011. Daily data acquisition, source deployment into the detector for energy calibration operated in December 2011 and the filtration campaign in 2012 are described in this section.

3.5.1 Data Acquisition

The data acquisition system and photo detector for KamLAND-Zen are shared with KamLAND, and the main settings of data acquisition for KamLAND-Zen 1^{st} phase are described below.

- ID Prompt Trigger Threshold : 70 [NSum]
- ID Delayed Trigger Threshold : 50 [NSum]
- Delayed Coincidence Gate Width : 1 [msec]
- ID Prescale Trigger Threshold : 70 [NSum]
- ID Prescale Trigger Fraction : 1.024 [%]

The threshold of prompt trigger is low enough to acquire the double beta decay signals and the backgrounds. The other settings such as OD triggers are the same as before.

3.5.2 Source Calibration Campaign

For the energy calibration with Xe-LS, gamma-ray source made of $\mathrm{ThO_2W}$ rods is deployed on 20th December 2011. The rods include $2 \sim 4$ % of $^{232}\mathrm{Th}$ which is parent of $^{208}\mathrm{Tl}$ in the decay chain, and $^{208}\mathrm{Tl}$ β-decays to the excited state of $^{208}\mathrm{Pb}$ which generates 2.61 MeV single gamma ray. A motivation of energy calibration is the unexpected background observed around 2.6 MeV after the start of data taking discussed in section 6.5. The level diagram of $^{208}\mathrm{Tl}$ is shown in Fig A.6.

The former z-calibration system for the source deployment into KamLAND called MiniCAL is removed from the top of the detector to construct the clean room for the IB installation, and there is M5 flange on the center of the chimney. Therefore, the manual deployment device is constructed around center hole at chimney in the clean room as shown in Fig 3.29(b). The $\mathrm{ThO_2W}$ source is covered with ~5-mm-thick lead block, and 4 rods are inside the lead capsule as shown in Fig 3.29(c). The string is the same one as used for suspending the IB in order not to damage the IB, and it is tied with the source and coated with adhesion bond used for the source deployment before. The glove box is circulated with nitrogen gas during deployment not to contaminate the seal gas with oxygen or radon. The geometric diagram of the source deployment is shown in Fig 3.29(a). The deployment operated by hands to make the source slowly go down by rotating the reel.

The source is deployed in a point above the IB to confirm the position by the data, and finally we took 3 hours data with the source located at 1,158 cm (length of the string) from the bottom of the glove box. The result of the source calibration is described in section 4.6.1.

3.5.3 Filtration Campaign

The filtration campaign is the first attempt to remove the unexpected background around 2.6 MeV (discussed in section 6.5) that is assumed to be contaminants of $^{110\mathrm{m}}\mathrm{Ag}$ isotope. To address the possibility that impurities such as $^{110\mathrm{m}}\mathrm{Ag}$ may be bound to suspended dust or fine particulate in the Xe-LS, we passed 37 m^3 of the Xe-LS, corresponding to 2.3 full volume exchanges through a 50 nm PTFE-based filter in February 2012. Before

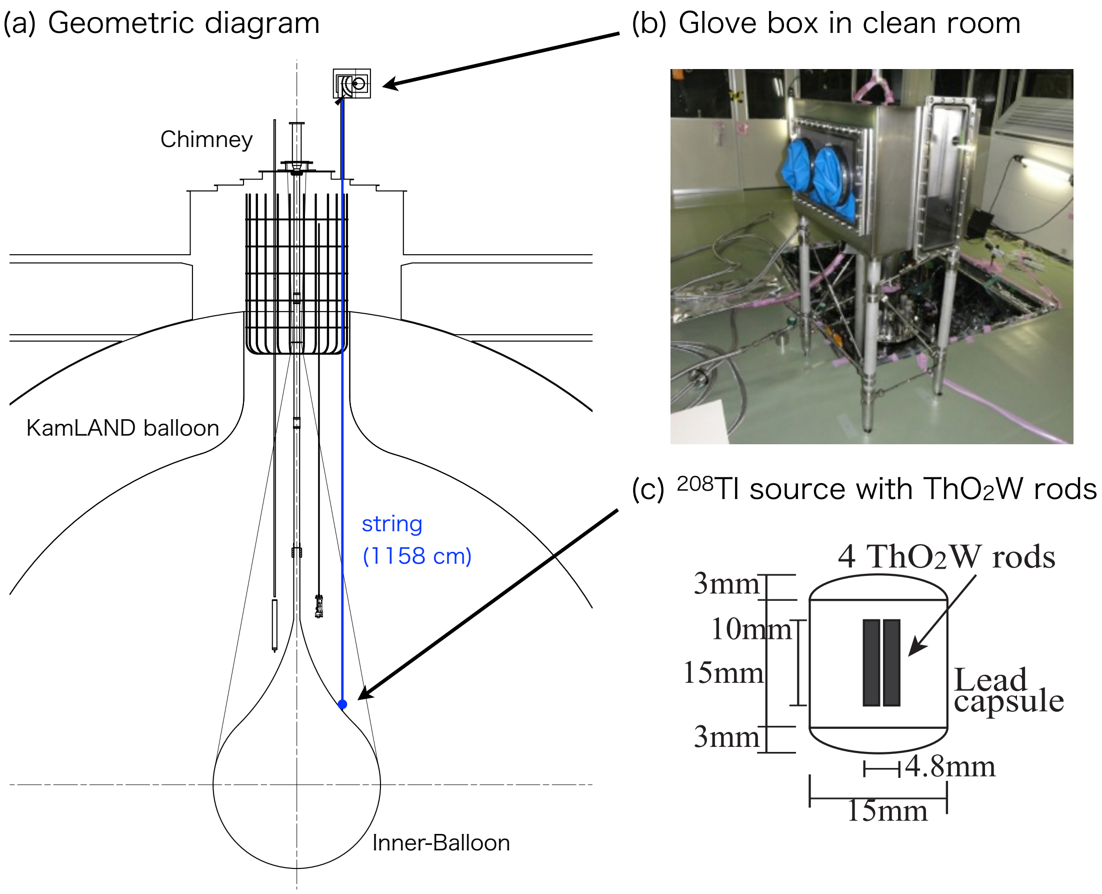

(a) Geometric diagram

(b) Glove box in clean room

(c) ^{208}Tl source with ThO$_2$W rods

Fig 3.29: The ThO$_2$W calibration campaign. (a) is geometric diagram of the deployment, and (b) is picture of the glove box in the clean room constructed on the chimney. (c) is design of the ThO$_2$W source.

the campaign, the teflon tube for the Xe-LS filling is installed again into near the bottom of IB after the outside and inside of the tube is cleaned with alcohol and 0.05 μm teflon filter. The installation of the tube is monitored with new camera unit. The camera unit is installed with the glove box used for the source calibration as described in section 3.5.2.

The operation flow of the campaign is shown in Fig 3.30, and it is simple operation of the filling and draining of Xe-LS using Sub-Tank only. For the effective circulation of Xe-LS, the layer of filling Xe-LS and remaining Xe-LS in the IB is made with temperature control. The layer is clearly shown in Fig 3.31 as vertex distribution of ^{222}Rn.

It took around 2 weeks to complete the filtration campaign including the preparation. After the filtration campaign, the teflon tube was left inside the IB because re-installation may be needed for next purification campaign if there are still the backgrounds. In fact, the background is still observed after the filtration campaign, and we concluded that the campaign was not effective for the background reduction as discussed in section 6.5.

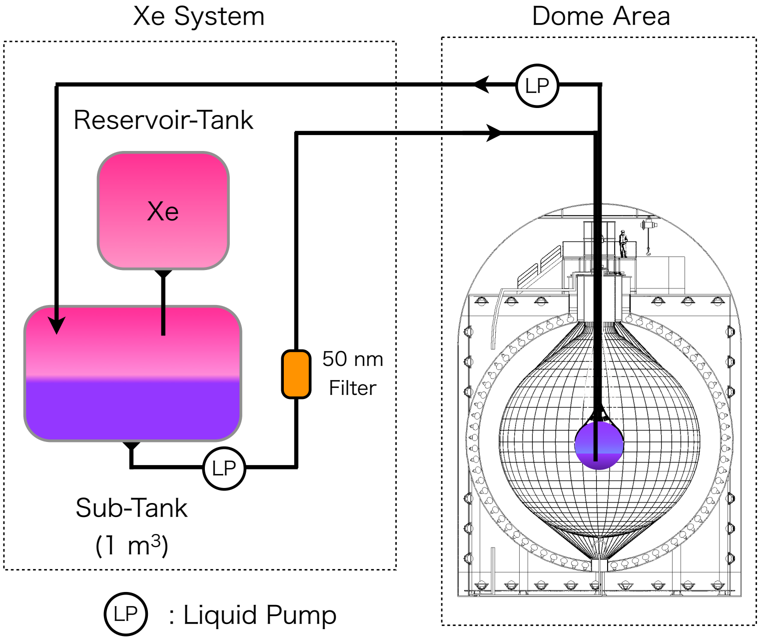

Fig 3.30: Diagram of filtration campaign operation. The drained Xe-LS from IB is sent to Sub-Tank, and Sub-Tank sends filtered Xe-LS into the IB. The xenon is supplied from Reservoir-Tank to keep the pressure in the Sub-Tank. The mesh size of PTFE-based filter is 50 nm, and 3 filters are deployed in the filter housing.

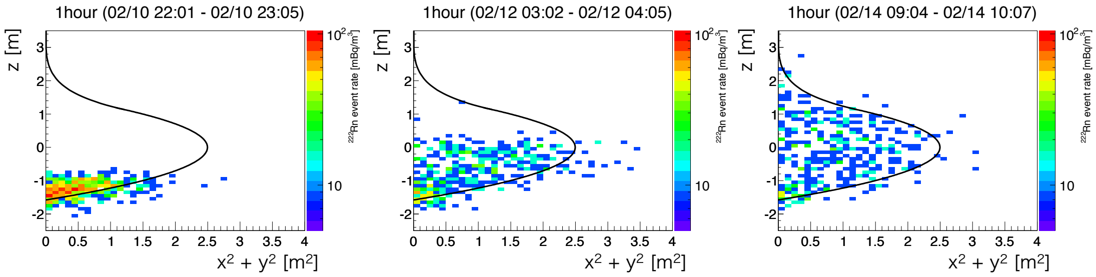

Fig 3.31: ^{222}Rn vertex distributions during the filtration campaign. The events are tagged with ^{214}Bi-Po delayed coincidence technique, and each plot shows vetex distribution of the prompt events (β decay of ^{214}Bi) in 1 hour's duration indicated above the plot.

Chapter 4

Event Reconstruction and Detector Calibration

In KamLAND detector, data is acquired with KamLAND Front-End Electronics (KamFEE) as digital waveform of PMT, and the physical event is reconstructed with the information of hit-time, charge, and PMT geometry. The reconstructed events have several informations such as time, energy, vertex position. The reconstruction procedure and method can be commonly applied for KamLAND-Zen experiment because the photodetector is the same as the KamLAND experiment. The procedure of event reconstruction and calibration is described in this chapter.

The reconstructed events are calibrated for their energy and vertex position with the source calibration data. The detector calibration is performed with the ThO_2W source for KamLAND-Zen, and the other calibration methods are applied in the same manner as KamLAND experiment.

4.1 Waveform Analysis

The signal from PMT is recorded with KamLAND Front-End Electronics (KamFEE) as a digital waveform. Each waveform is analyzed to extract time and charge information which are used for the event reconstruction in the detector. The waveform of a typical single photoelectron (p.e.) taken with KamFEE is shown in Fig 4.1(a), and it consists of 128 sampled 10-bit ADC counts for each gain channel. The sampling interval is ∼1.48 nsec, resulting that the length of each waveform is ∼190 nsec. The sampling rate is almost comparable to the transit time spread of the 17-inch PMTs, and the accuracy of waveform is good enough to see the single p.e. peak.

4.1.1 Algorithm of Waveform Analysis

Since ADC of KamFEE has unique offset for each channel, this structure is subtracted from the waveform. At the beginning of each run, the 50 pedestal waveforms are recorded for the estimation of the offset. These offsets are estimated by averaged pedestal waveforms without noise or dark hit pulse. After the pedestal subtraction, waveforms are smoothed to avoid the high frequency noise. And then, the baseline of the waveform is re-adjusted to be zero because the baseline can be moved event by event and channel by channel due to the after-effects of former pulse.

The signal peak is searched with the derivatives, and the leading-edge is defined as the start time bin for each signal as drawn in Fig 4.1(a). The leading-edge of the first signal in the waveform is used for the event reconstruction. The area of each pulse from the leading-edge to the end of pulse is normalized with the mean area of a single photoelectron

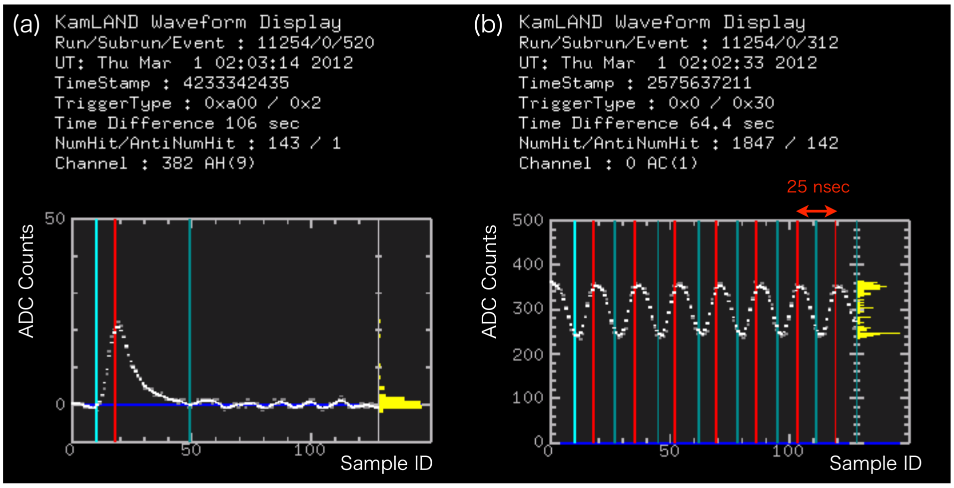

Fig 4.1: Waveforms taken with KamLAND Front-End Electronics. (a) shows H gain waveform of a typical one photon signal taken KamLAND Front-End Electronics. The red line indicates the analyzed peak postion of the pulse, and the blue line indicates the best baseline of for this waveform. (b) shows the waveform of clock test pulse for the calibration of time bin width. The time interval of the clock pulse is 25 nsec. The projections of y-axis (ADC counts) are drawn with yellow histogram for (a) and (b) both. These waveforms are taken from run 011254.

pulse, corresponds to the charge of the signal. This normalization is described in the next section 4.2.

4.1.2 Calibration of Time Bin Width

The clock test pulse is used for the calibration of the time bin width. The calibration is performed for each channel at the beginning of each run. The pulse taken with KamFEE is shown in Fig 4.1(b), and the time interval of the pulse is 25 nsec (40 MHz). Typically, KamFEE ADC samples around 17 points in the 25 nsec. The time bin width for each channel is corrected with the clock pulse run by run.

4.2 Time and Charge Calibration

4.2.1 TQ Correction

Because of characteristics of each PMT and electronics and cable length, the timing that signal is digitized after photon arrival to PMT is slightly different channel by channel. To calibrate the timing for more accurate event reconstruction, the dye-laser calibration have been performed. The wavelength of the laser is 500 nm which exceeds the absorption wavelength ($<$ 400 nm) of the scintillator. A light attenuation filter and spherical diffuser provide uniform and variable light intensities from a single p.e. level to $\sim$ 5,000 p.e. level. The dye-laser pulse is monitored with 2 inch PMT and the time information from the PMT is used for removal of offset comes from time resolution of the trigger.

In addition to the dye-laser calibration, ^{60}Co source calibration run is used for additional timing correction. Since the characteristics of liquid scintillator had changed after the purification campaign performed for the solar neutrino observation, ^{60}Co source calibration at center position (z=0) have been taken per $\sim$ 2 weeks after 2nd purification campaign before start of KamLAND-Zen construction phase.

The rise time of a pulse is different due to PMT gain and amplifier gain of the electronics. Therefore correlation between time and charge is evaluated channel by channel with various intensity of dye laser and corrected (TQ correction). Fig 4.2(a) shows the hit time distribution of 17 inch PMT of 1 p.e. with dye-laser, and (b) is the distribution after time correction. The correction makes the time distribution sharper, and the timing resolution is improved to 2.0 nsec from 6.7 nsec.

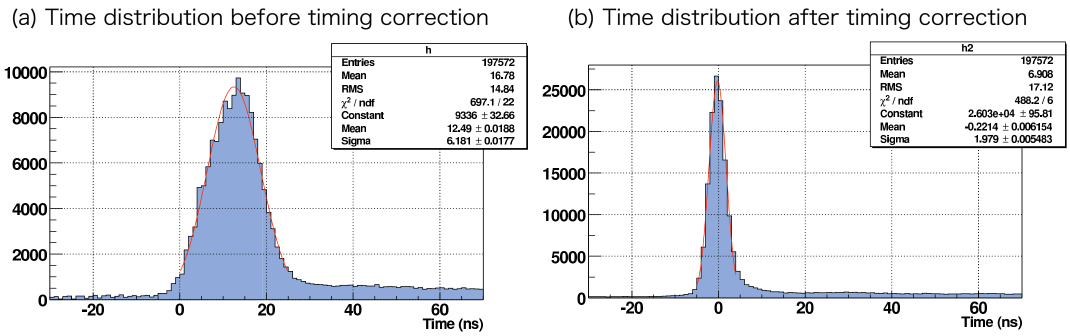
(a) Time distribution before timing correction

(b) Time distribution after timing correction

Fig 4.2: Time distribution of 1 photoelectron with dye-laser. (a) is 17 inch PMT time distribution of 1 p.e. events with dye-laser, and (b) shows the distribution after timing correction [65].

4.2.2 Gain Calibration

The single photoelectron charge is defined as the area of the pulse, and the charge fluctuates channel by channel and run by run. Therefore the gain calibration is performed for the gain correction to normalize the charge of 1 p.e..

The events selected for the correction are low energy events which is defined with NSumMax ($120 \leq$ NSumMax ≤ 230) to get the 1 p.e. signal for each channel, here, NSumMax is a number of NSum within trigger window length (125 nsec). The muon and noise events are rejected with veto, and the reconstructed vertex position of the events are inside balloon ($R < 6$ m) to be selected. In addition to the above criteria, the waveform with multiple peaks is rejected. A typical 1 p.e. distribution of 17 inch PMT is shown in Fig 4.3(a). The peak is fitted with gaussian function, and the fitting result is used for the gain correction for the run.

While, the 1 p.e. distribution of 20 inch PMT does not have a peak as shown in Fig 4.3(b). Therefore, the gain correction factor for 20 inch PMT is defined with average charge of 8 (geometrically) neighboring 17 inch PMT.

The gain correction factors are prepared for each PMT and each run, and the time variation of the average of them is drawn in Fig 4.4. They seems stable within data set of KamLAND-Zen in the plot, and the long-term changing of the gain is suppressed with these correction. However, the gain of some channels is getting worse in the long-term view, and low gain channels are unused in the analysis (see section 4.2.3).

4.2.3 Bad Channel Selection

In addition to low gain channels, there are some abnormal channels which have many hits, no hits or strange charge due to problems caused with high voltage supplier or PMT or KamFEE board. They are called bad channels, and the selected run by run not to use for the analysis.

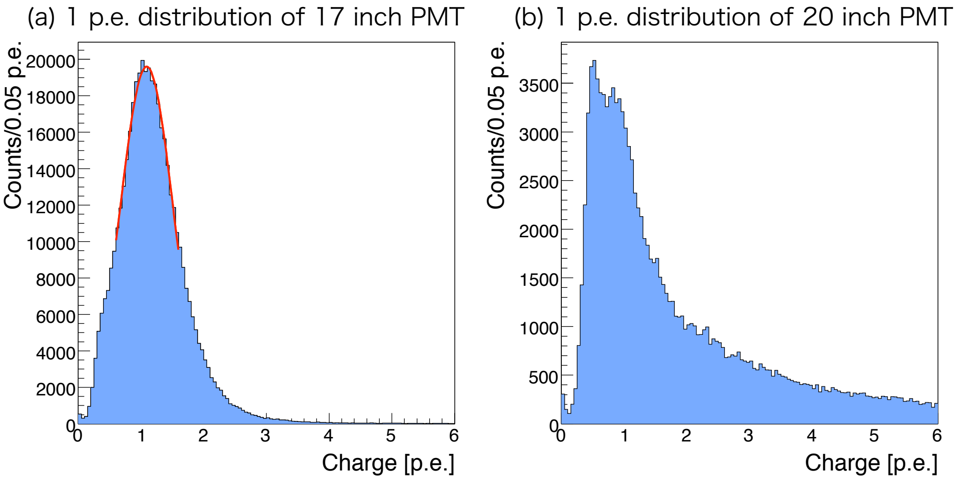

Fig 4.3: Single photoelectron distributions for the typical 17 inch PMT and 20 inch PMT. The distribution of 17 inch PMT (a) has a clear peak fitted with gaussian, and the distribution of 20 inch PMT (b) does not have a sharpe peak. These plots are taken from [65].

The bad channels are unused for event reconstruction, and the selection criteria of ID PMTs (1,325 × 17 inch and 554 × 20 inch) are described as follows;

1. Hit Rate $<$ 600 hits / 10,000 events
   to find low response channels due to high voltage or electronics problem

2. Hit Rate $<$ 480 hits / 10,000 events except for muon events
   to find low response channels due to high voltage or electronics problem

3. Q_0 Event Rate $>$ 1,000 / 10,000 events
   to find electronics failure, where Q_0 means the zero-charge with the waveform analysis

4. Muon Hit Rate $<$ 80 / 100 muon events
   to find excessively low gain channel

5. Difference of hit rate between A and B channel $>$ 22% in 10,000 events.
   to find electronics failure in channel switching A/B

6. Charge difference in high charge muon event described as;
   $$\frac{1}{N_i}\sum_{j=1}^{N_i}\frac{(Q_i-Q_j)^2}{Qj} > 1,000\text{p.e.} \qquad (Q_j > 0, j\,:\text{ neighbor PMT's ID})$$
   to find channels with a large gain difference compared with the gains of neighbor channels

7. Gain $<$ 1/4 p.e. or Gain $>$ 4 p.e.
   to find too low and too high gain channel

If a channel satisfied more than 1 criterion above, the channel is selected as bad channel. For bad channel of the OD PMTs (225 × 20 inch), there is a single criterion below.

1. Hit Rate $<$ 5 hits / 10,000 events
   to find low response channels due to high voltage or electronics or PMT problem

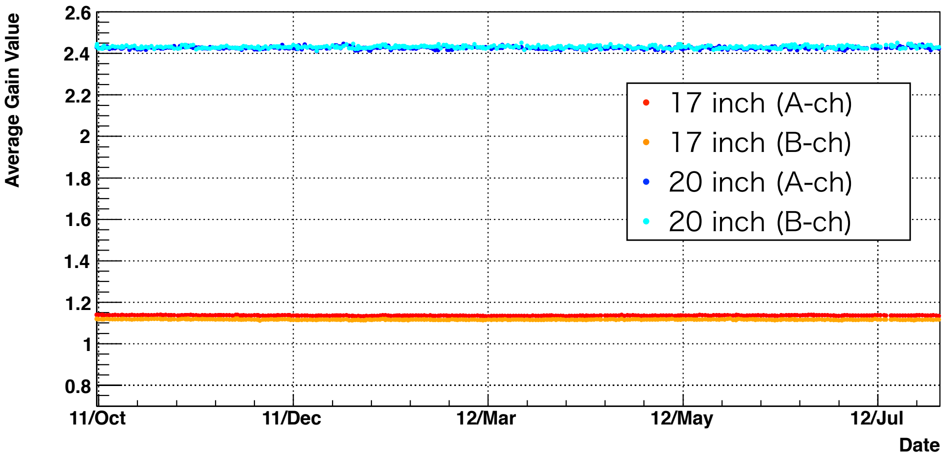

Fig 4.4: Time variation of averaged gain values. Red and orange points indicate the averaged gain value of 17 inch PMT for A channel and B channel, and blue and light blue points indicates that of 20 inch PMT. The period drawn in the plot includes DS-1, DS-2 and DS-3 which are data set used in this work.

Fig 4.5 shows the time variation of the number of bad channels in the data set for KamLAND-Zen 1st phase. The bad channel number of 17 inch PMT (red) is unstable and slightly increasing, while those of 20 inch PMT (blue) and OD PMT (light green) are stable. There are some small jumps due to the KamFEE board failure and recovered by the replacement of it. The number of OD bad channels are large due to the initial death after filling of water in the construction phase of KamLAND.

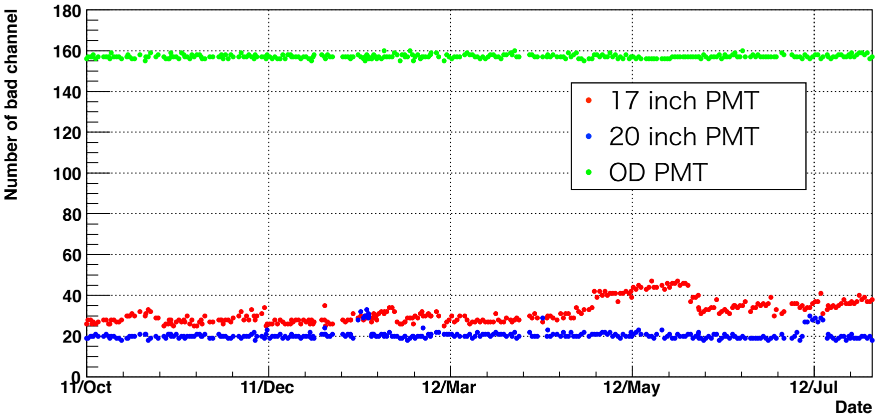

Fig 4.5: Time variation of the number of bad channels. The red and blue markers indicate the number of bad channels in the inner detector for 17 inch PMT and 20 inch PMT, and light green marker indicates the number of bad channels in the outer detector for 20 inch PMT. The period drawn in the plot includes DS-1, DS-2 and DS-3 which are data set used in this work.

The first criterion (Hit Rate) of the bad channel selection is also applied to seek bad periods due to high voltage trip during data taking, and the bad periods are added to dead time table as dead time. In the dead time, all events are vetoed and the duration is not considered as livetime in the analysis.

4.3 Muon Reconstruction

Although KamLAND detector is located at 1,000 depth of the rock in Kamioka mine, some cosmic-ray muons with high energy are arrived to the detector in some frequency. The muon penetrates the detector by interacting with the scintillator materials and produces the background events with spallation reaction. The backgrounds of spallation products are described in section 6.4. ^{10}C which is one of the spallation products is a serious background for ^{136}Xe $0\nu\beta\beta$ decay signal, therefore the identification of muon events is important to veto the background.

4.3.1 Muon Selection

Comic muon events are easily identified with their massive light output in the processes of the scintillation and/or Cherenkov light yield in the inner detector, and also the Cherenkov light emission is observed in the outer detector. The muon events are selected in the following procedure, and same selection criteria are applied for the analysis of KamLAND-Zen.

1. $Q_{17} \geq 10{,}000$ p.e.

2. $Q_{17} \geq 500$ p.e. and $N_{200}^{OD} \geq 5$ NSum

Here, Q_{17} is total charge of 17 inch PMT in ID, and N_{200}^{OD} is number of hits of 20 inch PMT in OD within 200 nsec after trigger issued. Selection criteria 2 is applied for the muon events which go through only buffer oil in ID, they do not have scintillation light and Q_{17} becomes relatively small.

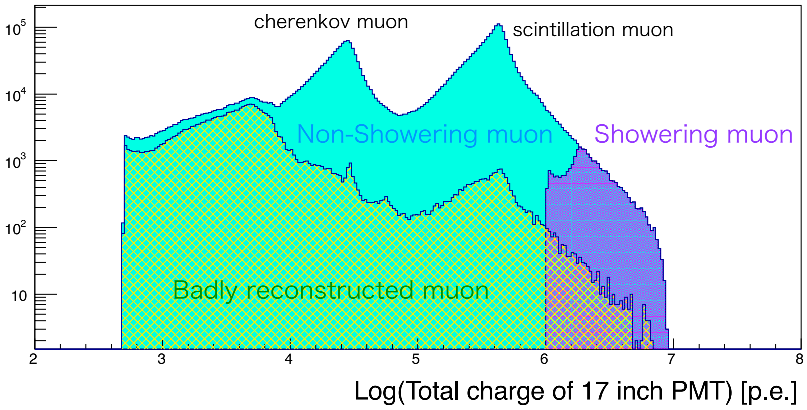

Fig 4.6: Charge distribution of muon events.

The distribution of Q_{17} in the selected muon events is shown in Fig 4.6. The definitions of the showering muon and badly reconstructed muon are described in next section 4.3.2. There are two peaks seen; higher charge events are called scintillation muon and lower ones are called Cherenkov muon. The scintillation muons penetrate the scintillator in ID and have scintillation light (dominant) and Cherenkov light. While, the Cherenkov muons penetrate the buffer oil layer only, and have Cherenkov light. The frequency of the incident muon events into the inner detector is ~ 0.35 Hz as shown in Fig 4.7, and the frequency is stable during data set used in the analysis.

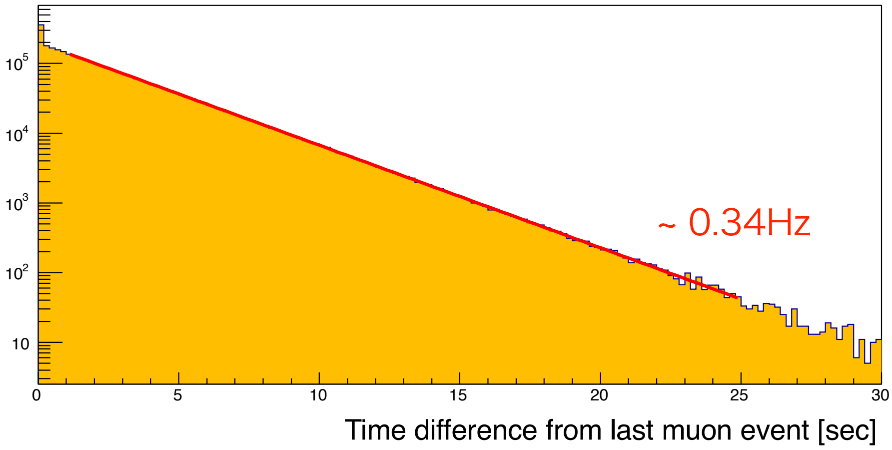

Fig 4.7: Time difference from last muon events.

4.3.2 Muon Track Reconstruction

The track is reconstructed for muon events penetrating the detector with timing information of each PMT. Using information of the reconstructed track, we can estimate the residual charge (ΔQ) of muon events which is extra charge to emit scintillation and Cherenkov light in the detector. The residual charge is written as equation 4.1 with length of the track and energy deposit factor. The length of the track in the inner detector (L_{ID}), the scintillator region (L_{LS}) and in the buffer oil region (L_{BO}) are held as $L_{\text{ID}} = L_{\text{LS}} + L_{\text{BO}}$.

$$\Delta Q = Q_{17} - L_{LS}(\frac{dQ}{dx})_{\text{Scintillation}} - L_{\text{BO}}(\frac{dQ}{dx})_{\text{Cherenkov}} \tag{4.1}$$

The energy deposit in the buffer oil $(\frac{dQ}{dx})_{\text{Cherenkov}}$ and in the scintillator $(\frac{dQ}{dx})_{\text{Scintillation}}$ are defined as the following.

$$\begin{aligned}
(\frac{dQ}{dx})_{\text{Cherenkov}} &= \frac{Q_{17}}{L_{\text{BO}}} \qquad \text{(only for Cherenkov muon events ; i.e. } L_{\text{LS}} = 0\text{)} \\
(\frac{dQ}{dx})_{\text{Scintillation}} &= \frac{Q_{17} - L_{\text{ID}}(\frac{dQ}{dx})_{\text{Cherenkov}}}{L_{\text{LS}}}
\end{aligned} \tag{4.2}$$

The contribution of the cherenkov light is subtracted to estimate the energy deposit factor in the scintillator. The ideal values of the factors are 31.45 p.e./cm for $(\frac{dQ}{dx})_{\text{Cherenkov}}$ and 629.4 p.e./cm for $(\frac{dQ}{dx})_{\text{Scintillation}}$ to be estimated in the beginning data in KamLAND. These factors are applied for the estimation of the residual charge (ΔQ) to categorize showering muon and non-showering muon. The showering muon is defined as the higher energy muon events ($\Delta Q > 10^6$ p.e.) to be able to generate shower of the events with the spallation reactions, and the other muon events are categorized as non-showering muon. This categorization is used for the intelligent veto to maximize the fiducial volume and livetime by using cylindrical cut along the muon track. However, we applied only simple veto for muon events in the double beta analysis as described in section 5.2.2.

4.4 Vertex Reconstruction

The vertex is a fundamental parameter for point-like events, and the parameters are used for energy reconstruction (section 4.5). The reconstruction uncertainty is essential for the estimation of fiducial volume uncertainty.

4.4.1 Algorithm of Vertex Reconstruction

The vertex reconstruction is based on the relative times of the PMT hits. The maximum likelihood approach is applied to determine the vertex position after subtracting time of flight of photon for each PMT. The time response of 17 inch PMT is better than 20 inch PMT due to the structure of dynode, and the time spectrum for vertex reconstruction is generated with only 17 inch PMTs. The time spectrum is given by,

$$\tau_i(x, y, z, t) = t_i - t - \mathrm{TOF}_i \qquad (i : \text{index of 17 inch PMT})$$

here, τ_i is a delay of the signal timing for i-th PMT, and calculated with observed timing t_i, TOF_i which is time-of-flight from reconstructed vertex (x, y, z) to i-th PMT with considering speed of light in the liquid scintillator, and time of reconstructed event t. The generated time spectrum is used for computing the maximum likelihood calculation written as,

$$\begin{aligned} L &= \prod_{i}^{\mathrm{Nsum}} \phi(\tau_i(x, y, z, t)) \\ \log(L) &= \sum_{i}^{\mathrm{Nsum}} \log(\phi(\tau_i(x, y, z, t))) \end{aligned}$$

where $\phi(\tau_i)$ is a function for the evaluation of time spectrum tuned with source calibration spectrum in KamLAND, and L is likelihood function to be computed. The maximum of $\log(L)$ is gained with a point of 4-dimensional gradient becomes zero, as written in the following.

$$\left.\frac{\partial \log(L)}{\partial \mathbf{x}}\right|_{\mathbf{x}=(x_j, y_j, z_j, t_j)} = 0 \tag{4.3}$$

The vertex fitter computes to search $\mathbf{x} = (x_j, y_j, z_j, t_j)$ satisfying the equation 4.3, and the best parameters are reconstructed as vertex position and time of the event.

4.5 Energy Reconstruction

The energy observed with KamLAND is defined as the deposit energy in the detector, called visible energy (E_{vis}). Most of the point-like events deposit all of their energy in the detector, and the (real) energy is calculated with the visible energy observed as scintillation light emission. There are non-linear relationship between real energy and visible energy due to the non-linearly distributions of the dark hit charge, single photoelectron detection efficiency, the quenching effect and Cherenkov light.

The visible energy is reconstructed with the charge of PMT signal, and various corrections are applied for each charge of the signal and total charge sum.

4.5.1 Visible Energy Calculation

The visible energy is calculated with the charge of each PMT. The charges are calibrated with the following items to reduce the time variation of the detector status.

Gain Calibration

The single photoelectron charge is defined by area of a 1 p.e. pulse in a waveform. The charge of each PMT is corrected with gain calibration using 1 p.e. charge distribution run by run as described in section 4.2.2.

Bad Channel Selection

The bad channels as selected in section 4.2.3 are masked not to use for energy reconstruction. The bad channel table is prepared for run by run with good condition (run grade is zero).

Software Signal Discrimination

The discriminator threshold is set for each channel of each electronics board, while the threshold is not well-defined because gain of each PMT is not constant as discussed in section 4.2.2. To reduce the uncertainties of the threshold effect, the software discrimination is applied at 0.3 p.e. threshold with gain calibration for each PMT signal.

Dark Charge Subtraction

Dark hit is one of noise signals caused by dark current due to the random generation of thermal electrons at PMT photocathode, and they are also found in the signals acquired with KamFEE. Fig 4.8 shows the timing distribution of 17 inch PMT hits after the subtraction of time-of-flight for each PMT. The contribution of the charge of the dark hits is $\sim$ 3 p.e. per 50 nsec time window, and it is estimated with the time window of $-100 \sim -50$ nsec in timing distribution as shown in Fig 4.8. The time variation of the dark charge is drawn in Fig 4.9, and it seems stable during data set for this work. The rate of dark hit depends on the temperature of PMT, and we know the temperature of the buffer oil layer correlates with the rate.

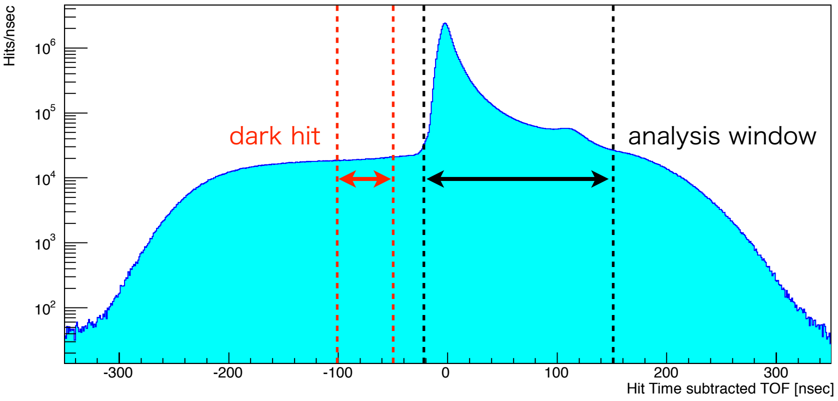

Fig 4.8: Timing distribution of 17 inch PMT hits. Time-of-flight is subtracted for each PMT to make the distribution. The 50 nsec time window of $-100 \sim -50$ nsec is opened for the charge estimation of dark hits.

4.5.2 Photon Yield Efficiency

The visible energy is reconstructed by considering photon yield effect as described in the following.

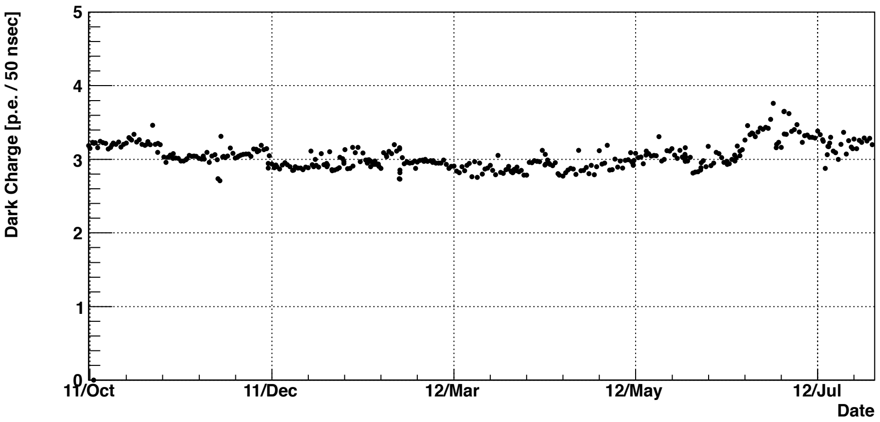

Fig 4.9: Time variation of dark charge in 50 nsec time window. The period drawn in the plot includes DS-1, DS-2 and DS-3 which are data set used in this work.

Shadow Effect

The KamLAND balloon and its supporting kevler ropes make shadow to prevent photons from yielding to PMTs at the top or bottom of inner detector. The effect is called shadow effect, and corrected with the ^{60}Co source calibration especially at the center of the detector. The correction improve a symmetrical angular-dependence of the photon yield.

Attenuation Length

The light attenuation length is important parameter to estimate the light yield in the liquid scintillator. The effective attenuation length includes the effect of photon absorption and re-emission during photon flight and it is evaluated to 18.0 ± 1.6 m with neutron captured gamma events which is uniformly distributed.

Single Photoelectron Efficiency

The inefficiency of 1 p.e. detection due to the 0.3 p.e. threshold causes the non-linear bias for the visible energy. Assuming that the detection probability is given by Poisson statistics, the effect of single photoelectron is parameterized as δ, and estimated with source calibration data taken with ^{60}Co and ^{65}Zn.

4.5.3 Algorithm of Energy Reconstruction

The visible energy is reconstructed by A2 energy fitter with hit, charge and time information of PMTs. In general, the hit information is used for the reconstruction of low energy event since it is not affected with the charge resolution and 1 p.e. threshold. While for the high energy event reconstruction, charge information has better performance due to high occupancy. Although implementation of combined fitter is even harder, the fitter newly developed for KamLAND provides a natural and seamless transition from a purely hit-based estimator at lower energies to a mostly charge-based one at higher energies.

The energy estimator determines the energy through maximum likelihood function method. The likelihood function consists of the probability density functions of hit, charge and hit time for each PMT, written in the following.

$$L = \prod_{i=1}^{\text{no hit}} \kappa_{i,0}(\overrightarrow{R}_{\text{PMT}}, \overrightarrow{R}_{\text{source}}, E_{\text{vis}}) \prod_{i=1}^{\text{hit}} \left[\sum_{j=1}^{\infty} \kappa_{i,j}(\overrightarrow{R}_{\text{PMT}}, \overrightarrow{R}_{\text{source}}, E_{\text{vis}}) f_{i,j}(q_i) \right] \eta(t_i|\mu_i)$$

where $\kappa_{i,j}$ and $f_{i,j}(q_i)$ is hit probability and charge probability density function of j-th photons hit at i-th PMT, respectively. A function $\eta(t_i|\mu_i)$ is hit time probability density function for i-th PMT, given by the time t_i and the expected number of incident photons μ_i. These functions and parameters are expressed with basic and correction parameters described in section 4.5.1 and 4.5.2. For example, $\kappa_{i,j}$ is provided by Poisson distribution as a function of μ_i and the function includes the detection efficiency of 1 p.e. threshold signal above 0.3 p.e., and μ_i is considered with the effective solid angle including attenuation and shadow effect. The charge probability density function $f_{i,j}(q_i)$ is modeled by Gaussian distribution including sigma of 1 p.e. distribution which is evaluated to be 0.39. The hit time probability density function $\eta(t_i|\mu_i)$ is a function of actual pulse shape function divided by μ_i.

From a definition of each function with observable and expected parameters, the likelihood function can be written with four terms (no-hit, hit, charge and time). The best reconstruction energy is derived from the maximization of log-likelihood function,

$$\frac{\partial \log(L)}{\partial E} = 0.$$

For the low energy region, no-hit, hit and time terms work effectively. On the other hand, charge term works effectually for high energy region. The maximum of the log-likelihood function is computed with modified Newton-Raphson method described below.

$$\Delta E_{\text{vis}} = -\frac{\partial \log(L)/\partial E}{\partial^2 \log(L)/\partial^2 E}$$

The visible energy is reconstructed by summing up of ΔE with several iterations, and it is computed with 17 inch PMTs ($E_{\text{17-inch}}$) and 20 inch PMTs ($E_{\text{20-inch}}$), respectively.

4.5.4 Combination with 20 inch PMTs

As described in section 4.2.2, 20 inch PMTs have poor 1 p.e. resolution compared with 17 inch PMTs. However, since 17 inch PMTs cover only 22% of the inner detector, the visible energy should be estimated by using the charge information from 17 inch and 20 inch PMTs to get better energy resolution. The mean value of visible energy with 20 inch PMTs ($E_{\text{20-inch}}$) is calibrated with that of 17 inch PMTs ($E_{\text{17-inch}}$), and combined to get the total visible energy (E_{vis}) as written in the following.

$$E_{\text{vis}} = (1 - \alpha)\, E_{\text{17-inch}} + \alpha\, E_{\text{20-inch}}$$

Here, α is a weighted factor, and it it evaluated with a various source calibration as shown in Fig 4.10(a). The α is optimized to be 0.3 to give the best energy resolution, indicated in yellow band in the figure. Fig 4.10(b) shows the deviation of the combined energy as a function of $E_{\text{17 inch}}$, and its non-linearity is controlled within 0.6%.

4.6 Detector Calibration for KamLAND-Zen

In addition to basic corrections applied for KamLAND experiment, some corrections are applied for KamLAND-Zen due to the additional components such as Xe-LS and inner balloon.

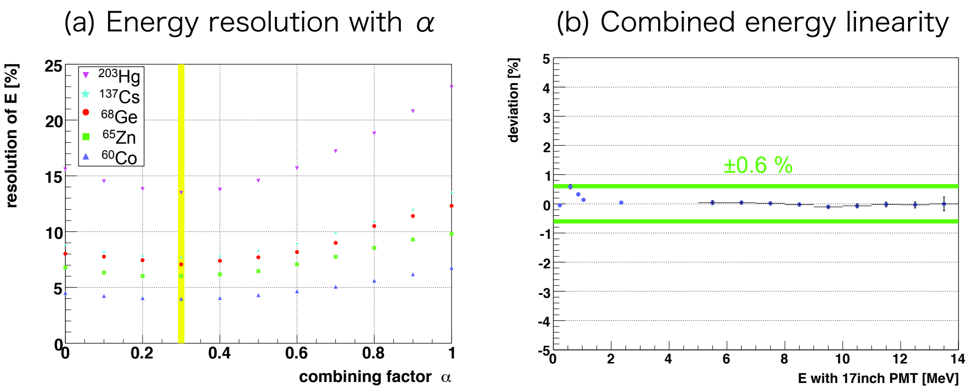

Fig 4.10: The optimization of combined energy and the stability. (a) shows the combined energy resolution as a function of the factor α. The yellow line indicates the best parameter ($\alpha = 0.3$) for combined energy resolution of various source calibrations. (b) shows the combined energy linearity as a function of 17inch energy. The uncertainty on the combined energy non-linearity is less than 0.6%. [65]

4.6.1 Energy Correction for KamLAND-Zen

$\mathrm{ThO_2W}$ Source Calibration

The $\mathrm{ThO_2W}$ source is deployed close to the outer surface of the IB for energy calibration as described in section 3.5.2. The most intense peak is primary 2.614 MeV γ of ^{208}Tl, and second one is a peak around 3.1 MeV from multiple-γ cascades of ^{208}Tl which is daughter isotope of ^{232}Th. The level diagram of ^{208}Tl is seen in Fig A.6, and the visible energy observed is shown in Fig 4.11. According to Monte Carlo (MC) studies, the degradation of the primary γ inside the source is negligible, and the distribution around the primary peak can be described by a Gaussian distribution and a third-order polynomial written in the following.

$$f(E) = a\ \exp\left[-\frac{1}{2}\left(\frac{E-\mu}{\sigma}\right)^2\right] + b_1\ E + b_2\ E^2 + b_3\ E^3 + c$$

where E is visible energy, and the others are general fitting parameters for Gaussian function and polynomial. The mean and width of the Gaussian distribution are relatively insensitive to the polynomial parameters. The resultant energy resolution at 2.614 MeV is $6.6 \pm 0.3\%\ /\sqrt{E[\mathrm{MeV}]}$ we obtained.

Spallation Neutron Capture

The neutrons produced with the spallation reaction by comic-ray muons are captured with mainly protons within several hundred μsec, and emit 2.225 MeV gamma rays. These events are simply selected with NsumMax (the number of hits when trigger was issued) and time difference from muons. The distribution of NsumMax is shown in Fig 4.12(a) with the time difference (ΔT_μ) cut, $150 < \Delta T_\mu < 1{,}000\mu$sec and the events with missing waveforms are rejected. A peak found in $350 <$ NsumMax < 500 is neutron capture events on protons. Fig. 4.12(b) shows the visible energy spectrum with NsumMax cut for neutron capture events. The visible energy is estimated to be 2.22 MeV with Gaussian function fitting, and the position dependence and time variation of the visible energy is within ±1.0% during the data set.

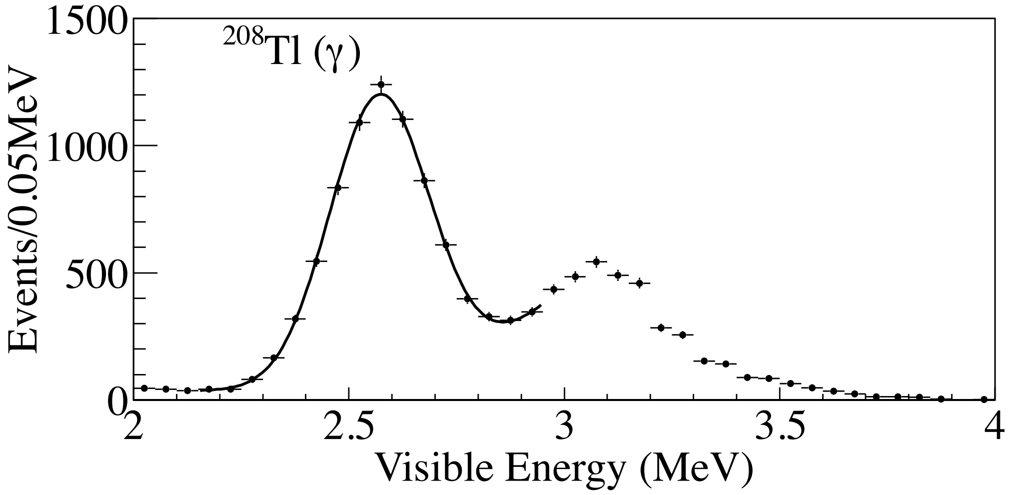

Fig 4.11: Observed energy spectrum with ThO$_2$W source calibration. The left peak is primary 2.614 MeV γ of ^{208}Tl, and fitted with a Gaussian distribution and a third-order polynomial. The black solid line shows the best fit of the fitting, and resulting $6.6 \pm 0.3\%$ $/\sqrt{E}$[MeV] as energy resolution with χ^2/d.o.f = 5.0/8.

Energy Scale Tuning with ^{214}Bi

The estimated visible energy is not exactly equal to the real deposited energy in the detector because it has non-linear relation due to quenching effects of the liquid scintillator, contribution of Cherenkov photons and some non-linearity effect. These non-linear sources generate uncertainties of energy scale. The quenching effect reduce the photon yield due to the different efficiency of light emission depending on the particle 's ionization density. For example, the quenching factor of several MeV α particles is $\sim 1/13$, while that of electron is only a few percent in the liquid scintillator. The contribution of this effect is estimated with Birks formula as a function of energy deposit dE/dx in the following.

$$\Delta E_{\mathrm{vis}} = A\,\frac{\Delta E}{1 + kB(dE/dx)} \tag{4.4}$$

kB is Birks constant determined with characteristics of the liquid scintillator. ΔE_{vis} is the luminescence which corresponds to the observed energy contributed with scintillation light here, and A is the luminescence at low specific ionization density.

Cherenkov photons are emitted only with electrons and positrons and the number of photons of those depend on their energy. The direct contribution of Cherenkov light is negligible because most of photons are absorbed in the liquid scintillator. The total photon yield (i.e. visible energy) is calculated as sum of scintillation and Cherenkov photon contributions in the following.

$$\begin{aligned}
\Delta E_{\mathrm{vis}} &= \left(A_{\mathrm{Scintillation}} \cdot \frac{N_{\mathrm{Scintillation}}}{dE} + A_{\mathrm{Cherenkov}} \cdot \frac{N_{\mathrm{Cherenkov}}}{dE}\right)\Delta E \\
&= \alpha\left(\frac{1}{1+r} \cdot \frac{1}{1 + kB(dE/dx)} + \frac{r}{1+r} \cdot \frac{N_{\mathrm{Cherenkov}}}{dE}\right)\Delta E
\end{aligned}$$

where $N_{\mathrm{Scintillation}}$ and $N_{\mathrm{Cherenkov}}$ are the numbers of scintillation and Cherenkov photons, and $A_{\mathrm{Scintillation}}$ and $A_{\mathrm{Cherenkov}}$ are normalization factors. $\frac{N_{\mathrm{Scintillation}}}{dE}$ is replaced with Birks formula (equation 4.4), and the 2 normalization factors are parameterized to α

(a) NsumMax distribution of neutron capture

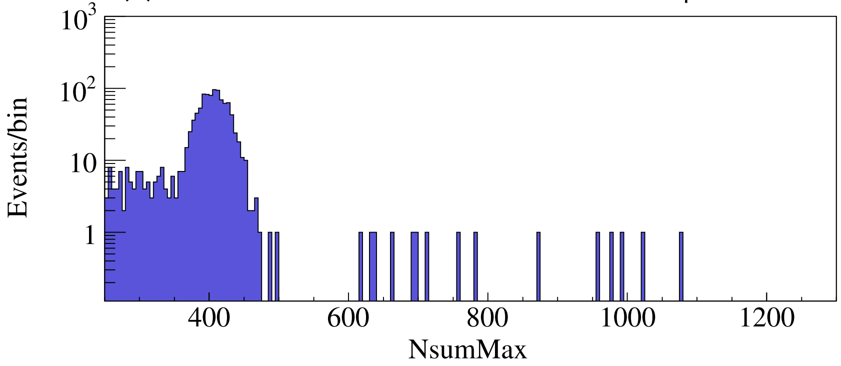

(b) Energy spectrum of neutron capture

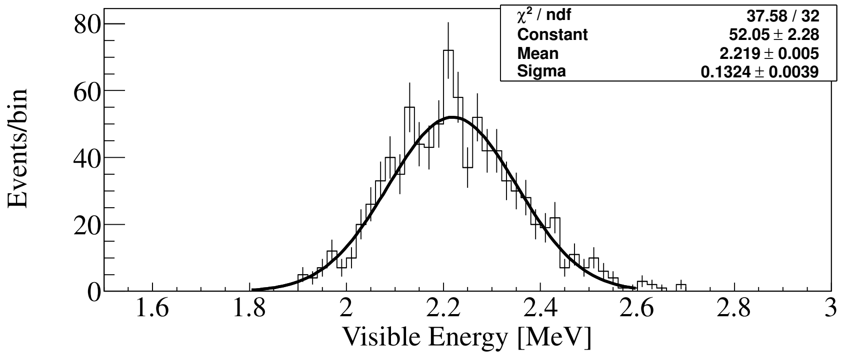

Fig 4.12: The NsumMax distribution and energy spectrum of neutron capture events on proton. (a) shows a peak around 400 NSum after ΔT_μ cut considering the life-time of thermal neutron produced with cosmic-ray muon spallation. (b) is energy spectrum of neutron capture events, and the best fit with Gaussian function is drawn in black solid line.[63]

and r. α is normalized energy scaling factor, and r is ratio of contribution from scintillation and Cherenkov light.

In this analysis, kB, α and r in above calculation for visible energy are used as energy scale parameters. They are tuned with combined data of the peak position of ^{208}Tl and spectral shape of ^{214}Bi events. ^{214}Bi events are tagged with time and space correlation of ^{214}Po with delayed coincidence techniques, and the visible energy spectra is shown in Fig 4.13 with best fit curves.

These parameters of sources of non-linearity, Birks constant (kB) and the ratio of scintillation photons to Cherenkov photons (r) are constrained with ^{208}Tl and ^{214}Bi calibration. The correlation of parameters is shown in Fig 4.14(a). Fig 4.14(b) shows the ratio of visible energy to real energy as a function of real energy for electron and gamma ray.

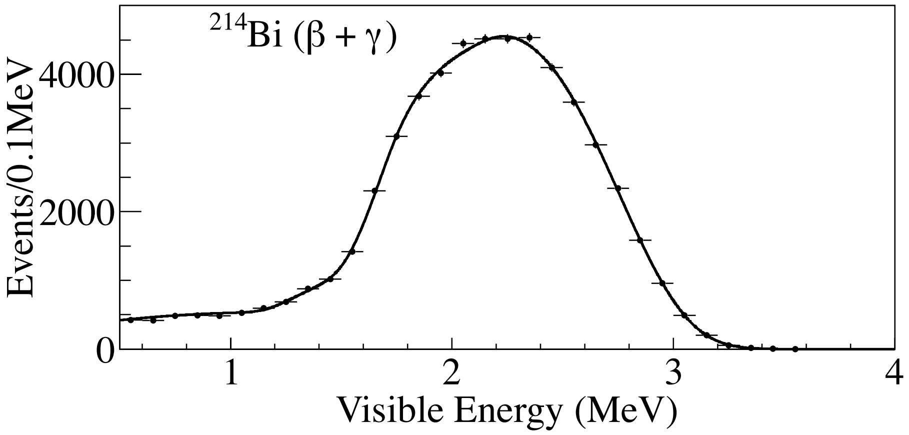

Fig 4.13: Observed energy spectrum of ^{214}Bi in Xe-LS. ^{214}Bi events are tagged with delayed coincidence technique with ^{214}Po, and the black solid line indicates the best fit curve with χ^2/d.o.f = 27.0/29.

Relative Light Yield Correction

The light yield in Xe-LS should be ideally equal to Outer-LS (KamLAND LS) to be designed and developed. However, we found that the light yield in Xe-LS is slightly different from that in Outer-LS by checking ^{208}Tl events. The different light yield makes the boundary effect to overestimate or underestimate the energy of events at near the surface of IB. Fig 4.15(b) indicates that the light yield in Xe-LS is ~3% lower than the that in Outer-LS. The MC simulation for the spectral fitting is computed by considering the differential light yield.

The MC simulation with 3% of differential light yield is used for the past analysis, and the boundary effect is almost negligible when the fiducial volume was 1.2 m. The relative light yield between Xe-LS and Outer-LS was determined at localized postion as shown in Fig 4.15(a), and we need to check the postion dependence of the relative light yield. Fig 4.16 shows radial distribution and $\cos\theta$ distribution of neutron capture events (2.2 MeV γ). The deviation of neutron capture energy in Outer-LS region is $\sim$ 4%, and the postion of ^{208}Tl calibration is indicated with green dotted line. Finally, we found that 5% of relative light yield (Outer-LS / Xe-LS = 1.05) reproduce the $\sim$ 4% of energy deviation with neutron capture gamma, by testing with MC simulation and χ^2 method as shown in Fig 4.17. The energy spectrum in 2-m-radius including the boundary effect is well-reproduced with the MC simulation. Further study gave more accurate estimation of the light yield against Outer-LS, and the MC simulation for the spectral fitting is computed with the 5% difference of relative light yield and used for the analysis.

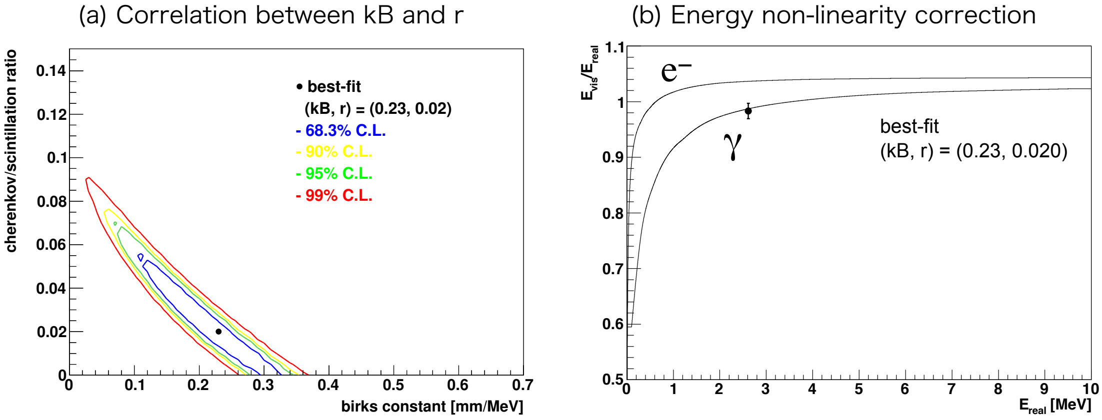

Fig 4.14: The distributions of energy scale parameters. (a) shows correlation of Birks constant (kB) and ratio of Cherenkov and scintillation photons (r). Best fit values are shown with black point. The blue, yellow, green and red contour plots show 68.3% (1σ), 90%, 95% and 99% C.L., respectively. (b) shows energy non-linearity correction for electron and gamma energy scale. The data point is given by the source calibration with ^{208}Tl (2.614 MeV γ ray).

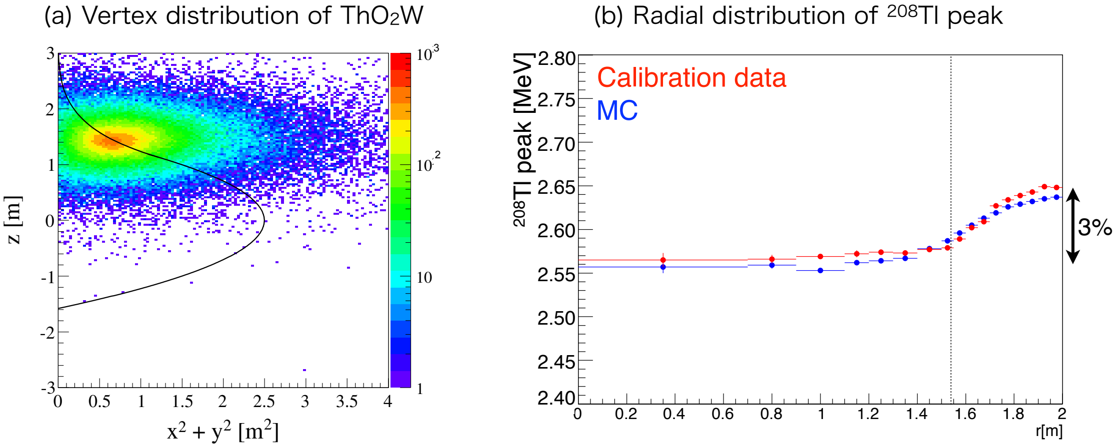

Fig 4.15: Distributions of ^{208}Tl events. (a) shows vertex distribution of ^{208}Tl source calibration events. The black solid line indicates the boundary of IB surface. (b) is distribution of ^{208}Tl energy peak as function of radius. Red points are data, and blue points are given with MC simulation. $\sim 3\%$ of peak shift is seen in Outer-LS region.

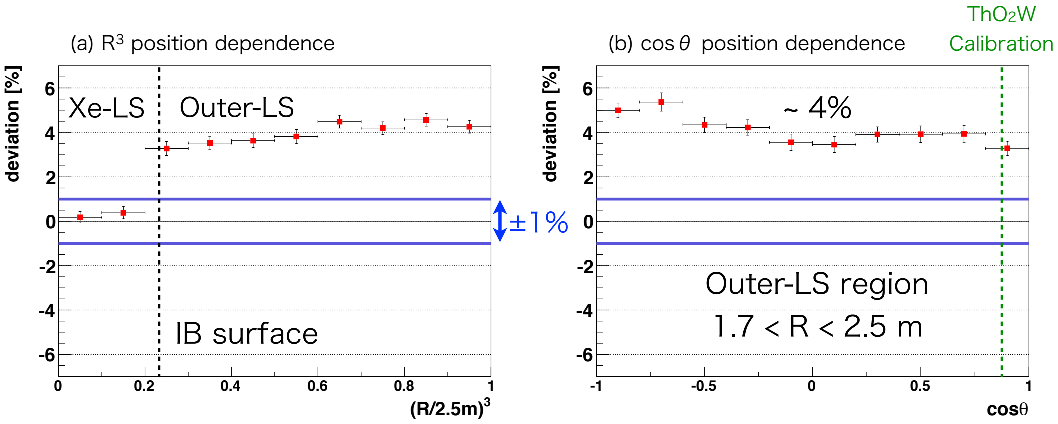

Fig 4.16: Position dependences of neutron capture events. (a) shows radial dependence of energy deviation, and (b) shows cos θ dependence in Outer-LS region ($1.7 < R < 2.5$ m). $\sim$ 4% of energy deviation is seen in Outer-LS. The green dotted line in (b) indicates the postion of ^{208}Tl source calibration events.

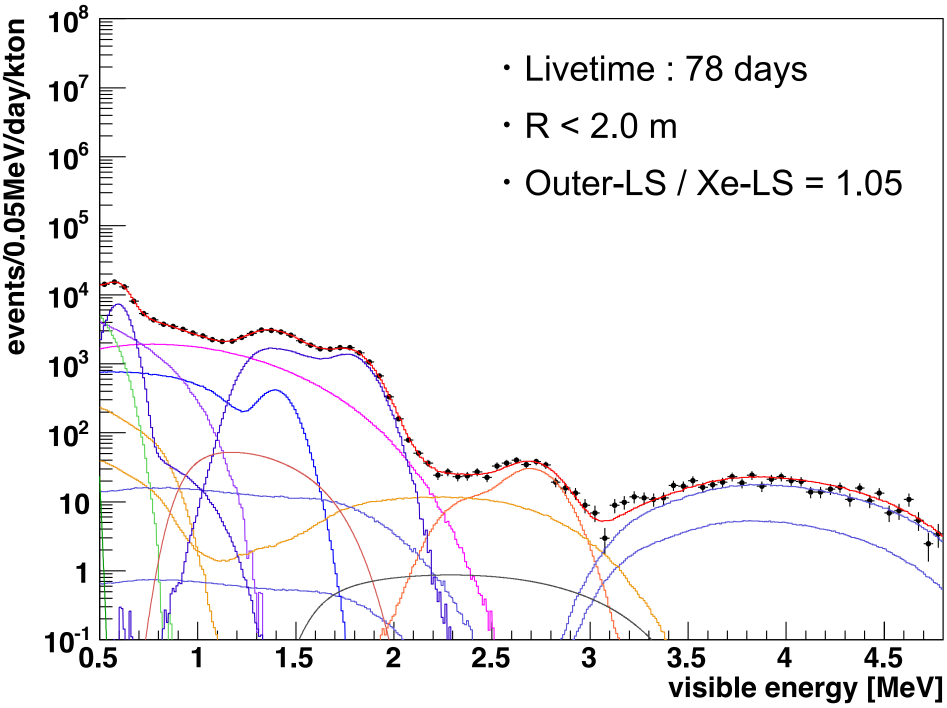

Fig 4.17: Energy spectrum in Xe-LS and Outer-LS. The livetime is 78 days, and the data set is same as [33], and the fiducial radius is 2.0 m. The spectral fitting result is drawn with spectrum of MC simulation which has 5% deviation of the relative light yield between Xe-LS and Outer-LS.

Chapter 5

Event Selection

This chapter describes how to select and evaluate reconstructed events for the analysis. After the data set for the double beta decay analysis is defined (section 5.1), the procedure of the event selection for double beta decay analysis is shown (section 5.2 $\sim$). There are non-physical events to be rejected, and some physical but potentially background events can be tagged, and the remaining events are collected as sigle events to be analyzed. The single events include signals of double beta decay and background events for spectral fitting described in chapter 6 and 7.

The fiducial volume is defined with background estimation to maximize the sensitivity for $0\nu\beta\beta$ decay signal, therefore it is described in the next chapter (see section 6.6).

5.1 Data Set

The data set for this thesis is divided to 2 periods, named DS-1 and DS-2, by the filtration campaign (see section 3.5.3) performed in February 2012. DS-1 is the same period as one used in [34] as the 2nd result of KamLAND-Zen, and corresponds run 011000-011212 and from 12th October 2011 to 9th February 2012. DS-2 is defined as the period after the filtration campaign and before xenon-extraction campaign described in section 8.1, and corresponds run 011254-011409 and from 1st March 2012 to 14th June 2012. The period which has high radon concentration after the filtration campaign is rejected.

In DS-1, 213 runs are taken in 119 days, and they include baseline run and background run which are weekly taken, and the calibration runs for ThO_2W source deployment. The remaining 171 runs are physics run taken for the double beta decay search. The quality of the detector condition is checked run by run, and it is defined as run grade ($0 \sim 10$). If there is no problem or failure in the detector and the data taking, the run grade becomes 0. The runs which have run grade 10 are rejected because the conditions of the detector are not good. The others are available runs by applying the dead time veto and/or the correction. Eventually, 147 runs are selected for DS-1. In the same manner as DS-1, 156 runs are taken in 105 days in DS-2, and 114 physics runs are selected for the analysis

The livetime in data sets is calculated in section 7.1.2.

5.2 Bad Event Rejection

Before event reconstruction, we apply a basic cut to reject non-physical events. Non-physical events are characterized with their abnormal PMT hit time distribution. A point-like vertex single physics event should have PMT hits distributed within about 100 nsec time window, which roughly corresponds to photon travel time throughout the detector including the effect of photon absorption and re-emission. The non-physical events are removed with their hit time distribution.

The reconstructed events are identified with some parameters to reject bad events generated with various reasons. The bad events are categorized into flasher events, muon events and noisy events after muon, missing waveform events and events with worse badness which is a parameter of event quality. Fig 5.1 shows the distribution of total charge of 17 inch PMTs (Q_{17}) for each category. The physical events are the remaining events after bad events rejection, and dominated in lower energy region.

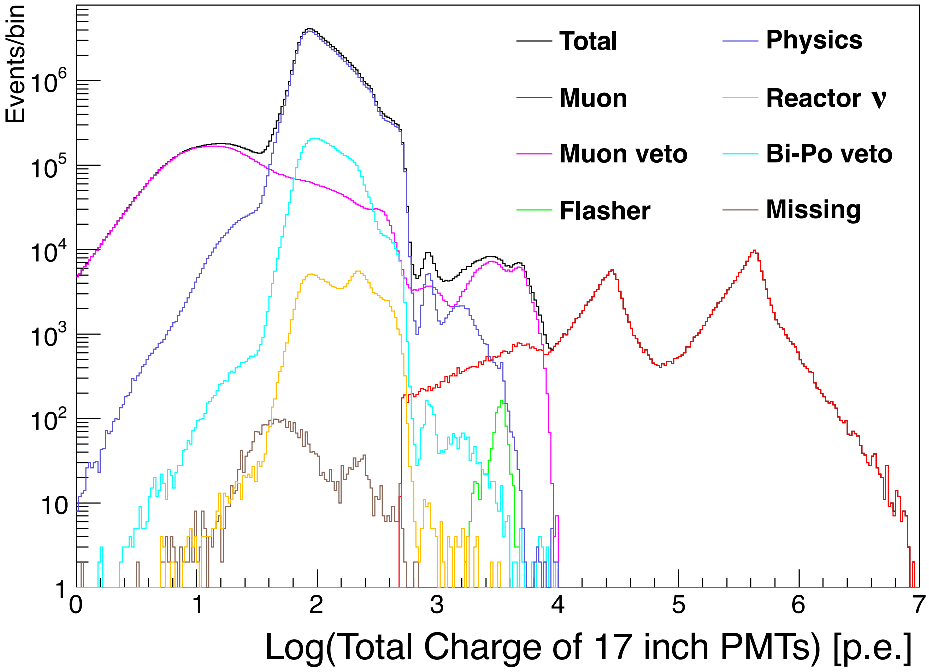

Fig 5.1: The distribution of total charge of 17 inch PMTs for each event category. The distributions of each selection, rejection, veto and tagging are drawn respectively, and the total of them is drawn in black line.

5.2.1 Flasher Event Cut

Flasher events are caused by light emission from the PMT due to discharge in the dynode. The surrounding PMTs detect the light from the discharge, generating an event. The hits time distribution of flasher events is similar to that of normal events, but their charge distribution is different from normal events. The selection criteria of flasher events are described in the following.

- $Q_{\rm ID} > 2,500$ p.e.
  $Q_{\rm ID}$ is total charge of 17 inch and 20 inch PMTs in the inner detector.
- Maximum single-PMT charge / $Q_{\rm ID} \geq 0.6$
  This criterion means that 60% of total charge is observed with a single PMT.
- Mean charge of the neighbor PMTs surrounding the flasher PMT ≥ 20 p.e.
  Higher charges are observed with the neighbor PMTs, and it is an evidence of flasher event.
- Not muon event or noise event
  The flasher events is not identified as muon event and noise event.

The events satisfying all criteria above are defined as flasher events. The noise events are defined with the number of maximum PMT hits within 100 nsec (N_{100}) and the number of all PMT hits in an event ($Nhit_{\mathrm{ID}}$), as $N_{100} \leq (Nhit_{\mathrm{ID}} + 50)/2$.

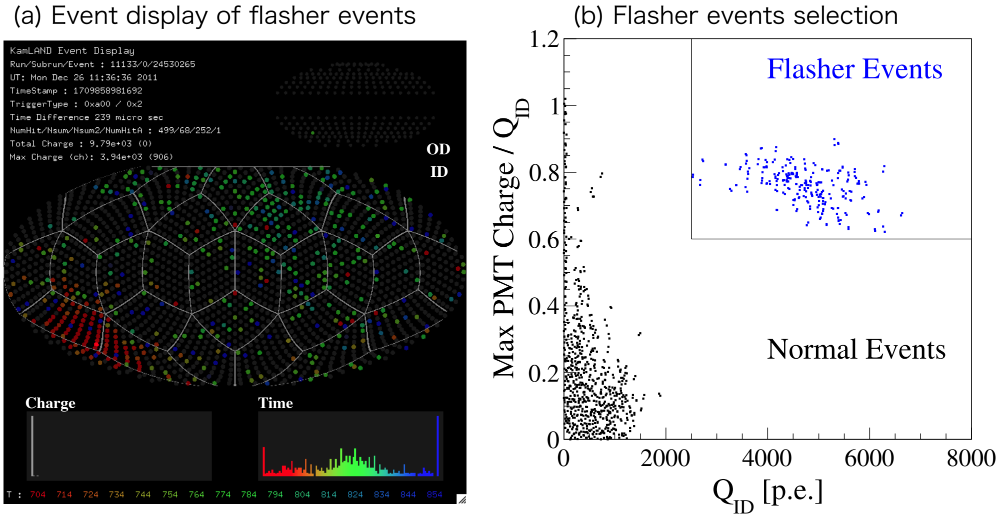

Fig 5.2: Event display of flasher events and the selection criteria. (a) shows event display of a typical flasher event with whole volume of KamLAND. The closed region in (b) is selected area as flasher events, and they are drawn in blue points and normal events are drawn in black.

Fig 5.2(a) shows the event display of a typical flasher event. The flasher events are clearly separated from normal events as shown in Fig 5.2(b). The event rate of flasher events is about 10^{-3} Hz, which corresponds to $\sim 0.001\%$ of all low energy events as shown in Fig 5.1.

5.2.2 Muon Veto

Cosmic-ray muon generates the spallation products which are potential backgrounds for signal. For example, neutrons generated with the muon events are captured on protons with life-time of a few hundreds μsec and emit 2.2 MeV γ then. In addition to the spallation products, the electrical noise can be induced with high charge for each channel. Moreover, after-pulse and overshoot comes from electrical design of PMT affect the detection efficiency of 1 p.e. signal.

Therefore, they all are vetoed within 2 msec after every muon events. The selection criteria for muon events are already mentioned in section 4.3.1. The muon events themselves are rejected, of course, and the veto time is taken into account to livetime calculation.

5.2.3 Missing Waveform Events Cut

Sometimes, the waveform information are lost in short time periods when the ATWD channels become busy due to high event rates. These events are called missing waveform events, and removed with the following selection.

$$Nhit_{17} < NsumMax \ ,$$

where $Nhit_{17}$ is the number of recorded waveforms of 17 inch PMTs, and NsumMax is the maximum number of 17 inch PMT hits within 125 ns period after trigger is issued. The selection criterion indicates that the number of recorded waveforms should be larger than the number of hits in some smaller window of time during the event. Fig 5.3 shows the selection of missing waveform events. The inefficiency of the missing waveform cut for physics events is estimated from ^{137}Cs source calibration to be about 0.01%.missing waveform cut.

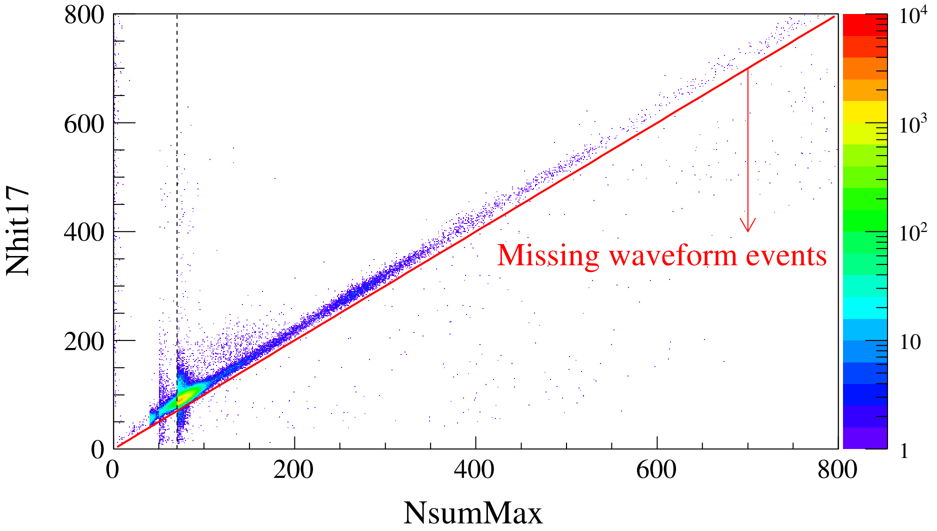

Fig 5.3: Selection criteria of missing waveform events. A vertical black dotted line indicates threshold of Nsum. Red line indicates the selection criterion of missing waveform events.

5.2.4 Badness Cut

The parameter badness is for additional rejection of potentially bad events. The badness is calculated with 9 evaluation parameters in the process of the event reconstruction. The detail of the parameters are found in [65], and the distribution of badness with visible energy is shown in Fig 5.4. The selection criteria for badness cut is defined with a function of visible energy, $f(E_{\rm vis}) = 41.1\exp(-9.7E_{\rm vis}) + 2.31$. The events with badness over the function, are rejected as noise events.

5.3 Anti-Neutrino Event Veto

Anti-neutrino mainly comes from nuclear reactors can be tagged with delayed coincidence technique, and the detection principle is drawn in Fig 5.5. In KamLAND detector, incident $\overline{\nu}_e$interacts with proton via inverse beta decay process. The prompt event is observed as electron-positron pair annihilation, and the delayed event is observed as thermal neutron capture event on proton. Although the prompt / delayed events originated with $\overline{\nu}_e$are categorized into physics events, they are potential background for double beta decay signal. Therefore, the events are tagged and vetoed as reactor neutrino events for the analysis.

The condition for delayed coincidence is described in the following.

- $E_{\rm delayed} \geq 1.5$ MeV
  $E_{\rm delayed}$ is visible energy of delayed events. The delayed events of neutron capture should be 2.2 MeV gamma-ray.
- $\Delta R < 200$ cm
  ΔR is a distance between prompt and delayed event.

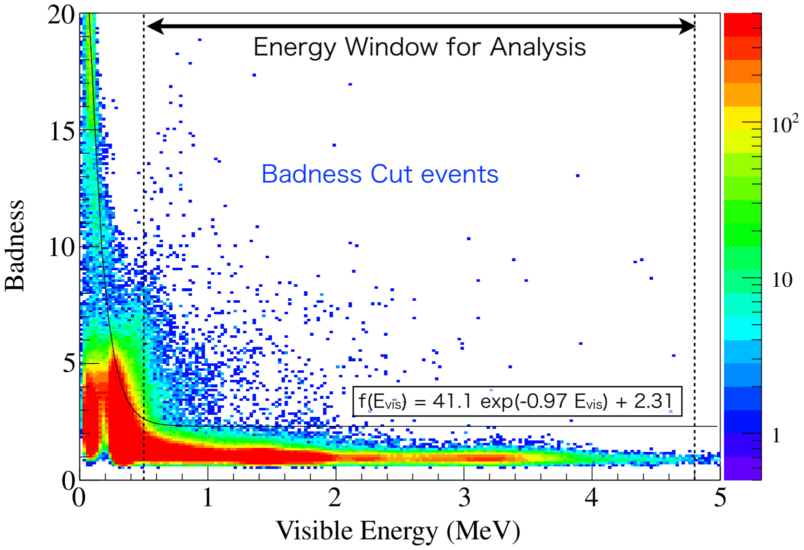

Fig 5.4: Badness distribution as a function of visible energy. Dotted vertical lines show energy window used for the analysis, and black solid curve indicates a function for badness cut.

- $\Delta T < 1.0$ msec
  ΔT is differential time between prompt and delayed event. The life-time of thermal neutron is $\sim 210\mu$sec.

Considering the anti-neutrino flux from nuclear reactor, the reactor neutrino event rate is very small in such small fiducial volume for KamLAND-Zen. In fact, the detected anti-neutrino events in the fiducial volume and data set is only a few events.

5.4 Bi-Po Delayed Coincidence Tagging

The decays of ^{214}Bi and ^{212}Bi in decay chains of ^{238}U and ^{232}Th in nature are background events for $0\nu\beta\beta$ decay signal due to their energy. They exist in the detector as daughter nuclei of ^{222}Rn and ^{220}Rn in the air, and ^{238}U and ^{232}Th in the materials. Owing to their sequential decays of their daughter nuclei (^{214}Po and ^{212}Po) with relatively short half-lives, they can be tagged with delayed coincidence techniques.

The selection criteria and tagging efficiency for Bi-Po tagging are summarized in Table 5.1. The energy spectrum and correlations of selected ^{214}Bi - ^{214}Po events are shown in Fig 5.6. Fig 5.6(a) shows energy spectrum of prompt events ($^{214}\mathrm{Bi} : \beta + \gamma$), and (b) shows energy spectrum of delayed event ($^{214}\mathrm{Po} : \alpha$). Kinetic energy of ^{214}Po alpha decay is 7.833 MeV, and it is quenched in the scintillator to $\sim$ 0.6 MeV peak. The space correlation is shown in Fig 5.6(c), and time correlation and the best fit with decay curve shows the half-life of ^{214}Po as shown in Fig 5.6(d).

In addition to usual delayed coincidence techniques used in KamLAND, pile-up Bi-Po events are tagged and rejected for more high efficiency. Fig 5.7 is an example of pile-up events with time spectrum and charge information extracted from waveforms. The selection criteria for the pile-up Bi-Po events are differential time between 2 signals ($\Delta T > 20$ nsec), delayed energy ($0.35 \leq E_{\mathrm{delayed}} < 1.2$ MeV) and the badness of fitting ($\chi^2_T > 1.5$).

The sequential Bi-Po tagging techniques result the tagging efficiency of $99.97 \pm 0.01\%$ for ^{214}Bi - ^{214}Po, and that of $89 \pm 2\%$ for ^{212}Bi - ^{212}Po, respectively. The tagging (rejection)

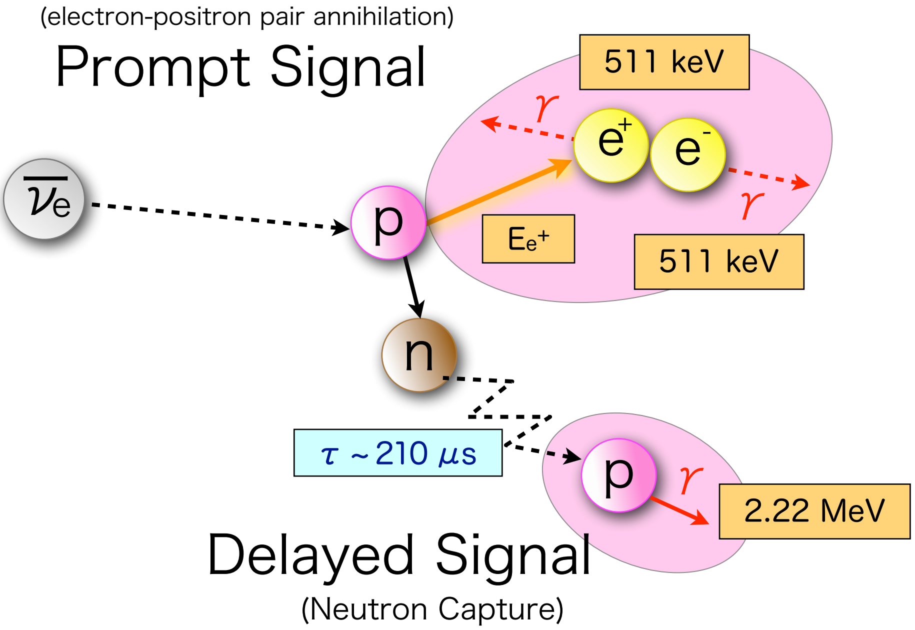

Fig 5.5: Detection principle of electron anti-neutrino with liquid scintillator. The incident electron anti-neutrino interacts with a proton, and the proton turns into neutron by emitting positron. The positron immediately annihilate with electron and γ (over 2 × 0.511 MeV) is generated. The electron-positron pair annihilation is detected as prompt signal in the detector. On the other hand, neutron is thermalized and captured with proton. The 2.2 MeV γ emitted with the neutron capture event is detected as delayed signal. The anti-neutrino is detected with the correlation between prompt and delayed event, namely delayed coincidence technique.

introduces less than 0.1% of detection inefficiency.

5.5 Single Event

The survived events with various cuts, rejections and tagging described above sections are collected as single events for the double beta decay analysis. The single events are evaluated for the backgrounds and the double beta decay signals in the latter chapters.

Table 5.1: Selection criteria and efficiency of Bi-Po tagging.

	^{214}Bi - ^{214}Po	^{212}Bi - ^{212}Po
Delayed Energy (E_{delayed})	$0.35 < E_{\text{delayed}} < 1.5$ MeV	
Spatial Correlation (ΔR)	$\Delta R < 300$ cm	
Time Correlation (ΔT)	$\Delta T < 3,000\mu$sec	
Tagging Efficiency	$99.97 \pm 0.01\%$	$89 \pm 2\%$

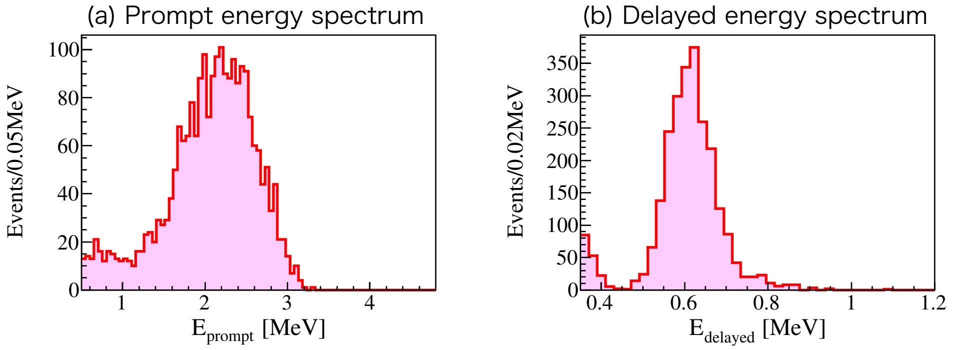
(a) Prompt energy spectrum

(b) Delayed energy spectrum

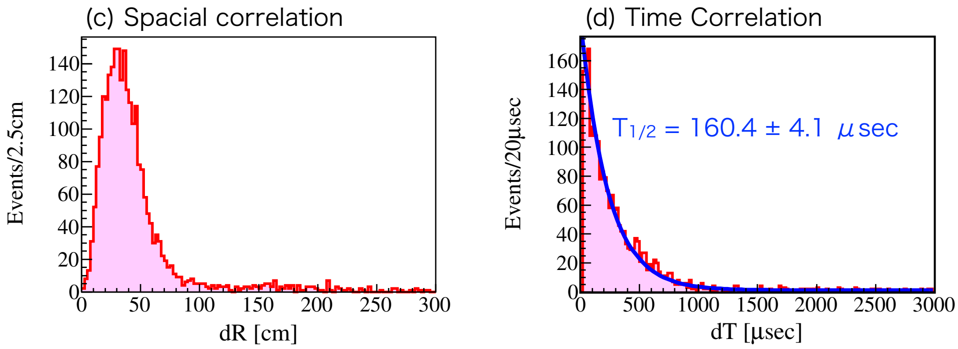
(c) Spacial correlation

(d) Time Correlation

Fig 5.6: Delayed coincidence events of ^{214}Bi-Po. (a) shows energy spectrum of prompt events (^{214}Bi : $\beta + \gamma$), and (b) shows energy spectrum of delayed event (^{214}Po : α). The space correlation between prompt and delayed events are shown in (c), and the time correlation is shown in (d). The blue curve indicates the best fit of decay curve of ^{214}Po.

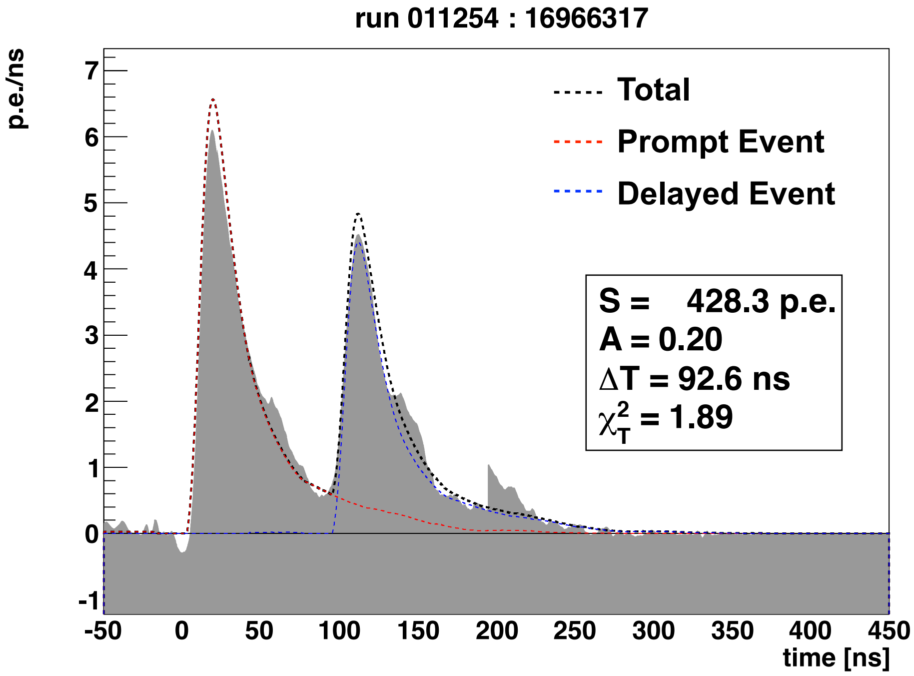

Fig 5.7: An example of double pulse event evaluated with time and charge distribution. The best fit of prompt signal is drawn in red dotted line, and that of delayed signal in blue dotted line.

Chapter 6

Backgrounds

The estimation of backgrounds is important to identify the signals of ^{136}Xe double beta decay by the energy spectral fitting. The spectral fitting is simultaneously computed with spectra of all backgrounds, signals and parameters of energy scale, therefore we have to estimate the backgrounds as rigorous as possible. The background events in the detector have been studied in the past analysis with KamLAND detector, such as radioactive impurities included in liquid scintillator (LS) and spallation products generated by cosmic-ray muon. Because inner balloon (IB) and Xe loaded liquid scintillator (Xe-LS) are newly installed into the detector for KamLAND-Zen, the background contribution from them is considered afresh.

The primary target of this work is a search for ^{136}Xe neutrinoless double beta decay. The fiducial volume of past works was decided for $2\nu\beta\beta$ decay spectrum to reject the external backgrounds from IB, while the sensitivity for $0\nu\beta\beta$ decay became worse. In this work, the enlargement of the fiducial volume is considered for $0\nu\beta\beta$ decay with the estimation of the external backgrounds, and it is described in the latter section.

6.1 Introduction of Backgrounds

The backgrounds for double beta decay analysis are classified into 4 categories depending on their origin.

- External backgrounds from IB
- Internal backgrounds in Xe-LS
- Spallation products by cosmic-ray muon
- Unexpected backgrounds in $0\nu\beta\beta$ energy region

The external backgrounds are mainly contributed from IB which is contaminated with radioactive impurities. The contribution from outer LS is not considered because KamLAND LS has very low radioactivity due to the distillation of LS. The material and the surface of IB are contaminated with highly radioactive impurities. The estimation of the external backgrounds are discussed in the next section 6.2.

The radioactive impurities in Xe-LS also make background events, which are called internal backgrounds. The usual purification as KamLAND LS has been processed for liquid scintillator to dissolve xenon; therefore the radioactive level of LS is expected to be low. The radioactive impurities which exist in nature are, however, still included in LS, and the event rate from the internal backgrounds is estimated in section 6.3.

Cosmic-ray muon comes into the detector in a certain frequency, and it induces spallation reaction with mainly ^{12}C which is constituent of LS. The radioactive isotopes such as neutron, ^{10}C and ^{11}C are generated as spallation products, then. ^{11}C and ^{10}C make background events against signal of double beta decay, and they are constantly generated everyday. In addition to carbon, spallation reaction with ^{136}Xe is also considerable. The estimation of background rate by the spallation products are explained in section 6.4.

Above 3 categories are expected backgrounds, and they are mostly common with the analysis of KamLAND. On the other hands, the unexpected peak around 2.6 MeV is observed after start of KamLAND-Zen. The peak provoked a controversy wether if the peak is signal of $0\nu\beta\beta$ decay or background. As we call it "background", finally we found that it is not signal but background peak accidentally introduced into the detector. The discussion is summarized in section 6.5.

6.2 External Backgrounds

Every material contains the radioactive impurities in nature such as ^{238}U and ^{232}Th decay chains and ^{40}K with a certain concentration, and we can only control the concentration. The radioactive level in the material of IB is under control by the measurement of ICP-MS from the stage as pellet which is plastic ingredient to make film. We expected that contribution of external backgrounds from IB is dominated by ^{238}U and ^{232}Th decay chains and ^{40}K, whereas there are another backgrounds from IB can be observed.

From a spectral analysis of events whose reconstruction is close to the IB boundary (R = 154 cm), we found that the activity in the energy region $1.2 < E_{\mathrm{vis}} < 2.0$ MeV ($2\nu\beta\beta$ energy region) is dominated by ^{134}Cs ($\beta + \gamma$). While, the spectrum is consistent with ^{214}Bi ($\beta + \gamma$) which is daughter of ^{238}U in the region $2.2 < E_{\mathrm{vis}} < 3.0$ MeV ($0\nu\beta\beta$ energy region).

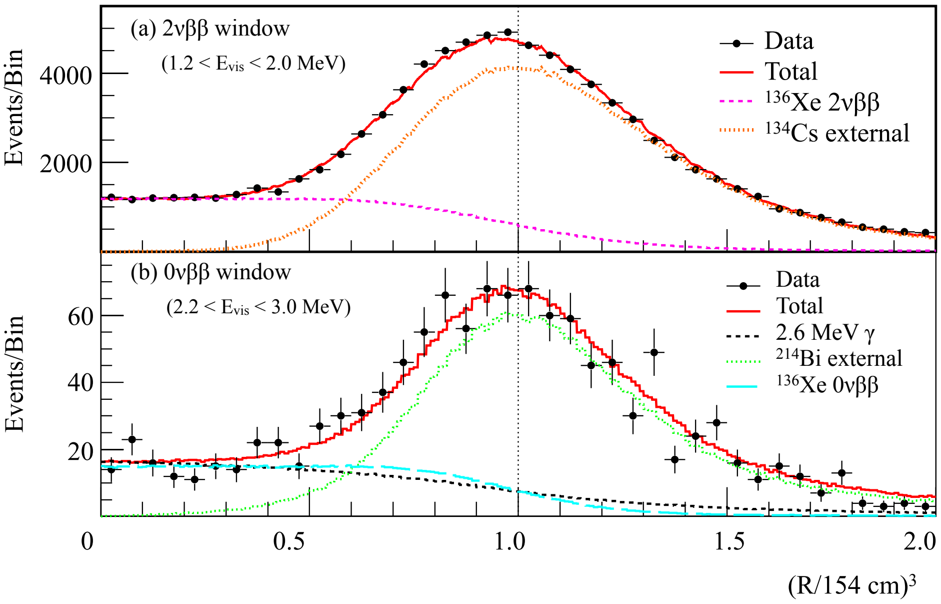

Fig 6.1: Radical distribution in the $2\nu\beta\beta$ (a) and $0\nu\beta\beta$ (b) energy window. The curves show the best-fit model components: (a) $2\nu\beta\beta$ (violet dashed) and ^{134}Cs (dotted). (b) 2.6 MeV γ 's (black dashed) and ^{214}Bi (light green dotted), the light blue long-dashed curve is for $0\nu\beta\beta$ instead of γ 's.

Fig 6.1 shows normalized radial distribution of events with the balloon radius (154 cm) in $2\nu\beta\beta$ energy window (a) and $0\nu\beta\beta$ energy window (b). There is large discrepancy between data and $2\nu\beta\beta$ spectrum without ^{134}Cs spectrum as shown in Fig 6.1(a). A spectrum of 2.6 MeV γ's in 6.1(b) is discussed in the latter section 6.5. Not only ^{134}Cs, we could see contribution of ^{137}Cs in energy spectrum. The isotopes of ^{134}Cs and ^{137}Cs do not exist in nature, therefore they should be provided with fall-out caused by the accident in Fukushima-I reactor in March 2011. The properties of them are listed in Table 6.1.

Table 6.1: Basic radioactive properties of ^{134}Cs and ^{137}Cs. The level diagrams of them are seen in Fig A.3.

	Decay Mode	Q-Value [MeV]	Half-Life [year]
^{134}Cs	$\beta^- + \gamma$ (99.9997%) EC (3×10^{-4}%)	2.06 1.23	2.06
^{137}Cs	$\beta^- + \gamma$ (0.662 MeV γ @ 94.4%)	1.18	30.07

The fabrication of IB is done in Sendai where is around 100 km far away from Fukushima-I reactor. According to the report of fall-out measurements [60] [61], ^{134}Cs and ^{137}Cs are detected in the surface soils sampled in Sendai. The fall-out measurements in surface soils around Sendai is summarized in Fig 6.2 [60].

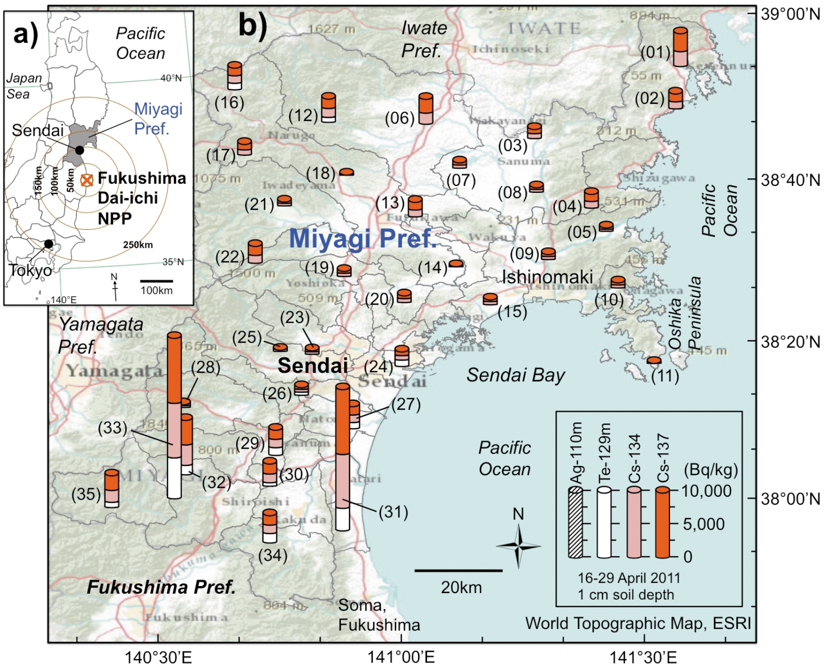

Fig 6.2: Distribution of artificial radioactivities in Miyagi Prefecture [60]. (a) indicates location of the study area (Miyagi Prefecture) and the Fukushima-I reactor plant. (b) shows distribution of artificial radionuclides (^{110m}Ag, ^{129m}Te, ^{134}Cs and ^{137}Cs) in surface soils (0∼1 cm depth) in Miyagi Prefecture during the period April 16—29, 2011.

6.2.1 Non-uniform Distribution in/on IB

Although We assumed uniform distribution of the external background in/on IB in the past analysis, actually the cesium and uranium are not distributed uniformly on the

IB film. Fig 6.3 shows theta distributions of $2\nu\beta\beta$ energy region ($1.2 < E_{\mathrm{vis}} < 2.0$ MeV) for top part ($0.8 < \cos\theta < 0.9$) shown in (a), equator part ($-0.1 < \cos\theta < 0$) shown in (b) and bottom ($1 < \cos\theta < 0.9$) part shown in (c). The higher concentration of ^{134}Cs is seen at top and bottom part than that at equator part, these radial distribution implies non-uniform z distribution of the external background in/on IB.

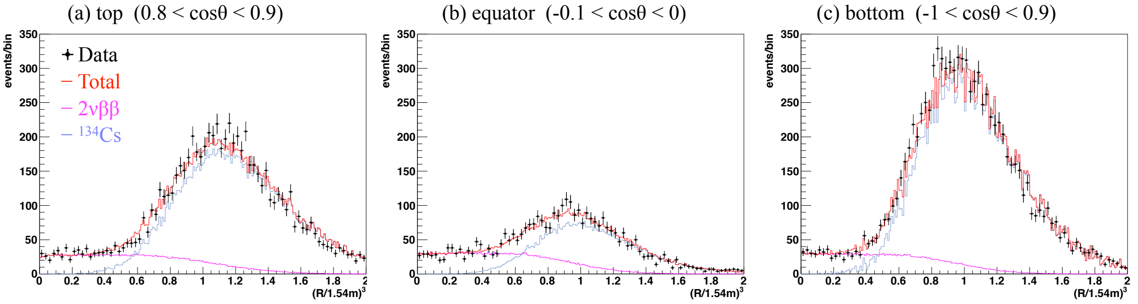

Fig 6.3: Radial distributions in $2\nu\beta\beta$ energy region ($1.2 < E_{\mathrm{vis}} < 2.0$ MeV) for 3 parts of IB.

Rather, their activity appears to increase proportionally with the area of the film welding lines. This indicates that the dominant IB backgrounds may have been introduced during the welding process from dust containing both natural U and Fukushima fallout contaminants. Theta distributions estimated with energy spectrum in each region divided by the θ for ^{134}Cs (a), ^{214}Bi (b) and ^{208}Tl (c) is shown in Fig 6.4.

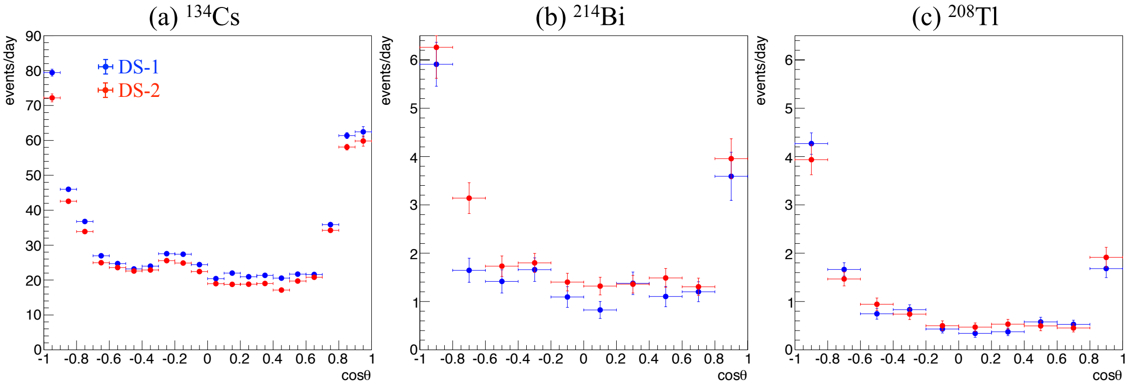

Fig 6.4: θ distribution of ^{134}Cs, ^{214}Bi and ^{208}Tl in/on IB. Blue points show θ distribution of DS-1, and red points show that of DS-2. [$\cos\theta = -1$] corresponds bottom part of IB, [$\cos\theta = 0$] is equator of IB and [$\cos\theta = 1$] is top part of IB. Event rate is estimated with energy spectral fitting in each region divided by the θ for ^{134}Cs, ^{214}Bi and ^{208}Tl respectively.

For spectral fitting, the external background events are generated with Monte Carlo (MC) simulation to reproduce the distribution shown in Fig 6.4, while MC events in the past analysis were uniformly distributed on/in IB assumed. These non-uniform distributions contribute to compensate the discrepancy of the vertex distribution at the equator area and the bottom part, and results more precise estimation of the external backgrounds. The non-uniform distribution of ^{134}Cs MC events can be seen in Fig 6.5. The black solid line indicates the boundary of IB ($R = 154$ cm), and the dotted line indicates the boundary of fiducial volume selection ($R < 135$ cm) in this analysis explained in the latter. Fig

6.5(a) is uniform distribution we assumed before, and Fig 6.5(b) shows the non-uniform distribution to reproduce θ distribution shown in Fig 6.4(a). Bottom and top parts have higher concentration of ^{134}Cs events than the equator area.

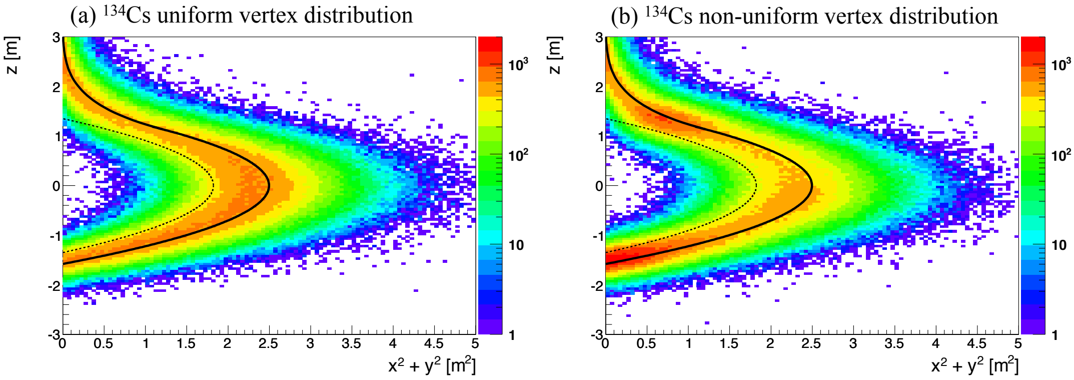

Fig 6.5: Vertex distributions of ^{134}Cs MC events. Black solid line shows the boundary of IB surface ($R = 154$ cm), and dotted line shows the boundary of fiducial volume ($R = 135$ cm). (a) is uniform distribution we applied for the past analysis, while (b) is non-uniform distribution with MC simulation to reproduce θ distribution shown in Fig 6.4(a).

Same as ^{134}Cs, non-uniform distributions are generated with MC simulation for ^{214}Bi, ^{208}Tl and also for ^{137}Cs which have statistically higher event rates in/on IB.

6.2.2 Estimation of External Backgrounds

Using the non-uniform distributions with MC simulation, the estimation of external backgrounds are computed by 2-Dimensional spectral fitting. Energy spectral fittings in divided 4 regions by radius (R) with the same volume, are simultaneously computed to minimize the quantity χ^2. χ^2 here is just of χ^2_{energy} and $\chi^2_{\mathrm{penalty}}$. The definition of χ^2_{energy} is same as described in analysis part (chapter 7). While $\chi^2_{\mathrm{penalty}}$ is contributed by only constrain of spallation product rates and energy scale parameters.

The fitting result is shown in Fig 6.6 and Fig 6.7 and summarized in Table 6.2. In Fig 6.6 and Fig 6.7, data, best fit of the total spectrum and contributions of the external backgrounds are drawn. The 2 decay chains of ^{222}Rn-^{210}Pb and ^{228}Th-^{208}Pb, ^{40}K and ^{208}Bi in nature are considered as external backgrounds in/on IB. As discussed above, ^{134}Cs and ^{137}Cs are artificial radioactive sources provided by fall-out from Fukushima-I nuclear reactor, and they are dominant backgrounds in/on IB as seen especially in outer region ($3/4 < (R/154)^3 < 4/4$) shown in Fig 6.6(d) and Fig 6.7(d). In addition, we found the unexpected background around 2.6 MeV, assumed as $^{110\mathrm{m}}$Ag here, in/on IB although the event rate is very small compared with the others. The contribution of external $^{110\mathrm{m}}$Ag background has not been considered in the past analysis. The estimation of that is important to maximize the sensitivity for $0\nu\beta\beta$ decay search and the fiducial volume selection. We assumed the distribution of the $^{110\mathrm{m}}$Ag in/on IB is uniform because the number of $^{110\mathrm{m}}$Ag events is too low statistics to estimate θ distribution. The topic of the background is discussed in the latter sections.

These fitting results summarized in Table 6.2 are used to constrain the background event rates when spectral fitting with time and energy is computed.

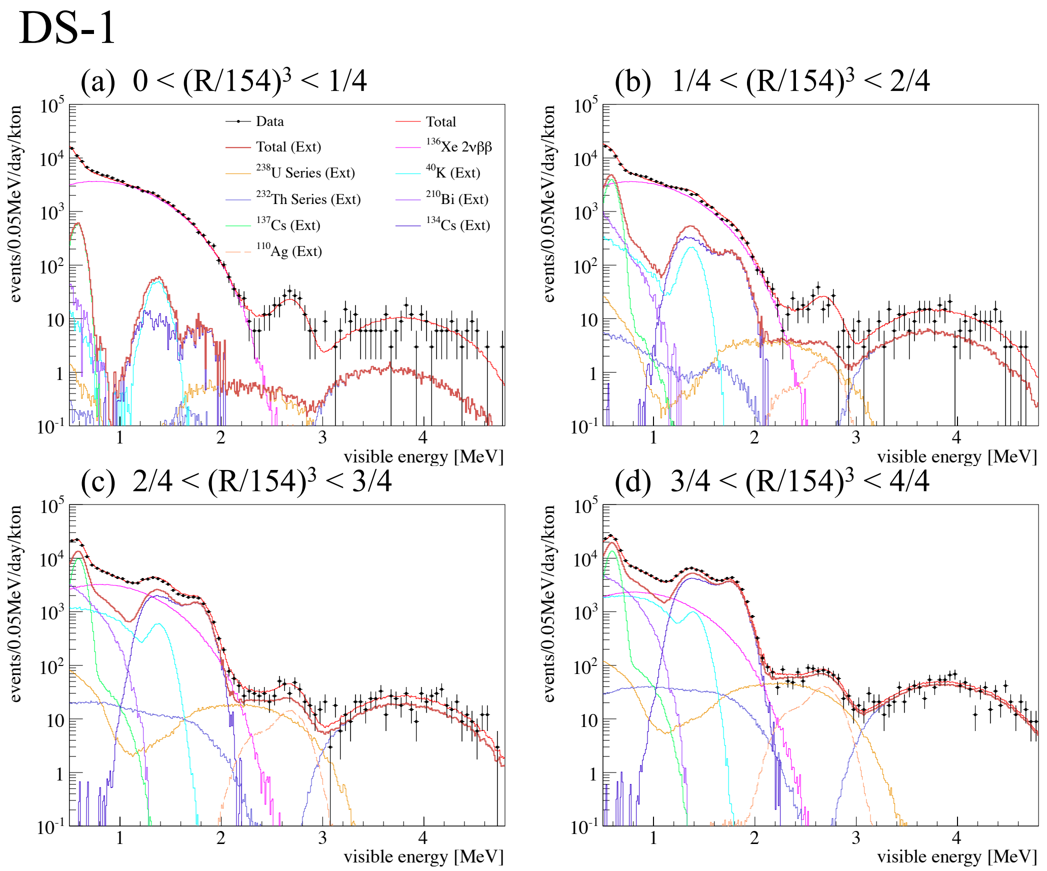

Fig 6.6: 2-Dimensional fitting with energy and radius for the estimation of external backgrounds in DS-1. Data, best fit of total spectrum and only spectra of each external background are drawn.

Table 6.2: Results of 2-dimensional spectral fitting for external backgrounds. The best fit of parameters with statistical uncertainties are summarized for each data set. These fitting results are used to constrain the external background rate in the spectral fitting with time and energy.

	DS-1 [events/day]	DS-2 [events/day]	origin
^{222}Rn-^{210}Pb	18.45 ± 1.78	18.18 ± 2.49	in nature
^{228}Th-^{208}Pb	31.54 ± 1.70	31.53 ± 2.68	
^{40}K	557.1 ± 14.1	625.9 ± 21.0	
^{210}Bi	1667 ± 77.5	1715 ± 95.5	
^{137}Cs	624.4 ± 8.39	588.6 ± 11.3	artificial radionuclides (from Fukushima-I)
^{134}Cs	571.0 ± 4.48	513.9 ± 5.86	
$^{110\text{m}}$Ag	3.404 ± 0.386	2.448 ± 0.399	not defined yet

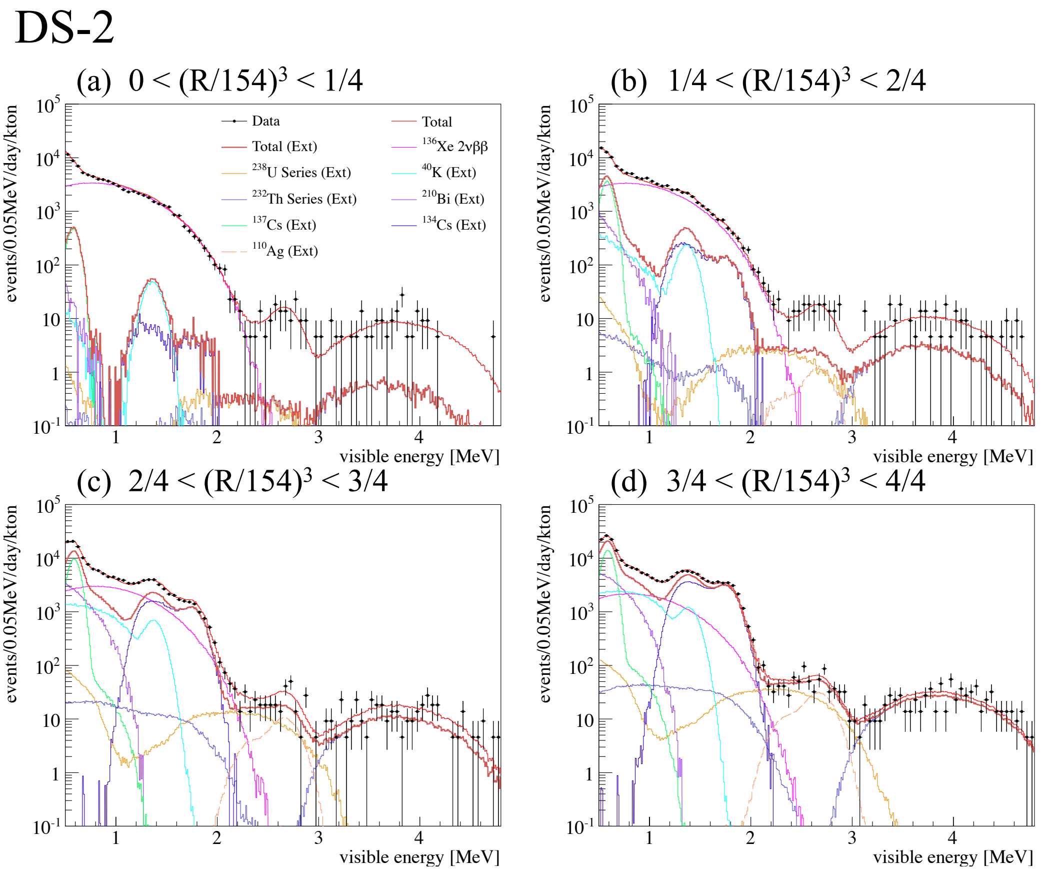

Fig 6.7: 2-Dimensional fitting with energy and radius for the estimation of external backgrounds in DS-2. Data, best fit of total spectrum and only spectra of each external background are drawn.

6.3 Internal Backgrounds

The internal backgrounds are defined as backgrounds from radioactive impurities in Xe-LS remaining after purification processes, and they are uniformly distributed inside IB. The internal backgrounds from decay chains of ^{238}U and ^{232}Th, ^{40}K are observed in Xe-LS, same as KamLAND LS. Noble gas ^{85}Kr and ^{210}Bi are also observed in low energy region in common.

Although all they are expected backgrounds in Xe-LS, another peak is observed in energy spectrum around 2.6 MeV. The peak is unexpected as backgrounds, and energy and shape of the peak seem to be different from $0\nu\beta\beta$ decay signal. The discussion about the unexpected background is found in section 6.5.

6.3.1 Decay Chains of ^{238}U and ^{232}Th

The concentrations of ^{238}U and ^{232}Th in Xe-LS are estimated with sequential decay of ^{214}Bi-^{214}Po and ^{212}Bi-^{212}Po, and ^{208}Tl shown in Fig 6.8 by the delayed coincidence techniques. The data set for the estimation is defined to reject ^{222}Rn and ^{220}Rn contamination by the filling or filtration activities in the beginning of DS-1 and DS-2. The longest half-lives in ^{222}Rn-^{214}Pb and ^{220}Rn-^{208}Pb are 3.824 days (^{222}Rn) and 10.6 hours (^{212}Pb), and the event rates are dominated by them. The data set is summarized in Table 6.3.

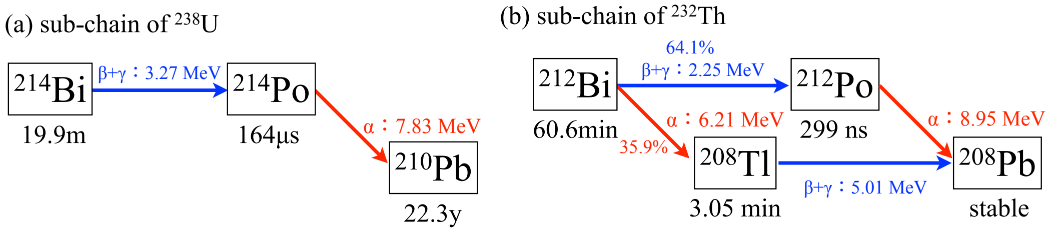

Fig 6.8: Sub-chains in ^{238}U and ^{233}Th. (a) is a sequential decays of ^{214}Bi-^{214}Po which is sub-chain of ^{238}U, and (b) shows branching decays of ^{212}Bi-^{208}Tl in ^{232}Th decay chain. Their half-lives are indicated under each nucleus. Blue arrows are decay of $\beta+\gamma$ mode with Q-Values, and red arrows indicate α decay with Q-Values. These chains are extraction from Fig A.1 and A.2.

Table 6.3: Data set for the estimation of ^{238}U and ^{233}Th.

	DS-1 (livetime [days])	DS-2 (livetime [days])
^{238}U estimation	run 11082-11212 (67.7)	run 11302 - 11409 (67.7)
^{232}Th estimation	run 11036-11212 (90.0)	run 11285 - 11409 (78.8)
ref) $0\nu\beta\beta$ analysis	run 11000-11212 (112.3)	run 11254 - 11409 (101.1)

^{214}Bi and ^{212}Bi events are tagged by the delayed coincidence technique, and the event rates are estimated by considering the efficiency of the tagging. For more precise estimation, radial distribution of ^{214}Bi and ^{212}Bi are used for the fitting to remove the contribution by the external ^{214}Bi and ^{212}Bi from IB as shown in Fig 6.9. Fig 6.9(a) shows the best fit of ^{214}Bi in Xe-LS and from IB for DS-1, and Fig 6.9(b) shows that of ^{212}Bi.

The estimation is done for DS-1 and DS-2. The radial fitting is also computed for single events of ^{208}Tl same as Bi. The fitting results are summarized in Table 6.4.

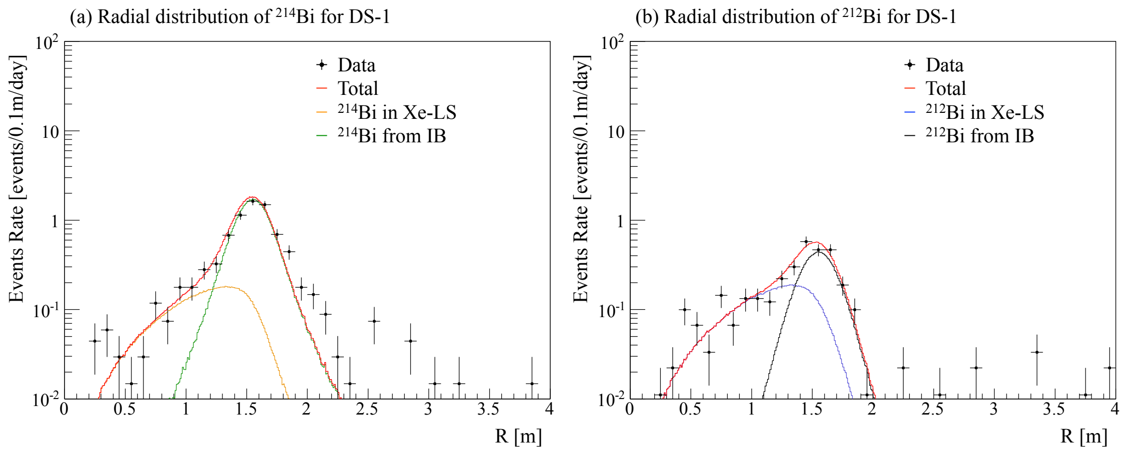

Fig 6.9: Best fit of radial distribution with ^{214}Bi and ^{212}Bi for DS-1. The fitting is computed with external background of ^{214}Bi and ^{212}Bi from IB to properly estimate the event rates in Xe-LS. The fitting is also computed for DS-2 in the same manner.

Table 6.4: Fitting results for event rates of ^{214}Bi-^{214}Po, ^{212}Bi-^{212}Po and ^{208}Tl in Xe-LS.

	Event rate for DS-1 [events/day]	Event rate for DS-2 [events/day]
^{214}Bi-^{214}Po	1.73 ± 0.24	0.80 ± 0.23
^{212}Bi-^{212}Po	2.15 ± 0.23	1.15 ± 0.26
^{208}Tl	2.90 ± 0.28	2.16 ± 0.32

The concentration of ^{238}U and ^{232}Th in Xe-LS can be estimated with the event rates summarized in 6.4. For ^{232}Th estimation, there are branches of ^{212}Bi-^{212}Po (64.1%) and ^{212}Bi-^{208}Tl (35.9%), and the event rate of ^{212}Bi is calculated with weighted average considering the uncertainties and branching ratio. Table 6.5 shows summary of the concentration of ^{238}U and ^{232}Th in Xe-LS for each data set. The concentration in DS-2 seems to be lower after filtration operation. These concentrations indicate very small contribution from ^{232}U-^{222}Rn and ^{232}Th-^{228}Th which have longer half-lives, therefore these chains are treated as unconstrained parameters in the spectral fitting. In contrast, sub-chains of ^{222}Rn-^{210}Bi and ^{228}Th-^{208}Pb have large contribution to signal of double beta decay. They are constrained by the event rate with delayed coincidence of ^{214}Bi-^{214}Po and ^{212}Bi-^{212}Po for the spectral fitting.

6.3.2 ^{40}K, ^{210}Bi and ^{85}Kr

^{40}K, ^{210}Bi and ^{85}Kr are known as backgrounds in the lower energy observed in the liquid scintillator in KamLAND detector. Basic properties of them are summarized in Table 6.6. ^{40}K is a radioactive isotope in nature, and it is evaluated as background in Xe-LS. ^{210}Bi is downstream isotope in ^{238}U decay chain, and its event rate is almost constant due to much long half-life (22.3 year) of parent ^{210}Pb. ^{85}Kr is noble gas imperceptibly

Table 6.5: Concentration of ^{238}U and ^{232}Th in Xe-LS.

	DS-1 [g/g]	DS-2 [g/g]
^{238}U concentration	$(1.3 \pm 0.2) \times 10^{-16}$	$(5.8 \pm 1.7) \times 10^{-17}$
^{232}Th concentration	$(1.9 \pm 0.2) \times 10^{-15}$	$(1.4 \pm 0.2) \times 10^{-15}$

included in the air (~ 1 Bq/m^3) or pure nitrogen gas, and it also has a long half-life (10.7 year).

Table 6.6: Basic radioactive properties of ^{40}K, ^{210}Bi and ^{85}Kr.

	Decay Mode	Q-Value [MeV]	Half-Life
^{40}K	β^-(89.28%) EC (10.2%)	1.311 1.504	1.277×10^9 [year]
^{210}Bi	β^-	1.162	5.013 [day]
^{85}Kr	β^-	0.687	10.756 [year]

These 3 backgrounds are single events, and it is difficult to tag or veto them. Therefore they are treated as free parameters for the spectral fitting explained in chapter 7. The event rates are estimated with the fitting, and summarized in Table 7.5.

6.3.3 The Other Backgrounds

In addition to radioactive isotopes in nature, we evaluated the other potential backgrounds originated from fall-out by Fukushima-I accident. ^{137}Cs, ^{134}Cs, ^{110m}Ag, ^{129m}Te, ^{95}Nb, ^{90}Y and ^{89}Sr are candidates which are actually observed in the soil samples or ocean water around Fukushima-I and have half-lives longer than 30 days to survive in data set. Their event rates are estimated by energy spectral fitting, and we got only upper limit of ^{137}Cs and ^{134}Cs in Xe-LS, corresponds < 0.94 and < 0.25 events/day/ton at 90% C.L., respectively. For ^{129m}Te, ^{95}Nb, ^{90}Y and ^{89}Sr, we found no significance of their existence in Xe-LS.

However, ^{110m}Ag is a powerful candidate of unexpected peak around 2.6 MeV originated from the fall-out. The discussion of the unknown background is seen in section 6.5

6.4 Spallation Products

KamLAND detects cosmic-ray muon incident into the detector in 0.3 Hz, and the muon generates some radioactive products by the spallation reaction. The spallation reaction with ^{12}C have been studied [31], and the background rates are estimated in this section. On the other hand, the reaction with xenon have not been studied before, and the potential background rate with xenon is evaluated for KamLAND-Zen.

6.4.1 Neutron Capture

Neutron is major product of spallation reaction by cosmic-ray muon, and it is captured on protons or ^{12}C in the liquid scintillator after thermalization. Energy of the emitted γ when thermal neutron is captured is 2.225 MeV for proton and 4.946 MeV for ^{12}C with 210 μsec live-time. The events after 2 msec from muon events are vetoed, therefore these γ events of neutron capture do not contribute to the background.

By contrast, the neutron capture on ^{136}Xe may produce ^{137}Xe which is candidate of the background for double beta decay. ^{137}Xe undergo beta decay with life-time (5.5 min) and the Q-Value is 4.17 MeV, it it difficult to veto after muon for ^{137}Xe decay due to its long life-time. The capture probabilities are estimated for proton, ^{12}C, ^{136}Xe and ^{134}Xe with their cross sections and number of target, and they are summarized in Table 6.7. Neutron capture on proton is major process, and neutron capture on ^{136}Xe is occurred in small probability. In fact, no evidence of neutron capture on ^{136}Xe and ^{134}Xe are found in KamLAND-Zen. Using the estimation, the expected production rate of ^{137}Xe is $\sim 2.9 \times 10^{-3}$ events/day/ton, and it is negligible level in this work.

Table 6.7: Probabilities of neutron capture in Xe-LS.

	γ Energy [MeV]	Capture Probability
Proton	2.225	0.994
^{12}C	4.946	0.006
^{136}Xe	4.026	9.5×10^{-4}
^{134}Xe	6.364	9.4×10^{-5}

6.4.2 Spallation Products with ^{12}C

The spallation reaction by muon with ^{12}C which is primary component of LS generates various radioactive isotopes as studied in KamLAND detector [31]. ^{11}C and ^{10}C are potential backgrounds for double beta decay signal due to their energy spectrum and half-lives. Table 6.8 summarizes their properties and production rate measured with KamLAND detector [31].

Table 6.8: Basic radioactive properties of ^{11}C and ^{10}C and expected production rate in KamLAND . The level diagrams of them are seen in Fig A.4.

	Decay Mode	Q-Value [MeV]	Half-Life	Production Rate [events/day/ton]
^{11}C	β^+	1.98	20.4 min	1.11 ± 0.18
^{10}C	β^+	3.65	19.3 sec	$(2.11 \pm 0.18) \times 10^{-2}$

^{11}C and ^{10}C backgrounds can be rejected by a triple-coincidence tag of a muon, a neutron, and the their β decay. This is not pursued in the current analysis because the spallation background rate is not serious in the current sensitivity for $0\nu\beta\beta$ decay search. The $13 \pm 6\%$ increase in the spallation neutron flux in the Xe-LS relative to the outer LS is observed because neutron is additionally generated by the spallation reaction with xenon. This results 19% systematic uncertainty on the calculated spallation yields. We expected the production rate of 1.11 ± 0.28 events/day/ton for ^{11}C and $(2.11 \pm 0.44) \times 10^{-2}$ events/day/ton for ^{10}C respectively, with consideration of the additional systematic uncertainty.

The event rates of ^{11}C and ^{10}C are constrained by the expected production rate in the spectral fitting.

6.4.3 Spallation Products with ^{136}Xe

Spallation products by cosmic-ray muon with xenon are studied in 2 categories by their live-times.

Short-lived Products ($T_{1/2} < 100$ sec)

For the muon induced products from xenon, we have no past experimental data. Spallation products from ^{136}Xe whose half-lives are less than 100 sec, are studied with present data whether a event has time correlation with muons depositing more than ~3 GeV (called showering muons). As a result, no correlated event is found in $2\nu\beta\beta$ energy region ($1.2 < E_{\rm vis} < 2.0$ MeV). The 90% C.L. upper limit is calculated with Feldman Cousins method to be 171 events or 0.27 events/day/ton by counting the number of events in on-time window ($\Delta T_{\rm muon} < 500$ sec) and off-time window ($500 \leq \Delta T_{\rm muon} < 5,000$ sec). Time distribution is shown in Fig 6.10(a). In $0\nu\beta\beta$ energy region ($2.2 < E_{\rm vis} < 3.0$ MeV), there is also no correlated event. To calculate the upper limit in this energy region, spallation products from ^{12}C are also considered as backgrounds. Time distribution is shown in Fig 6.10(b). The obtained 90% C.L. upper limit is 4.87 events or 7.67×10^{-3} events/day/ton. Therefore, short-lived spallation nuclei seldom or never contribute to the signals nor be candidate of 2.6 MeV peak.

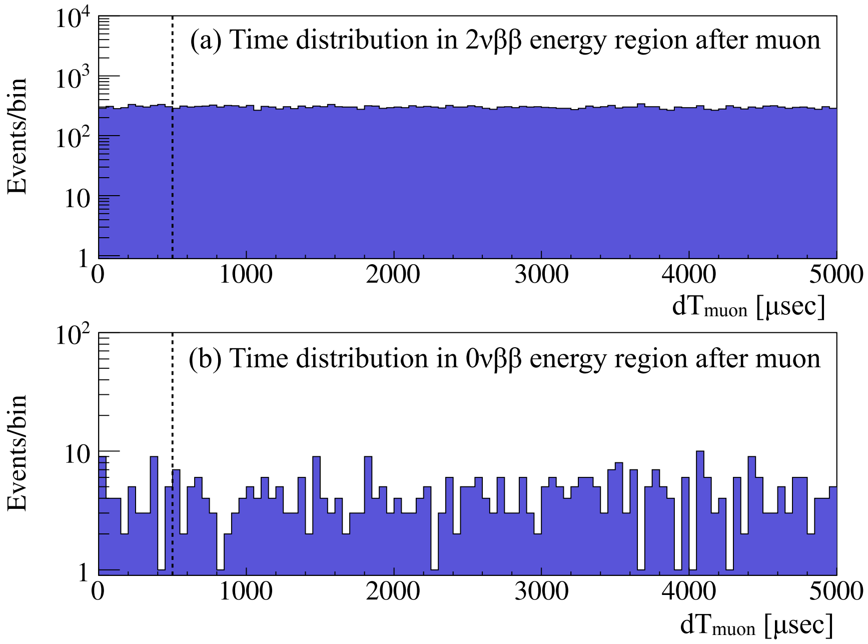

Fig 6.10: Time distribution from last muon events ($dT_{\rm muon}$). (a) shows $dT_{\rm muon}$ distribution in $2\nu\beta\beta$ energy region ($1.2 < E_{\rm vis} < 2.0$ MeV), and (b) shows that in $0\nu\beta\beta$ energy region ($2.2 < E_{\rm vis} < 3.0$ MeV).

Long-lived Products (100sec $< T_{1/2} <$ 30 days)

The cross section data evaluated from ^{136}Xe + 1 GeV proton is provided by [57]. Spallation products from ^{136}Xe whose half-lives are shorter than 30 days are studied with energy spectra scaled by the cross sections. This study is focused on the possibility that the unknown 2.6 MeV peak is provided from continuous muon spallation. If the 2.6 MeV peak is produced by muons, other nuclei which have similar A and Z, should be also produced with yields proportional to their cross sections. Candidates of 2.6 MeV event are selected from ENSDF database [13] and summarized in Table 6.9. They have a peak in energy region $2.4 < E_{\mathrm{vis}} < 2.8$ MeV. From comparison of KamLAND-Zen data with energy spectra of co-generate with 2.6 MeV peak scaled by their cross sections, it reveals that their contributions are negligible.

Table 6.9: Candidates of the unexpected background generated by spallation with xenon. They have half-lives (100sec $< T_{1/2} <$ 30 days) to explain the event rate of the background. The values of cross section are provided by [57].

	Decay Mode	Cross Section [mbarn]
$^{82\mathrm{m}}$Br	β^-	0.0583
$^{83\mathrm{m}}$Se	β^-	0.00098
$^{116\mathrm{m}}$Im	β^-	4.79
^{52}Mn	β^+/EC	0.0384
^{57}Ni	β^+/EC	not detected
^{86}Y	β^+/EC	1.298
^{82}Rb	β^+/EC	0.778
^{93}Mo	β^+/EC	3.16
^{92}Tc	β^+/EC	0.301
^{93}Tc	β^+/EC	1.23
^{100}Rh	β^+/EC	5.63
^{106}Ag	β^+/EC	8.56
^{108}In	β^+/EC	5.81
^{110}In	β^+/EC	9.87
^{115}Te	β^+/EC	2.97

6.5 Unexpected ($^{110\mathrm{m}}$Ag) Background

As mentioned in the beginning of this chapter, there is unexpected peak observed in energy spectrum. Fig 6.11 shows the energy spectrum with expected backgrounds and $2\nu\beta\beta$ decay spectrum in DS-1. There is a peak seen around 2.6 MeV in $0\nu\beta\beta$ energy region, and there is no expected background we supposed except $0\nu\beta\beta$ decay signal. The background events are uniformly distributed in Xe-LS inside IB, and the event rate seems stable during the data set. The peak is not found in KamLAND LS, outer region of IB.

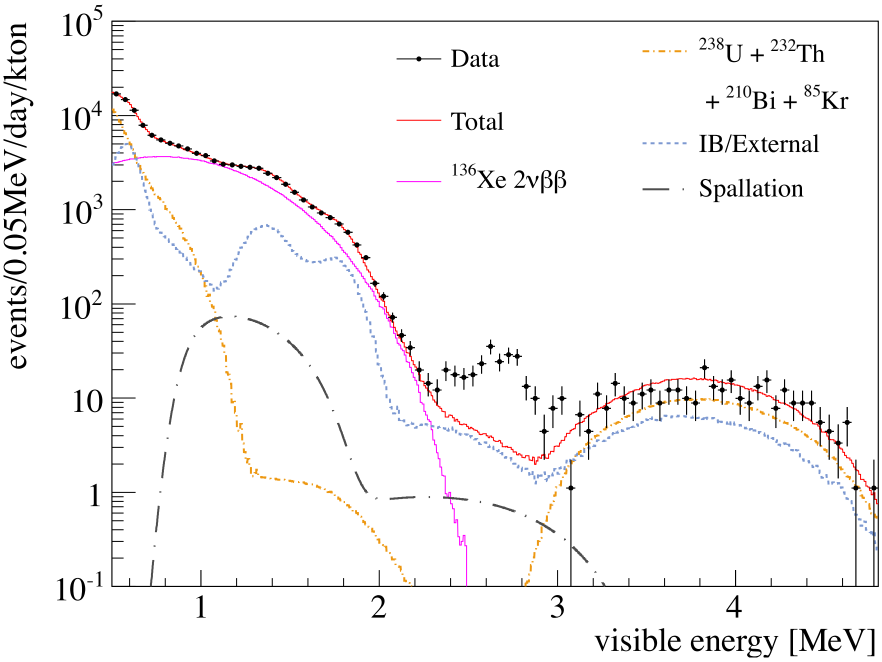

Fig 6.11: Energy spectrum with $2\nu\beta\beta$ decay signal and only expected backgrounds in DS-1. The event rates of $2\nu\beta\beta$ decay and backgrounds are fixed to the best fit by spectral fitting with fiducial radius ($R < 135$ cm).

6.5.1 Candidates of the Background

We started to search for candidates of the unexpected background in all nuclei. The event rate of the background is $\sim$ 0.2 events/day/ton, and the rate is stable in the data set (more than 100 days). $Q_{\beta\beta}$ of ^{136}Xe double beta decay is 2.467 MeV, and it is 3% lower than the observed peak. Although we tried to explain the peak with $0\nu\beta\beta$ decay signal at first, the hypothesis that the peak is contributed only from $0\nu\beta\beta$ decay without any introduction of background is denied at more than 5σ confidence level by χ^2 test with energy spectral fitting.

We came up with the solution to explain the background introduced by alternative ways. First one is the possibility of Xe-LS contamination with unexpected long-life radioactive nuclei, not may be in nature. Second way is also contamination with long-life nuclei produced by cosmogenic spallation with xenon. The amount of the background is too small to measure by another detector, and we tried to find a clue of origin of the background.

Using ENSDF (Evaluated Nuclear Structure Data File) database [13], we search for a candidate of nucleus or decay path to compensate. The procedure and condition of the search are described below. In this search, origin of the candidate is not considered.

1. Format database extracted from ENSDF
   For all tabulated decay chains in the database, basic decay information such as Q-value, life time, and the following cascade paths with energies of γ rays and their life time is extracted from ENSDF database. In the cascade decay, the effect of quenching of multiple γ rays and meta stable states are also considered.
2. Calculate energy spectrum in KamLAND detector
   Energy spectrum in visible energy in KamLAND detector is calculated for each decay

mode based on database made in the process (1.) considering alpha quenching, energy resolution ($\sim 7\%/\sqrt{E[\mathrm{MeV}]}$) and energy scale parameters.

3. Search for candidate
   The nulei or cascade decay which has a peak within $2.4 < E_{\mathrm{vis}} < 2.8$ MeV and no tail in higher energy region are selected as candidate. After that, candidates with the half-life longer than 30 days or candidates whose parent has long life-time (> 30 days) survived as final candidates.

The search narrowed candidates to only 4 isotopes summarized in Table 6.10. Their visible energy spectra are shown in Fig 6.12. ^{208}Bi and ^{88}Y have similar shape of energy spectrum, and peak of ^{60}Co is lower than the others. The spectrum of $^{110\mathrm{m}}$Ag is distinguishing shape and peak position is slightly higher than ^{208}Bi and ^{88}Y. It is helpful to distinguish which background exists in Xe-LS by their spectral shape. The half-lives of ^{208}Bi and ^{60}Co are relatively longer, and the time spectra of them should be almost flat in current data set. On the other hands, the half-lives of $^{110\mathrm{m}}$Ag and ^{88}Y are not so long, and there is a possibility to distinguish by time spectrum in data set we collected.

Table 6.10: Basic radioactive properties of $^{110\mathrm{m}}$Ag, ^{208}Bi, ^{88}Y and ^{60}Co as candidates of the unexpected background peak around 2.6 MeV. The level diagrams of them are found in Fig A.5

	Decay Mode	Q-Value [MeV]	Half-Life
$^{110\mathrm{m}}$Ag	β^-	3.01	249.79 day
^{208}Bi	EC	2.88	3.68×10^5 year
^{88}Y	EC	3.62	106.65 day
^{60}Co	β^-	2.82	5.2714 year

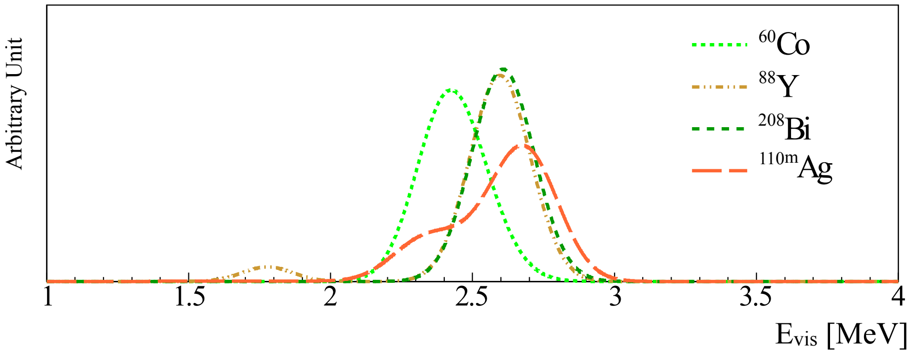

Fig 6.12: Expected energy spectra of ^{60}Co, ^{88}Y, ^{208}Bi and $^{110\mathrm{m}}$Ag in the detector by the theoretical calculation considering energy resolution. The area of each spectrum is normalized to 1.0.

As already mentioned, the event rate of the background is very low ($\sim$ 0.2 events /day/ton in Xe-LS), and it is impossible to identify the background or detect the isotope from sampling measurement. KamLAND is only detector to measure such a low rate events. Not only the background in Xe-LS, we have also difficulty to find the route of the contamination by same reason. Therefore, we conservatively introduced these 4 background candidates to the spectral fitting.

Fig 6.13 shows closeup of energy spectrum and the best fit in $0\nu\beta\beta$ energy region ($2.2 < E_{\mathrm{vis}} < 3.0$ MeV) in DS-1 (a) and DS-2 (b). The spectral fitting is computed in whole energy range ($0.5 < E_{\mathrm{vis}} < 4.8$ MeV) with signals, expected backgrounds and unexpected background candidates. The peak is dominated by $^{110\mathrm{m}}$Ag in both data sets, and the others including $0\nu\beta\beta$ decay signal is almost zero. Indicated χ^2 values are calculated with only energy spectrum (not including χ^2 from time spectrum and energy scale parameters) in $0\nu\beta\beta$ energy region ($2.2 < E_{\mathrm{vis}} < 3.0$ MeV) for each data set.

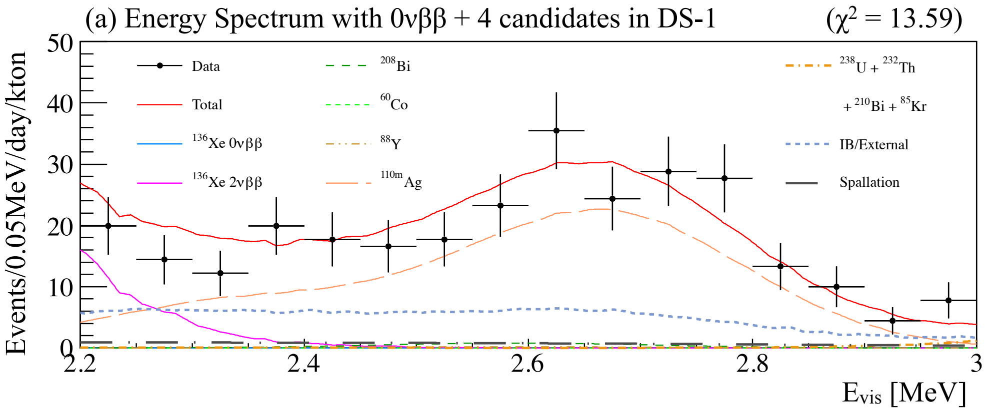

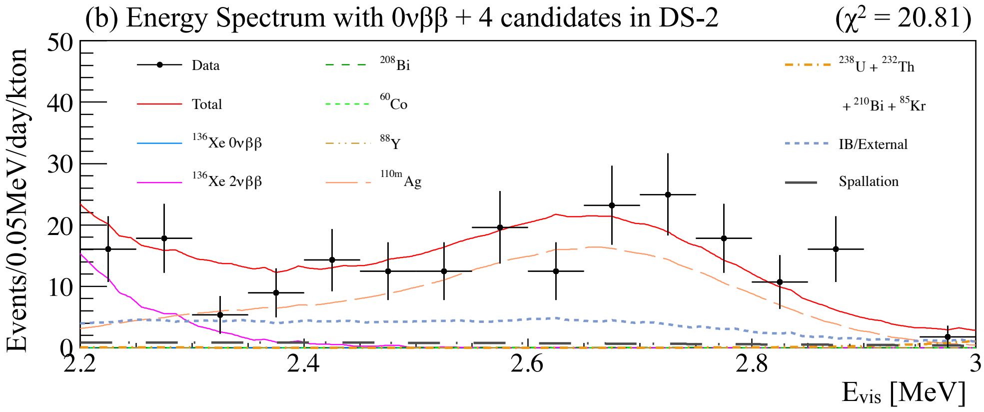

Fig 6.13: Closeup of energy spectrum with the best fit in $0\nu\beta\beta$ energy region. (a) shows the best fit with $0\nu\beta\beta$ decay signal and 4 candidates of unexpected background ($^{110\mathrm{m}}$Ag, ^{208}Bi, ^{88}Y and ^{60}Co) in DS-1, and (b) shows that in DS-2. The spectral fitting is computed with energy only (not using time spectrum) in energy range ($0.5 < E_{\mathrm{vis}} < 4.8$ MeV) , and each χ^2 is calculated in $0\nu\beta\beta$ energy region ($2.2 < E_{\mathrm{vis}} < 3.0$ MeV).

The hypothesis that $0\nu\beta\beta$ decay signal only and signal with one candidate is tested as shown in Fig 6.14 (DS-1) and Fig 6.15 (DS-2). These spectra are computed and drawn in the same manner as Fig 6.13 except the introduction of the background candidates. Both (a) shows energy spectrum with $0\nu\beta\beta$ signal only, and χ^2 value is significantly worse compared with χ^2 value with $0\nu\beta\beta$ + 4 candidates. (b) shows energy spectrum with spectral fitting with $0\nu\beta\beta$ + $^{110\mathrm{m}}$Ag. χ^2 value is similar to χ^2 value with $0\nu\beta\beta$ + 4 candidates and the best among these comparison, and it means that $^{110\mathrm{m}}$Ag is the most promising candidate of the unexpected background with energy spectral fitting. (c) and (d) shows spectrum with $0\nu\beta\beta$ + ^{208}Bi and ^{88}Y, and their χ^2 values imply that they are still potential candidates of the background. Although there is no figure of ^{60}Co, the best fit of ^{60}Co event rate is negligible small or zero because of its energy and shape, and χ^2 value and spectrum is almost same as (a) in both data set.

In this comparison, we found that $^{110\mathrm{m}}$Ag has higher potential candidate for the unexpected background around 2.6 MeV in energy spectral fitting test. In contrast, the hypothesis that only $0\nu\beta\beta$ decay signal and the hypothesis that the background source is ^{60}Co are excluded at more than 5σ. However, ^{60}Co is still embraced as the weakest candidate for conservatively estimation.

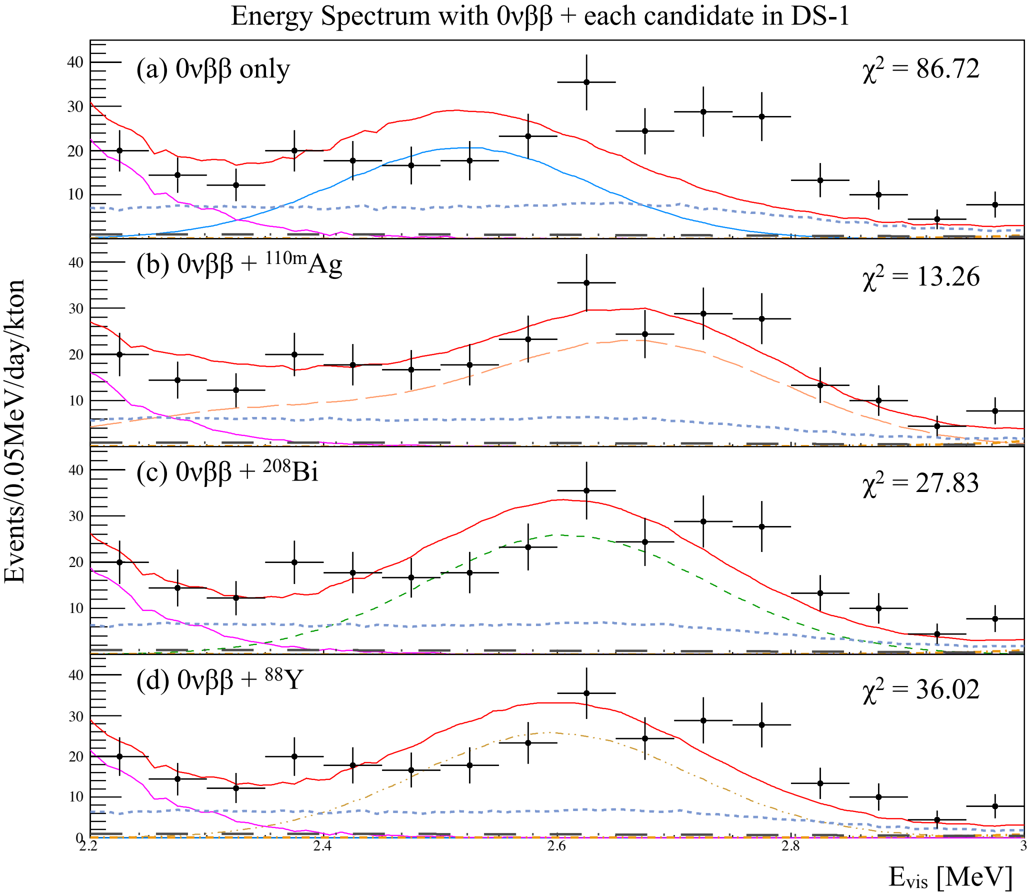

Fig 6.14: Comparison of energy spectrum and χ^2 with $0\nu\beta\beta$ decay signal and each candidate in DS-1. Each spectra are drawn in same legends as Fig 6.13. Fiducial volume selection is same as double beta decay analysis determined in section 6.6. The χ^2 values do not include penalty χ^2 from time spectrum. Each plots show energy spectra with the best fit of $0\nu\beta\beta$ decay only (a), $0\nu\beta\beta$ decay + $^{110\mathrm{m}}$Ag (b), $0\nu\beta\beta$ decay + ^{208}Bi (c) and $0\nu\beta\beta$ decay + ^{88}Y (d). The best fit of $0\nu\beta\beta$ decay + ^{60}Co results almost same as (a), because spectrum shape and energy of ^{60}Co is similar to $0\nu\beta\beta$ decay signal, and ^{60}Co rate is minimized.

6.5.2 $^{110\mathrm{m}}$Ag Background

As discussed above sections, $^{110\mathrm{m}}$Ag is the most powerful candidate to explain the background contribution in $0\nu\beta\beta$ energy region. The event distribution, time variation and the route of contamination are considered in this section.

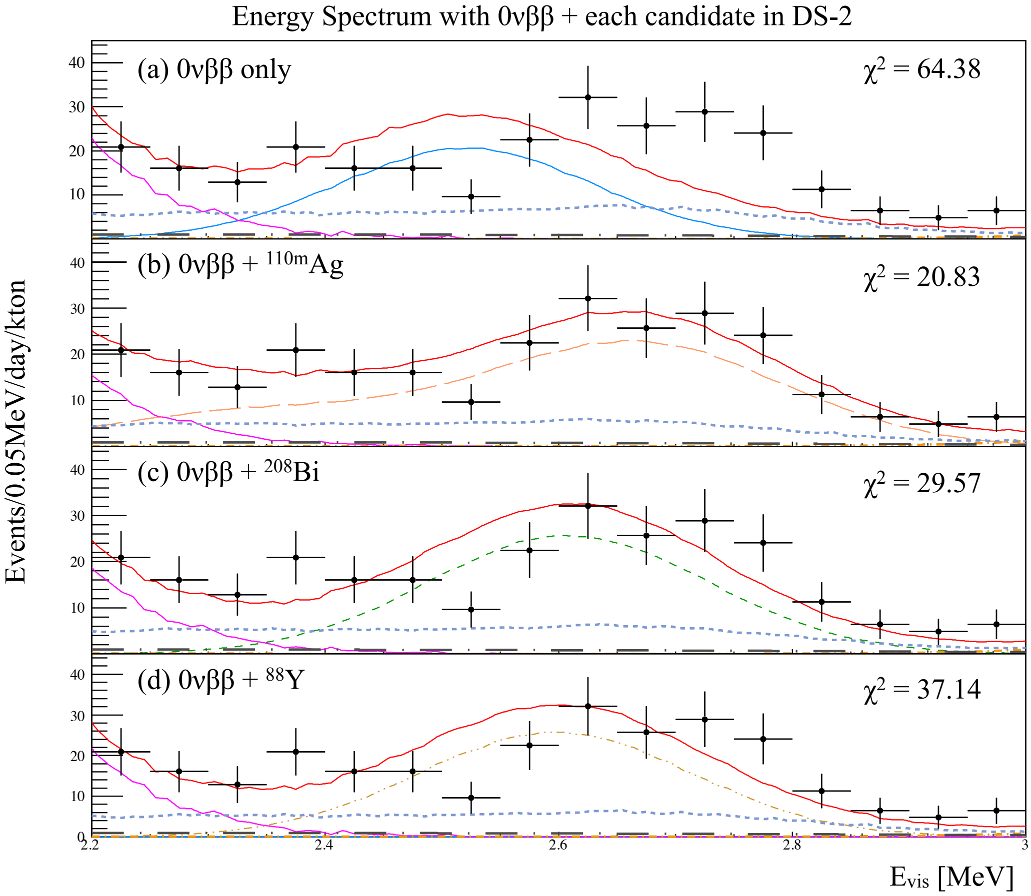

Fig 6.15: Comparison of energy spectrum and χ^2 with $0\nu\beta\beta$ decay signal and each candidate in DS-2. The description is in common with Fig 6.14 except data set.

$^{110\mathrm{m}}$Ag **Distribution**

The vertex distribution of $^{110\mathrm{m}}$Ag (assuming all single events in $0\nu\beta\beta$ energy region) is shown in Fig 6.16(a). The events seem to be uniformly distributed in fiducial volume indicated with red dot-dashed line. On the other hands, the concentration of $^{110\mathrm{m}}$Ag seems higher on/in IB surface indicated with black solid line. Fig 6.16(b) shows radial distribution of the event rate estimated by the spectral fitting in each region, and the distribution indicates $^{110\mathrm{m}}$Ag contribution in/on IB surface.

$^{110\mathrm{m}}$Ag is introduced to the fitting as the external background to precisely estimate the contribution of $^{110\mathrm{m}}$Ag in/on IB surface as described in section 6.2, and the estimated event rate of $^{110\mathrm{m}}$Ag in/on IB is constrained in the final spectral fitting for double beta decay analysis.

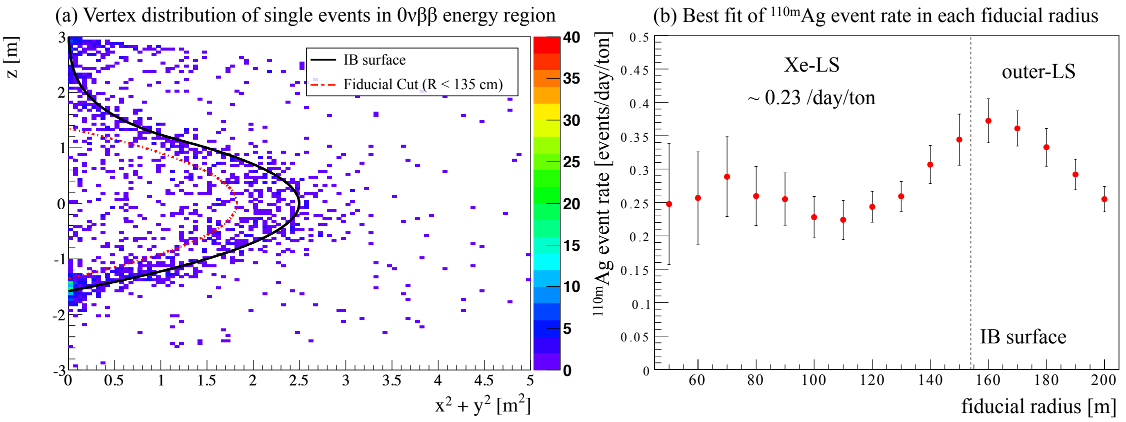
(a) Vertex distribution of single events in 0νββ energy region
(b) Best fit of $^{110\mathrm{m}}$Ag event rate in each fiducial radius

Fig 6.16: Spatial distribution of $^{110\mathrm{m}}$Ag. (a) shows vertex distribution of single events in $0\nu\beta\beta$ energy region ($2.2 < E_{\mathrm{vis}} < 3.0$ MeV). The horizontal axis is $x^2+y^2[m^2]$, and vertical axis indicates z [m] in optical coordinate in the detector. The black solid line shows the boundary of IB surface, and the red dot-dashed line indicates the fiducial radius ($R < 135$ cm). (b) shows the best fit of $^{110\mathrm{m}}$Ag event rate for each fiducial radius normalized by the volume.

Fig 6.17 shows time variation of the number of single events in $0\nu\beta\beta$ energy region ($2.2 < E_{\mathrm{vis}} < 3.0$ MeV), which exhibits a strong preference ($\chi^2 = 2.22$) for the life-time of $^{110\mathrm{m}}$Ag, if the filtration is assumed to have no effect. Allowing for the $^{110\mathrm{m}}$Ag levels between DS-1 and DS-2 to float, the estimated removal efficiency of $^{110\mathrm{m}}$Ag is $(1 \pm 19)\%$, indicating that the Xe-LS filtration was not effective in reducing the background. The fitting with half-life as free parameter results $T_{1/2} = 250.4 \pm 107$ [days], and it is consistent with half-life of $^{110\mathrm{m}}$Ag.

The Origin of $^{110\mathrm{m}}$Ag

$^{110\mathrm{m}}$Ag which is artificial isotope, was detected in soil sample in Sendai (Miyagi Prefecture) where IB has been fabricated in April 2011, 1 month after from the accident of Fukushima-I nuclear reactor. The fall-out from Fukushima-I is possible source to contaminate the IB surface. $^{110\mathrm{m}}$Ag is distributed in/on IB as described above same as ^{134}Cs and ^{137}Cs. In turn, IB installed to KamLAND detector might contaminated Xe-LS by $^{110\mathrm{m}}$Ag.

Another possible source is $^{110\mathrm{m}}$Ag generation by the cosmogenic spallation with xenon aboveground or during airborne transportation. The spallation products with xenon which have short half-lives are already discussed in section 6.4, and we considered the products with long half-lives (more than 30 days). Xenon for KamLAND-Zen was enriched in

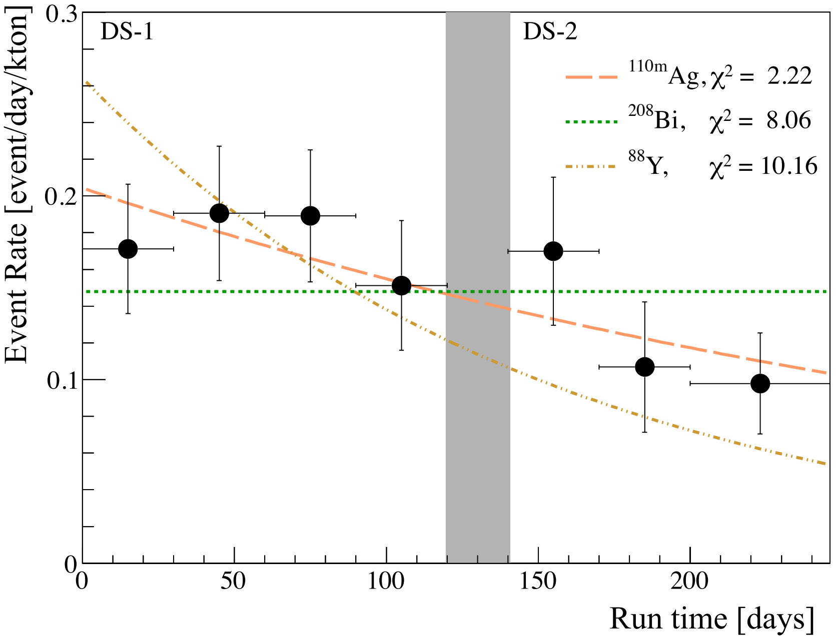

Fig 6.17: Event rate variation in the $0\nu\beta\beta$ energy region ($2.2 < E_{\mathrm{vis}} < 3.0$ MeV) after subtracting known background contributions. The three fitted curves correspond to the hypotheses that all events in the $0\nu\beta\beta$ window are from ^{110m}Ag (dashed line), ^{208}Bi (dotted line), or ^{88}Y (double-dot-dashed line). The gray band indicates the Xe-LS filtration period; no reduction in the fitted isotope is assumed for the χ^2 calculation.

Russia, and transported to Japan by air. Cosmic-ray intensity at altitude of flight is $\sim$ 100 times higher than that at aboveground level, and it might generate radioactive isotopes by the spallation reaction. The spallation products are found in other experiments like ^{57}Co, ^{54}Mn, ^{68}Ge, ^{65}Zn and ^{60}Co from the ^{76}Ge experiment [58], and ^{110m}Ag and ^{106}Ru from the ^{116}Cd experiment [59], in fact.

Enriched xenon gas ($>$ 400 kg) has been transported to the mine with small bottles ($\sim$ 20 kg / bottle) over more than 1 year, and the periods in the mine are variety depending on the bottle arrival date.

We surveyed spallation products which have long half-lives more than 30 days by checking their survivability after hundreds of days transported to the mine where the cosmic-ray intensity is suppressed to 10^{-5}. The condition of the simulation is 100 days above ground, the intensity of cosmic-ray corresponds $\sim$ 1 day trip by air craft, with cross section of ^{136}Xe + 1 GeV proton provided by [57]. The visible energy spectra after hundreds days in the mine are shown in Fig 6.18. Each plot shows energy spectra after 0 (a), 100 (b), 300 (c) and 500 (d) days in the mine. ^{110m}Ag and ^{88}Y can be seen, therefore we can say that ^{110m}Ag and ^{88}Y might be generated by the spallation reaction with xenon and survive after hundreds days in the mine.

6.5.3 Summary of Unexpected Background

We have gradually revealed the unknown and unexpected background with longer data set. ^{110m}Ag is the most probable candidate of the background with the energy spectrum, time variation and the route into the detector. However, the others are still potential candidates and we introduced all of them into the double beta decay analysis conservatively. The summary of our survey for four candidates is shown in Table 6.11.

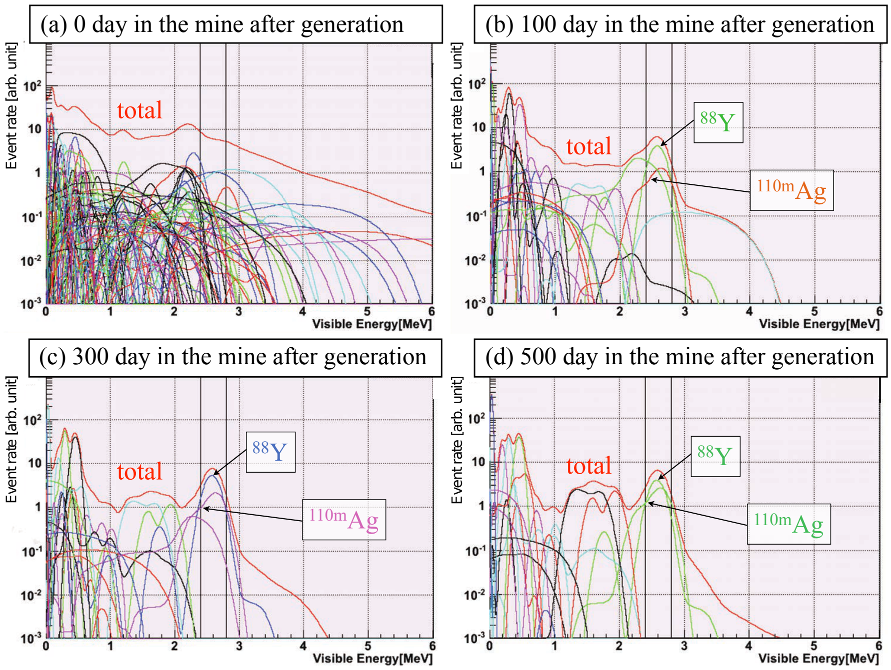

Fig 6.18: Energy spectra of survived isotopes after each period from their generations by spallation. Spectra of ^{110m}Ag and ^{88}Y are clearly seen after 100 days and later.

Table 6.11: Summary of background candidates (^{110m}Ag, ^{208}Bi, ^{88}Y and ^{60}Co). "preferable" means the best *chi*^{2} among 4 candidates, "acceptable" is consistent with the best and "excluded" is the worst χ^2 to be denied at high confidence level.

	Energy (Shape)	Time Variation	Route
^{110m}Ag	preferable	preferable	fall-out / spallation
^{208}Bi	acceptable	acceptable	unexpected
^{88}Y	acceptable	acceptable	spallation
^{60}Co	excluded	acceptable	unexpected

6.6 Fiducial Volume Decision

The fiducial volume selection for the past analysis of double beta decay was $R < 120$ cm to avoid the interfusion of the external backgrounds such as ^{134}Cs. The primary target of this work is $0\nu\beta\beta$ decay not $2\nu\beta\beta$ decay, to maximize the sensitivity for $0\nu\beta\beta$ decay signal, we tried to optimize the fiducial volume selection.

6.6.1 Fiducial Volume Enlargement

To test the sensitivity for $0\nu\beta\beta$ decay, an ensemble of experiments based on the best fit backgrounds spectrum in DS-1 (112 days) is generated with Toy Monte Carlo simulation. The lower limit of $0\nu\beta\beta$ decay half-lives at 90% C.L. are calculated with each simulated data in the same manner of spectral fitting explained in chapter 7. The probabilities of the limits which are obtained with fiducial volume ($R < 120$ cm) is shown in Fig 6.19(a), and the sensitivity is defined as center value, in other words, 50% probability. For example, Fig 6.19(a) indicates that the sensitivity of fiducial radius $R < 120$ cm is 4.7×10^{24} years. For each fiducial radius ($110 \leq R \leq 155$ cm in every 5 cm), the sensitivity is computed in the same way, and the result of sensitivity dependency with fiducial radius is shown in Fig 6.19(b).

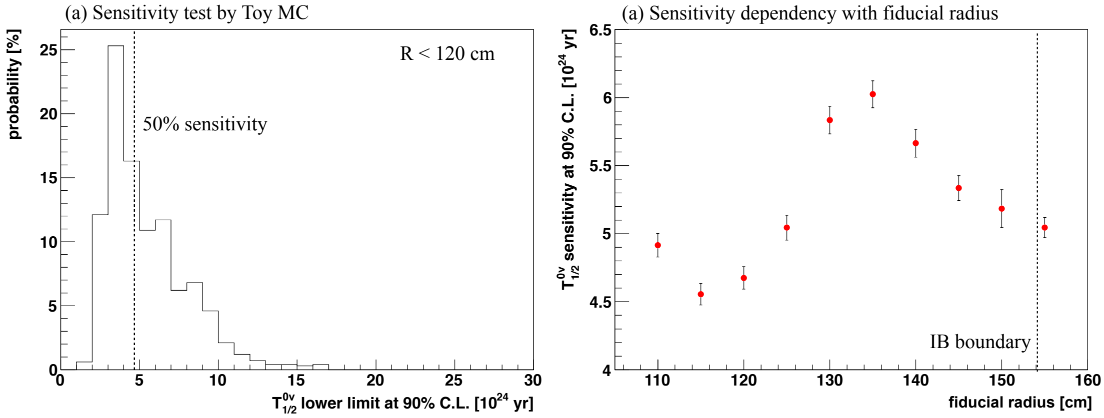

Fig 6.19: Sensitivity for $0\nu\beta\beta$ decay half-life and sensitivity estimation with fiducial radius. (a) shows the probability that we get the lower limit of $0\nu\beta\beta$ decay half-lives in x-axis for the case that fiducial radius is 120 cm. The sensitivity is defined as 50% probability in each fiducial radius, and the expected sensitivities are indicated in (b). The fiducial radius to derive the most high sensitivity is 135 cm.

The fiducial radius which maximizes the sensitivity for $0\nu\beta\beta$ decay half-life is 135 cm as indicated in Fig 6.19(b), and we decided to apply the fiducial radius of 135 cm. The fiducial volume with ($R < 135$ cm, 10.3 m^3) is 1.42 times enlarged compared with ($R < 120$ cm, 7.24 m^3), and the sensitivity is 1.38 times improved although the higher sensitivity does not always lead the better result.

6.6.2 Inlet Cut

In DS-2, there are teflon tube and the inlet part to input / output LS installed in IB for the filtration campaign. The picture of teflon tube and inlet part is shown in Fig 6.20, and the there is joint portion made of SUS inside inlet part for the connection. LS flows to horizontal directions at inlet part not to make vertical convection in IB because the filling of LS is operated by the pile-up of LS layers. The joint portion abundantly include the radioactive impurities because of the material (stainless steel, SUS), and they are potential backgrounds for $0\nu\beta\beta$ decay. Same as external background, ^{214}Bi decay induced from ^{238}U decay chain in natural and ^{208}Tl decay induced from ^{232}Th decay chain in natural make background spectra in $0\nu\beta\beta$ energy region. In addition, ^{60}Co is also included in SUS joints, and it is high potential background for $0\nu\beta\beta$ decay to be considered.

Fig 6.21(a) shows vertex distribution of single events in $0\nu\beta\beta$ energy region ($2.2 < E_{\rm vis} < 3.0$ MeV). The black solid line indicates the boundary of IB, the red dot-dashed line indicates the boundary of fiducial volume ($R < 135$ cm). The blue dashed line indicates 120 cm radius sphere from inlet part (defined as $dR_{\rm inlet}$), and we can find a concentration of background events there. The position of the inlet part is defined as Fig 6.21(b), by event distribution in each coordinate fitted with gaussian shape distribution. To reject the background contribution from inlet part, volume cut is introduced, named as "Inlet Cut".

Fig 6.20: Picture of teflon tube and inlet part. The teflon tube is connected to inlet part with joint portion made of stainless steel (SUS). The directions of LS flow is horizontal not to make vertical convection in IB because the filling is operated by pile-up of LS layers.

The energy spectrum of single events around inlet part ($dR_{\mathrm{inlet}} < 70$ cm) is shown in Fig 6.22(a), The spectral fitting is computed with MC spectra of $2\nu\beta\beta$ decay, ^{134}Cs from IB bottom and backgrounds come from SUS joint inside inlet part (^{214}Bi, ^{60}Co and ^{208}Tl). The event rates from inlet part are estimated from the fitting, corresponding to 12.6 ± 4.59, 30.0 ± 1.39 and 21.6 ± 0.756 evens/day for ^{214}Bi, ^{60}Co and ^{208}Tl, respectively. Fig 6.22(b) shows dR_{inlet} distribution in $0\nu\beta\beta$ energy region ($2.2 < E_{\mathrm{vis}} < 3.0$ MeV) with estimated events rates with energy spectrum in Fig 6.22(a). We decided the inlet cut criteri as $dR_{\mathrm{inlet}} > 120$ cm to reject background events, and the rejection efficiency is 99.5% calculated with the MC simulation spectra. The expected events observed beyond inlet cut is less than the external background event from IB.

6.6.3 Tube Cut

In addition to the inlet part, we should consider the background contribution from connected tube. The tube is made of teflon, 3/4 inch diameter, 1.6 mm thickness of teflon and $\sim$ 15 m length. The tube was washed by circulation of ethanol with filter for inside and outside tube using large pipe line before installation, and the mass of the tube is considerably smaller than the inlet part. We checked ρ $(= \sqrt{x^2 + y^2})$ distribution to estimate event rates around the teflon tube. Fig 6.23(a) shows ρ distribution in $0\nu\beta\beta$ energy region ($2.2 < E_{\mathrm{vis}} < 3.0$ MeV) after applying inlet cut as determined in section 6.6.2, and we found no clear background events distributed around teflon tube. In the other energy regions, we could not see any significant background around the teflon tube, therefore we estimated the upper limit of event rate for ^{214}Bi and ^{208}Tl which are potential background sources for $0\nu\beta\beta$ decay. Fig 6.23(b) shows the 90% C.L. upper limit of ^{214}Bi event rate calculated with Feldman-Cousins technique for each ρ cut indicated in horizontal axis. The estimation with Feldman-Cousins technique is computed by assuming all events

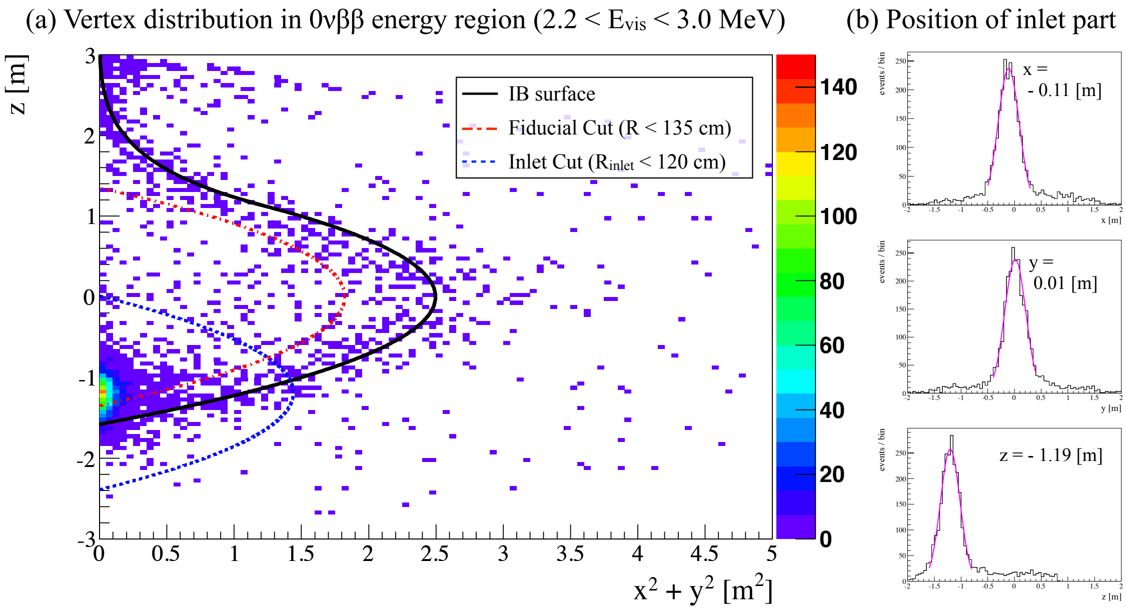

Fig 6.21: Vertex distribution of single events in $0\nu\beta\beta$ energy region and the positon of inlet part. In (a), the horizontal axis is $x^2 + y^2 [m^2]$, and vertical axis indicates z [m] in optical coordinate in the detector. The black solid line shows the boundary of IB surface, and the red dot-dashed line indicates the fiducial radius ($R < 135$ cm). The blue dashed line indicates 120 cm radius sphere from inlet part. Single events in $0\nu\beta\beta$ energy region ($2.2 < E_{\mathrm{vis}} < 3.0$ MeV) are concentrated around inlet part near bottom part of IB in (a). The position of inlet part is defined as plots in (b), by fitting with gaussian shape distribution.

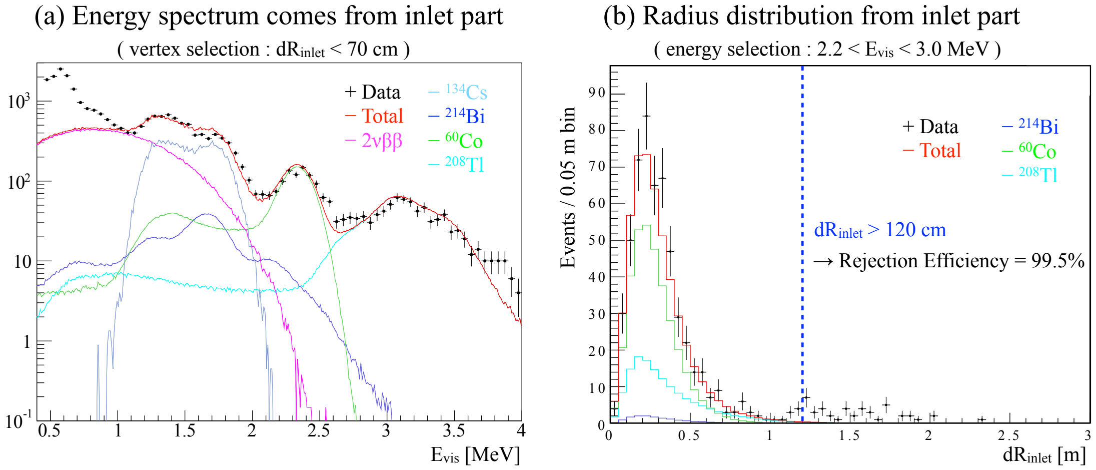

Fig 6.22: Energy spectrum around inlet part and radius distribution from inlet part. The energy spectral fitting around the inlet part ($dR_{\mathrm{inlet}} < 70$ cm) with $2\nu\beta\beta$, ^{134}Cs, ^{214}Bi, ^{60}Co and ^{208}Tl is shown in (a). The background rates contributed by the inlet part is estimated the fitting, and dR_{inlet} distribution in $0\nu\beta\beta$ energy region based on the estimation from (a) is shown in (b). The inlet cut is decided to be $dR_{\mathrm{inlet}} > 120$ cm, and the background rejection efficiency is 99.5%.

in $2.2 < E_{\mathrm{vis}} < 3.0$ MeV are ^{214}Bi, and all events in $3.0 < E_{\mathrm{vis}} < 5.0$ MeV are ^{208}Tl, conservatively. The ρ cut condition is decided to make the upper limit of ^{214}Bi and ^{208}Tl event rates less than 10 events/day/kton which corresponds $\sim 1/20$ of $^{110\mathrm{m}}$Ag background rate in Xe-LS. The condition is $dL_{\mathrm{tube}} > 20$ cm as the tube cut, where dL_{tube} is the distance from tube.

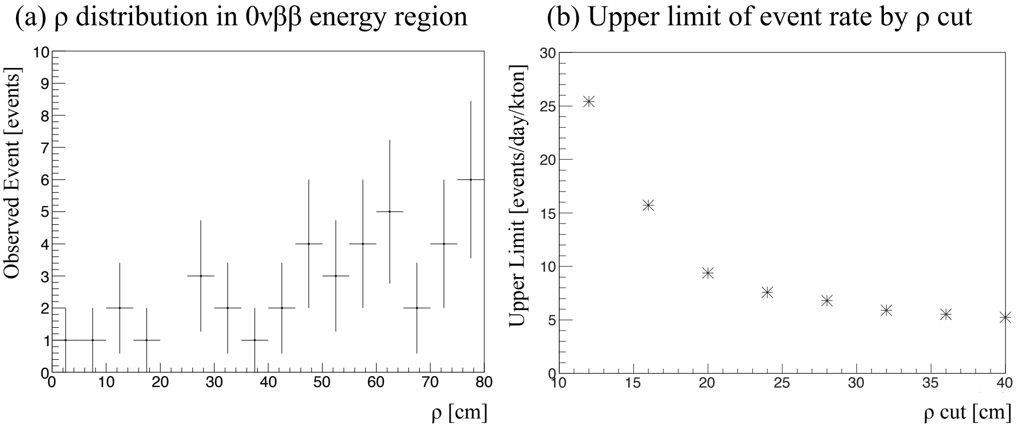

Fig 6.23: ρ distribution and the estimation of 90% C.L. upper limit of single event rate in $0\nu\beta\beta$ energy region. (a) shows ρ distribution of single events in $0\nu\beta\beta$ energy region ($2.2 < E_{\mathrm{vis}} < 3.0$ MeV). The 90% C.L. upper limit of ^{214}Bi event rates estimated with Feldman-Cousins technique is shown in (b) for each ρ cut conditions.

6.6.4 Summary of Fiducial Volume Selection

The different fiducial volume selection is applied for DS-1 and DS-2 because teflon tube and inlet part which are potential background sources for $0\nu\beta\beta$ decay signal are installed in DS-2. The diagram of fiducial volume selection is shown in Fig 6.24, and cut condition is summarized in Table 6.12. The fiducial volume is 1.4 times enlarged from the past analysis ($R < 120$ cm, 7.24 m^3) in DS-1 (10.3 m^3), and almost same in DS-2 (7.11 m^3). Although the fiducial volume becomes smaller in DS-2, we succeed to reject the background contribution from inlet part and teflon tube. These conditions are applied for double beta decay analysis.

Table 6.12: Summary of fiducial volume cut condition. Only spherical cut is applied for DS-1, and inlet cut and tube cut are additionally applied for DS-2. The fiducial volume is 1.4 times enlarged from the past analysis ($R < 120$ cm, 7.24 m^3) in DS-1, and almost same in DS-2.

Data Set	Fiducial Radius	Inlet Cut	Tube Cut	Fiducial Volume
DS-1	$R < 135$ cm	-	-	10.3 m^3
DS-2	$R < 135$ cm	$dR_{\mathrm{inlet}} > 120$ cm	$dL_{\mathrm{tube}} > 20$ cm	7.11 m^3

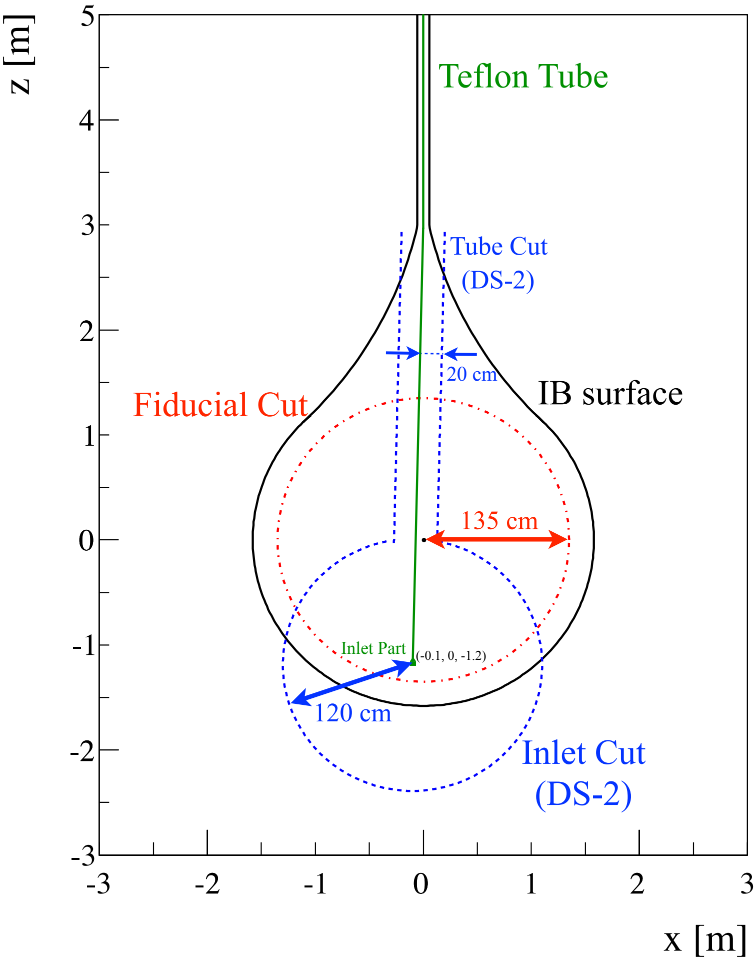

Fig 6.24: Diagram for fiducial volume selection. The horizontal and vertical axises indicate optical coordinates in the detector, x and z [m]. The black solid line shows the boundary of IB surface, and the red dot-dashed line indicates fiducial radius (R < 135 cm). The blue dashed line indicates volume cut for inlet part (dR_{inlet} > 120 cm) and teflon tube (dL_{tube} > 20 cm) in DS-2.

Chapter 7

Double Beta Decay Analysis

This chapter summarizes double beta decay analysis of ^{136}Xe from the first phase of KamLAND-Zen experiment.

7.1 Exposure

The exposure is defined as the product of mass of the target and livetime, and the typical unit of exposure for double beta decay is [kg-year] of ^{136}Xe. The exposure is directly converted to the number of the nuclei, and used for the calculation of half-life of double beta decay. The precise estimation of xenon mass and livetime is absolutely imperative for the measurement of double beta decay.

7.1.1 Xe Mass Estimation

It is not easy to measure the mass of Xe because it is a noble gas and some Xe gas can remain everywhere it goes through. We have calculated the Xe mass in inner balloon in two ways.

The first way is subtraction of the total leftover Xe mass from the initial mass. The initial mass is measured by a weighing scale bottle by bottle before opening the bottle. The total initial mass is 409.1 kg and the uncertainty is less than 0.1 kg. However, the mass of leftover Xe is measured by the same weighing scale with empty bottle which has poor uncertainty of ± 0.5 kg. The mass of Xe remaining in Xe system is 6.0 ± 0.5 kg, and the mass of collected Xe gas including nitrogen from LS25 tank to the storage by nitrogen purge is 103.5 ± 0.5 kg. The N_2 concentration in the storage is measured in three ways, $55 \pm 5\%$ by Gas-Chromatography (GC) measurement in IPMU, $47 \pm 5\%$ by A. Kozlov's measurement, and $50.7 \pm 1.25\%$ by the Hokusan company measurement. We employed these three measurement with weighted average, and the mass of collected Xe is calculated, corresponding to 85.3 ± 0.4 (Collected Gas Error) ± 0.7 (N_2 Concentration Error) kg. The mass of Xe remaining in LS25 tank calculated with GC measurement of remaining LS is 1.87 ± 0.5 kg. Finally, the mass in the IB is calculated and it is 315.9 ± 1.09 kg, and the summary of Xe mass subtraction is shown in Fig 7.1.

The second way is calculation with GC measurement of Xe-LS sampled during the circulation phase of Xe-LS before the start of DS-1. The measurement provides 2.52 ± 0.07 wt% of Xe weight fraction in Xe-LS, and this corresponds to 325.95 ± 9.65 kg of Xe mass in the IB considering LS volume uncertainty ($16.58 \pm 0.17 m^3$).

With these two calculations, Xe mass in inner balloon for DS-1 is estimated as 315.99 ± 1.08 kg with calculation of weighted average. For DS-2, 4.3 ± 0.5 kg of Xe is added to Xe-LS during filtration campaign (3.5.3), and Xe mass is estimated as 320.30 ± 1.19 kg with weighted average of the value for DS-1 and additional mass.

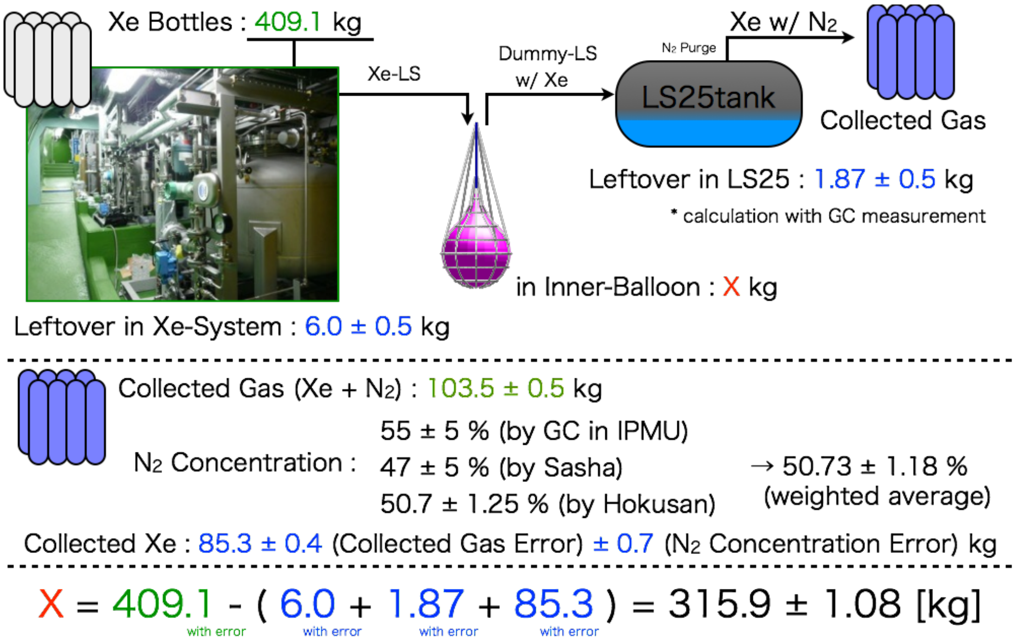

Fig 7.1: Summary of Xe mass subtraction. The Xe mass in Inner Balloon is X, is calculated with subtraction of remaining Xe mass from the initial mass.

The uncertainties of ^{136}Xe amount mainly come from the concentration of enriched Xe in Xe-LS and the enrichment factor of ^{136}Xe. The uncertainties of the concentration are estimated to be 0.34% for DS-1 and 0.37% for DS-2 as discussed above. The measurement of enrichment factor (0.9093 ± 0.0005) has 0.05% of the uncertainty.

Number of ^{136}Xe Target

The number of ^{136}Xe target must be evaluated to calculate the half-life of ^{136}Xe double beta decay. Assuming the uniform distribution of ^{136}Xe in IB, Xe mass in the fiducial volume is calculated to be 197.4 kg for DS-1 (1.35 m radius) and 141.3 kg for DS-2 (1.35 m radius and inlet/tube cut). The number of ^{136}Xe nuclei is calculated with Avogadro's number ($N_A = 6.022045 \times 10^{23}$ [atom/mol]), measured mass number of enriched Xe gas ($M_{Xe} = 135.722$ [g/mol]) and enrichment factor of ^{136}Xe in enriched Xe gas (0.9093). The numbers are estimated to be 7.96×10^{26} for DS-1 and 5.70×10^{26} for DS-2.

7.1.2 Livetime Calculation

The livetime should be accurately calculated to measure a half-life of double beta decay. Each events acquired by KamFEE come with 40 MHz clock timestamps which are synchronized to the GPS clock via the trigger circuit. Therefore, we can derive the precise time information for each physics event with the timestamps. KamFEE, however, has dead time which means there are moment when it is not sensitive to detect single event such as double beta decay because of electronics problem or physical design of the detector. To calculate the livetime correctly, there is need to consider the deadtime.

As explained in section 5.1, the data for double beta decay analysis is divided to two periods labeled DS-1 and DS-2. DS-1 corresponds to run11000-11212 which were taken from October 12th, 2011 to February 9th, 2012, and DS-2 corresponds to run11254-11409 which were taken from February 18th to June 14th in 2012. The livetime for DS-1 and DS-2 are 112.3 days and 101.1 days, which are calculated in following procedure.

The livetime is defined as sensitive period for the detector to observe physics events, and the condition of the detector should be normal. The condition of each run is classified with the situation of the detector, operation and data taking settings by run grade ($0 \sim 10$). Only physics runs with normal condition (good run and half-bad run) are selected for the analysis processes in this work. The other runs are conservatively eliminated to avoid additional uncertainties from them. Each run is typically changed once a day, and also changed before and after the activity related detector condition or data taking.

The livetime is calculated with run time, dead time and veto time. Run time is the period between the first event and the last event in the run, and calculated for each run. Typically, run time is $\sim$ 24 hours except when there are problems or activities. Dead time consists of following four types of the periods in this work.

- Bad period
  Period of run satisfy the conditions of bad run. Typically, a trouble on HV supply in some crate leads to the bad period because trigger efficiency and the gain becomes worse.
- Trigger disable period
  The trigger module sometimes becomes busy and disables during data taking. When trigger module is disabled and recovered, the disabled flag is recorded in the data. The periods that trigger module could not work are regarded as dead time and are calculated with the flags.
- Trigger dead time
  The trigger dead period is caused by the broken data packet by network problem. That is tagged by the large time intervals ($>$ 100 msec) between each history events.
- Noisy period
  The multiple noise events are usually coming within 150 μsec after muons because of the ringing on FEE baseline. If there are no muons within 150 μsec before a cluster of noise events, there is a possibility that a muon was missed because of an unknown deadtime. Missing muons are tagged by multiple noise events preceded by no muons within 1 msec, and this period is conservatively taken to be deadtime. Another method, that the missing muon is tagged by missing waveform, i.e. Nhit (number of reconstructed waveform) $<$ NsumMax.

Veto time is introduced to reject the background events. In the double beta decay analysis, vetoes are categorized to following three selections.

- Muon veto
  Cosmic muons induce shower of events in the detector, and veto is performed to reject them. Events in the whole volume are vetoed in 2 msec after every muon events. The veto time is $\sim$ 0.07 % of run time estimated by the muon rate (0.35 Hz).
- Delayed coincidence veto
  Delayed events are tagged by certain correlation of time, space and energy with prompt events. They are vetoed for the delayed coincidence events of anti-neutrino - neutron and ^{214}Bi - ^{214}Po. The length of the veto gate is 1 msec for anti-neutrino events, and 3 msec for Bi-Po events. The total veto time is very small.
- 1PPS veto
  1PPS trigger forces all channels of the electronics to digitize waveform, and electronic noise is caused after the digitization. The events in 100 μsec after 1PPS triggers are vetoed, and the veto time introduced is very small (100 μsec / 1 sec = 0.01 %).

The livetime is computed with Monte Carlo (MC) method to estimate the overlap of the dead time and veto time on the time and space. Using generated events which are uniformly distributed in time and space in the fiducial volume (FV), the livetime is calculated with following equation for each run.

$$\text{livetime} = \frac{\text{number of generated events surviving in FV after applying all cut}}{\text{number of generated events in FV}} \times \text{run time}$$

The uncertainty of the livetime calculation mainly depends on the number of the generated events, which is about 10^7 events per day. The estimated uncertainty of livetime calculation is 0.003%.

The total livetimes for DS-1 and DS-2 are 112.3 days and 101.1 days. The total systematic uncertainty for livetime calculation is estimated with a quadratic sum of uncertainties of run time (8×10^{-6}%), dead time (0.0017%) and calculation (0.003%) to be 0.003%.

7.1.3 Summary of Exposure

Table 7.1 shows the summary of Xe exposure in the first phase of KamLAND-Zen experiment. The total exposure, 89.5 kg-year, is more than 3 times larger than the first result of KamLAND-Zen [33], and it is the largest exposure of double beta decay experiment in ^{136}Xe up to now.

Table 7.1: Summary of Xe exposure in the first phase of KamLAND-Zen.

	DS-1	DS-2	Total
Livetime [days]	112.3	101.1	213.4
Fiducial Xe-LS Mass [ton]	8.04	5.55	-
Xe Weight Fraction [wt%]	2.44	2.48	-
^{136}Xe Mass [kg]	178.6	124.9	-
^{136}Xe Exposure [kg-year]	54.9	34.6	89.5

7.2 Systematic Uncertainties

The systematic uncertainties are estimated in the same manner as past analysis of KamLAND, and additionally considered with xenon as target.

7.2.1 Fiducial Volume Uncertainty

The fiducial volume is decided to maximize the sensitivity of $0\nu\beta\beta$ decay as described in section 6.6. The fiducial volumes are 10.3 m^3 for DS-1 ($R <$ 135 cm), and 7.28 m^3 for DS-2 ($R <$ 135 cm, $dR_{\text{inlet}} >$ 120 cm and $L_{\text{tube}} >$ 20 cm). Whole volume of IB, measured with flow meter during Xe-LS filling, corresponds to $16.51 \pm 0.17 m^3$ including a correction for the volume of the corrugated tube which is made of not transparent material. The ratio of fiducial and whole volume is 0.624 ± 0.006 for DS-1 and 0.431 ± 0.004 for DS-2. Ideally this ratio should correspond the event ratio in fiducial volume and in whole volume. The difference between volume ratio and event ratio is employed for as uncertainty of fiducial volume.

The delayed coincidence events of ^{214}Bi - ^{214}Po are used to estimate the event ratio, because they are uniformly distributed in IB with filled Xe-LS and they are unambiguous events due to high tagging efficiency. The same data set is used for DS-1 and DS-2 both for the estimation of event ratios, corresponding to run 11000-11044 (26 days) which is the radon rich period in IB. The event ratio is calculated with the equation below.

$$\text{event ratio} = \frac{\text{number of } ^{214}\text{Bi events in FV}}{\text{number of } ^{214}\text{Bi events in IB } (R < 3 \text{ m})} \times \text{boundary correction factor}$$

The statistical error of event ratio is dominated by the number of ^{214}Bi events, and the systematic error is dominated by the estimation of external ^{214}Bi event rate from IB surface. The boundary correction factor is calculated with MC simulation. The factor is the number of ^{214}Bi events with true vertex in the FV divided by the number of ^{214}Bi events with reconstructed vertex in the FV, and the uncertainty of the factor is conservatively estimated as 100% of the deviation of the factor from 1.0. The boundary correction factors are 0.967 ± 0.0033 for DS-1 and 0.965 ± 0.0035 for DS-2. The calculated ratios and their uncertainties are summarized in Table 7.2.

Table 7.2: Event ratios with boundary correction and volume ratios for DS-1 and DS-2. The statistical errors (stat) of event ratios come from the number of ^{214}Bi events, and systematic errors mainly (syst) come from the uncertainties of external ^{214}Bi rate from IB. The uncertainties of boundary correction (corr) are conservatively evaluated as 100% error of the deviation of the factor from 1.0. The systematic uncertainties of volume ratio is caused by the volume measurement with the flow meter.

	Event Ratio with boundary correction	Volume Ratio
DS-1	$0.620 \pm 0.007(stat) \pm 0.006(syst) \pm 0.020(corr)$	$0.624 \pm 0.006(syst)$
DS-2	$0.431 \pm 0.007(stat) \pm 0.004(syst) \pm 0.015(corr)$	$0.431 \pm 0.004(syst)$

The discrepancies between event ratio and volume ratio are evaluated as the difference between each center value and statistical error, and the uncertainties are 0.11 for DS-1 and 0.008 for DS-2. The total systematic uncertainty for fiducial volume is a quadratic sum of the uncertainties of the discrepancy, the event ratio, the boundary correction factor and the volume measurement. They are 3.89% for DS-1 and 4.08% for DS-2. The surface area of fiducial volume for DS-2 is relatively larger than that for DS-1, and the uncertainty for DS-2 becomes worse because of the boundary effect. However, the uncertainties are improved from the past estimation (5.2% [33] [34]) by considering the boundary effect.

7.2.2 Summary of Systematic Uncertainties

The uncertainties from Xe are already discussed in section 7.1.1. The uncertainties of the concentration are estimated to be 0.34% for DS-1 and 0.37% for DS-2, and the uncertainty of the enrichment factor is 0.05%. The summary of the systematic uncertainties for double beta decay is shown in Table 7.3.

The total systematic uncertainties on the double beta decay half-life measurements for DS-1 (DS-2) are 3.92% (4.11%), resulting from the quadrature sum of the uncertainties in the fiducial volume (3.89% and 4.08%), enrichment level of ^{136}Xe (0.05%), Xe concentration (0.34% and 0.37%), detector energy scale (0.3%) [2], and detection efficiency (0.2%).

7.3 Spectral Fit with Time and Energy

The simultaneous fitting with time and energy spectra is independently computed for DS-1 and DS-2 to estimate the event rate of double beta decay and the other backgrounds.

Table 7.3: Summary of systematic uncertainties.

	DS-1	DS-2
Livetime [%]	0.03	
Fiducial Volume [%]	3.89	4.08
Xe Concentration [%]	0.34	0.37
^{136}Xe Enrichment [%]	0.05	
Detector Energy Scale [%]	0.3	
Detector Efficiency [%]	0.2	
Total [%]	3.92	4.11

This section shows detail of the fitting and the analysis results of double beta decay.

7.3.1 Fitting Method

Double beta decay rates and the other background rates are estimated from a likelihood fit to the binned energy spectrum between 0.5 and 4.8 MeV with 0.05 MeV bin width for each data set. The exposure of each data set is summarized in Table 7.1. The likelihood fit minimizes the quantity χ^2 (defined as equation 7.1) with 13 free parameters and 12 constrained parameters. The minimization is computed using the *Minuit* package included in *ROOT* developed and supported by *CERN* [16]. The parameters are categorized to signal event rates, background event rates and energy scale parameters, and are summarized in Table 7.4.

Table 7.4: Summary of fitting parameters with energy spectrum.

		Free Parameters	Constrained Parameters
Signal		^{136}Xe $0\nu\beta\beta$ decay ^{136}Xe $2\nu\beta\beta$ decay	-
Background	External (IB)	-	^{222}Rn-^{210}Pb ^{228}Th-^{208}Pb ^{40}K, ^{210}Bi ^{137}Cs, ^{134}Cs, ^{110m}Ag
	Internal (Xe-LS)	^{238}U-^{222}Rn ^{232}Th-^{228}Th ^{40}K, ^{210}Bi, ^{85}Kr ^{208}Bi, ^{60}Co, ^{88}Y, ^{110m}Ag	^{222}Rn-^{210}Pb ^{228}Th-^{208}Pb
	Spallation	-	^{11}C, ^{10}C
Energy Scale		-	α, k_B, r

The event rates of ^{136}Xe double beta decay are free parameters as signal. The backgrounds are categorized as the internal backgrounds in Xe-LS, the external backgrounds from IB and the spallation products in LS from cosmic muon. They are respectively mentioned in chapter 6. Two decay chains of the internal backgrounds are constrained with the estimation of the concentration in LS by the delayed coincidence tagging, and the other parameters are unconstrained. For conservative estimation, ^{208}Bi, ^{60}Co, ^{88}Y and ^{110m}Ag are fitted as candidates of unexpected peak around 2.6 MeV. The external backgrounds are constrained by the estimation with energy and radius as explained in section 6.2. The event rates of spallation products generated by cosmic muon in the detector have been measured with KamLAND [31], therefore ^{11}C and ^{10}C are constrained by that measurement. There are 3 parameters of energy scale; α is the absolute scale of the visible energy, k_B is Birks constant which characterizes the luminescence of liquid scintillator, r is ratio of scintillation and cherenkov light yield. These 3 parameters are constrained by calibration with the ^{208}Tl source and the sample of tagged ^{214}Bi events.

The χ^2 is defined as following equation.

$$\chi^2 = \chi^2_{\text{energy}} + \chi^2_{\text{time}} + \chi^2_{\text{penalty}}. \tag{7.1}$$

The quantity χ^2_{energy} is calculated using the method of goodness-of-fit with maximum likelihood [12] for binned energy spectrum. The calculation is computed in the range between $0.5 < E_{\text{vis}} < 4.8$ with 0.05 MeV (86 bin) following equations blow.

$$\chi^2_{\text{energy}} = \begin{cases} 2\sum\limits_{n=1}(n_i log\dfrac{n_i}{\nu_i} + \nu_i - n_i) & (n_i \neq 0) \\ 2\sum\limits_{n=1}(\nu_i - n_i) & (n_i = 0). \end{cases}$$

Here, n_i is the number of observed events in the i-th bin, and ν_i is the number of expected events in the i-th bin.

The quantity χ^2_{time} is introduced for the restriction in $0\nu\beta\beta$ energy region ($2.2 < E_{\text{vis}} < 3.0$ MeV) using the time spectrum of the signals and backgrounds. The shape of their time spectra should be distributed according to their lifetimes. The contribution in $0\nu\beta\beta$ energy region is dominated by ^{136}Xe $2\nu\beta\beta$ decay, ^{208}Bi, ^{60}Co, ^{88}Y, ^{110m}Ag (internal/external both) and ^{222}Rn-^{210}Pb (external). ^{208}Bi ($\tau = 7.6$ years), ^{88}Y ($\tau = 154$ days) and ^{110m}Ag ($\tau = 360$ days) have relatively shorter life-times, and the numbers of expected events for χ^2_{time} calculations are distributed following decay curves with their lifetimes. The others have much longer lifetimes, therefore numbers of expected events are uniformly distributed in the time domain. Actual calculation is computed with following equation in each run.

$$\chi^2_{\text{time}} = \begin{cases} 2\sum\limits_{j=1}(m_j log\dfrac{m_j}{\mu_j} + \mu_j - m_j) & (m_j \neq 0) \\ 2\sum\limits_{j=1}(\mu_j - m_j) & (m_j = 0), \end{cases}$$

m_j is the number of observed events in $0\nu\beta\beta$ energy region ($2.2 < E_{\text{vis}} < 3.0$ MeV) in the j-th run, and μ_j is the number of expected events in the j-th run, and M is number of runs. The number of expected events is normalized, and weighted by each parameter with each life-time.

The quantity χ^2_{penalty} is contributed from the expectation of the constrained background rates and energy scale. The constrained parameters summarized in Table 7.4 give χ^2_{penalty} with following equation.

$$\chi^2_{\text{penalty}} = \sum_{k=1}(\frac{q_{\text{obs}} - q_{\text{exp}}}{\sigma_{\text{exp}}})^2 \ ,$$

q_{obs} is the observed event rate or energy scale parameter, q_{exp} is the expected event rate or energy scale parameter, and σ_{exp} is the standard deviation of the expected event rate or energy scale parameter.

The spectral fitting is computed to minimize the χ^2 with 25 parameters, independently for DS-1 and DS-2.

7.3.2 Fitting Result

The results of spectral fitting is summarized in Table 7.5, and each energy spectrum is shown in Fig 7.2. The minimum χ^2 values are 268.9 for DS-1 and 246.5 for DS-2. The peak around 2.6 MeV is mainly contributed from $^{110\mathrm{m}}$Ag in Fig 7.2(a) and (b) both.

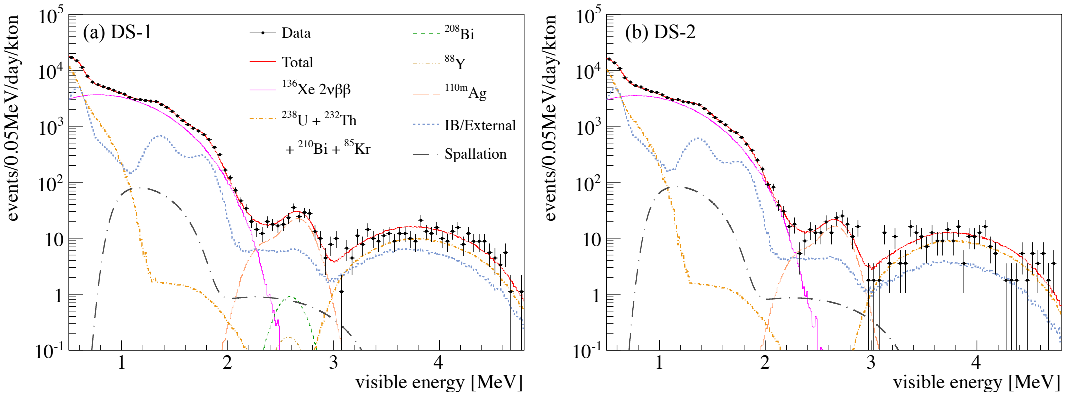

Fig 7.2: Energy spectra with best fit. Figure (a) shows spectrum in DS-1, and figure (b) shows spectrum in DS-2 with same legends. For simplicity of the display, the spectra of external backgrounds and spallation products are respectively integrated to a single spectrum.

7.3.3 Half-Life of $2\nu\beta\beta$ Decay

The energy spectrum of ^{136}Xe $2\nu\beta\beta$ decay is drawn in Fig 7.2, and the shape of the spectrum is calculated in reference to [56] The best-fit event rates in DS-1 and DS-2 correspond to 8.26×10^4 events/day/kton and 8.01×10^4 events/day/kton respectively, and are summarized in Table 7.5. With the exposure of ^{136}Xe summarized in Table 7.1, the events rates correspond the half-lives below.

$$\text{DS-1} : T^{2\nu}_{1/2} = 2.26 \pm 0.03(stat) \pm 0.09(syst) \times 10^{21}[\text{year}]$$
$$\text{DS-2} : T^{2\nu}_{1/2} = 2.37 \pm 0.05(stat) \pm 0.10(syst) \times 10^{21}[\text{year}]$$

The statistical uncertainties are estimated with the 1σ with $\Delta\chi^2$ method. The half-lives are consistent with past results from KamLAND-Zen [33] [34], and from EXO-200 [35]. However, the uncertainties become larger because of the external backgrounds coming from enlargement of the fiducial volume.

7.3.4 Half-Life of $0\nu\beta\beta$ Decay

The best fit of ^{136}Xe $0\nu\beta\beta$ decay is zero, namely the level of potential $0\nu\beta\beta$ decay is below our sensitivity. The upper limit of the event rates can be calculated by $\Delta\chi^2$ method by changing event rate of $0\nu\beta\beta$ decay. The systematic uncertainties (3.89% for DS-1 and 4.08% for DS-2) are respectively smeared to the χ^2, although the differences between with and without the smearing are very small and negligible. The $\Delta\chi^2$ curve is shown in Fig 7.3, and 90% C.L. upper limit corresponds $\Delta\chi^2 = 2.71$. The upper limits are 0.00080

Table 7.5: Results of spectral fitting. The best-fit parameters with statistical uncertainties are summarized for each data set. The unit of signal, internal backgrounds and spallation products are events/day/kton, while the unit of external backgrounds is events/day from whole IB.

	Parameters	DS-1	DS-2
Signal [events/day/kton]	$0\nu\beta\beta$ decay	0.00001 ± 0.92	0.0011 ± 1.18
	$2\nu\beta\beta$ decay	$(8.26 \pm 0.0047) \times 10^4$	$(8.01 \pm 0.0058) \times 10^4$
Internal Background [events/day/kton]	^{238}U-^{222}Rn	16.6 ± 30.8	16.2 ± 30.4
	^{222}Rn-^{210}Pb	$(3.44 \pm 0.17) \times 10^3$	$(1.94 \pm 0.096) \times 10^4$
	^{232}Th-^{228}Th	4.62 ± 11.6	4.66 ± 13.5
	^{228}Th-^{208}Pb	605 ± 51.0	558 ± 56.7
	^{40}K	0.981 ± 37.3	7.41 ± 44.4
	^{210}Bi	$(8.31 \pm 0.234) \times 10^4$	$(7.96 \pm 0.261) \times 10^4$
	^{85}Kr	$(2.30 \pm 0.0593) \times 10^5$	$(1.98 \pm 0.0722) \times 10^5$
	^{208}Bi	6.07 ± 8.58	0.155 ± 6.86
	^{60}Co	0.00175 ± 1.11	0.00337 ± 1.27
	^{88}Y	1.11 ± 3.49	0.0880 ± 4.95
	$^{110\mathrm{m}}$Ag	189 ± 25.0	139 ± 25.8
External Background [events/day]	^{222}Rn-^{210}Pb	18.7 ± 2.13	17.4 ± 2.59
	^{228}Th-^{208}Pb	30.3 ± 2.33	30.5 ± 3.15
	^{40}K	547 ± 27.0	614 ± 37.6
	^{210}Bi	$(1.66 \pm 0.0900) \times 10^3$	$(1.70 \pm 0.102) \times 10^3$
	^{137}Cs	598 ± 17.4	524 ± 18.7
	^{134}Cs	472 ± 14.9	402 ± 18.7
	$^{110\mathrm{m}}$Ag	3.42 ± 0.500	2.44 ± 0.450
Spallation Products [events/day/kton]	^{11}C	915 ± 121	962 ± 184
	^{10}C	21.6 ± 4.26	20.9 ± 4.21
Energy Scale	α	0.99	0.99
	k_B	0.08	0.10
	r	0.075	0.070

(DS-1), 0.00068 (DS-2) and 0.00044 (DS-1 + DS-2) events/day/^{136}Xe-kg, and they are converted to half-lives.

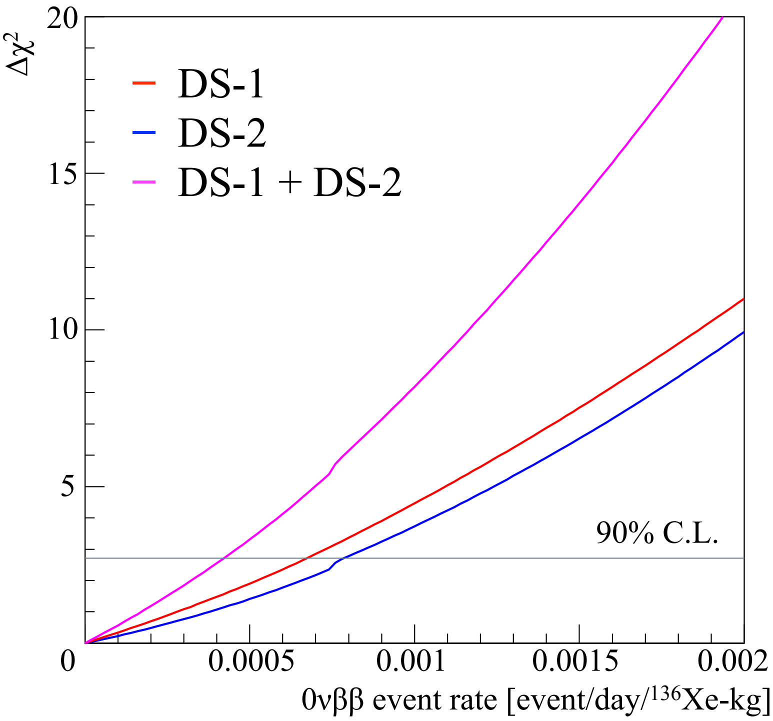

Fig 7.3: The $\Delta\chi^2$ curve with event rate of ^{136}Xe $0\nu\beta\beta$ decay. Red solid line is the calculation for DS-1, blue line is for DS-2, magenta line is combination of DS-1 and DS-2.

The 90% C.L. lower limit on the half-life of ^{136}Xe neutrinoless double beta decay derived from KamLAND-Zen are

$$\begin{aligned} \text{DS-1} : T^{0\nu}_{1/2} &> 1.05 \times 10^{25}\ \text{[year] (90\% C.L.)}, \\ \text{DS-2} : T^{0\nu}_{1/2} &> 1.24 \times 10^{25}\ \text{[year] (90\% C.L.)}, \\ \text{DS-1 + DS-2} : T^{0\nu}_{1/2} &> 1.91 \times 10^{25}\ \text{[year] (90\% C.L.)}. \end{aligned}$$

Fig 7.4 shows combined energy spectrum from DS-1 and DS-2, and the spectrum of $0\nu\beta\beta$ decay with 90% C.L. upper limit is drawn. Fig 7.5 is a closeup of Fig 7.4 for $2.2 < E_{\text{vis}} < 3.0$ MeV after subtracting known background contributions. Contributions from $^{110\text{m}}$Ag, ^{88}Y, ^{208}Bi and ^{60}Co are considered as potential background sources in the $0\nu\beta\beta$ energy region of interest.

The fit finds that the event rate in the $0\nu\beta\beta$ energy region is dominated by $^{110\text{m}}$Ag. In addition, the increased exposure time of this data set allows for improved constraints on the identity of the background due to the different lifetimes of the considered isotopes.

As supplemental information, we are able to get limit on neutrinoless double beta decay by assuming only $^{110\text{m}}$Ag as potential background source in the $0\nu\beta\beta$ energy region. The limit is slightly improved,

$$\begin{aligned} \text{DS-1} : T^{0\nu}_{1/2} &> 1.08 \times 10^{25}\ \text{[year] (90\% C.L.)}, \\ \text{DS-2} : T^{0\nu}_{1/2} &> 1.28 \times 10^{25}\ \text{[year] (90\% C.L.)}, \\ \text{DS-1 + DS-2} : T^{0\nu}_{1/2} &> 2.11 \times 10^{25}\ \text{[year] (90\% C.L.)}. \end{aligned}$$

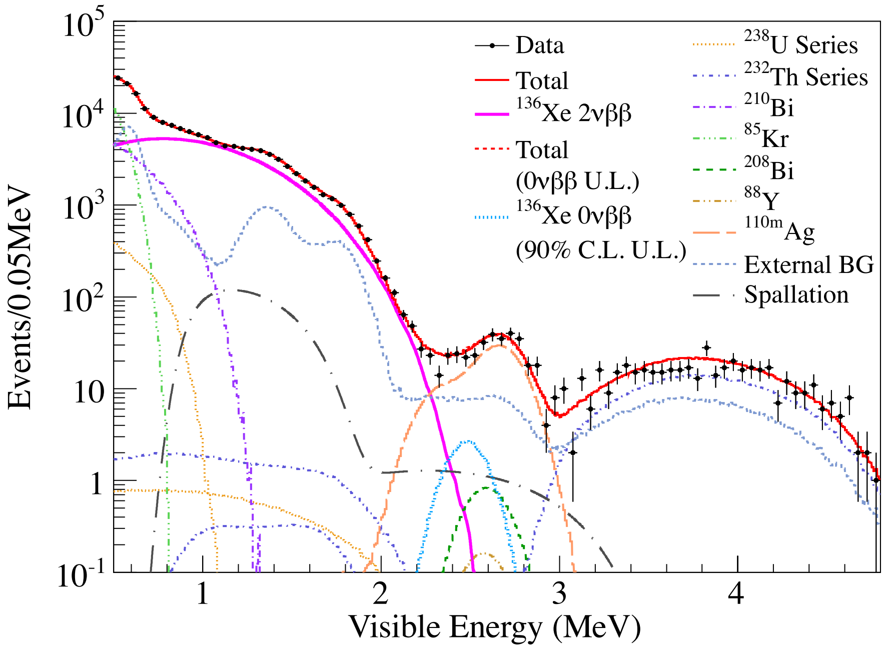

Fig 7.4: Energy spectrum of selected candidate events together with the best-fit backgrounds and $2\nu\beta\beta$ decays, and the 90% C.L. upper limit for $0\nu\beta\beta$ decays, for the combined data from DS-1 and DS-2.

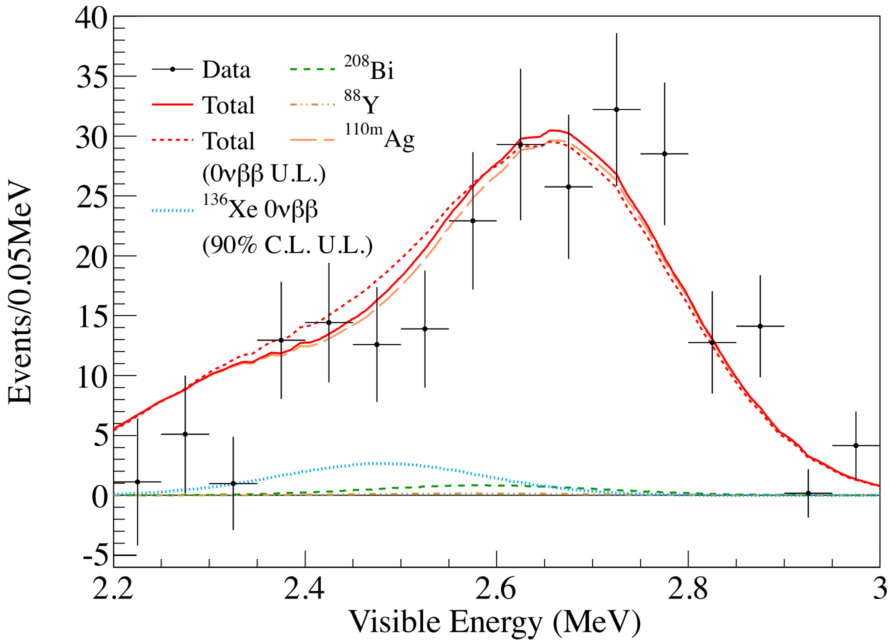

Fig 7.5: Closeup of energy spectrum for $2.2 < E_{\mathrm{vis}} < 3.0$ MeV after subtracting known background contributions. The unexpected peak at 2.6 MeV is dominated with ^{110m}Ag, and spectrum of $0\nu\beta\beta$ decay has small contribution even if 90% C.L. upper limit.

The best fit of $^{110\mathrm{m}}$Ag event rate is 192 ± 19.0 events/day/kton for DS-1 and 136 ± 20.1 events/day/kton for DS-2, and the minima of χ^2 are slightly better than that with 4 backgrounds. The hypothesis that background source is $^{110\mathrm{m}}$Ag is not still completely proved because the event rate in $0\nu\beta\beta$ energy region is too poor to measure with another detector. Therefore, we conservatively argue that our result is the limit on half-life of ^{136}Xe $0\nu\beta\beta$ decay considering 4 isotopes as potential background sources.

7.4 Combination with KamLAND-Zen and EXO-200

7.4.1 Re-analysis of EXO-200 result

In 2012, EXO-200 Collaboration reported the lower limit of ^{136}Xe $0\nu\beta\beta$ decay half-life [36]. We tried to combine the result from EXO-200 and our result from KamLAND-Zen by re-analyzing the result of EXO-200 shown in Fig 7.6. Fig 7.6 is closeup of energy spectra for $0\nu\beta\beta$ energy region, the $\Delta\chi^2$ is reproduced with the spectra and data points.

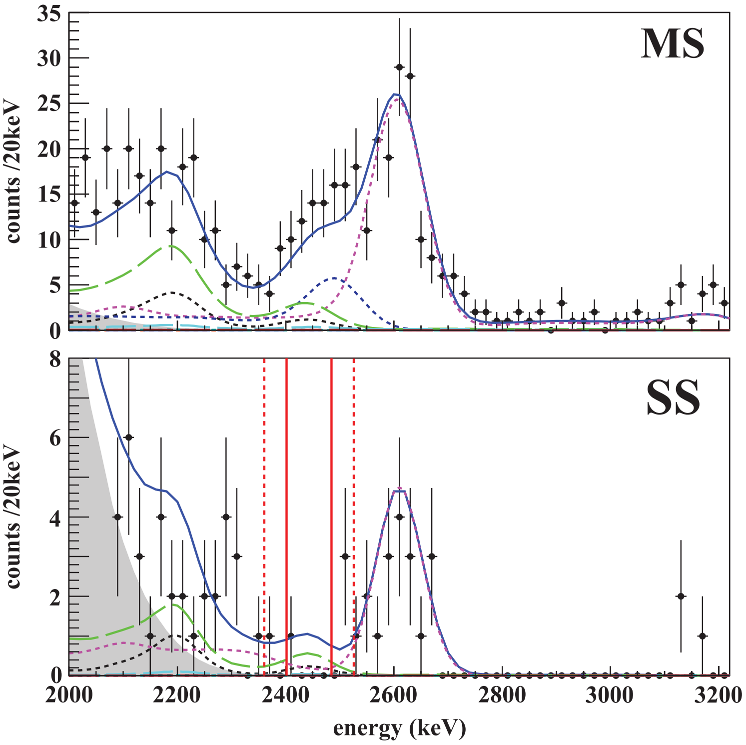

Fig 7.6: Energy spectra in the $0\nu\beta\beta$ energy region for MS (top) and SS (bottom) events from EXO-200 [36]. The best-fit line (solid blue) is shown. The background components are $2\nu\beta\beta$ (grey region), ^{222}Rn in the cryostat-lead air-gap (long-dashed green), ^{238}U in the TPC vessel (dotted black), ^{232}Th in the TPC vessel (dotted magenta), ^{214}Bi on the cathode (long-dashed cyan), ^{222}Rn outside of the field cage (dotted dark cyan) and ^{222}Rn in active xenon (long-dashed brown). The 1 (2) σ regions around $Q_{\beta\beta}$ are shown by solid (dashed) vertical red lines.

The $\Delta\chi^2$ curve of KamLAND-Zen (this work) and EXO-200 are shown in Fig 7.7, and combined $\Delta\chi^2$ with KamLAND-Zen and EXO-200 is drawn. The combined $\Delta\chi^2$ gives the improved lower limit of ^{136}Xe neutrinoless double beta decay half-life below.

$$\begin{aligned} \text{KamLAND-Zen}: T^{0\nu}_{1/2} &> 1.91 \times 10^{25}\ [\text{year}]\ (90\%\ \text{C.L.}) \\ \text{EXO-200}: T^{0\nu}_{1/2} &> 1.6 \times 10^{25}\ [\text{year}]\ (90\%\ \text{C.L.}) \\ \text{Combined}: T^{0\nu}_{1/2} &> 3.4 \times 10^{25}\ [\text{year}]\ (90\%\ \text{C.L.}) \end{aligned}$$

This combined result is the most stringent limit on the neutrinoless double beta decay in ^{136}Xe. Discussion of this result, comparison with KK-Claim [2], which is a positive observation result of ^{76}Ge neutrinoless double beta decay, and conclusions are noted in chapter 9.

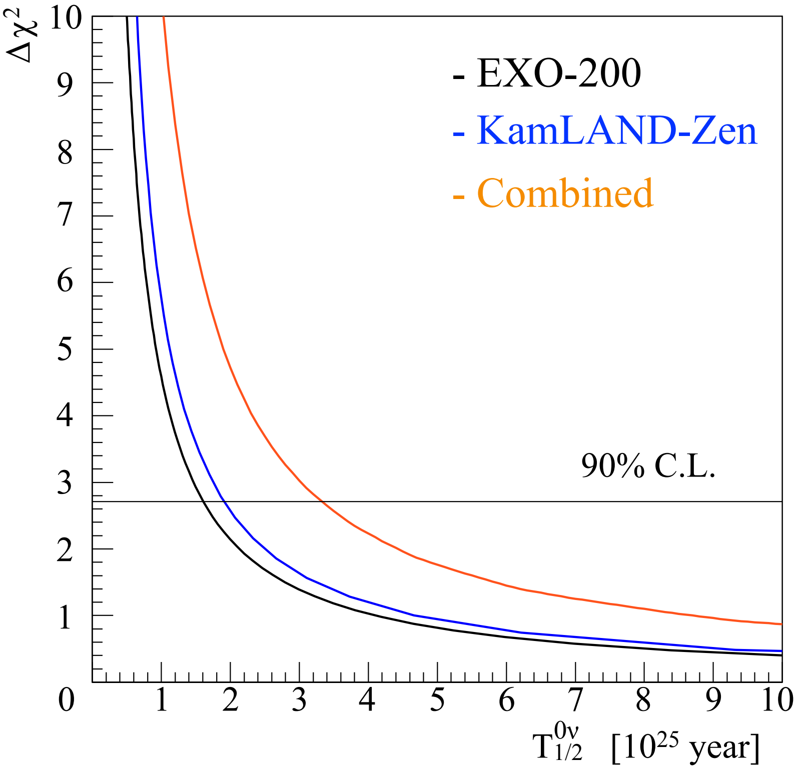

Fig 7.7: The $\Delta\chi^2$ curve with half-lives of ^{136}Xe $0\nu\beta\beta$ decay for KamLAND-Zen, EXO-200 and combined result. The reanalyzed $\Delta\chi^2$ curve of EXO-200 is drawn by black line, and $\Delta\chi^2$ curve of KamLAND-Zen (this work) is drawn by blue line.

Chapter 8

KamLAND-Zen Zero-Xe Phase

Because of the unexpected background events in $0\nu\beta\beta$ energy region, the sensitivity for $0\nu\beta\beta$ decay was worse than the original expectation before start of KamLAND-Zen. To reduce the background which is attributed to $^{110\mathrm{m}}$Ag, a purification campaign was planned. At first stage of the campaign, a massive amount ($\sim$ 320 kg) of expensive xenon gas must be preserved, we extracted xenon gas from Xe-LS in the Inner Balloon (IB). This process, called Xe extraction campaign, is described in the next section 8.1.

Not only for the purification campaign, confirmation of the existence of the background is possible by checking events in IB after Xe extraction (Zero-Xe phase). If we could find the background spectrum of $^{110\mathrm{m}}$Ag, it is further confirmation that the peak at 2.6 MeV is not $0\nu\beta\beta$ signal because there is no xenon dissolved in LS. In addition, we can say that the sources of the background should be together with the liquid scintillator not with Xe gas, and they could be potentially removed by the purification techniques such as distillation.

This chapter provides supplemental information about the background events after Xe extraction, although it is not essential for the result of double beta decay analysis presented in chapter 7. The background estimation after Xe extraction is an important cross check of the assumptions in the background model used to fit to the data described in chapter 7, and it can be reason to start purification campaign to remove the backgrounds. This chapter also presents future (or already done, but not be included in this thesis) plans for next stage of KamLAND-Zen.

8.1 Xe Extraction Campaign

Xe extraction campaign started in June 2012, and its start is terminal of DS-2. In principle, the procedure of Xe extraction is just inverse process of Xe loading. The following steps are repeatedly processed until more than 90% of xenon in IB is collected. The schematic diagram of the procedure is drawn in Fig 8.1.

1. Replacement of Xe-LS (IB $\rightarrow$ Main-Tank) with Zero-Xe-LS (Sub-Tank $\rightarrow$ IB).
2. Degassing of Xe from Xe-LS at Main-Tank (Xe-LS $\rightarrow$ Low-Xe-LS)
3. Send degassed Zero-Xe-LS to Sub-Tank from Main-Tank
4. Density adjustment of Low-Xe-LS by adding pseudocumene at Sub-Tank
5. Disposal of unnecessary amount of Low-Xe-LS to LS25-Tank from Sub-Tank

The two pipes are located in the IB since the filtration campaign on February in 2012, and they are also used for the extraction process to send/drain LS to/from IB. In the step 1, the replacement of Xe-LS and Zero-Xe-LS [1] is proceeded at same time in parallel not

---

[1] Xe degassed Xe-LS: actually few Xe may be still disolved in LS after degassing

to change the load-cell value much. After completion of the replacement, xenon gas is extracted from Xe-LS at Main-Tank with vacuum pump and LS-Trap into Reserver-Tank in the step 2. The step 3 is just sending Zero-Xe-LS to Sub-Tank. After that, the density is adjusted by adding PC in Control-Tank for the compensation of extracted Xe mass, this is step 4. The volume of LS become larger than drained one because of added PC, extra volume of LS is sent to LS25-Tank in the last step 5. After step 5, it is ready to restart step 1 again. The collected Xe at Reserver-Tank is sent to Xe-Storage by air compressor at regular intervals.

One batch (Step 1 - 5) can process ∼620 liter of LS, and it takes about 27 batches to replace whole IB volume. The collection efficiency of each batch becomes worse in the second IB volume because almost all Xe has already extracted by batches in the first IB volume.

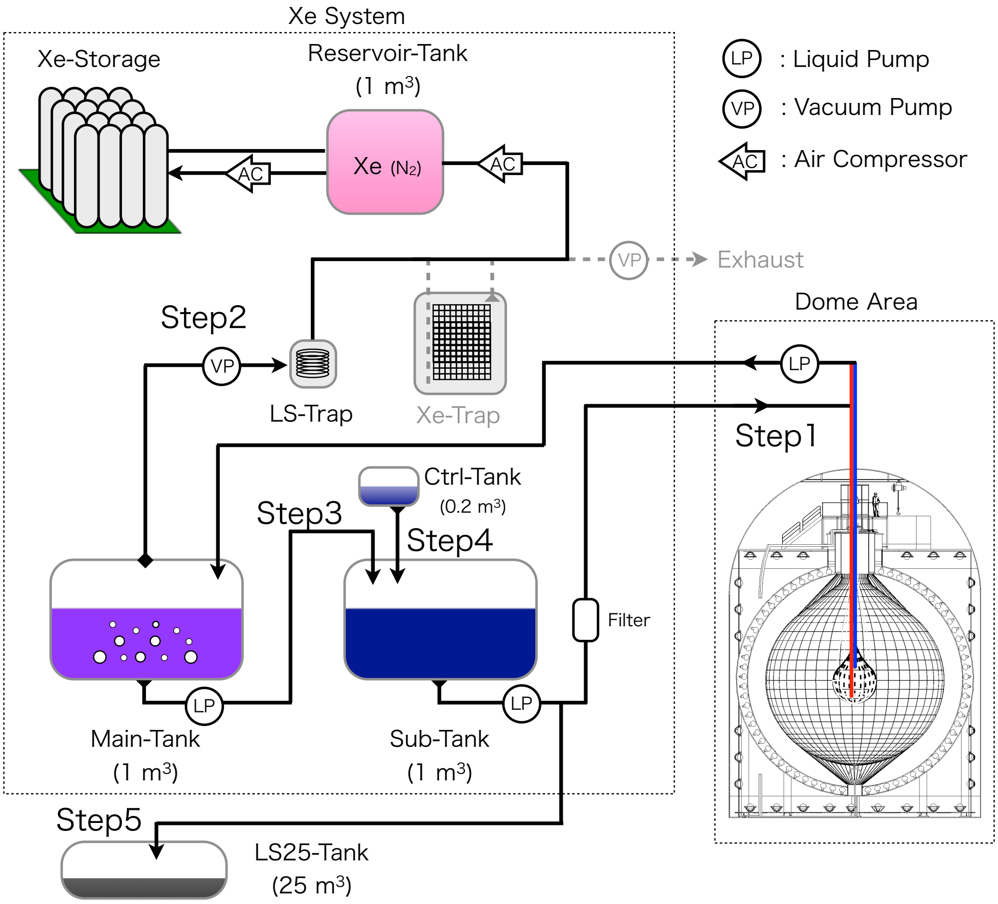

Fig 8.1: Schematic diagram of procedure in Xe extraction campaign. The apparatuses which are not used in this campaign are not drawn or drawn in gray color.

Accident on Drain-Pump

At the end of the first cycle, the radon concentration of LS in IB estimated by ^{214}Bi-Po with delayed coincidence tagging rapidly increased as shown in Fig 8.2. In Fig 8.2, it is evident that the radon event rate started to increase twice. The first increase was caused by a seal pot problem in the distillation system. This caused the exhaust line of distillation towers and tanks at the distillation area to be connected to atmosphere in the mine and thus PC supplied from the distillation area may have been contaminated with radon rich air. This problem is solved as soon as it was found, and increase of radon concentration ceased.

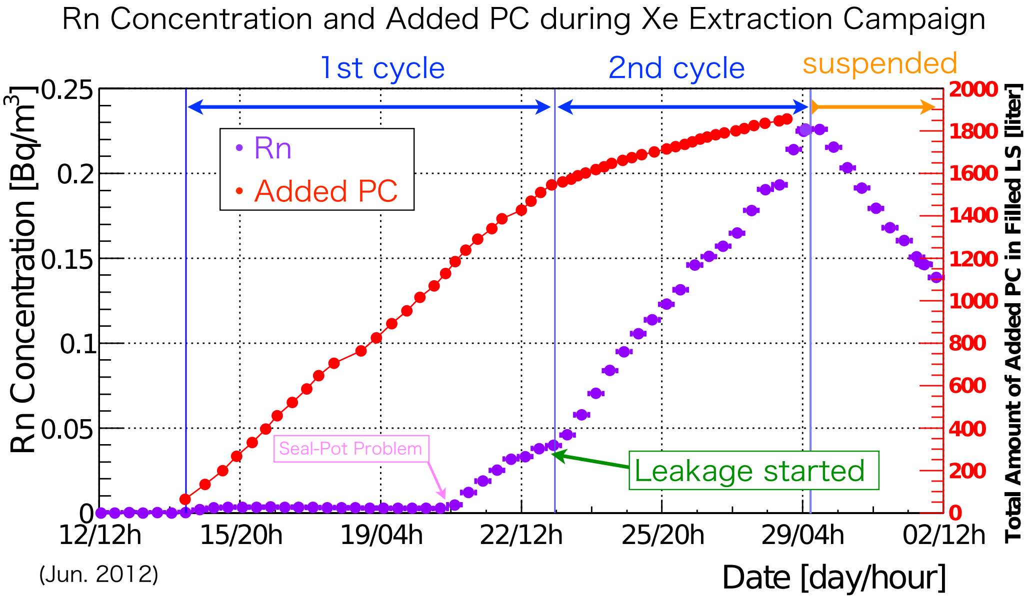

Fig 8.2: Rn concentration and added PC amount during Xe extraction campaign. Left y-axis indicates radon concentration estimated with delayed coincidence events of ^{214}Bi-Po, and right y-axis indicates added PC amount to adjust the density of Zero-Xe-LS.

The second increase of radon concentration is caused by an accidental breakdown of diaphragm pump at dome area used to drain Xe-LS from IB. There was a leak at diaphragm part of the drain pump because of aging deterioration and bad operation with vacuum, as shown in Fig 8.3, and impurities were supplied to LS pumped up from IB. Radon concentration in IB rapidly increased in Fig 8.2, hence LS which contains the impurities is sent to IB again after degassed in the cycle. This campaign is suspended due to this accident, and resumed after replacement of diaphragm part. The impurities which contained not only radon was sent, and we can see additional background events after degassing in the cycle as discussed in the next section.

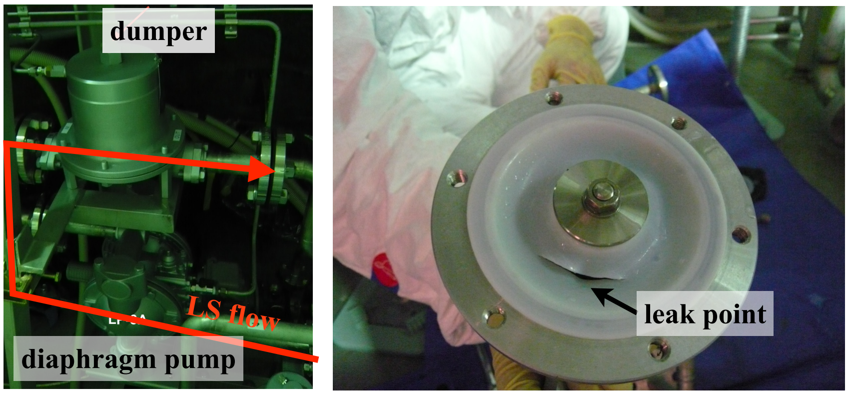

Fig 8.3: Pictures of diaphragm pump at dome area and the leak point.

Summary of the Campaign

Finally, 287.0 ± 0.5 kg of Xe has been collected in Xe-Storage bottles by Xe extraction campaign, corresponding to a collection efficiency of 90.8%. 1 kg of Xe remaining in the pipe lines at Xe system was collected by small sampling bottle. The disolved xenon in LS sent to LS25-Tank, estimated to be about 1.5 kg, will be collected in the future. The amount of remaining Xe in IB is estimated 18.5 ± 4.0 kg by the measurement with gas chromatography (0.12 - 0.17 wt% in the sample). The sum of collected and estimated amount of Xe is smaller than original amount in IB, so Xe may not be uniformly existing in the IB and not to be correctly measured as the weight fraction by the sampling.

In summary, Xe extraction campaign successfully collected over 90% of Xe from IB without any damage to IB in 25 days. The collected Xe was processed with a distillation tower borrowed from XMASS Collaboration in Tokyo University, and re-used for next Xe phase. The remaining Xe and Zero-Xe-LS in IB which may be contaminated with the impurities by accidental leak at diaphragm pump was washed away by new Dummy-LS to LS25-Tank, and Xe remaining in LS25-Tank will be collected at the end of KamLAND-Zen first phase.

8.2 Background Status after Xe Extraction Campaign

Xe extraction campaign finished on 8th July in 2012, and 16 days of data was acquired after that before new Dummy-LS Filling, the next stage of the purification campaign. Data with Zero-Xe-LS (less than 10% of original Xe amount in IB) corresponds run 11461-11489, and it is named DS-3. The procedure of analysis (event reconstruction, detector calibration and event selection) is the same as for DS-1 and DS-2. The livetime of DS-3 is calculated with the same method used for the double beta decay analysis (section 7.1.2), and it is 15.5 days.

The visible energy in DS-3 changed relative to DS-1 and DS-2 because Xe which decreases the light yield was extracted, and the concentration of PPO is decreased due to added PC. The energy correction is processed in the same manner as DS-2 with the peak of ^{214}Bi tagged by delayed coincidence method. The Zero-Xe-LS has blighter light intensity than before, and the difference of light intensity between inside (Zero-Xe-LS) and outside (KamLAND-LS) IB has also changed much. The original Xe-LS is 5% darker than KamLAND-LS, while Zero-Xe-LS is +11% blighter than KamLAND-LS. The simulation events for spectrum fitting is rebuilt with this parameters, and used for the background estimation in DS-3.

Fig 8.4 shows energy spectrum and the best fit of the backgrounds with energy and radius for each region equally divided by volume. The fitting with energy and radius is simultaneously processed for each region to estimate the external background rates from IB. Only $^{110\mathrm{m}}$Ag is introduced for 2.6 MeV peak for the internal (in LS) and the external backgrounds (from IB) both, and $^{110\mathrm{m}}$Ag peak can be seen in each regions. The livetime of DS-3 is only 15% of DS-2, therefore the statistical uncertainty is larger. The $2\nu\beta\beta$ decay rate is treated as free parameter because the uncertainty of the dissolved Xe mass in IB is large after Xe extraction campaign. We found that the internal backgrounds of ^{137}Cs and ^{134}Cs in LS can be seen while they are absent or negligibly small in DS-1 and DS-2. Most likely they were accidentally introduced by the leak at diaphragm pump, because the tightness of the system (Xe system, IB and the system between them) has been confirmed in the filtration campaign. The pump was made and assembled in the north of Kanto area, there was fall-out of radioactive impurities coming from Fukushima-I nuclear reactor as in Sendai.

The estimated external backgrounds from IB are used to constrain them in the time and energy spectrum fitting. The fitting result and energy spectrum are shown in Fig 8.5,

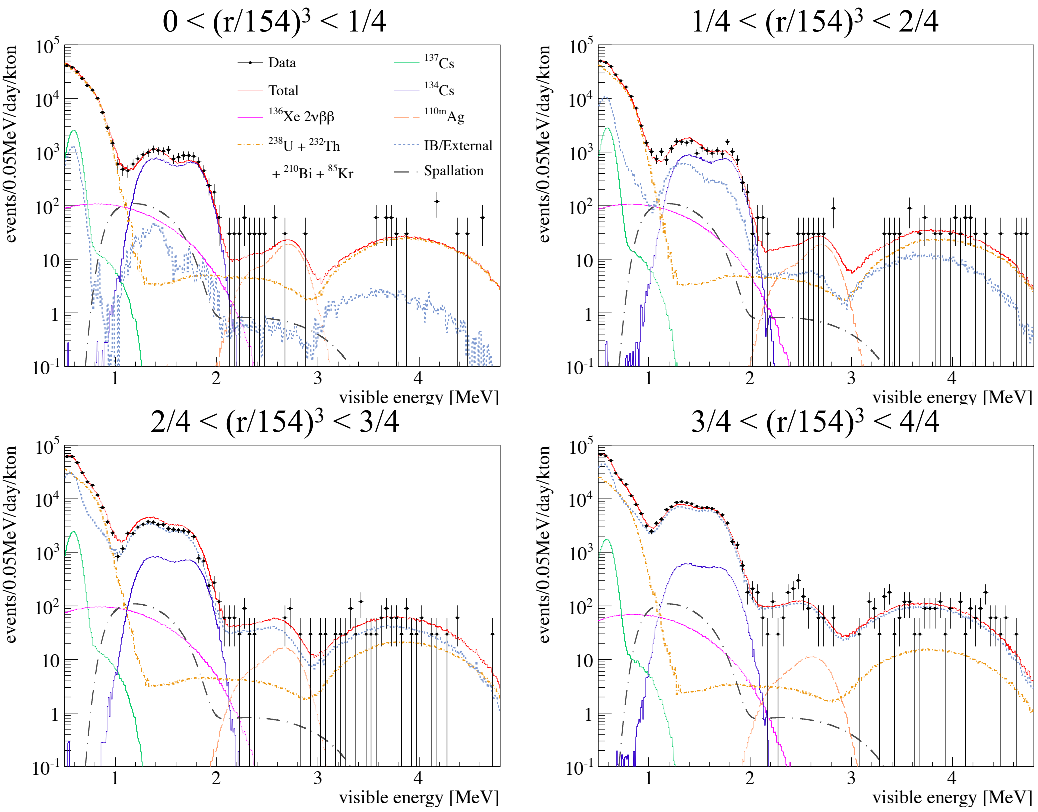

Fig 8.4: Energy spectrum and the best fit of the backgrounds with energy and radius for each region equally divided by volume in $0.5 < E_{\mathrm{vis}} < 4.8$ MeV in DS-3. The inlet part at bottom in IB is not used same as DS-2. The internal backgrounds of ^{137}Cs and ^{134}Cs in LS are added for DS-3, and their event rates are higher than external backgrounds of them from IB in central part.

and the event selection criteria are the same as DS-2 except the radius and fiducial volume. The radius for event selection is less than 120 cm to estimate the ^{110m}Ag event rate with smaller uncertainties of IB backgrounds. The essential point is that a ^{110m}Ag peak is observed while there is significantly less (less than 10% relative to DS-2) Xe dissolved in the LS. In addition to the shorter livetime of DS-3 than that of DS-2, the concentration of radon which generates ^{214}Bi background in the energy region of ^{110m}Ag in DS-3 is about twice as high as that of DS-2. This smaller statistics and higher ^{214}Bi event rate contribute to a large uncertainty of ^{110m}Ag event rate. The event rate of ^{110m}Ag in DS-3 is 222.1 ± 77.3 [events/day/kton], and the rate in DS-2 is 166.4 ± 23.1 [events/day/kton] which is re-calculated with the same assumptions as made for DS-3, i.e. R < 120 cm and introduction of only ^{110m}Ag.

The background status in DS-3 is changed from DS-2 because of contamination by the accidental leak during Xe extraction campaign. Two peaks of ^{134}Cs around $1.0 < E_{\mathrm{vis}} < 2.0$ MeV region are seen in Fig 8.5. The peak at 2.6 MeV is clearly observed in DS-3 without Xe, this is further evidence that the peak is not related to $0\nu\beta\beta$ but must be attributed to some other source, most pobably some ^{110m}Ag contamination.

The ^{110m}Ag background does not go with Xe gas but with liquid scintillator according to the result after Xe extraction, we concluded that removal of the background is possible by replacement of LS and LS distillation. The next stage of the purification campaign,

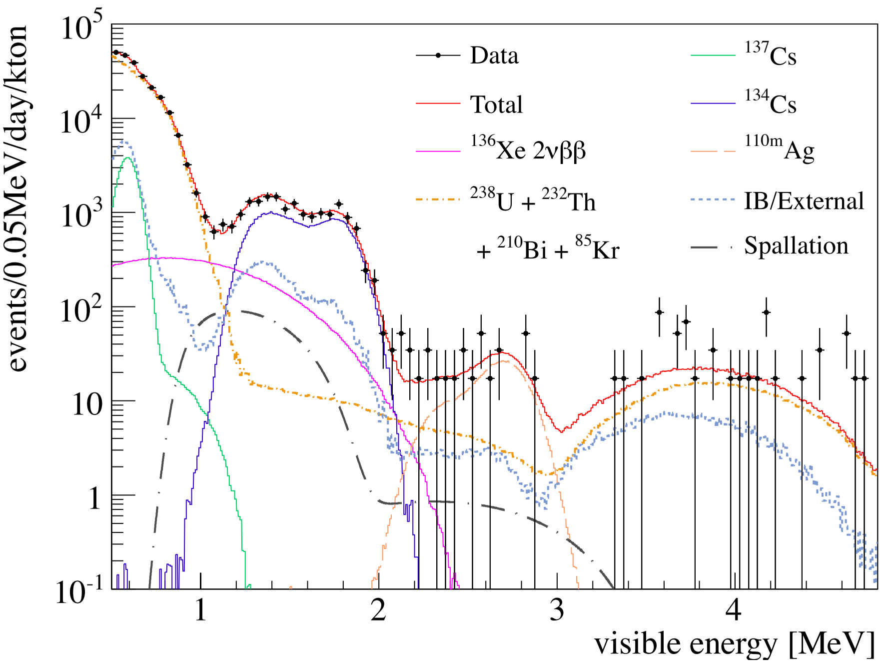

Fig 8.5: Energy spectrum and the best fit of the backgrounds in $0.5 < E_{\mathrm{vis}} < 4.8$ MeV in DS-3. The condition of fiducial volume decision is R < 120 cm to reduce the contribution from IB backgrounds, and events near inlet part is not used with same cut condition as DS-2. The internal backgrounds of ^{137}Cs and ^{134}Cs is additionally introduced in DS-3, and two peaks of ^{134}Cs around $1.0 < E_{\mathrm{vis}} < 2.0$ MeV region is observed instead of $2\nu\beta\beta$ spectrum. The peak of $^{110\mathrm{m}}$Ag is still seen around 2.6 MeV after Xe extraction.

new Dummy-LS Filling, has started in July 2012 to wash away LS in IB contaminated with the impurities of $^{110\mathrm{m}}$Ag and Cs. The purification campaign is for the next phase of KamLAND-Zen, only prospects are discussed in this thesis (see the next section).

8.3 Future Plans

There are some options for the future of KamLAND-Zen experiment including the purification campaign. The aim of the purification campaign is to remove the impurities providing the background which is expected as $^{110\mathrm{m}}$Ag, and the target of reduction factor is $< 1/100$. KamLAND-Zen 1.5th phase is a search for neutrinoless double beta decay with lower background than first phase. Next phase is also planned to use larger mass scale of Xe (800 $\sim$ 1,000 kg), optionally by pressurizing Xe-LS, with another recipe of the liquid scintillator and with upgrade of the detector. The upgrade of the detector is essentially desirable to make the sensitivity for neutrinoless double beta decay better to separate $0\nu\beta\beta$ signal and $2\nu\beta\beta$ background.

8.3.1 KamLAND-Zen 1.5th Phase (Purification Campaign)

The most extensional option is removal of the background with existing system and techniques, that is the purification, and it is on going (actually will be done by December

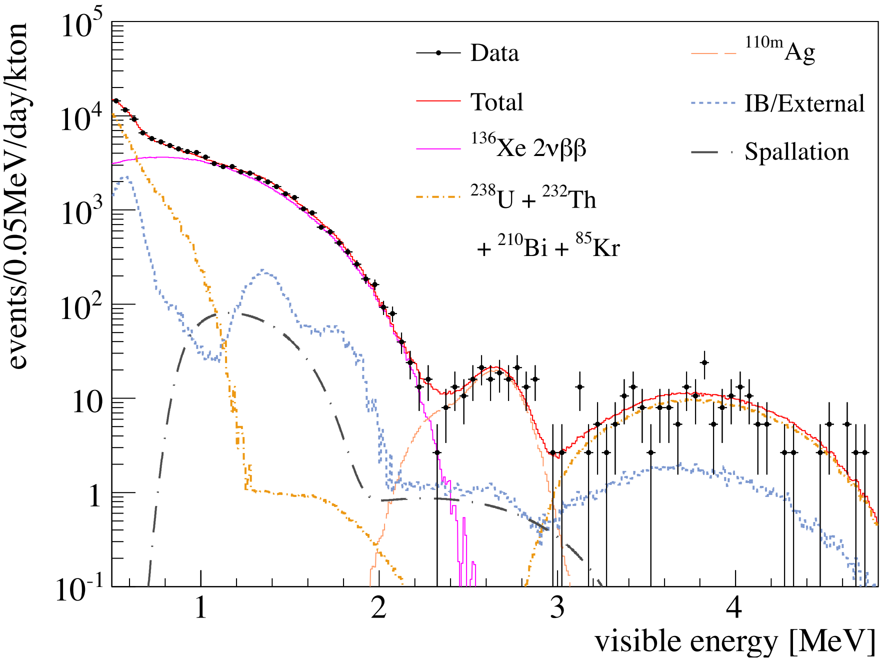

Fig 8.6: Energy spectrum and the best fit of the backgrounds in $0.5 < E_{\rm vis} < 4.8$ MeV in DS-2. The condition of fiducial volume selection is $R < 120$ cm for comparison with DS-3, and events near the inlet part is not used by applying the same cut condition as the original analysis. Only $^{110\rm m}$Ag background is introduced for the 2.6 MeV peak.

2013). The target of the purification campaign is to reduce the $^{110\rm m}$Ag background in factor 1/100, ideally zero. KamLAND-Zen 1.5th phase is the next stage of first phase without the $^{110\rm m}$Ag background before second phase.

If the background of $^{110\rm m}$Ag become negligible, the most dominant background is ^{10}C decay. Because ^{10}C is spallation product of cosmic muon, the production is unavoidable in KamLAND. The ^{10}C decay can be tagged, however, by the triple delayed coincidence with muon, neutron and ^{10}C, called ^{10}C tagging technique with dead-time free electronics –MoGURA– as explained in chapter 3. The latest study shows 84% tagging efficiency can be achieved with MoGURA, and the prospects for $0\nu\beta\beta$ decay search in the next phase include the introduction of ^{10}C tagging.

The sensitivity for half-life of $0\nu\beta\beta$ decay is calculated with the condition above ($^{110\rm m}$Ag reduction factor is 1/100 and ^{10}C tagging efficiency is 84%). The other conditions of the backgrounds such as concentration of radioactive impurities in LS and contribution from IB is assumed as same level as DS-1. Fig 8.7 shows sensitivity curves with running time of KamLAND-Zen 1.5th phase. The four Horizontal blue lines are the limits from KamLAND-Zen and combination of KamLAND-Zen and EXO-200. The sensitivity with original fiducial volume (R < 120 cm) same as previous work is better than that with larger fiducial volume (R < 135 cm) same as this work because the background contributions from the IB become more serious in the lower background scenario in the LS. They are drawn in red solid line and dotted line in Fig 8.7. According to the simulation, it takes around 150 days to improve on the current limit in this work, and KamLAND-Zen can independently exclude KK-Claim within 1 year.

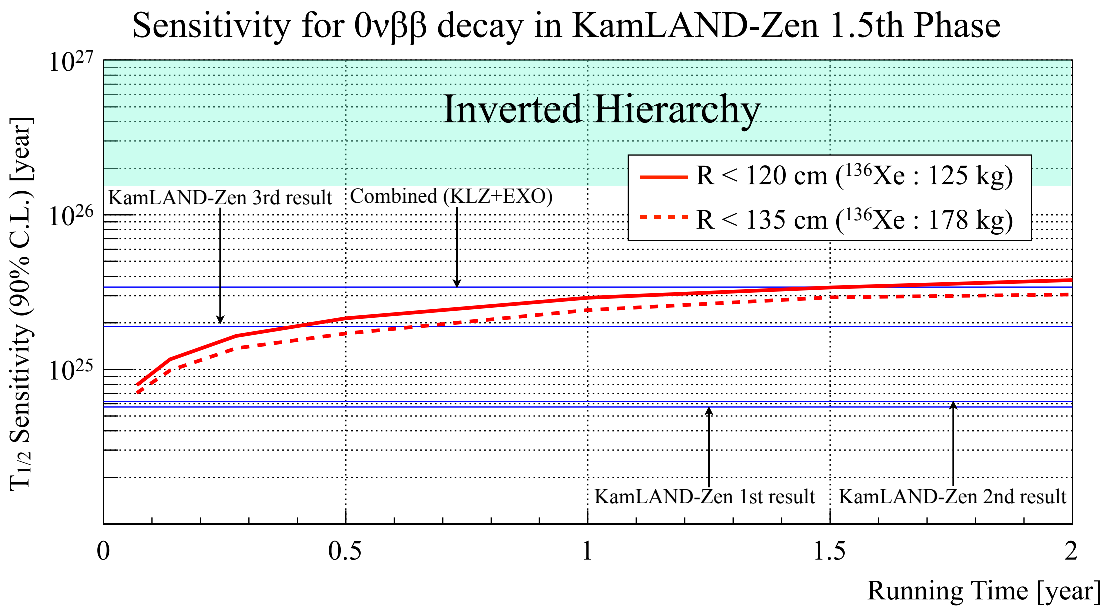

Fig 8.7: The sensitivity for $0\nu\beta\beta$ decay in KamLAND-Zen 1.5th phase by simulation. The x-axis is running time, and y-axis is the sensitivity for half-life of ^{136}Xe $0\nu\beta\beta$ decay. The sensitivity is calculated by the simulation with 1/100 of reduction of $^{110\mathrm{m}}$Ag by the purification campaign and 84% of ^{10}C is tagged by dead time free electronics MoGURA. The red solid line shows sensitivity curve with the fiducial volume R $<$ 120 cm, and red dotted line shows with the fiducial volume R $<$ 135 cm same condition in this work. Each horizontal blue lines indicate the lower limits of half-life at 90% C.L. given by KamLAND-Zen and Combined with KamLAND-Zen and EXO-200. We can update our limit in $\sim$ 5 month after start of KamLAND-Zen 1.5th phase.

The goals of KamLADN-Zen 1.5th phase are accomplishment of complete exclusion of KK-Claim with KamLAND-Zen alone, demonstration of the backgrounds reduction by the purification campaign and also search for ^{136}Xe $0\nu\beta\beta$ decay in the most sensitive region. After that, KamLAND-Zen will move to the next phase.

8.3.2 KamLAND-Zen 2nd Phase

The KamLAND-Zen 2nd phase is a challenge to approach the sensitivity that has never been accomplished, and finally to evaluate the structure of neutrino mass hierarchy. Fiducial mass of Xe in 2nd phase will be increased to the scale of 800 kg $\sim$ 1.0 ton to improve the sensitivity. The larger mass scale is the main improvement, although the sensitivity is just linearly improved by the factor. There are some options planed to improve the sensitivity in the 2nd phase summarized below.

- Higher Xe density by pressurizing
- Lower radioactive impurities in IB
- Better energy resolution with new LS recipe
- Better energy resolution by upgrade of the detector
- Higher ^{10}C tagging efficiency (currently 84%)

The expected event rate of $0\nu\beta\beta$ decay can be relatively increased by pressurizing because the background event rates are basically constant. On the other hand, higher

Xe density makes light yield of LS worse, and physical forces against IB become stronger in proportion to the pressure. A stronger IB against high pressure will be needed for pressurizing phase.

It is important for decision of fiducial volume to fabricate a cleaner IB. According to the original prospects, we can use 100% fiducial volume if radioactive impurities in the IB are sufficiently small as discussed in section 3.1.2. The radioactive impurities in current IB, however, are much higher than expected from the measurement of the film. There might have been problems in the fabrication in the clean room in Sendai because the impurities includes Cs which does not exist in natural and supplied by the fall-out from Fukushima-I. It should be possible to fabricate cleaner IB, and the processes and place are under consideration.

The upgrade of the liquid scintillator is also planned to get better energy resolution with brighter LS. The density and light transparency are also considerable performances of LS for the 2nd phase. Brighter LS can contribute to the energy resolution to separate the signal of $0\nu\beta\beta$ decay from the backgrounds.

On the other hand, there is an idea to upgrade photo-detector of KamLAND. Some PMTs are not available now after 10 years from the construction of the detector, and replacement of the photo-detector and use of new PMTs with higher quantum efficiency are considered because the legal inspection of the stainless tank will be done in the near future. In addition, mirrors of Winston-Cone shape for PMT has been developed to enlarge the photo-coverage of the inner detector. The photon collection efficiency will be 1.8 times improved by the cones.

The ^{10}C tagging efficiency is estimated to be 84% according to the latest study. However, It can be ideally improved to be 90% by tagging all neutron events after muon with MoGURA, and ^{10}C tagging forces to veto relatively longer periods compared the other vetoes. ^{10}C events will be dominant and serious background when we reached to higher sensitivity of $0\nu\beta\beta$ decay, and the improvement of the tagging is an important consideration for the 2nd phase.

Chapter 9

Discussion and Conclusion

The discussion with the limit on neutrinoless double beta decay from KamLAND-Zen experiment and the conclusion of the thesis are presented in this chapter.

9.1 Results and Discussion

The topics of results of this work and discussion are ^{136}Xe double beta decay, Majorana neutrino mass derived with the limit on $0\nu\beta\beta$ decay, and KK-claim which is a claim of the observation of $0\nu\beta\beta$ decay in ^{76}Ge.

9.1.1 ^{136}Xe Double Beta Decay

Half-life of $2\nu\beta\beta$ Decay

The two neutrino double beta decay of ^{136}Xe has not been observed before EXO-200 and KamLAND-Zen experiment, and there was only the lower limit of the half-life of $2\nu\beta\beta$ decay given by the DAMA experiment in 2002 [38]. The observation of ^{136}Xe $2\nu\beta\beta$ decay counts, theoretically and experimentally both, in nuclear physics. The half-life measurement of ^{136}Xe $2\nu\beta\beta$ decay may contribuite to the effort to determine the nuclear matrix element for $0\nu\beta\beta$ decay which depends on various models.

In this thesis, the analysis is optimized for $0\nu\beta\beta$ decay by enlargement of fiducial volume. The larger number of backgrounds events from IB made the uncertainty of $2\nu\beta\beta$ decay worse than previous results in spectrum fitting. On the other hands, the systematic uncertainties are improved by the update of analysis. The half-lives and their statistical uncertainties of $2\nu\beta\beta$ decay in DS-1 and DS-2 are calculated by the delta-χ^2 method. These half-lives are consistent with each other within their uncertainties, and consistent with the previous measurement of KamLAND-Zen in 2012 [33] [34]. The half-life of $2\nu\beta\beta$ decay is measured by KamLAND-Zen in 2012 [34] to be

$$T^{2\nu}_{1/2} = 2.38 \pm 0.02(stat) \pm 0.14(syst) \times 10^{21} \text{ [year]},$$

where the statistical error is 0.74% and the systematic error is 5.2%, respectively.

The half-lives measured by KamLAND-Zen are also consistent with the half-lives measured by EXO-200 in 2011 [35] and 2012 [36]. The half-life with the smallest uncertainties is measured by EXO-200 in 2013 [37] by an improvement of analysis method. The limit on the half-life given by DAMA in 2002 is 5 times longer than KamLAND-Zen and EXO-200 results, and the comparison with these measurements is summarized in Fig 9.1 and Table 9.1.

Nuclear Matrix Element of $2\nu\beta\beta$

The half-life of $2\nu\beta\beta$ decay is expressed in Equation 9.1 with phase space factor of

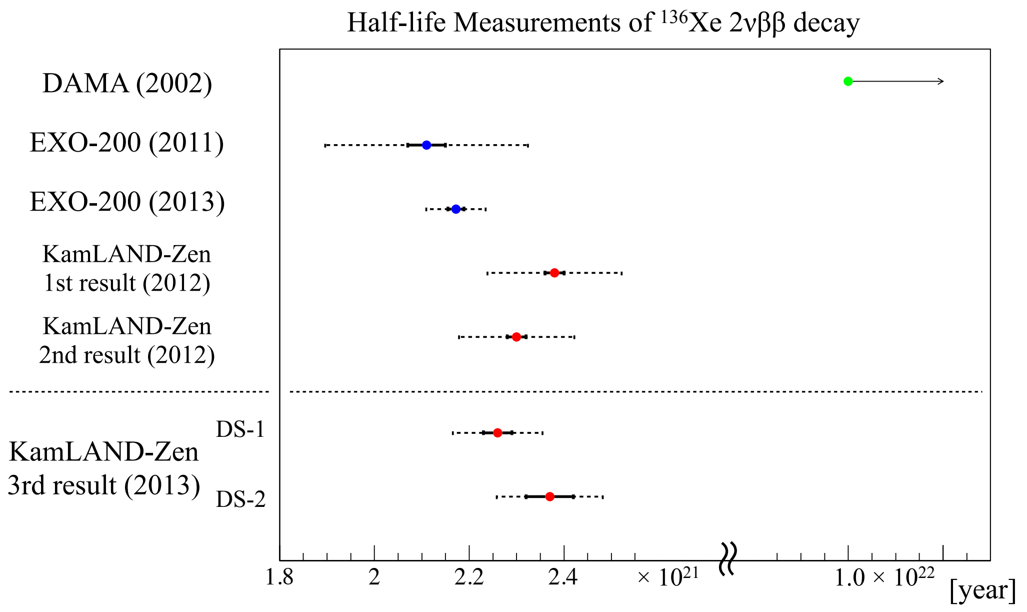

Fig 9.1: Summary of half-life measurements of ^{136}Xe $2\nu\beta\beta$ decay. DAMA experiment gives lower limit at 90% C.L. by green circle in 2002. EXO-200 and KamLAND-Zen shows their measurements by blue and red circle, and statistical uncertainties are indicated with solid error bars and quadratic sum of statistical and systematic uncertainties are shown with dotted error bars.

Table 9.1: Summary of half-life measurement of ^{136}Xe $2\nu\beta\beta$ decay. This table shows a limit of half-life by DAMA and measured half-lives by KamLAND-Zen and EXO-200 with statistical and systematic errors.

Measurements	$T^{2\nu}_{1/2}$ (Half-life of ^{136}Xe $2\nu\beta\beta$ decay) [year]
DAMA (2012) [38]	$> 1.0 \times 10^{22}$ at 90% C.L.
EXO-200 (2011) [35]	$2.11 \pm 0.04(stat) \pm 0.21(syst) \times 10^{21}$
EXO-200 (2012) [36]	$2.23 \pm 0.017(stat) \pm 0.22(syst) \times 10^{21}$
EXO-200 (2013) [37]	$2.165 \pm 0.016(stat) \pm 0.059(syst) \times 10^{21}$
KamLAND-Zen 1st result (2012) [33]	$2.38 \pm 0.02(stat) \pm 0.14(syst) \times 10^{21}$
KamLAND-Zen 2nd result (2012) [34]	$2.30 \pm 0.02(stat) \pm 0.12(syst) \times 10^{21}$
KamLAND-Zen 3rd result (2013) [1] (in this work)	DS-1 : $2.26 \pm 0.03(stat) \pm 0.09(syst) \times 10^{21}$ DS-2 : $2.37 \pm 0.05(stat) \pm 0.10(syst) \times 10^{21}$

$2\nu\beta\beta$ decay, $G^{2\nu}$ and nuclear matrix element (NME) of $2\nu\beta\beta$ decay, $M^{2\nu}$.

$$(T^{2\nu}_{1/2})^{-1} = G_{2\nu}|M^{2\nu}|^2 \tag{9.1}$$

The phase space factor can be calculated by the numerical integration of electron energy for each double beta decay nuclei, and here it is evaluated for ^{136}Xe as $G_{2\nu} = 4.9 \times 10^{-18}$[year^{-1}] with $g_A = 1.254$ [49]. The NME corresponding to half-life of $2\nu\beta\beta$ decay from KamLAND-Zen is calculated,

$$\begin{aligned} M^{2\nu} &= (T^{2\nu}_{1/2}G_{2\nu})^{-\frac{1}{2}} \\ &= (1.06 \pm 0.24) \times 10^{-2}\ [\mathrm{m_e^{-1}}] \\ &= (2.08 \pm 0.47) \times 10^{-2}\ [\mathrm{MeV^{-1}}]. \end{aligned}$$

Here, m_e is an electron mass, corresponding to 0.511 MeV. The NME value for $2\nu\beta\beta$ decay becomes a parameter of NME for $0\nu\beta\beta$ which is still not determined, to optimize the calculation.

Half-life of $0\nu\beta\beta$ Decay

Observation of $0\nu\beta\beta$ decay would demonstrate that the neutrino is a Majorana particle, it is one of the most interesting topics in neutrino physics. The neutrinoless double beta decay, however, has not been observed with exposure of 89.5 kg-year of ^{136}Xe.

The lower limit on half-life of ^{136}Xe neutrinoless double beta decay given by this work is the most sensitive measurement so far. We obtain a 90% C.L., upper limit of < 0.16 events/kg/year in units of ^{136}Xe, or lower limit of half-life,

$$T^{0\nu}_{1/2} > 1.9 \times 10^{25}\ \text{[year] (90\% C.L.)}.$$

This corresponds to a factor of 3.3 improvement over the first result of KamLAND-Zen [33].

The lower limit of half-life given by EXO-200 experiment in 2012 [36] is,

$$T^{0\nu}_{1/2} > 1.6 \times 10^{25}\ \text{[year] (90\% C.L.)}.$$

This measurement was the best limit before this work.

A combination (see section 7.4) of the limits from KamLAND-Zen and EXO-200, constructed by a χ^2 test tuned to reproduce the result, gives

$$T^{0\nu}_{1/2} > 3.4 \times 10^{25}\ \text{[year] (90\% C.L.)}.$$

This limit rightfully deserve the most sensitive limit on half-life of ^{136}Xe neutrinoless double beta decay in the world. KamLAND-Zen provided the first limit and the most sensitive limit, and the update history of limits are summarized in Fig 9.2

9.1.2 Majorana Neutrino Mass and KK-Claim

Similar to half-life of two neutrino double beta decay, half-life of neutrinoless double beta decay, $T^{0\nu}_{1/2}$ can be represented in equation 9.2.

$$(T^{0\nu}_{1/2})^{-1} = G_{0\nu}|M'^{0\nu}|^2\langle m_{\beta\beta}\rangle^2 \tag{9.2}$$

$G_{0\nu}$ is phase space factor of $0\nu\beta\beta$ decay, $M^{0\nu}$ is nuclear matrix element of $0\nu\beta\beta$ decay, and $\langle m_{\beta\beta}\rangle$ is Majorana neutrino mass as additional factor. Majorana neutrino mass $\langle m_{\beta\beta}\rangle$

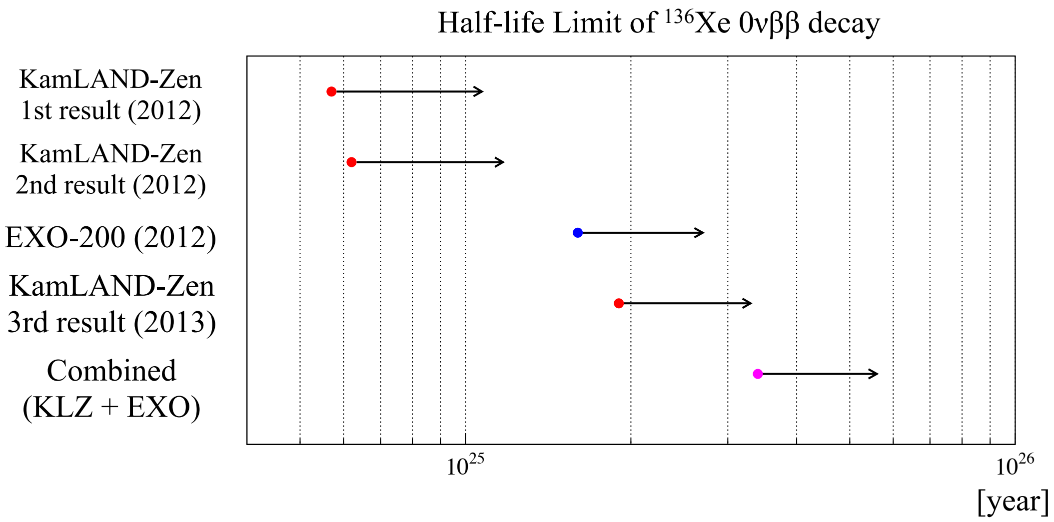

Fig 9.2: Summary of half-life limit of ^{136}Xe $0\nu\beta\beta$ decay. All points shows lower limits at 90% C.L.. Three red points are given by KamLAND-Zen, and two blue point is by EXO-200. A purple point is combined limit with limits from KamLAND-Zen 3rd result (this work) and EXO-200.

can be estimated with the other parameters in equation 9.2, and it is a hint for neutrino mass hierarchy as discussed in chapter 2.

However, $M^{0\nu}$ varies depending on the NME models and nuclei of $0\nu\beta\beta$. The quasi-particle random phase approximation (QRPA) has been used over many years for the calculation of $0\nu\beta\beta$ decay NMEs. The QRPA treats a large, single particle model space, but heavily truncates the included configurations. In the step of QRPA method, the linearized equations of motion are solved in order to describe small amplitude vibrational-like modes around the minimum. The violation of the Pauli exclusion principle is partially corrected in the renormalized version of QRPA (RQRPA). The nuclear matrix element $M'^{0\nu}$ is defined as

$$M'^{0\nu} = (\frac{g_A^{\mathrm{eff}}}{g_A})^2\, M^{0\nu}.$$

Here, g_A^{eff} is the quenched axial-vector coupling constant, and g_A is (unquenched) axial-vector coupling constant. The nuclear matrix element $M^{0\nu}$ consists of that of Fermi ($M_{\mathrm{F}}^{0\nu}$), Gamow-Teller ($M_{\mathrm{GT}}^{0\nu}$), and tensor ($M_{\mathrm{T}}^{0\nu}$) parts as

$$M^{0\nu} = -\frac{M_{\mathrm{F}}^{0\nu}}{(g_A^{\mathrm{eff}})^2} + M_{\mathrm{GT}}^{0\nu} - M_{\mathrm{T}}^{0\nu}\ .$$

We applied available $M^{0\nu}$ calculations of QRPA and RQRPA to convert to Majorana neutrino mass from half-life of ^{136}Xe $0\nu\beta\beta$ decay, and they are listed in Table 9.2 cited from [50]. They are categorized by the type of two-nucleon short-range correlations (SRC) considered, because the QRPA-like approaches originally do not allow the introduction of short-range correlations (SRCs) into the two-nucleon relative wavefunction. Three calculations of them are methods of introduction of correlation function or operater; Milller-Spencer Jastrow SRCs (Jastrow), Fermi hypernetted chain SRCs (FHCh), unitary correlation operator method SRCs (UCOM). The other two calculations are called as the coupled cluster method SRCs (CCM SRC); derived from the Argonne and CD-Bonn potentials based on an extension of the Brueckner theory. In addition, two different values of the axial coupling constant, free nucleon $g_A^{\mathrm{eff}} = g_A = 1.254$ and quenched $g_A^{\mathrm{eff}} = 1.0$, are taken into account. The strength of the particle-particle interaction is adjusted so the experimental value of the $2\nu\beta\beta$ decay nuclear matrix element is correctly reproduced. The value of $\langle M'^{0\nu}\rangle$ is essentially independent of the size of the single-particle basis and rather stable with respect to the possible quenching of the g_A.

Table 9.2: Averaged $0\nu\beta\beta$ nuclear matrix element $\langle M'^{0\nu}\rangle$ for ^{136}Xe and their variance σ (in parentheses) calculated within the QRPA and the RQRPA [50]. Different types of two-nucleon short-range correlations (SRC) are considered : Jastrow, FHCh, UCOM, Argonne and CD-Bonn. The strength of the particle-particle interaction is adjusted so the experimental value of the $2\nu\beta\beta$ decay nuclear matrix element is correctly reproduced. Both free nucleon ($g_A^{texteff} = g_A = 1.254$) and quenched ($g_A^{\mathrm{eff}} = 1.0$) values of axial-vector coupling constant are considered.

		SRC			CCM SRC	
g_A^{eff}	Method	Jastrow	FHCh	UCOM	Argonne	CD-Bonn
1.25	QRPA	2.16(0.13)	2.25(0.12)	2.73(0.13)	2.88(0.14)	3.23(0.14)
	RQRPA	2.02(0.12)	2.11(0.14)	2.54(0.15)	2.68(0.16)	3.00(0.17)
1.00	QRPA	1.70(0.09)	1.77(0.09)	2.12(0.11)	2.21(0.10)	2.47(0.09)
	RQRPA	1.59(0.09)	1.66(0.10)	1.97(0.11)	2.06(0.11)	2.30(0.12)

With these $M^{0\nu}$ values and uncertainties in Table 9.2, the half-life limit of ^{136}Xe $0\nu\beta\beta$ decay from combination of KamLAND-Zen and EXO-200 ($T_{1/2}^{0\nu} > 3.4 \times 10^{25}$ [year]) is converted to the upper limit of Majorana neutrino mass with the minimum and maximum values. The upper limit ranges in

$$\langle m_{\beta\beta}\rangle < (120 - 250) \ \ [\mathrm{meV}] \quad (90\% \ \mathrm{C.L.}),$$

and this is the strongest limit on Majorana neutrino mass among any double beta decay experiments in any nuclei considering available and reasonable NME calculations at this time.

Exclusion of KK-Claim

The observation of neutrinoless double beta decay of ^{76}Ge was reported by part of Heidelberg-Moscow Collaboration in 2006 [2] with half-life

$$T_{1/2}^{0\nu}(^{76}\mathrm{Ge}) = 2.25\ ^{+0.44}_{-0.31} \times 10^{25}\ [\mathrm{year}].$$

This measurement, however, is controversial in double beta decay community, and this claim (KK-Claim) should be pursued by another measurements.

Because of different double beta decay nuclei (^{136}Xe and ^{76}Ge), test of the claim depends on the NME models and calculations.

The comparisons have done on Majorana neutrino mass scale with each NME calculations and models. NME calculations and models we adopted are the QRPA and RQRPA calculations in Table 9.2 [50], the generating coordinate method (GCM) [51], the nuclear shell model (NSM) [52] and the microscopic interacting boson model (IBM-2) [53]. The nuclear matrix element values for ^{136}Xe $0\nu\beta\beta$ dcay provided with the latter three models are listed in Table 9.3. The phase space factors $G_{0\nu}$ for conversion to Majorana neutrino mass are same ones used in each NME calculation.

Table 9.3: Nuclear matrix element $\langle M'^{0\nu} \rangle$ for ^{136}Xe $0\nu\beta\beta$ decay calculated with GCM [51], NSM [52] and IBM-2 [53].

Models	GCM	NSM	IBM-2
$M^{0\nu}$	4.20	1.77	3.67

The predicted Majorana neutrino mass with each NME models for ^{76}Ge from KK-claim are shown in Fig 9.3 as shaded bands on the scalers calculated with same NME models for ^{136}Xe in logarithmic scale. The half-life limits of ^{136}Xe $0\nu\beta\beta$ from KamLAND-Zen and EXO-200 both are compatible with the prediction from KK-Claim. However, our combined limit has reached to the sensitivity to exclude the KK-Claim in all scalers calculated with available NME models and calculations. We find that the combined result refutes the KK-Claim at $> 97.5\%$ C.L. for all NME considered assuming that $0\nu\beta\beta$ decay proceeds via light Majorana neutrino exchange. While the statistical treatment of the NME uncertainties is not straightforward, even if we apply the uncertainties and correlations in [54], which assumes a statistical distribution of the NME for various (R)QRPA models and does not include a tuning of the parameter g_{pp} for ^{136}Xe based on its measured $2\nu\beta\beta$ decay half-life, we find the rejection significance is still 95.6% C.L..

9.2 Conclusion

The KamLAND-Zen performed as an experiment to search for neutrinoless double beta decay with KamLAND detector and 300kg of ^{136}Xe, resulting the exposure of 89.5 kg-year of ^{136}Xe in 2011-2012. Although the signal of $0\nu\beta\beta$ decay have not be observed, the lower limit on $0\nu\beta\beta$ half-life at 90% C.L. we obtained is the strongest limit in ^{136}Xe $0\nu\beta\beta$ decay with the highest statistics and the improvement of analysis. This updated limit is 3.3 times improved over the first result of KamLAND-Zen [33], and also it is better than the EXO-200 result [36]. The combined limit with KamLAND-Zen (this work) and EXO-200 furthermore becomes the best limit which enables to constrain the KK-Claim [2].

The comparison between experimental results on $0\nu\beta\beta$ half-life in ^{76}Ge and ^{136}Xe is shown in Fig 9.4. The diagonal lines are drawn with Majorana neutrino mass scale predicted with various NME calculations, and gray band which is indicates the half-life of ^{76}Ge $0\nu\beta\beta$ decay at 68% C.L. by KK-Claim is excluded by the combined limit. The rejection significance is over 97.5% C.L. for all NME calculations, or 95.6% when we apply the uncertainties and correlations discussed in [54]. KamLAND-Zen and EXO-200 demonstrated that we have arrived at an exciting new era in the field, and that the technology needed to judge the claimed ^{76}Ge $0\nu\beta\beta$ decay with other nuclei has been archived.

The search for neutrinoless double beta decay is now on the next stage after exclusion of KK-Claim. The next target of Majorana neutrino mass is a range of inverted hierarchy which is expected in lower than 50 meV shown in Fig 9.5. However, the KamLAND-Zen result is still limited by the background from $^{110\mathrm{m}}$Ag. Improved statistics on the distribution of $^{110\mathrm{m}}$Ag on the IB may help reveal the source of the contamination. In the meantime, we have removed the Xe from the Xe-LS by vacuum extraction and verified that the $^{110\mathrm{m}}$Ag rate in the LS remains at its present level. We try to distill the LS to

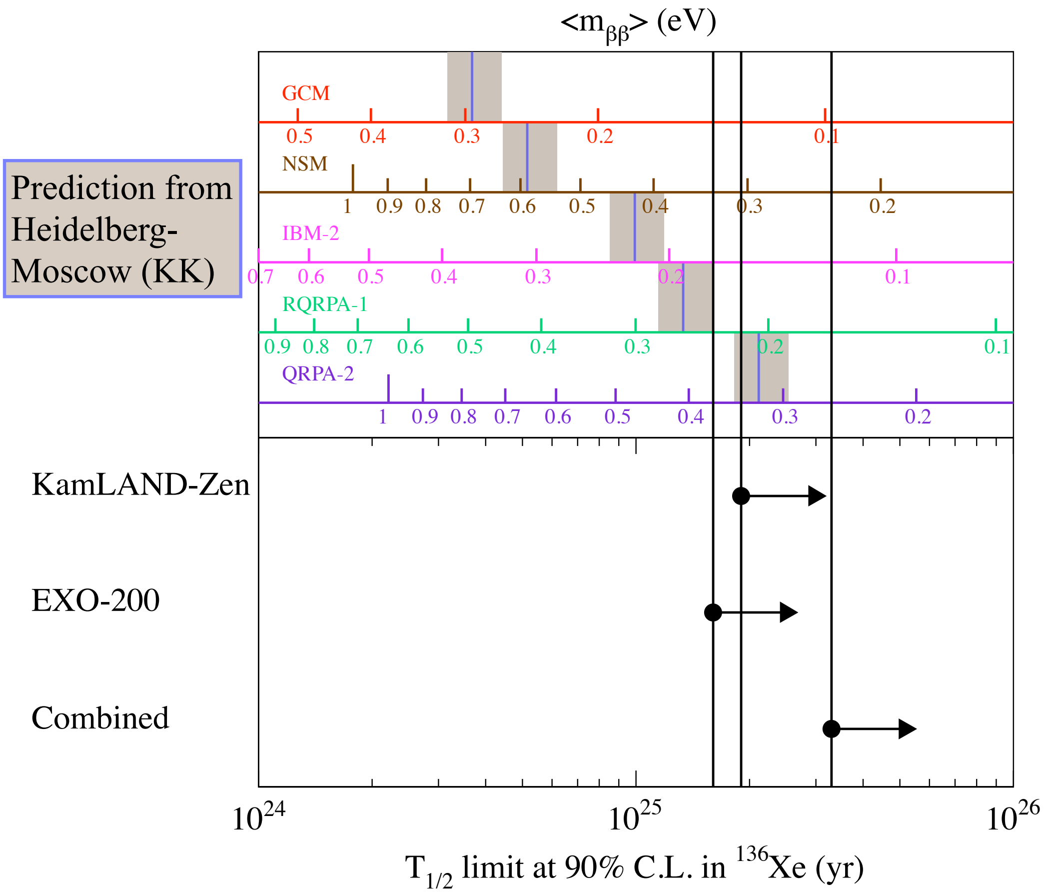

Fig 9.3: Scale of Majorana neutrino mass calculated from $0\nu\beta\beta$ limit. Three points and arrows shows the lower limit of ^{136}Xe $0\nu\beta\beta$ decay half-life from KamLAND-Zen, EXO-200 and the combination of them in lower graph, and five color lines in upper graph are Majorana neutrino mass $\langle m_{\beta\beta}\rangle$scalers of each NME models in logarithmic scale. The shaded bands shows prediction of $\langle m_{\beta\beta}\rangle$from KK-Claim converted with same NME model as the scaler.

remove the $^{110\mathrm{m}}$Ag, while we also pursue options for IB replacement and further detector upgrades to approach the range of inverted hierarchy. At the moment, we will report update of double beta decay measurement without $^{110\mathrm{m}}$Ag background after purification (distillation) work.

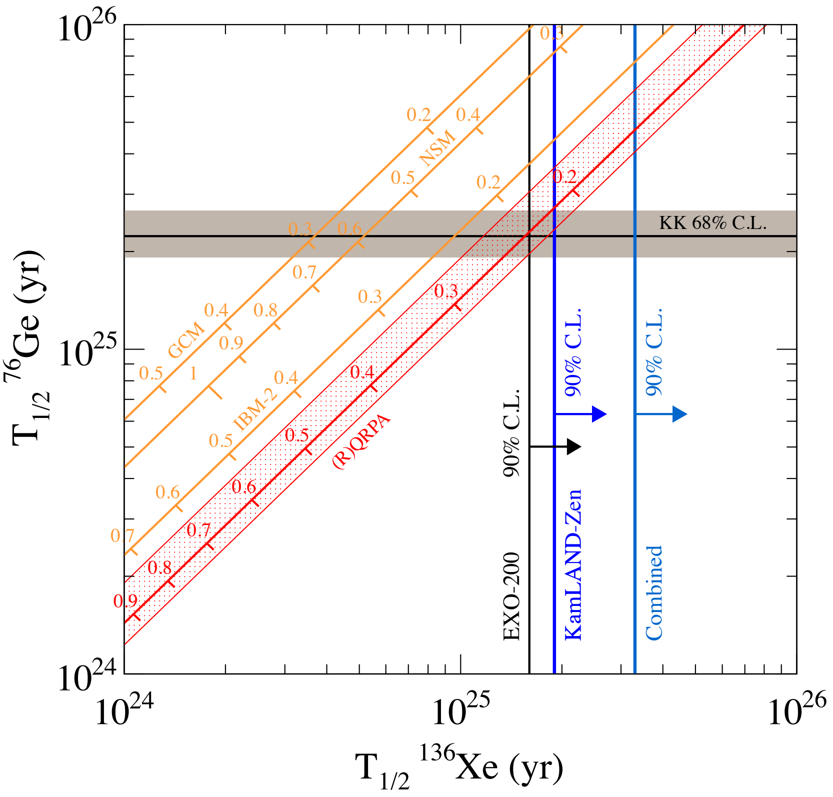

Fig 9.4: Comparison between experimental results on $0\nu\beta\beta$ half-life ($T^{0\nu}_{1/2}$) in ^{76}Ge and ^{136}Xe. The 68% C.L. limit from the KK-Claim in s indicated by the shaded band. The limits for KamLAND-Zen (this work), EXO-200, and their combination are shown at 90% C.L. The correlation between the ^{76}Ge and ^{136}Xe half-lives predicted by various NME calculations is drawn as diagonal lines together with the $\langle m_{\beta\beta}\rangle$scale of logarithm (the unit is eV). The band for QRPA and RQRPA represents the range of these NME calculations under the variation of model parameters.

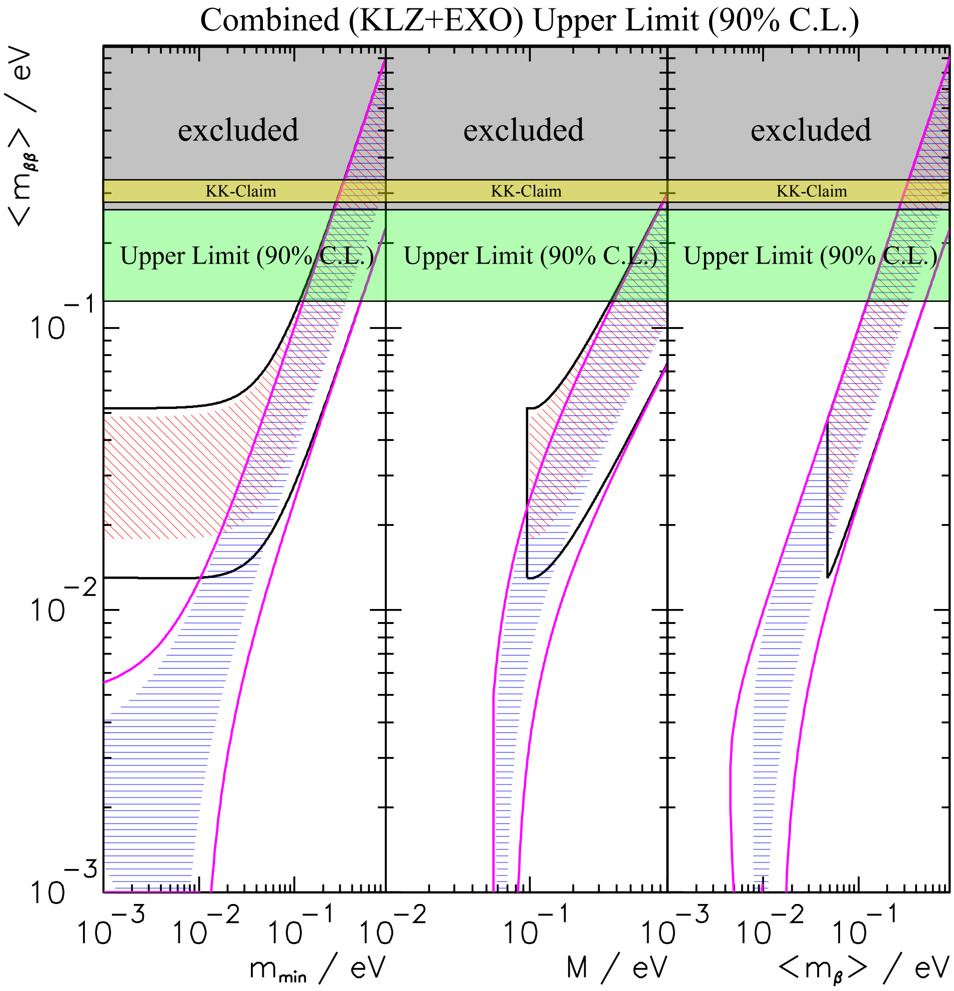

Fig 9.5: The limit on neutrino mass and hierarchy with Majorana neutrino mass. The left panel shows the dependence of $\langle m_{\beta\beta}\rangle$on the absolute mass of the lightest neutrino $\mathrm{m_{min}}$. The middle panel shows $\langle m_{\beta\beta}\rangle$as a function of the summed neutrino mass M, while the right panel depicts $\langle m_{\beta\beta}\rangle$as a function of the mass m_{β}. The yellow bands (KK-Claim) indicate the Majorana neutrino mass range by the claim of evidence for ^{76}Ge $0\nu\beta\beta$ decay. The green bands (this work) are upper limit at 90% C.L. by the combined limit of ^{136}Xe $0\nu\beta\beta$ decay from KamLAND-Zen and EXO-200. The gray bands are excluded region (including KK-Claim) by this work. The original panels (without bands) is given by [10].

Appendix A

Properties of Radioactive Isotopes

A.1 Decay Chains in Nature

A.1.1 ^{238}U

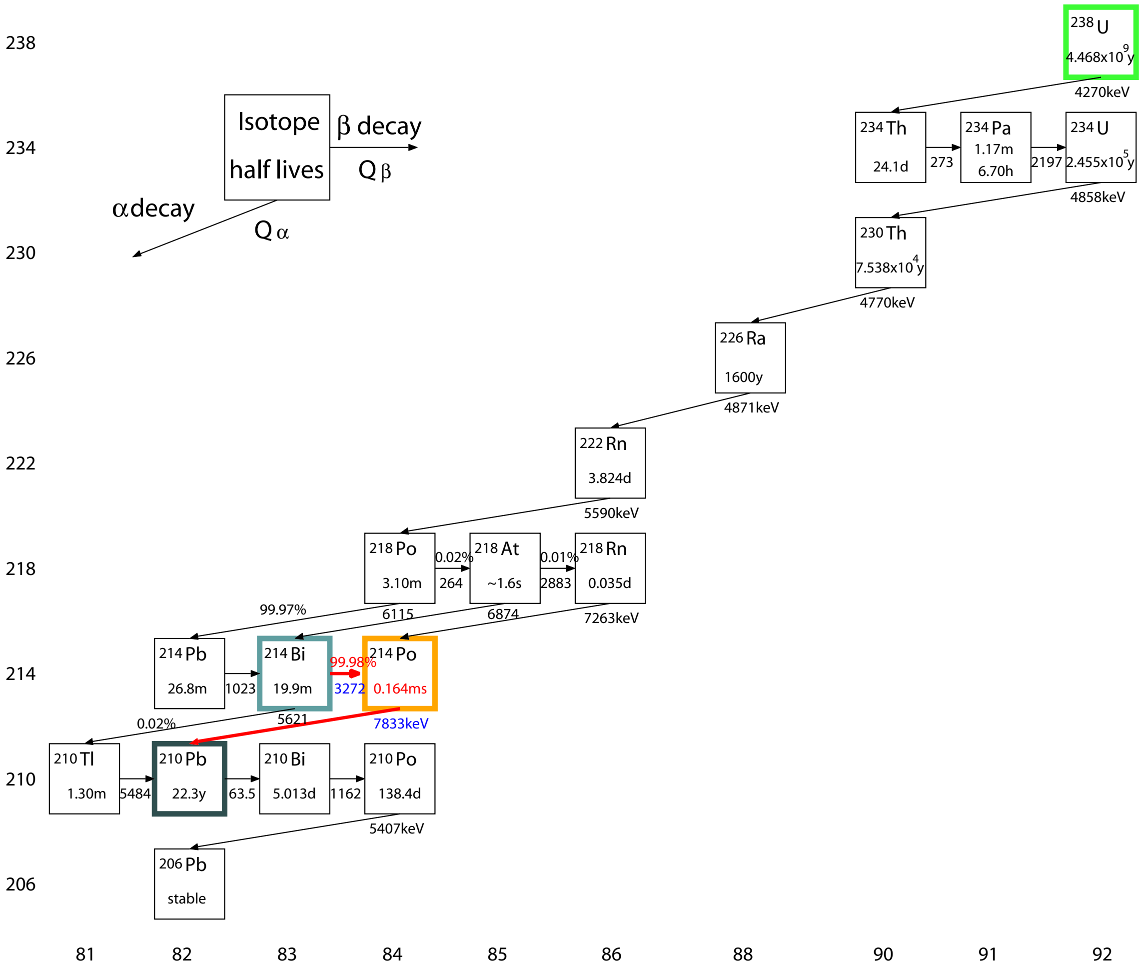

Fig A.1: ^{238}U decay chain

A.1.2 ^{232}Th

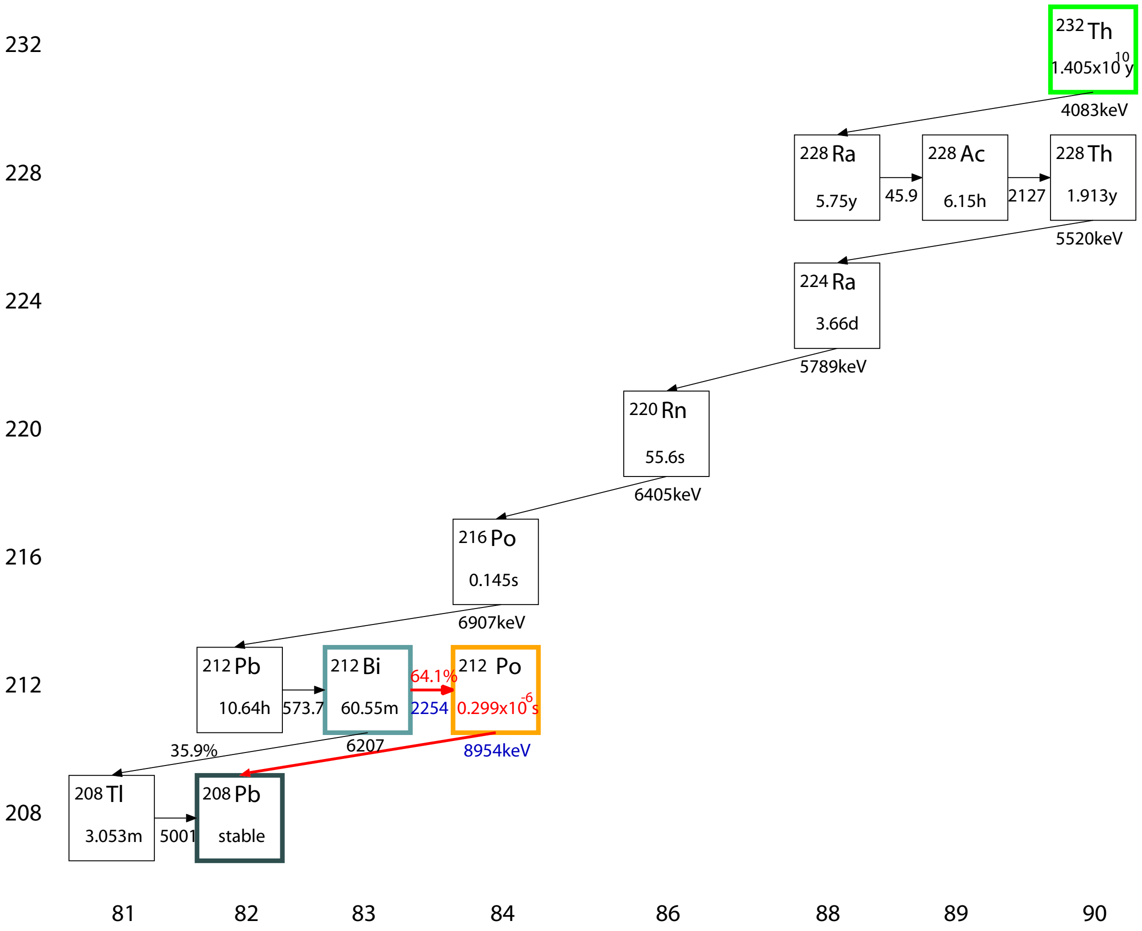

Fig A.2: ^{232}Th decay chain

A.2 Level Diagrams of Isotopes Observed in KamLAND-Zen

A.2.1 ^{134}Cs and ^{137}Cs

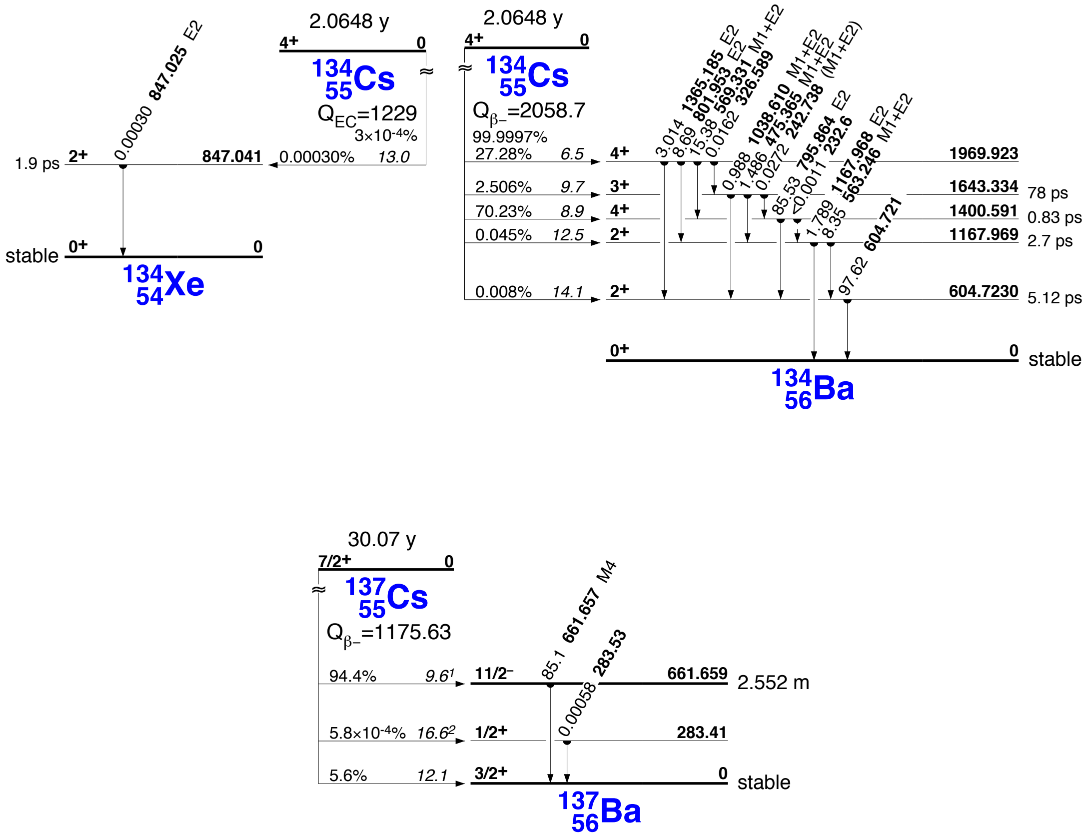

Fig A.3: Level diagram of ^{134}Cs and ^{137}Cs [11].

A.2.2 ^{11}C and ^{10}C

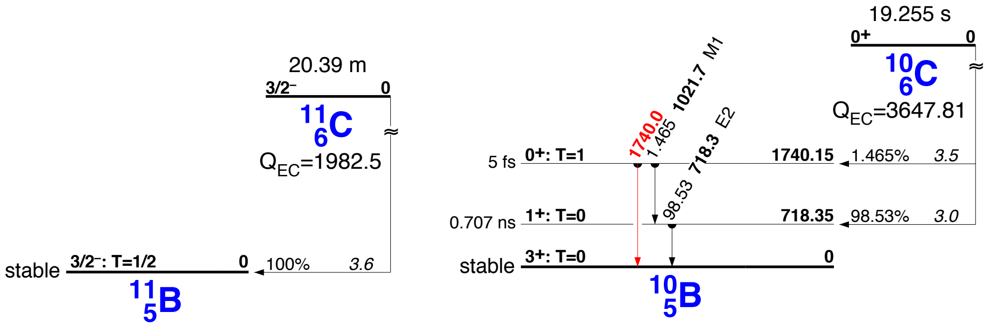

Fig A.4: Level diagram of ^{11}C and ^{11}C [11].

A.2.3 ^{110m}Ag, ^{208}Bi, ^{88}Y and ^{60}Co

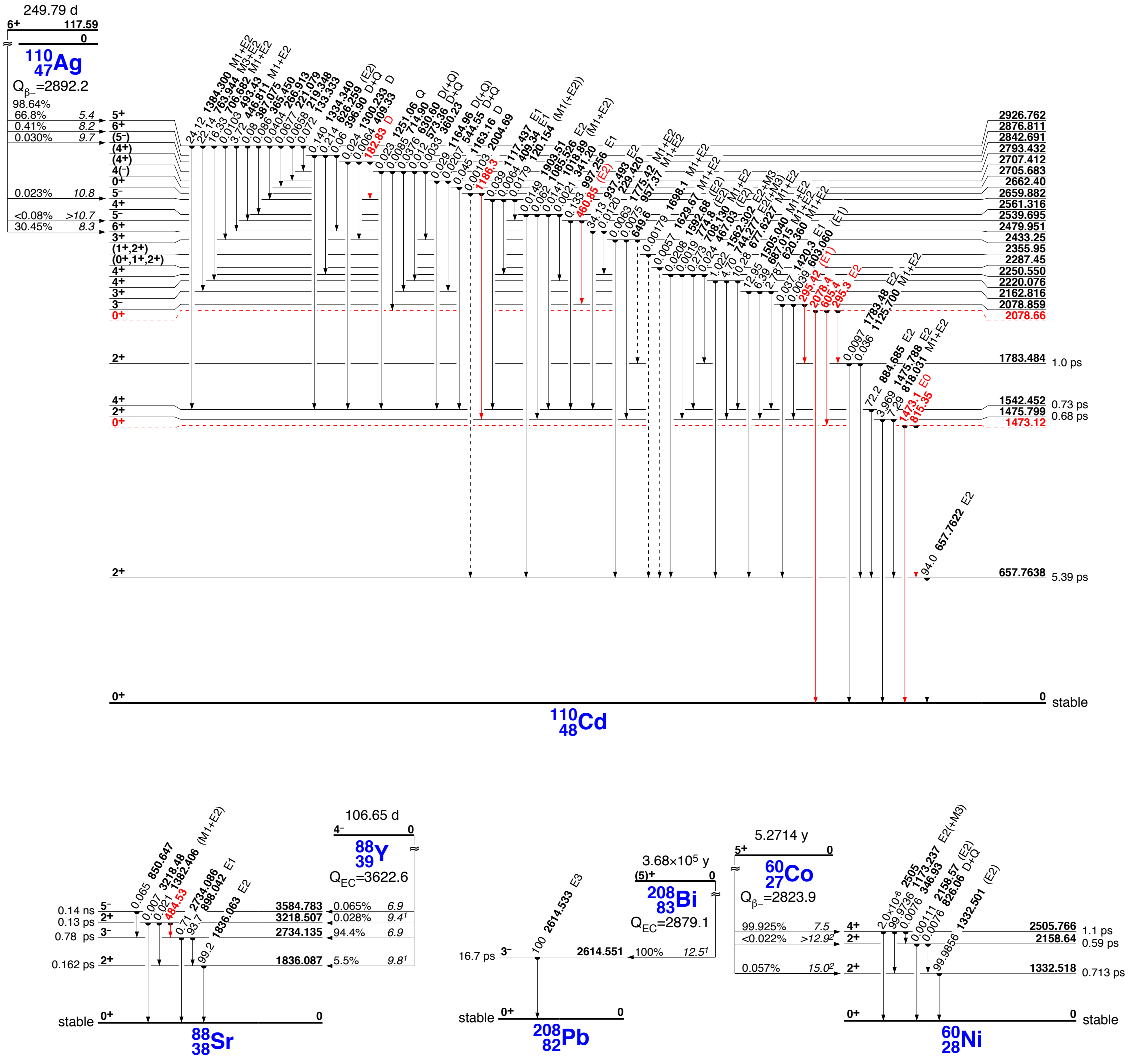

Fig A.5: Level diagram of ^{110m}Ag, ^{208}Bi, ^{88}Y and ^{60}Co as candidates of unexpected background [11].

A.2.4 ^{208}Tl

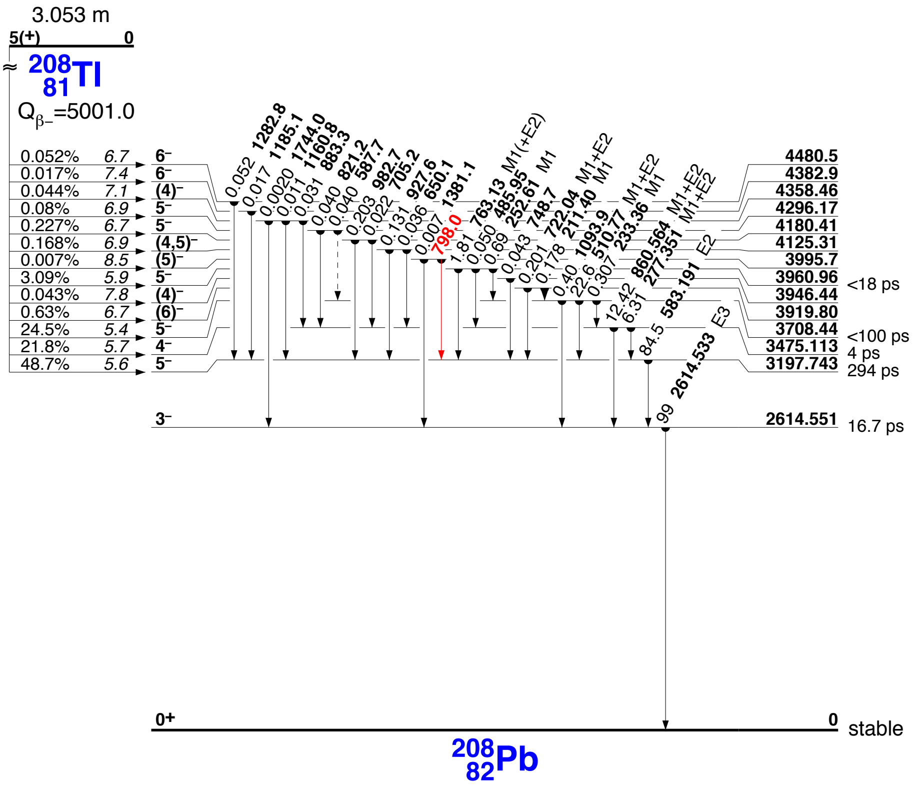

Fig A.6: Level diagram of ^{208}Bi [11].

Bibliography

[1] A. Gando, *et al.*, (KamLAND-Zen Collaboration), *Phys. Rev. Lett.* **110**, 062502 (2013).

[2] H. V. Klapdor-Kleingrothaus and I. V. Krivosheina, *Mod. Phys. Lett. A* **21**, 1547 (2006).

[3] W. Pauri, Letter to L. Meitner and her colleagues (letter open the participants of the conference in Tübingen)(1930), recorded in W. Pauli, Wissenschaftlicher Briefwechsel, Band II (Springer, Berlin, 1985) S.39; the first publication was given in W. Pauli, Septieme Conseil de Physique Solvay 1933: Noyaux Atomiques, Paris 1934, p.324f.

[4] E. Fermi, Ricercha Scient. 2, No 12 (1933); *Z. Phys.* **8**, 161 (1934).

[5] F. Reines and C. L. Cowan, Jr., *Nature* **178**, 446, (1956); C. L. Cowan *et al.*, *Science* **124**, 103 (1956).

[6] G. Danby, *et al.*, *Phys. Rev. Lett.* **9** 36 (1962).

[7] K. Kodama, *et al.*, *Phys. Lett. B* **504**, 218 (2001).

[8] ALEPH, DELPHI, L3, OPAL, and SLD Collaborations, and LEP Electroweak Working Group, and SLD Electroweak Group, and SLD Heavy Flavour Group, *Phys. Reports* **427**, 257 (2006).

[9] J. N. Bahcall and R. Davis, *SCIENCE* **191**, 264 (1976).

[10] J. Beringer, *et al.*, (Particle Data Group), *Phys. Rev. D* **86**, 010001 (2012).

[11] R. B. Firestone, Table of Isotopes (Eighth Edition, 1999 Update) (1999).

[12] G. Cowan, STATISTICAL DATA ANALYSIS, *OXFORD SCIENCE PUBLICATIONS* (1998).

[13] National Nuclear Data Center, Evaluated and Compiled Nuclear Structure Data: ENSDF Dataset Retrieval, http://www.nndc.bnl.gov/ensdf/ .

[14] H. Murayama, Neutrino Physics, http://hitoshi.berkeley.edu/neutrino/

[15] G. L. Fogli *et al.*, *Phys. Rev. D* **86**, 013012 (2012).

[16] CERN, ROOT — A Data Analysis Framework, http://root.cern.ch/ .

[17] K.N. Abazajian *et al.*, *Astropart. Phys.* **35**, 177 (2011).

[18] P. A. R. Ade *et al.*, (Planck Collaboration), arXiv:1303.5076, to be published in *Astrophys. J.*

[19] C. L. Bennett *et al.*, arXiv:1212.5225, to be published in *Astrophys. J. Supp.*

[20] J. Dunkley *et al.*, *JCAP* **1307**, 025 (2013).

[21] C. Weinheimer and K. Zuber, *Ann. Phys.* **525**, 565 (2013).

[22] V. N. Aseev *et al.*, *Phys. Rev. D* **84**, 112003 (2011).

[23] Ch. Kraus, *et al.*, *Eur. Phys. J. C* **40**, 447 (2005).

[24] A. S. Barabash, *Phys. Rev. C*, **81** 035501, (2010).

[25] J. J. Gómez-Cadenas, *et al.*, *Riv. Nuovo Cim.* **35**, 29 (2012); arXiv:1109.5515v2 [hep-ex].

[26] G. Pantis, *et al.*, *Phys. Rev. C*, **53** 695, (1996).

[27] F. Simkovic, *et al.*, *Phys. Rev. C*, **60** 055502, (1999).

[28] K. Eguchi, *et al.*, (KamLAND Collaboration), *Phys. Rev. Lett.* **90**, 021802 (2003).

[29] T. Araki, *et al.*, (KamLAND Collaboration), *Phys. Rev. Lett.* **94**, 081801 (2005).

[30] S. Abe, *et al.*, (KamLAND Collaboration), *Phys. Rev. Lett.* **100**, 221803 (2008).

[31] S. Abe, *et al.*, (KamLAND Collaboration), *Phys. Rev. C* **81**, 025807 (2010).

[32] S. Abe, *et al.*, (KamLAND Collaboration), *Phys. Rev. C* **84**, 035804 (2011).

[33] A. Gando, *et al.*, (KamLAND-Zen Collaboration), *Phys. Rev. C* **85**, 045504 (2012).

[34] A. Gando, *et al.*, (KamLAND-Zen Collaboration), *Phys. Rev. C* **86**, 021601 (2012).

[35] N. Ackerman, *et al.*, (EXO Collaboration), *Phys. Rev. Lett.* **107**, 212501 (2011).

[36] M. Auger, *et al.*, (EXO Collaboration), *Phys. Rev. Lett.* **109**, 032505 (2012).

[37] B. Albert, *et al.*, (EXO Collaboration), *arXiv*:1306.6106v3 (2013).

[38] R.Bernabei, *et al.*, *Phys. Lett. B* **546**, 23 (2002).

[39] H. V. Klapdor-Kleingrothaus, A. Dietz, H. L. Harney, I. V. Krivosheina, *Mod. Phys. Lett. A* **16**, 2409 (2001).

[40] H. V. Klapdor-Kleingrothaus, I.V. Krivosheina, A. Dietz and Chkvorets, *Phys. Lett. B* **586**, 198-212 (2004).

[41] M. Agostini et al. (GERDA Collaboration) *Phys. Rev. Lett.* **111**, 122503 (2013)

[42] S. Umehara, *et al.*, *Phys. Rev. C* **78**, 058501 (2008).

[43] A. S. Barabash, and V. B. Brudanin, (NEMO Collaboration), *Phys. Atom. Nucl.* **74**, 312 (2011).

[44] J. Argyriades, *et al.*, (NEMO-3 Collaboration), *Nucl. Phys. A* **847**, 168 (2010).

[45] F. A. Danevich, *et al.*, *Phys. Rev. C* **68**, 035501 (2003).

[46] E. Andreotti, *et al.*, *Astropart. Phys.* **34**, 822 (2011).

[47] H. V. Klapdor-Kleingrothaus, *et al.*, *Eur. Phys. J. A* **12**, 147 (2001).

[48] C. E. Aalseth, *et al.*, (IGEX Collaboration), *Phys. Rev. D* **65**, 092007 (2002).

[49] J. Suhonen and O. Civitarese, *Phys. Rep.* **300**, 123 (1998).

[50] A. Faessler and V. Rodin and F. Šimkovic *J. Phys. G* **39**, 124006 (2012).

[51] T. R. Rodríguez and G. Martínez-Pinedo, *Phys. Rev. Lett.* **105**, 252503 (2010).

[52] J. Menéndez, A. Poves, E. Caurier, and F. Nowacki, *Nucl. Phys. A* **818**, 139 (2009).

[53] J. Barea, J. Kotila, and F. Iachello, *Phys. Rev. Lett.* **109**, 042501 (2012).

[54] A. Faessler, *et al.*, *Phys. Rev. D* **79**, 053001 (2009).

[55] G. J. Feldman and R. D. Cousins, Phys. Rev. D **57**, 3873 (1998).

[56] W. C. Haxton and G. J. Stephenson, Jr., *Prog. Part. Nucl. Phys.* **12**, 409 (1984).

[57] P. Napolitani *et al.*, *Phys. Rev. C* **76**, 064609 (2007).

[58] S. R. Elliott, V. E. Guiseppe, B. H. LaRoque, R. A. Johnson, and S. G. Mashnik, *Phys. Rev. C* **82**, 054610 (2010).

[59] A. S. Barabash *et al.*, *JINST* **6**, P08011 (2011).

[60] T. Watanabe, *et al.*, *Geochem. J.* **46**, 279 (2012).

[61] M. Aoyama, *et al.*, *Geochem. J.* **46**, 321 (2012).

[62] M. Redshaw, E. Wingfield, J. McDaniel and E. G. Myers, *Phys. Rev. Lett.* **98**, 053003 (2007).

[63] A. Gando, Doctor Thesis (First Results of Neutrinoless Double Beta Decay Search with KamLAND-Zen), Tohoku University (2012).

[64] H. Watanabe, Doctor Thesis (Comprehensive Study of Anti-neutrino Signals at KamLAND), Tohoku University (2011).

[65] K. Nakajima, Doctor Thesis (First Results from ^{7}Be Solar Neutrino Observation with KamLAND), Tohoku University (2009).